Microstructural evolution of polycrystalline ice during non-steady state creep

Meike Elisabeth Seidemann

a thesis submitted for the degree of

Doctor of Philosophy

at the University of Otago, Dunedin,

New Zealand.

July 30, 2017

Abstract

The mechanics (rheology) of polycrystalline ice Ih are important to understand the dynamics of glaciers, ice sheets and icy moons in the outer solar system. Moreover, the microstructure and rheology of deforming polycrystalline ice are analogous to the creep of quartz in the Earth's crust. The exact relationship between naturally evolving microstructures in rocks (including polycrystalline ice) and aggregate rheology is still unconstrained. Creep experiments on polycrystalline ice offer a way to study this link but have been limited by the assumption that flow under mechanically constant conditions corresponds to a microstructural steady-state, meaning that deformation proceeds with some average microstructural property that does not change with time. To experimentally investigate non-steady state creep, a reliable sample-scale (10x mm) and grain-scale (μm) imaging method providing full crystallographic orientations is required.

In this thesis, the creep of ice under constant stress conditions is explored using experimentally deformed, initially fine-grained ($\sim$250 μm) laboratory-made polycrystalline ice with a homogeneous microstructure, random crystallographic preferred orientation and no impurities. High-temperature (-2°C), low-stress (0.2-0.6 MPa) uniaxial compression experiments target deformation conditions relevant for glaciological purposes. Particle image velocimetry on the surfaces of deforming samples was used in this context to reconstruct velocity fields and strain rate distributions. A triaxial creep apparatus is employed to reach the high confining stresses (50 MPa) and low temperatures (-33°C) needed to use polycrystalline ice as a rock analogue. Microstructural information was extracted post-deformation from statistically significant datasets and grain-scale maps collected with cryogenic electron backscatter diffraction.

Under glaciological deformation conditions, lobate grain boundaries and an increase in grain size from the starting material is observed at stresses of 0.6 MPa indicating that dislocation creep accompanied by grain boundary migration was prevalent. Samples deformed at 0.2 MPa show straight grain boundaries and an increase in grain size from the starting material and are interpreted to undergo normal grain growth. Grain boundary migration produces grain size distributions that are skewed towards large grain sizes, whereas normal grain growth yields bell-shaped distributions. Arithmetic mean and median grain

size results suggest that the driving force for strain-induced grain boundary migration is larger than for normal grain growth. Constraints on the driving forces and the finding that grain size statistics can be employed to distinguish between normal grain growth and grain boundary migration are relevant for glacier field studies, in which these recrystallisation mechanisms can be superimposed. Particle image velocimetry results show bands of high strain rate one order of magnitude above their surroundings, which change their location with progressive strain (transient shear zones). A spatial comparison of the particle image velocimetry results with post-deformation microstructures reveals that transient shear zones do not cause permanent microstructural modifications. The particle image velocimetry findings offer a new explanation for previously unexplained deviations in flow velocities in glaciers and ice sheets: the inert deformation heterogeneity of polycrystalline ice.

Rheological weakening during deformation, strain localisations with local thickening of the deformed samples and microstructural shear zones with a reduced grain size from the starting material are observed under deformation conditions allowing extrapolations to the creep of quartz. The local appearance of a few recrystallised grains with a reduced grain size from the starting material correlates with strain weakening. Constant strain rates are concurrent with interconnected bands of recrystallised grains in the strain-localised areas. The mechanical evolution can be explained with a two-phase model if the small recrystallised grains deform by grain-size sensitive creep. A load-bearing framework model with a few highly viscous recrystallised grains in a less viscous remnant grain matrix is associated with strain weakening. A constant strain rate is established when the highly viscous bands of recrystallised grains form a grid, representing an interconnected weak phase model. The coherence between the two-phase model and the experimental observations demonstrates the impact of a single changing microstructural property, as the grain size, on aggregate rheology. Recrystallised grains are found to have straight grain boundaries, mostly $\sim 90^\circ$ angles and the same crystallographic orientation to the shortening direction in adjacent grains. Straight grain boundaries and subgrains with 90° angles are also detected in kinked remnant grains. These similarities between kinked grains and recrystallised grains indicate that grain boundary formation by kinking could cause the grain size reduction necessary for shear zone development. Kinking in single

grains is characterised by slip on two crystallographic a-axes. The same slip direction is statistically preferred for the aggregate, confirming that kinking is the dominant strain accommodation and grain size reduction mechanism. The extension of kink boundaries into neighbouring grains suggests the ability of kinking to influence the local stress and strain field and to thus trigger shear zone propagation. This kink investigation illustrates the influence of grain-scale processes on aggregate rheology.

In summary, the findings of this thesis demonstrate that dynamically evolving rock microstructures are subject to localisation. These localisations are the determining factor of the rheology in cases where no change in deformation conditions or composition occurs and are the key to understand and predict the rock rheology. Knowledge of rock (including polycrystalline ice) rheology is crucial for related research disciplines as ice sheet modelling for climate purposes, rock mechanics in the crust associated with earthquake nucleation and our general understanding of the solar system.

Acknowledgements

Over the years, more people than I could have ever imagined have contributed to this journey. My first and foremost thanks goes to my primary supervisor, Dave Prior. I am grateful for his ongoing guidance and enthusiasm during this project, entertaining stories and the many opportunities to learn, travel and expand my horizon.

I also owe many thanks to the other members of the Otago ice team, my self-proclaimed partner in crime and fellow PhD student Matt Vaughan and Antarctica and isotope veteran Kat Lilly, who have greatly contributed to the scientific framework of this thesis. A special thanks belongs to Kat, for subconsciously making the 'winning' point that ultimately drove me to finish this PhD. I would also like to thank the ice students I have had the pleasure of getting to know and work with, Leeza, Cameron, Nathaniel, Lauren, Lisa, Harriet and Mathilde.

This project would have been impossible without the continued support of the ice research group in the physics department. Especially thanked are my secondary supervisor Pat Langhorne and Pat Wongpan for many helpful chats and open-end cold room usage and Shae from the reception for making sure no one dies in the process. Also thanked are the staff of the Otago Centre of Electron Microscopy, James (Jim) Woods and Leo van der Reins in the Anatomy workshop for technical support. Peter Fleury fixed countless thermocouples and made many people in the icelab particularly happy when he put gargoyles on a piece of equipment.

One of the highlights of my PhD was a research visit to MIT. Many thanks to Bill Durham and Narayana Golding for letting me use their gorgeous rig, teaching me and introducing me to a world of ice deformation as seen by planetary scientists and engineers. Tess Casswell and Narayana are also thanked for showing me around New England and Narayana for giving me one of the best pep talks ever.

A big thanks goes to the amazing staff and students of the Geology department, who made me feel welcome from the minute I walked in and for all the good conversations during morning and afternoon tea. Brent, Hamish, Damian and Luke have provided excellent support during various unexpected challenges. I would also like to thank my fellow grad students, office mates

and friends, Andy, Chris, Imogen, Jack, Kat, Rosie, Pepe, Matteo and Halal for many chats, Friday beers and funny moments.

Another huge part was played by the many healthcare professionals who have gradually helped me recover from a spinal and brain injury sustained three months into my PhD. I would like to acknowledge my amazingly creative physiotherapists, Anne and Claire, osteopaths YewJin and Charles, my GP Fiona Pickering from Student Health, Lucy from LWP, cognitive functioning and pain management specialist Fiona Partridge and Cathy from the Brain Injuries Association Otago. Kathy Halliwell from Student Visa Services is thanked for going above and beyond to help me make my chaotic recovery schedule work with the New Zealand student visa requirements.

Last not least, I would like to thank my family and friends for being supportive through this challenging time. So much credit belongs to my partner Kolja, most of all for having the brilliant idea of giving me the best gift and most powerful motivator, Hemi the dog. Thanks to my family back in Swabia, the United States and France- you have taught me so much and I would never have made it to New Zealand without you. Moreover, I would like to thank my incredible friends, Danni, Caro, Myrna, Felsi, Jenny, Vladi and Blasi, many of whom have literally travelled around the world to meet up with me. This thesis is dedicated to my grandparents, Linde and Hartl- you have inspired me.

Contents

List of Tables

List of Figures

List of common abbreviations

BDT - brittle-ductile transition zone

CPO - crystallographic preferred orientation, a synonym for lattice preferred orientation (LPO)

DCC - direct cross-correlation

DFT - discrete Fourier transform

DIC - digital image correlation

EBSD - electron backscatter diffraction

ECS - environmental control system

FFT - fast Fourier transform

GB - grain boundary

GBM - grain boundary migration

GBMR - grain boundary migration recrystallisation, also termed migration recrystallisation

GBS - grain boundary sliding

GSI -grain size insensitive

GSS - grain size sensitive

IPF - inverse pole figure

MAD - misorientation angle distribution

MIT - Massachusetts Institute of Technology

MP - megapixels

n\a - not available, not applicable, no answer

PIV - particle image velocimetry

SGRR - subgrain rotation recrystallisation, synonyms are polygonisation and rotation recrystallisation

ROI - region of interest in particle image velocimetry tool PIVlab

2D - two dimensional

3D - three dimensional

Chapter 1

Introduction

1.1 Creep of ice: a universal picture

The solid-state flow (creep) of polycrystalline ice is a universal process. Creep occurs in the Earth's major ice sheets of Antarctica and Greenland, glaciers on mountaintops and drives the dynamics of icy moons in the outer solar system. It is, therefore, no surprise that the creep of ice has been investigated by a variety of scientific disciplines with different terminologies, foci and agendas.

In its terrestrial setting, the creep of ice influences the Earth's climate system. Gravitational flow of both glaciers and ice sheets is often non-steady state and governed by rapid fluctuations (i.e. Vaughan, 2006), albeit with respect to different time and length scales. Comparatively broad-scale flow fluctuations influence ice sheet height and volume, which couples with atmospheric circulation and sea level on a global scale, respectively. On an even broader time scale, more gradual changes in ice flow are associated with long-term climate change (Clark *et al.*, 1999; Alley *et al.*, 2005). Relatively short-term ice shelf collapse occurs mechanically, and microstructural components, such as crystal size, crystal shape and crystallographic preferred orientation (CPO) are increasingly recognized to be of paramount importance to the overall rheological properties of polycrystalline ice masses (Pimienta and Duval, 1987; Cuffey *et al.*, 2000; Duval *et al.*, 2010; Piazolo *et al.*, 2013). For the reconstruction of paleo-flow patterns in ice sheets and for present-day ice sheet modelling, an understanding of the microstructural evolution and its relationship to deformation mechanisms and mechanical properties (rheology) is of fundamental importance in glaciology.

Much knowledge on the mechanics of ice deformation and the coupled underlying processes on a micro-scale can be derived from the material sciences, which have a long-standing tradition of investigating ice to constrain the overall physics of deformation.

Many of these studies with a focus on the ductile regime (Table 1.1, see Duval *et al.*, 2010 for a historical summary) have analysed the kinetics of specific dislocation mechanisms and yielded fundamental equations connecting the overall plasticity of crystalline solids to dislocation movements on an atom-scale (i.e. Orowan, 1940). Recent material sciences-based studies have taken advantage of the transparency of ice by employing X-ray Laue diffraction to further examine aspects of ice plasticity on a dislocation level (i.e. Chevy *et al.*, 2010).

Not only the mechanics and microstructural changes during the creep of terrestrial hexagonal ice Ih but also of its low-temperature polymorph, cubic ice Ic are required in the planetary sciences to gain insight into the dynamics of icy planets and moons in our solar system (Pappalardo *et al.*, 1998; Barr and McKinnon, 2007; Banks and Pelletier, 2008). Assessing the potential for a transition to grain size sensitive creep in ice Ih and the rheological repercussions of such a transition are, for instance, considered relevant to ice shelf stability on Jupiter's moon Europa (McKinnon, 1999) and the history and dynamics of martian polar deposits (Barr and Milkovich, 2008).

The creep of ice is also an inherent part of geology. Polycrystalline ice is a 'naturally occurring, solid crystalline material' and thus, per definition, a rock. Ice shares many of the creep characteristics of all rocks, including a power-law creep relationship and possible transition to grain size sensitive creep at low stresses for small grain sizes. Large-scale continental ice masses and ice shelves, like rock aggregates in the Earth's interior, exhibit folding and faulting (crevasse formation in ice terminology) (Koehle, 1964; Larour *et al.*, 2014; Bons *et al.*, 2016). Ductile shear zones as found in rocks below the brittle-ductile transition (Table 1.1) appear to be part of the natural deformation in glaciers (Petrenko and Whitworth, 1999; Maltman *et al.*, 2000). Most importantly for a geologic understanding of ice deformation, a conversion from the laboratory-derived Glen Flow Law for uniaxially deformed polycrystalline ice (Glen, 1952) to differential stresses employed in rock mechanics was developed by Nye, 1953. In its converted form, the equation is often referred to as the *Glen-Nye Flow Law* (section 1.4.2, equation 1.4).

In geology, polycrystalline ice is also an important analogue for quartz, the most abundant mineral in the Earth's upper crust. Similarities between ice and quartz include 1) a similar crystal system (ice is hexagonal, quartz is trigonal), 2) the operation of similar slip systems (see Fig. 3, Wilson *et al.*, 2014) and 3) a similar behaviour under dynamic recrystallisation at high-homologous temperatures (Hirth and Tullis, 1992; Stipp *et al.*, 2001, Fig. 1.1). The advantage of employing ice instead of quartz in laboratory creep experiments lies in the comparatively low pressures and low differential stresses required

to deform ice, which circumvents engineering complexities and enables the study of rock creep with large sample sizes. Moreover, strain rates in long-term ice creep experiments ($\sim 10^{-11}$ /s) are are slower than in quartz ($\geq 10^{-8}$ /s), facilitating extrapolations to geologic processes in the Earth's interior ($\sim 10^{-10}$-10^{-14} /s).

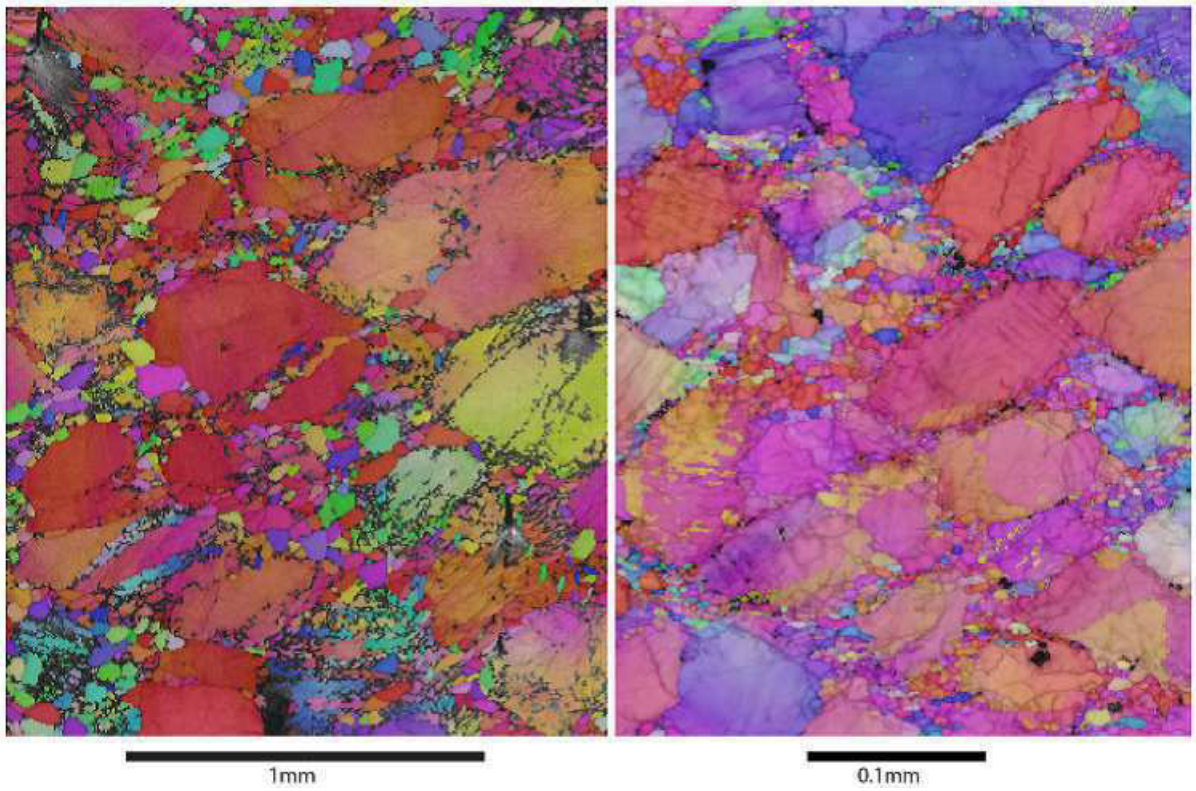

Figure 1.1: Microstructures of experimentally deformed ice (sample MIT 635, left) and natural quartz (both courtesy of D.J. Prior). Colours indicate different grain orientations.

1.2 Steady state creep

'Non-steady state creep is probably the rule in nature' —Barclay Kamb (1973)

The term steady state creep can have different connotations depending on author and discipline. In glaciology, steady state creep is of mechanical nature and denotes a constant strain rate under experimentally imposed constant stress or load conditions (Jacka and Maccagnan, 1984; Budd and Jacka, 1989; Treverrow *et al.*, 2012, Fig. 1.2a). In geology-based rock mechanics, a *mechanical steady state* is more commonly defined as a stationary flow stress under constant strain-rate boundary conditions and closely associated with a *microstructural steady state* with no changes in recrystallised grain size with progressive

strain (Twiss, 1977; Montési and Hirth, 2003; Kidder *et al.*, 2016, Fig. 1.2b). Both a *steady state stress* under constant strain rate conditions and a *steady state strain rate* under constant stress conditions are summarised under the term *tertiary creep* (see section 1.4.1). The *steady state* (recrystallised) *grain size* during the tertiary creep of rocks is often explained by a counterbalance between grain size reducing and grain size coarsening processes (de Bresser *et al.*, 1998; De Bresser *et al.*, 2001; Pieri *et al.*, 2001; Montési and Hirth, 2003). A steady state gain size has also been demonstrated for polycrystalline ice undergoing tertiary creep (Jacka, 1994).

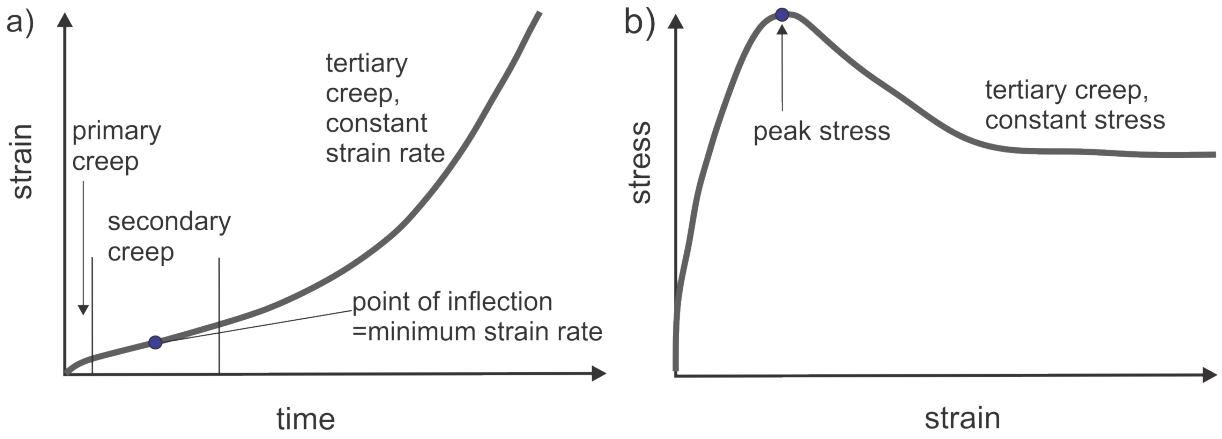

Figure 1.2: Comparison between an idealised strain-time curve for a constant stress test (a) and a stress-strain curve for a constant strain rate test (b) on polycrystalline ice (after Mellor and Cole, 1982).

In some studies, the concept of microstructural steady state goes beyond a constant recrystallised grain size and refers more generally to a constant texture (Table 1.1). Means (1981) discussed whether foliations in naturally deformed rocks could reach a microstructural steady state, characterised by constant orientations and intensity. Herwegh and Handy (1996) remark that localisation of deformation into micro-shear zones in an experimentally deformed quartz analogue can be a part of microstructural steady state. This observation contradicts some general definitions that require constant flow patterns or flow parameters during steady state deformation (i.e. Fossen, 2016).

For the purposes of this thesis, we differentiate between a mechanical steady state during tertiary creep and a microstructural steady state to allow for the observation that mechanical and microstructural steady state in polycrystalline ice are not necessarily concurrent (Jacka and Maccagnan, 1984; Piazolo *et al.*, 2013). The term steady state creep

is only used when a mechanical steady state coincides with a *steady state microstructure*, as indicated by some constant microstructural property that does not change with time.

Table 1.1: Definitions of ambiguous terms used in this thesis.

Term	Definition
Brittle	Deformation with features as fractures, (micro-) cracks and faults
Brittle-ductile	Transition zone in which fractures, cracks and faults can co-exist with ductile flow
Ductile	'Non-brittle' or 'plastic' deformation; flow of solid rock (Fossen, 2016); in absence of fractures (micro-) cracks and faults
Texture	Summary term for microstructure and CPO

1.3 Deformation mechanisms and relevance to ice deformation

Several mechanisms can contribute to overall deformation at the same time or subsequently, in which case microstructural overprinting can take place. Which deformation mechanism operates under a certain set of deformation conditions (pressure, temperature, grain size, strain rate) is captured in deformation mechanism maps (i.e. Frost and Ashby, 1982; Durham *et al.*, 2001) for a given material. Deformation mechanisms have been primarily constrained in rocks, metals and alloys (Poirier, 1985; Paterson, 2013). Deformation mechanisms in polycrystalline ice are similar to those in rocks and metals (Schulson and Duval, 2009; Wilson *et al.*, 2014; Faria *et al.*, 2014) and comprise the following:

1.3.1 Dislocation creep

Dislocation creep is driven by the movements of defects in the crystal lattice. Point defects are flaws in the crystal lattice that concern only one lattice site. There are several kinds of point defects in ice including empty molecular sites (vacancies), foreign solutes, additional native atoms within usually open space (interstitials) and protonic defects, minimal variations in the configuration of the H_2O molecule (Schulson and Duval, 2009).

Dislocations are line defects within the crystal lattice and can be classified into two end-members based on the orientation of the Burgers vector with respect to the dislocation line: edge and screw dislocations (Fig. 1.3). The Burgers vector b describes the offset between the unflawed and the flawed part of the crystal lattice.

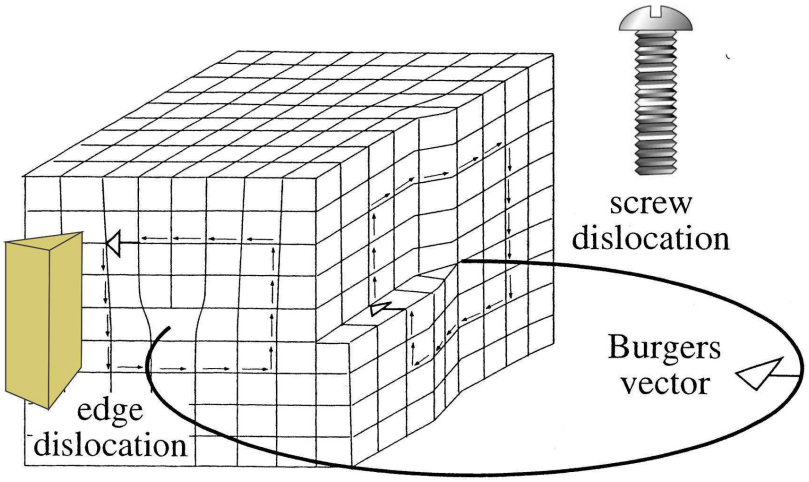

Figure 1.3: Effects of an edge (left corner) and a screw (right corner) dislocations on the crystal lattice (modified from Passchier and Trouw, 2005). The edge dislocation is accommodated by dislocation *glide* along a single lattice plane, whereas the screw dislocation involves *climb* to a second lattice plane.

1.3.2 Recrystallisation mechanisms

The term *recrystallisation* is employed to describe the strain-dependent response of a material to plastic deformation. Depending on the imposed deformation conditions, different recrystallisation mechanisms become active during dislocation creep to accommodate strain and allow for large-scale material plasticity.

Grain boundary migration (GBM) or *grain boundary migration recrystallisation (GBMR)* is a strain-induced process that occurs during deformation and is regarded as one of the key processes to modify the grain size (Poirier, 1985; Karato, 2008). The driving force for grain boundary migration is a difference in dislocation density $\Delta\rho$ between two neighbouring crystals (Karato, 2008):

$$F_{GBMR} = \mu b^2 \Delta\rho \tag{1.1}$$

With the shear modulus μ and the Burgers vector b (Fig. 1.3). During GBM parts of grains with high dislocation densities (many defects in the crystal lattice) are replaced by parts of neighbouring grains with lower dislocation densities. As the dislocation density varies across the length of boundaries, the grain boundaries become sutured and an interlocking grain shape develops (Fig. 1.4a).

New grain nucleation happens when deformed remnant grains with high dislocation densities are replaced with dislocation-free nuclei. New grains are commonly small in comparison to remnant grain size and equant-shaped (Table 1.2). In the ice literature, new grain nucleation mostly refers to the creation of new dislocation-free grains by the process of grain boundary bulging during strain-induced grain boundary migration (Fig. 1.4b). The progressive bulging of the grain boundaries to the extent that new grain formation can occur in polycrystalline ice requires a high grain boundary mobility, which is exclusive to the deformation regime of strain-induced grain boundary migration. It is noted, however, that some authors (i.e. Stipp *et al.*, 2001; Vernon, 2004) regard grain boundary bulging as a separate recrystallisation mechanism.

New grain nucleation was historically regarded as a fixed part of any recrystallisation scenario (Drury and Urai, 1990; Humphreys *et al.*, 2004; Rios *et al.*, 2005). Nowadays, it is accepted in ice physics and geology that recrystallisation is more diverse than initially thought and can occur irrespective of whether new grains are created or not (Drury and Urai, 1990; Wilson *et al.*, 2014).

Normal grain growth is a grain size coarsening mechanism (Table 1.2). In polycrystalline ice, normal grain growth can occur during deformation (Faria *et al.*, 2014), but is also often associated with *(static) annealing* or *static recrystallisation* in deformation experiments (Wilson and Russell-Head, 1982; Wilson *et al.*, 2014). Annealing refers to a stage post-deformation during which the temperature remains high but stress has been lowered or removed. Normal grain growth also occurs in undeformed polycrystalline ice under high-homologous temperatures (Alley *et al.*, 1986a,b; Azuma *et al.*, 2012; Becroft, 2015). The driving force for normal grain growth F_{GG} is the boundary or surface energy γ, which depends on the radius of grain boundary curvature r (Burke and Turnbull, 1952):

$$F_{GG} = \frac{2\gamma}{r} \tag{1.2}$$

Hence, the driving force is high for small grain sizes and decreases with an increase in grain size. As the driving force depends on the surface energy, grains migrate towards the centre of their curvature (Humphrey and Hatherly, 1996). Large hexagonal grains with concave grain boundaries grow at the expense of small grains with convex grain bound-

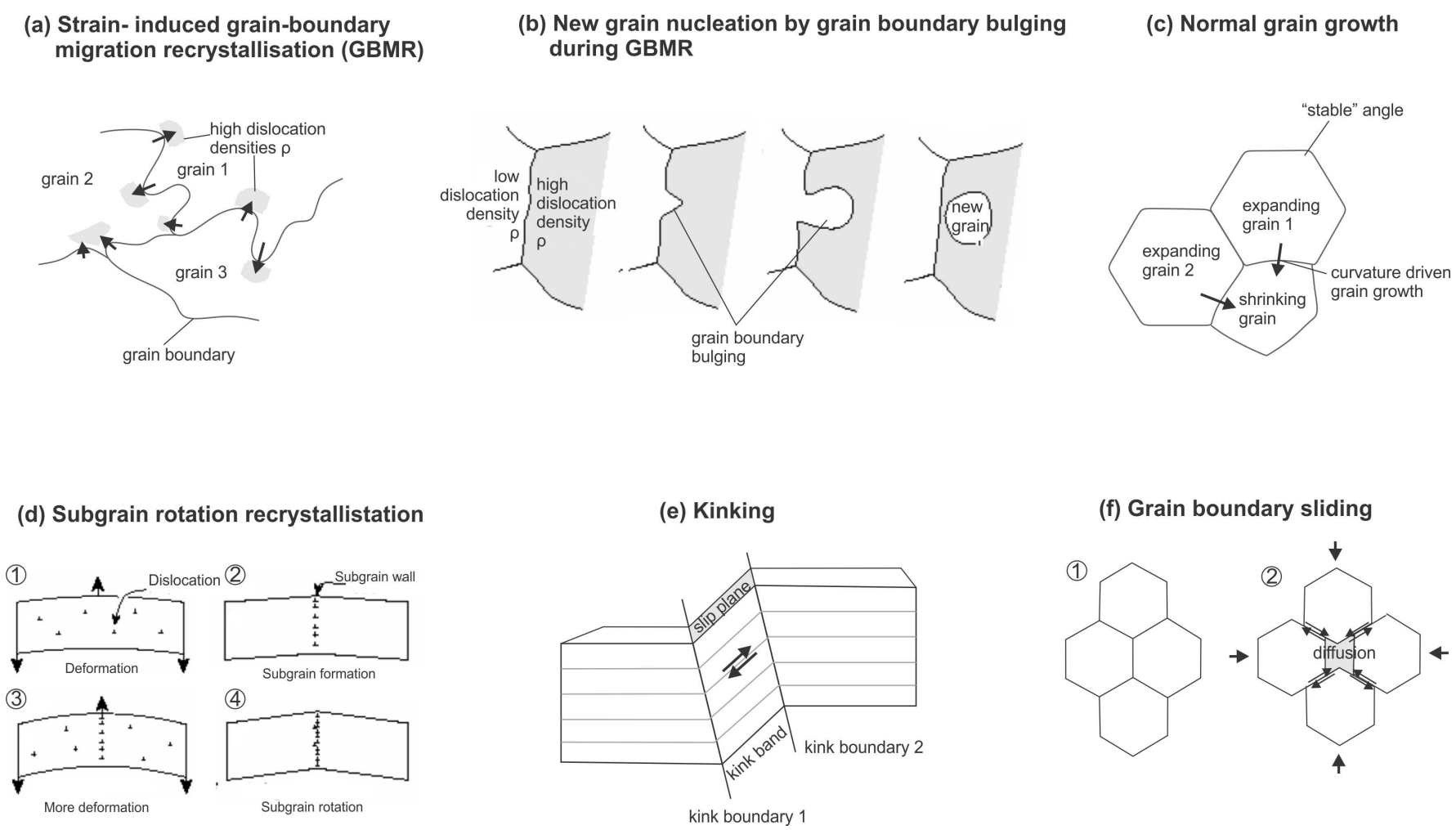

Figure 1.4: Schematic models to illustrate the mechanisms of a) strain-induced grain boundary migration at a triple junction, b) new grain nucleation by grain boundary bulging (after Urai *et al.*, 1986; Bestmann and Prior, 2003), c) normal grain growth (Hillert, 1965; Humphrey and Hatherly, 1996), d) subgrain rotation recrystallistion, e) kinking (mod. from Wadee *et al.*, 2012) and f) grain boundary sliding (after Poirier, 1985).

aries (Fig. 1.4c). Grains that have undergone normal grain growth or polygonisation consequently have a foam structure with polygonal grain shapes (Table 1.2).

Subgrain rotation or *subgrain rotation recrystallisation (SGRR)* is a process that ultimately results in the formation of new high angle grain boundaries through a progressive increase in misorientation (Urai *et al.*, 1986; Prior and Bestmann, 2004). The introduction of dislocations to the crystal lattice leads to a bending of the crystal planes (Fig. 1.4d). Further bending causes the dislocations to line up and form a subgrain boundary with a low misorientation. With progressive deformation, the misorientation angle increases and a new high angle boundary is created. A microstructural indicator for SGRR are new grains with grain sizes similar to subgrains (Table 1.2).

Kinking is a process similar to deformation twinning of single grains. Kinking is characterised by a greater degree of freedom than deformation twinning with respect to the involved slip systems, rotation angles and glide planes (Passchier and Trouw, 2005). The sharp bending of the crystal lattice planes through high angle grain boundaries leads to a breaking up of existing grains into kink bands with alternating orientations (Fig. 1.4e, Table 1.2).

In laboratory studies, GBMR, SGRR, new grain nucleation and kinking have been detected as part of the *dynamic* (during deformation) *recrystallisation* of polycrystalline ice (Table 1.2, Wilson *et al.*, 1986; Montagnat *et al.*, 2011; Piazolo *et al.*, 2015). Normal grain growth, SGRR and GBMR are considered to be the dominant processes in major terrestrial ice sheets (Duval and Castelnau, 1995; De La Chapelle *et al.*, 1998; Duval and Montagnat, 2006). Kinking has not yet been observed under natural conditions.

1.3.3 Diffusion creep

Diffusion creep is governed by diffusion processes within the crystals. Processes can be subdivided depending on where in the crystal diffusion is most prominent. During *Nabarro-Herring creep* lattice diffusion dominates, whereas the transport of matter occurs by grain boundary diffusion during *Coble creep*. *Intergranular pressure-solution* or *solution-transfer creep* is characterised by a local dissolution of material and diffusion along grain boundaries via a solution or partial melt phase. As the viscosity of the material varies with grain size during diffusion creep (i.e. Poirier, 1985), diffusion creep is often referred to as grain size sensitive (GSS) creep.

One process that is a part of GSS creep is *grain boundary sliding (GBS)*. GBS has been found particularly relevant to the deformation of polycrystalline ice under laboratory conditions (Goldsby and Kohlstedt, 1997, 2001; Goldsby, 2006). The relationship between

Table 1.2: Creep mechanisms and their signatures regarding microstructure and CPO. Dynamic recrystallisation mechanisms are labelled with an asterisk.

Mechanism	Microstructural Traits	CPO Development	References
Grain boundary migration (GBMR)*	sutured grain boundaries, interlocking grainshapes, grain size coarsening	global scale, significant	Urai *et al.* (1986); Guillope and Poirier (1979); Drury and Urai (1990)
Subgrain rotation recrystallisation (SGRR)*	grain size reduction, sizes of subgrains similar to recryst. grains	limited	Hobbs (1968); Guillope and Poirier (1979); Drury and Urai (1990); Bestmann and Prior (2003); Thorsteinsson (2007); Drury and Pennock (2007)
Normal grain growth (grain boundary bulging)*	grain size coarsening, polygonal grain shapes, rounded grain boundaries	no	Bailey and Hirsch (1962); Drury *et al.* (1985); Wilson and Russell-Head (1982)
Kinking*	long straight kink band boundaries, alternating orientations between kink bands	n/a	Hobbs (1968); Blumenfeld and Wilson (1991); Montagnat *et al.* (2015)
Grain boundary sliding (GBS), Grain size sensitive creep (GSS)	micron-scale grain size, equant grain shapes, random misorientation axes, quadrupole grain junctions	still debated, mostly argued to randomise CPOs	Goldsby and Kohlstedt (1997); Bestmann and Prior (2003); Prior and Bestmann (2004); Warren and Hirth (2006); Barreiro *et al.* (2007); Hansen *et al.* (2011)

GSS creep and GBS in the literature is often ambiguous. In fact, grain boundary sliding and GSS creep are by necessity coupled, coeval processes (Poirier 1985; Wheeler *et al.* 2003, Fig. 1.4f) and GBS must accompany diffusion creep to maintain continuity of the rock mass. Thus, GBS can be accommodated by GSS and vice versa and the terms GSS and GBS creep are almost used interchangeably (Table 1.2).

Whether GSS creep occurs in ice sheets, shelves and glaciers is still debated (Goldsby, 2006; Wilson *et al.*, 2014). Stress exponents of $n \sim 2$ derived from laboratory experiments during GSS creep (Goldsby and Kohlstedt, 1997, 2001) are more consistent with flow rates of continental ice sheets ($n \sim 2$) than the $n \sim 3$-4 determined for grain size insensitive diffusion creep. However, no microstructural evidence in the form of small equant-shaped grains or quadruple junctions has been recovered from ice coring. Another common argument against GSS creep in polar ice is that strong CPOs are almost ubiquitous in ice cores and GSS creep is not regarded as a fabric forming mechanism (Duval *et al.*, 2010).

1.4 The creep of polycrystalline ice

1.4.1 The creep curve

The creep curve of initially isotropic ice for temperatures of -0.05 to -50°C and stresses of 0.02-1 MPa exhibits the traditional stages known from other polycrystalline materials undergoing high-temperature creep (Budd and Jacka, 1989; Wilson *et al.*, 2014; Faria *et al.*, 2014). After a relatively instant elastic (recoverable, if the load is removed) strain *primary creep* commences. Primary creep is characterised by a decrease in the strain rate and is superseded by *secondary creep* (Fig. 1.5). The most distinguishable feature of secondary creep is the point of inflection of the creep curve at an octahedral shear strain of ~ 1 % strain, which denotes the minimum strain rate. Strain rates accelerate during secondary creep until a constant strain rate is established with the onset of tertiary creep at an octahedral shear strain of ~ 10 %.

Accelerations and decelerations in the strain rate, known as strain softening and strain hardening, respectively, reflect an interplay of micro-physical or microstructural accommodation processes to the imposed deformation. Strain hardening occurs during primary creep and has been explained with increases in the internal stresses that develop due to incompatibilities in the deformation of neighbouring grains and a shift in crystal plasticity from accommodation by the easy-slip system (0001)<11-20> (Fig. 1.7b) to hard glide system (Faria *et al.*, 2014 and references therein). Nevertheless, basal dislocations appear

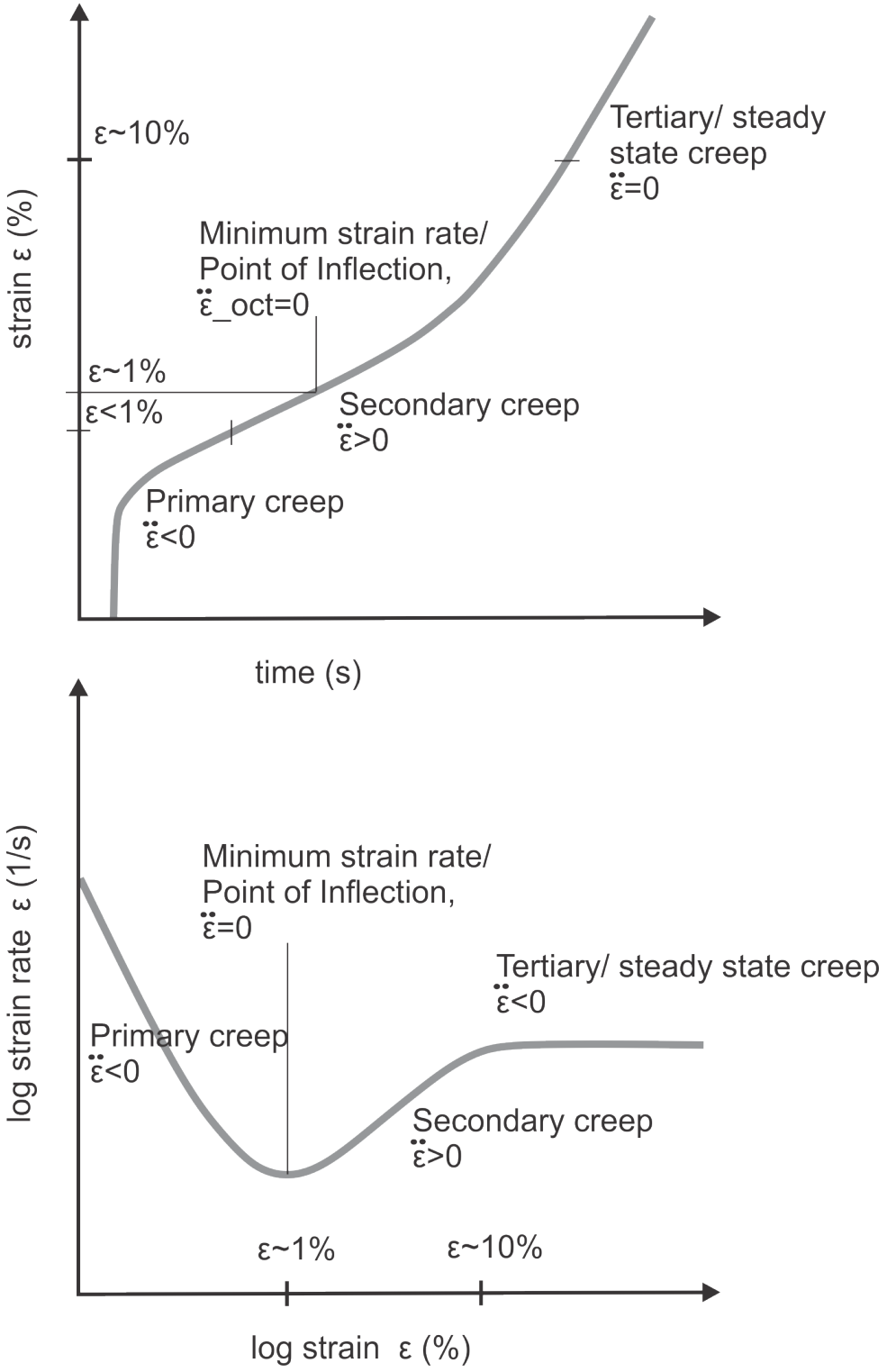

Figure 1.5: Creep curves for polycrystalline ice: strain vs. time curve (top) and log strain rate vs. log strain at the bottom (modified from Budd and Jacka, 1989. In contrast to (Budd and Jacka, 1989), a structural geology rather than glaciology definition of secondary and tertiary creep is used here and in all subsequent chapters.

to be the main agents of deformation during primary creep (Montagnat *et al.*, 2006).

The minimum strain rate as the characteristic feature of secondary creep is characterised by the activation of recrystallisation and other processes that aim to reduce the dislocation density (recovery) (Wilson *et al.*, 2014 and references therein). With the onset of recrystallisation, strain weakening as observed during secondary creep occurs. Processes, which are strongly intertwined with recrystallisation are the development of a CPO and changes in grain size until the CPO intensifies and a steady state grain size is established during tertiary creep (Faria *et al.*, 2014). Analogous to the paleopiezometry literature in geology (i.e. Twiss, 1977; Kohlstedt and Weathers, 1980; Cross *et al.*, 2017), an aim has been to establish a constitutive equation linking the recrystallised steady state grain size D_{ss} to the differential stress σ (Jacka, 1994):

$$D_{ss}^2 = \frac{1}{\sigma^n} \tag{1.3}$$

with n denoting the stress exponent.

Strain rates during the tertiary creep of polycrystalline ice are heavily influenced by the stress configuration (i.e. simple shear, pure shear etc.) and deformation patterns (Jun *et al.*, 1996; Treverrow *et al.*, 2012). The development of a CPO particularly introduces a strong mechanical anisotropy, meaning that the strain rate is no longer independent of the stress direction (Thorsteinsson, 2007). Both the dependence of the stress orientation after primary creep and the fact that anisotropic ice with a CPO may deform up to one order of magnitude faster in a certain stress direction (Budd and Jacka, 1989) pose challenges to the formulation of a generalised flow law for polycrystalline ice.

1.4.2 Flow laws

The first rate equation for the tertiary creep of polycrystalline ice was *Glen's Flow Law* (Glen, 1952, 1955), which follows the general power-law structure known from the creep of many materials. Glen's Flow Law was modified by Nye, 1953 to incorporate the differential rather than uniaxial stress:

$$\dot{\epsilon} = A\sigma^n \tag{1.4}$$

with $\dot{\epsilon}$ the strain rate, A a dimensionless parameter and σ the differential stress and a stress exponent n=3 for what is presumed to be dislocation creep in most laboratory and field studies (see Faria *et al.*, 2014 and references within). The power-law creep equation for polycrystalline ice was later modified to address two limitations (Goldsby and Kohlstedt,

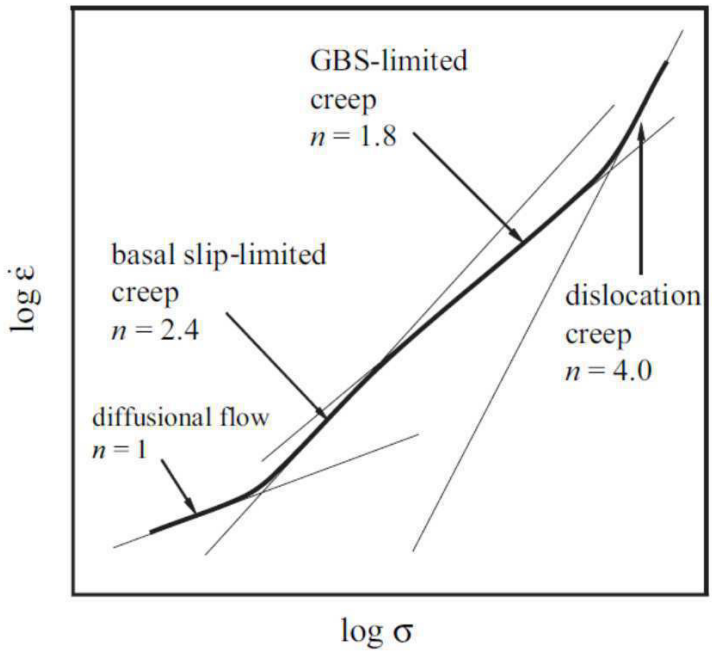

Figure 1.6: Schematic diagram depicting the changing deformation mechanisms with strain rate and stress conditions (Goldsby, 2006). Note that the speed of deformation, as reflected in the stress exponent n (equation 1.4) depends on the deformation mechanism. The thick solid line represents results from equation 1.6, the combined creep equation incorporating the strain rate contributions from all four regimes.

2001; Goldsby, 2006). First of all, the flow law was generalised to describe the rheological behaviour of ice deforming by deformation mechanisms other than dislocation creep and to incorporate the fact that the stress exponent n is deformation mechanism-specific (Fig. 1.6):

$$\dot{\epsilon} = B\frac{1}{d^p}\sigma^n \exp(\frac{-Q}{RT}) \tag{1.5}$$

with a dimensionless parameter B, the activation energy Q, the gas constant R and the temperature T. The grain size d dependence of diffusion creep is represented in the p exponent, which is 0 for dislocation creep.

The second modification allows for the simultaneous contributions of two or more deformation mechanisms to the overall strain rate. Goldsby and Kohlstedt (2001) proposed a new flow law combining the contributions from four regimes to the overall strain rate of polycrystalline ice during tertiary creep:

$$\dot{\epsilon} = \dot{\epsilon}_{diff} + (\frac{1}{\dot{\epsilon}_{basal}} + \frac{1}{\dot{\epsilon}_{GBS}})^{-1} + \dot{\epsilon}_{disl} \tag{1.6}$$

with $\dot{\epsilon}_{diff}$,$\dot{\epsilon}_{basal}$, $\dot{\epsilon}_{GBS}$ and $\dot{\epsilon}_{disl}$ denoting the strain rate contributions of diffusion, basal slip-limited, GBS-limited and dislocation creep, respectively. In its more simplified form the equation can also be written as:

$$\dot{\epsilon} = \dot{\epsilon}_{GBS} + \dot{\epsilon}_{disl} \tag{1.7}$$

Complications regarding the application of theses flow laws in the ice literature arise from a mixed usage of the minimum strain rates $\dot{\epsilon}_{min}$ in glaciology (i.e. Glen, 1952, 1955; Goldsby and Kohlstedt, 2001) and tertiary strain rates $\dot{\epsilon}_{ter}$ used in rock mechanics (i.e. Durham *et al.*, 2001). Because tertiary strain rates are regarded as more relevant to natural processes in glaciers and ice sheets, glaciologists employ an *Enhancement factor* E, to quantify the rate difference between secondary and tertiary creep (i.e. Lile, 1978; Budd and Jacka, 1989):

$$E = \frac{\dot{\epsilon}_{ter}}{\dot{\epsilon}_{min}} \tag{1.8}$$

1.4.3 Anisotropy on a crystal scale and ice slip systems

The strength of a given ice grain is strongly orientation-dependent and yields a high visco-plastic anisotropy on a crystal scale (Duval *et al.*, 1983; Trickett *et al.*, 2000). This crystal-scale anisotropy triggers internal stresses and strain heterogeneities between adjacent grains during the deformation of polycrystalline ice, which are accommodated by micro-physical or microstructural processes as point and lattice defects, dislocation generation and GBS. (Alley, 1988; Hondoh, 2000; Montagnat *et al.*, 2011).

The secret behind the strong deformation heterogeneity of single ice crystals lies in the strong preference of deformation by basal slip on (0001) <11-20> (Fig. 1.7a,b), with the experimentally determined critical resolved shear stress necessary to activate non-basal slip systems being up to 60 times higher than for basal slip (Duval *et al.*, 1983). Initial studies presumed that only basal dislocations contribute to the plastic deformation (Shearwood and Whitworth, 1991). Newer studies still recognize the importance of basal slip as the main agent of macroscopic crystal plasticity in polycrystalline ice, but also acknowledge the importance of prismatic slip (Fig. 1.7c) in local deformation (Hondoh, 2000) and single crystal plasticity at a high-homologous temperatures of -15°C (Chevy *et al.*, 2010).

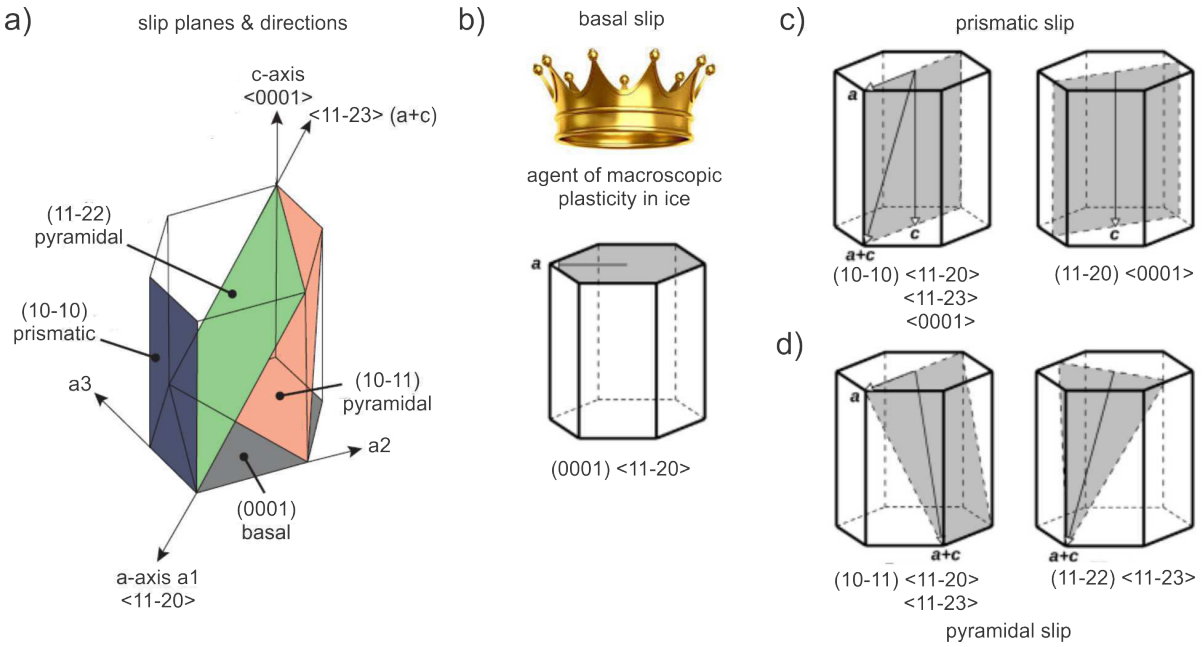

Figure 1.7: Slip systems in ice (modified after Hondoh, 2000; Faria *et al.*, 2014. a) Ice crystal with relevant crystal planes and axes. b) Basal slip, c) prismatic slip and d) pyramidal slip are illustrated within a schematic ice crystal.

Statistical investigations of local subgrain boundaries in polar ice have revealed that a significant number of non-basal dislocations are produced by internal stresses and strain incompatibilities between grains (Weikusat *et al.*, 2010, 2011). Further evidence for stress concentrations on grain boundaries and triple junctions due to grain-scale incompatibilities were provided by analyses and modelling of dislocation fields in experimentally deformed ice (Piazolo *et al.*, 2015). The role of local stress concentrations and non-basal dislocations in the overall deformation of polycrystalline ice aggregates, however, is still unclear.

1.5 Microstructural indicators

1.5.1 The Schmid factor as an indicator of crystal slip

A quantity often encountered in microstructural investigations within the material sciences, structural geology and glaciology is the Schmid factor S. For single crystals, the Schmid factor describes how much shear stress can be resolved by a certain slip system on a scale from 0 to 0.5, with 0 being equivalent to no crystal slip and 0.5 representing the ability of the slip system to accommodate the maximum amount of the imposed shear

stress. The Schmid factor originates from Schmid's Law (Schmid and Boas, 1935) and determines whether the critical resolved shear stress τ_c, the critical stress necessary to activate a slip system is reached:

$$\tau_c = \sigma * S = \frac{F}{A} * S \tag{1.9}$$

with the applied stress σ and A the cross-sectional area of the crystal targeted by the applied force F. The Schmid factor can be expressed as a geometric function of the angle between the normal to the slip plane and the applied force (θ) and the angle between the applied force and the slip direction ϕ:

$$S = cos(\theta) * cos(\phi) \tag{1.10}$$

In glaciology, the Schmid factor is often given as $S = cos(\theta) * sin(\theta)$, with θ the angle between c-axis (coinciding with the normal to the slip plane) and the applied force (i.e. Alley, 1988; van der Veen and Whillans, 1994b; Wilson *et al.*, 2014). This glaciological formulation of the Schmid factor implies the assumption that the slip system under investigation is ice's most prominent (0001)<11-20> slip system (section 1.4.3). The Schmid factor for an ice aggregate is accordingly given by the arithmetic mean distribution of c-axes with respect to the direction of the applied force.

Loosely associated with the Schmid factor are the terms *hard-slip* and *easy-slip* attributed to grains in structural geology and sometimes glaciology. In this context, a hard-slip grain will often denote a grain with an unfavourable orientation with respect to the imposed force resulting in a low Schmid factor for a chosen slip system and no or hardly any accommodation of shear stress by the grain. An easy-slip grain, on the other hand, will have a high Schmid factor and is oriented in a favourable orientation to resolve a high component of the imposed shear stress. There is no consensus on an exact threshold of transition from a hard-slip to a soft-slip grain within the literature but S=0.3 is proposed based on the results of Chapter 2 and is henceforth used within the framework of this thesis.

1.5.2 Constraints on slip systems with misorientation axes and determination of recrystallisation mechanisms and CPO development with misorientation angle distributions

The geometric relationship between grains depends on the recrystallisation process and can accordingly be used as a diagnostic tool in microstructural investigations. Grain

boundaries are described with two properties: 1) the orientation of the misorientation axis and 2) the misorientation angle between two grains.

Misorientation axes or *rotation axes* are often plotted in inverse pole figures (IPFs) when microstructures are examined. Because the reference frame for an IPF is a crystallographic one, the correspondence of misorientaton axes and certain crystallographic axes can be determined. This correspondence can allow for a deduction of the slip system that generated the grain boundary with the misorientation axis, although sometimes several slip systems can create the same misorientation axis and the solution is not unique. Using the example of polycrystalline ice, an alignment of the misorientation axis of a selected grain boundary with the crystallographic <10-10> axis can be produced by either basal or prism slip (Fig. 5.2a,c).

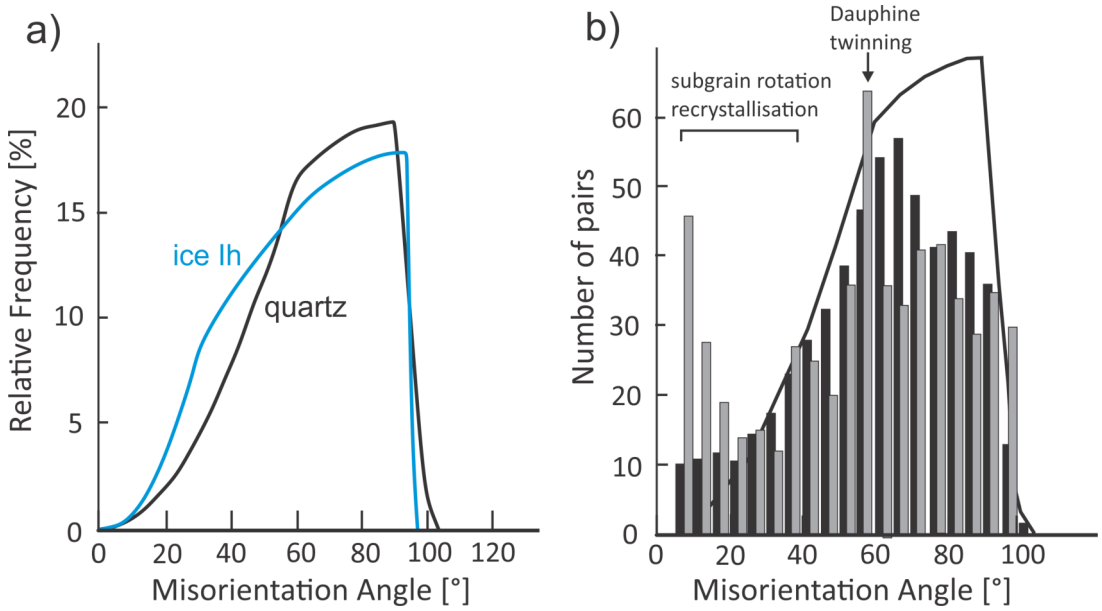

Figure 1.8: Exemplary misorientation angles distributions. a) Theoretical curves for hexagonal ice Ih (point group $6/mmm$) and quartz ($\bar{3}m$). b) Complete misorientation angles analysis with neighbour-pair MAD (silver bars), random-pair MAD (black bars) and the theoretical curve (black solid line) for an experimentally deformed quartzite (modified from Wheeler *et al.*, 2001).

The applications of the analysis of misorientation angles are more widespread and are explained here in more detail. Misorientation angles are mostly not individually considered but regarded as *misorientation angles distributions (MADs)* for an aggregate. For the calculation of the neighbour-pair or correlated MAD, misorientation angles of pairs of neighbouring grains are employed (i.e. Wheeler *et al.*, 2001; Randle, 2006).

Table 1.3: Types of misorientation angle distributions and examples of their applications in microstructural studies. The information in this table was extracted from (Wheeler *et al.*, 2001)

MAD	Usage	Determination via
Neighbour-pair	(1) to detect twinning (i.e. Dauphine twins in quartz)	peaks in the neighbour-pair MAD for certain misorientation angle according to twin law (i.e. 60° for Dauphine twins) not found in random-pair MAD (Fig. 1.8b)
	(2) to detect presence of subgrain rotation recrystallisation as a recrystallisation mechanism	skewed neighbour pair distribution towards large misorientation angles and peaks for small misorientation angles absent in random-pair MAD (Fig. 1.8b)
Random-pair	to detect presence of a CPO	deviation of random-pair MAD from the theoretical curve
Theoretical curve	shows random-pair distribution for an undeformed crystal	theoretical calculation based on crystal symmetry (i.e. Mackenzie, 1964)

Contrastingly, the *random-pair* or *uncorrelated* MAD compares the misorientation angles of pairs of randomly chosen grains throughout the aggregate (i.e. (Mainprice *et al.*, 1993; Randle, 2006)). The third distribution is the *theoretical random-pair MAD* or *theoretical curve* for an undeformed crystal. This theoretical curve is heavily influenced by the crystal system and is therefore varies in appearance for the specific point group (Wheeler *et al.*, 2001, Fig. 1.8a).

The three MADs are commonly displayed in a single histogram as microstuctural information is derived from the comparison of the distributions (Table 1.3, Fig. 1.8b). A comparison of the neighbour-pair with the random-pair MAD typically provides insight about whether adjacent grains have somehow interacted (i.e. twinning) or were originally created from the same original grain (i.e. subgrain rotation recrystallisation). A difference in the random-pair MAD from the theoretical curve indicates the presence of a CPO, since some orientations and misorientations are preferred. Accordingly, differences between the random-pair and theoretical curve increase with strengthening of the CPO during deformation (section 2.4.3). More information on the microstructural background and detailed examples of MAD analyses are given in Wheeler *et al.*, 2001.

1.6 Scope of thesis: Motivation, methodology and objectives

The ultimate aim of this thesis is to quantify the microstructural evolution and coupled rheological response of polycrystalline ice under mechanical non-steady state conditions using statistically significant datasets collected with cryogenic electron backscatter diffraction (cryo-EBSD). Previous studies were limited by the absence of an imaging method that allows for the reliable acquisition of full (c- and a-axis) crystallographic orientations of both large numbers of grains and, at the same time, micro-scale features (see Appendix A and Faria *et al.* (2014) for a detailed discussion on ice imaging methods).

It was originally intended to commence the investigation under supposedly steady state (constant stress) conditions and progress to more complicated stress paths to extrapolate findings to the mechanical and microstructural processes in glaciers and ice sheets after changes in the stress field (i.e. as a result of crevasse formation) and to the ductile deformation rocks below the brittle-ductile transition zone (BDT). Rocks below the BDT have been suspected to deform under non-steady state conditions due to stress cycling as part of the natural earthquake cycle (Küster and Stöckhert, 1999; Trepmann and Stöckhert, 2001, 2002, 2003). Investigating the non-steady state creep of crustal rocks

with ice as a rock analogue yield experimental advantages, as ice deformation does not require high pressures and temperatures and is thus not complicated by small sample sizes and engineering complexities.

The microstructural evolution under more complicated stress paths could, however, only be studied in this thesis to a lim ited extent in Chapter 2 and the experiments in Appendix B. With the collection of the datasets presented in Chapters 4, 5 and Appendix B it became apparent, that microstructurally caused localisation of deformation plays an undeniable role in the mechanical evolution of polycrystalline ice (Chapters 4, 5), and that the exploration of the creep of ice under more complicated stress paths (Appendix B) will only be possible once localisation phenomena are better understood. The overall research questions and objectives within this thesis were adjusted accordingly and can be summarised as follows:

Scientific questions

- How can we quantify the microstructural evolution of polycrystalline ice with progressive strain?
- What are the effects of the microstructural evolution on the rheology of the samples?
- How does deformation heterogeneity on a sample- and grain-scale affect the overall rheology?
- How can we extrapolate the findings of this thesis to natural scenarios regarding ice sheets, glaciers and the creep of rocks below the BDT?

Technical objectives

- Development of sample preparation procedures for deformed and undeformed polycrystalline ice samples prior to EBSD imaging without causing microstructural modifications
- Development of a method which allows for the visualisation of flow and deformation heterogeneity during deformation within classical glaciological low-pressure ice deformation experiments
- Development of mechanical data processing and microstructural analysis techniques to characterise localisation of deformation and microstructural change

1.7 Structure of thesis

This thesis follows a hybrid model with several stand-alone chapters aimed to improve our understanding of the complexities of ice deformation, based largely on new microstructural information. The introduction (Chapter 1) outlines the state-of-art of ice research relevant to the topic and explains the motivations that lead to this PhD. Chapters 2 and 3 deal with the high-temperature, low-pressure experiments more tailored to studies regarding the properties of terrestrial ice sheets. Chapters 4 and 5 focus on high-stress, low-temperature experiments more relevant to the ice deformation under planetary conditions and for geological analogies. Although the two parts may seem independent at a first glance, many of the techniques of data processing, especially with respect to EBSD data and grain size statistics are similar, and knowledge gained from Chapter 2 and 3 was incorporated into the later chapters. A joint conclusion summarises the main findings of all chapters and aims to extrapolate the findings to larger-scale natural scenarios. A brief synopsis of chapter contents and contributors is presented here:

Chapter 2: New insights into the evolution of microstructure and CPO during the high-temperature creep of polycrystalline ice

Context: A chapter based on an initial set of experiments conducted with the newly-built environmental control system (ECS) in Otago, which houses a glaciological Jacka rig. Some of the research questions in this chapter are: What microstructural processes drive the development of a two cone CPO? And what are the microstructural signatures of grain boundary migration and normal grain growth in the grain size statistics?

Contributors: Experiments were conducted with the help and support of Matthew J. Vaughan, Jan Leunissen and Leeza Becroft. Matthew J. Vaughan, David J. Prior and Kat Lilly helped gather the EBSD maps employed for this contribution. Data processing profited greatly from comments of David J. Prior and Andrew J. Cross. Andrew J. Cross also developed the grain size conversion script in MTEX, which allowed for a calculation of grain size statistics for a coarser step size than the original one.

Chapter 3: Particle image velocimetry in unconfined ice creep experiments

Context: A technical chapter commenting on the combined use of time-lapse photography and EBSD mapping to gain a better understanding of 1) deformation heterogeneity, 2) strain rate distribution and magnitude and 3) the influence of boundary conditions in

unconfined ice deformation experiments.

Contributors: Deformation experiments from Chapter 2 were employed for this chapter. Matthew J. Vaughan initially developed the technique of attaching graphite particles to the samples surface and selected PIVlab as a processing tool. EBSD maps for this study were collected with the assistance of Kat Lilly, Matthew J. Vaughan and David J. Prior.

Chapter 4: Localisation in polycrystalline ice under high confining pressure: the link between strain distribution, microstructural heterogeneity and rheological properties

Context: A chapter presenting and interpreting some of the results of the high-pressure deformation experiments conducted at the Massachusetts Institute of Technology (MIT). The main goal was to analyse previously unreported sample-scale localisation patterns and investigate if and how this localisation process relates to erratic strain weakening observed during the experiments.

Contributors: The deformation experiments in this chapter were performed under the supervision of Narayana Golding and William B. Durham. Narayana Golding additionally deformed ice sample 785, which plays a central role in this study. Susan Ellis adapted a pre-existing numerical model to experimental constraints and material parameters. Matthew J. Vaughan assisted with ice growing and EBSD mapping was performed with the combined efforts of Kat Lilly, Matthew J. Vaughan and David J. Prior.

Chapter 5: The role of kink boundaries in the shear localisation of experimentally deformed polycrystalline ice

Context: This chapter follows up on one of the central questions raised by results of the MIT experiments in Chapter 4 on a grain-scale level: What are the causes and effects of local grain size reductions that ultimately lead to shear zone development and a modification of the mechanical properties? This study examines whether the microstructural process of kinking could provide an answer.

Contributors: David J. Prior provided essential input on the microstructural methods that allowed for the investigation of the research question. See Chapter 4 for contributions in the experimental procedures and EBSD mapping.

Appendix A

Context: This publication provides background information on the technique of cryo-EBSD. It explains the difficulties and pitfalls of earlier ice EBSD investigations and outlines the technical adjustments that made the routine imaging of fine-grained polycrystalline ice possible. All thesis chapters rely heavily on the small and large-scale EBSD maps collected with this technique.

Contributors: The entire first year of this PhD was spent on the development of an ice growing protocol, thermal evolution experiments and initial attempts at creating a stable, non-frosty surface during the EBSD imaging of ice, making this appendix an important part of this PhD. My work on this publication was initiated and supervised by David J. Prior and Kat Lilly, the principal investigators on the project. Several co-authors provided input on the previous state-of-art of ice EBSD and sample preparation techniques and supplied undeformed and deformed samples of ices and ice composites with different grain sizes.

Appendix B

This appendix shows the remaining, otherwise unmentioned results of the MIT experiments with more complex stress paths.

Chapter 2

New insights into the evolution of microstructure and CPO in the high-temperature creep of polycrystalline ice with large-scale cryo-EBSD

Meike Seidemann[1], Matthew J. Vaughan[1], David J. Prior[1], Andrew J. Cross[2]

[1]Department of Geology, University of Otago, Dunedin, New Zealand
[2]Department of Earth and Planetary Sciences, Washington University, St. Louis, USA

Abstract

Microstructural changes and, by association, changes in the CPO are increasingly recognised to play a tremendous role in the rheology and dynamics of glaciers and ice sheets. However, the microstructural deformation mechanisms and their interplay with changing environmental (or experimental) conditions is not well-constrained. Our current understanding of these processes is based on experiments conducted on coarse-grained, small samples with a few ice grains. In this study, we employ blocks of fine-grained ($\sim$ 250 μm) polycrystalline ice with dimensions of $\sim$20 mm x 20 mm x 40 mm, deformed by uniaxial compression at 0.2-0.7 MPa and T $\approx$-2.5°C for 26-43 hours, equivalent to axial shortenings of 0.7-18.1 %. Cross-sections of deformed samples were subsequently imaged with cryo-EBSD to obtain large-scale maps and grain size statistics. Results indicate that high-stress samples at approximately 0.6-0.7 MPa deform by dynamic recrystallisa-

tion accommodated by grain boundary migration. C-axes of deforming crystals assemble in small circles between angles of 30-50° to the axis of compression, which correlated with areas of high Schmid factors ≥0.3. Low stress at 0.2 MPa and annealed samples are microstructurally modified by normal (static) grain growth. Comparisons between samples deformed by grain boundary migration and normal grain growth suggest that the deformation mechanism influences the grain size distribution. Skewed grain size distributions with standard deviations triple of the starting material develop under dynamic recrystallisation for shortenings ≥ 5.3 %. Normal grain growth preserves the shape of the original distribution but increases the standard deviation and causes a shift towards larger grain sizes. A decrease in mode is indicative of new grain nucleation. Overall grain coarsening is more rapid under dynamic than static conditions.

2.1 Introduction

The deformation of polycrystalline ice at high-homologous temperatures leads to rapid microstructural alterations. These influence flow behaviour and anisotropy of glaciers and continental ice sheets and are analogous to the high-temperature deformation of quartz (for a summary, see Wilson *et al.*, 2014). Recent advances in cryogenic electron backscatter diffraction (cryo-EBSD) enable the collection of statistically significant data sets over entire cross-sections of deformed samples (Prior *et al.*, 2015) and thus offer the possibility to develop the means to quantify microstructural evolutions and associate these with deformation mechanisms.

Investigating the microstructural evolution and development of a crystallographic preferred orientation (CPO) under non-steady state conditions is of particular value. Even though experimental and computational validations of anisotropic flow laws have shown that steady-state creep is a reasonable assumption for large parts of ice sheets and shelves (Treverrow *et al.*, 2015; Graham *et al.*, 2017), localised zones with variations in stress and strain rate still exist (Budd and Jacka, 1989). In this case, the steady-state creep assumption may not hold up. Steady-state creep without exemption is also doubtful in the case of quartz, which can be exposed to fluctuating temperatures and stresses during burial and exhumation as a part of the Earth's metamorphism, as well as stress-cycling in tectonically active regions (i.e. Trepmann and Stöckhert, 2001, 2002; Little *et al.*, 2002; Trepmann and Stöckhert, 2003; Okudaira *et al.*, 2012). A first step towards non-steady state experimental conditions can be to examine the evolution of the microstructure and CPO under constant stresses with the goal to compare the results to experiments with

varying stresses like stress reduction experiments. Rapid stress reductions are of particular interest in geological settings, as they are likely to occur in the Earth's crust after an earthquake. Similar drastic stress reductions take place in natural ice systems like glaciers and ice sheets during crevasse formation.

Microstructural and CPO evolution under steady state conditions (constant stress configuration and temperatures throughout the experiment) are well-documented. Results have demonstrated, that the c-axes of ice crystals rotate towards compressional axes (Wilson, 1982; Wilson and Russell-Head, 1982; Jacka and Maccagnan, 1984; Azuma and Higashi, 1985; Budd and Jacka, 1989) and that fabric strengthens with increasing shortening (Jacka and Maccagnan, 1984; Wilson *et al.*, 2014). If the deformation is followed by static annealing (continuous exposure to high temperatures post-deformation), Wilson and Russell-Head (1982) report an increase in grain size and unchanged CPO over periods from 17-42 days. However, the evolution of a microstructure and CPO under a low residual stress remains unknown. During rapid dynamic recrystallisation, experimental evidence suggests that preferential grain growth or grain nucleation with particular orientations can eliminate some grain orientations (Duval, 1981; Burg *et al.*, 1986), therein reinforcing the already existing fabric. Recrystallisation experiments on single crystals of quartz (Hobbs, 1968; Vernooij *et al.*, 2006) and extrusion experiments on halite (Skrotzki and Welch, 1983) have also reported similar nucleation of new grains in heavily deformed grains.

The orientation of grains with respect to the stress plays a crucial role in the deformation of polycrystalline ice aggregate, as well. The plasticity in the high-temperature deformation of ice is governed by slip on the basal plane (0001) <11-20> (Shearwood and Whitworth, 1991). Grains, that are favourably oriented for slip on the basal plane are sometimes referred to as 'easy-slip' grains, whereas grains unfavourably oriented for activation of this slip system are termed 'hard-slip' grains (section 1.5.1). A physical quantity that describes how much shear stress (critically resolved shear stress) can be accommodated by a specific slip system in a grain of a particular orientation is the Schmid factor. Schmid factors range from 0-0.5, with 0 being equivalent to no shear stress resolved by a slip direction on a certain crystal plane and 0.5 being attributed to the maximum amount of shear stress being accommodated by a given slip system. Internal shortening markers, such as kinks and the development of polygonal subgrains have been detected in hard-slip grains in ice (Wilson and Zhang, 1996) and halite (Trimby *et al.*, 2000). In contrast to that, 'easy-slip' grains have been observed to grow by grain boundary migration in experiments conducted whilst watching the microstructural evolution (Wilson and Zhang,

1996).

In this study, the effect of different stresses on microstructure and CPO development is investigated. Fine-grained (250 μm), laboratory-grown polycrystalline ice specimens are deformed in unconfined uniaxial compression experiments at -2.5°C with stresses of ∼0.6 MPa and ∼0.2 MPa. These samples are compared to an annealed sample and a sample subjected to a stress reduction. Using new approach to cryo-EBSD that allows the imaging of fine-grained ice with high indexing rates (Prior *et al.*, 2015), large-scale EBSD maps of areas up to 30 mm x 30 mm were collected that contain a statistically significant number of grains. To analyse the samples, CPO, grain size statistics and misorientation angle distributions were extracted from the EBSD data. One key aim of this contribution was to first identify the deformation mechanism prominent in each sample based on microstructure and CPO and to later connect it to its signature in the grain size and misorientation angle distributions. Additional aims were the testing of 1) sample preparation and imaging methods for fine-grained polycrystalline ice and 2) a new transparent experimental setup, which allows for the visual observation of the deforming ice sample. The advantages of a transparent experimental setup are discussed in more detail in Chapter 3.

2.2 Method

2.2.1 Experimental setup

Polycrystalline ice samples are produced from crushed ice particles of 0-180 μm according to a technique presented in Durham *et al.* (1983), commonly referred to as the Standard ice method (Stern *et al.*, 1997). The polycrystalline ice block produced was pre-chilled to -80°C, to prevent grain growth due to annealing (Prior *et al.*, 2015) and subsequently cut into samples with a height of 40 mm and 22 mm in width and length. Standard ice is transparent, macroscopically bubble-free with an average grain size of 250 μm, a random CPO, polygonal grain shapes, a uniform microstructure and very low porosity (Fig. 2.4a). The Standard ice samples are subjected to differential stresses of about 0.6 and 0.2 MPa, at a temperature of -2.5°C with the long axis parallel to the shortening direction, in a glaciological Jacka rig (Fig. 2.1 ,Treverrow *et al.*, 2012). The Jacka rig is a direct load apparatus; a constant load during an experiment will, therefore, correspond to a decreasing stress with shortening. An additional sample was annealed for a similar period of time to constrain the influence of the temperature on the microstructure in

the absence of deformation. Silicone oil was employed as a non-reactive cooling medium around the rig, which is housed in an environmental control system (ECS), which allows for the performance of experiment in a room-temperature environment. In order to simulate a microstructural evolution, loading and annealing times were variable and depended on the experiment (Fig. 2.2, Table 2.1).

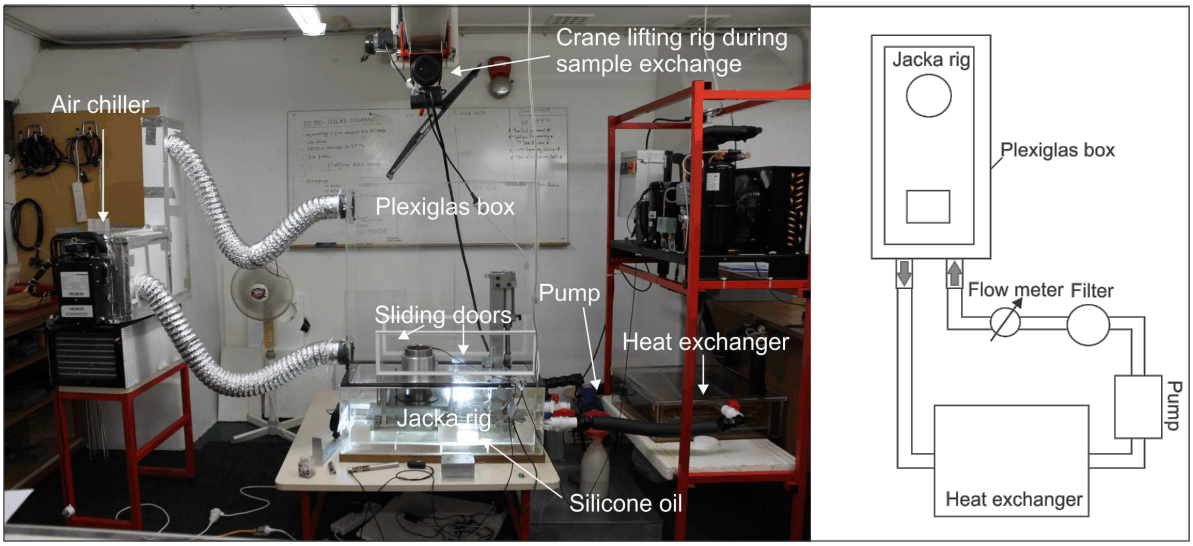

Figure 2.1: Experimental setup. The environmental control system (ECS) consists of a double-walled Plexiglas box, a copper-coil heat exchanger and an air chiller and houses a Jacka rig (left). Slicone oil is circulated as a cooling medium. Sliding doors on both sides of the ECS facilitate sample exchanges. Schematic flow diagram showing the view of the ECS from the top (right).

After the conclusion of an experiment, the deformed samples were cooled rapidly by immersion into nitrogen mist to preserve the microstructure. Samples were prepared for EBSD imaging with a procedure similar to Prior *et al.*, 2015, which involved storage in liquid nitrogen mist and cutting the pre-chilled sample in half along the axis of compression. The formerly outer rim of the pre-chilled (∼-120°C) sample was subsequently mounted on a +2°C warm 30 mm by 30 mm copper SEM ingot. The top surface of the sample was then polished at -30°C ambient temperature in a cryomicrotome for under 5 minutes. Excess frost on the samples surface was removed once the sample was lodged in the chamber of the microscope, by employing a one-time sublimation by pressure cycling approach (Prior *et al.*, 2015) with a minimum cold stage temperature of -70°C.

Table 2.1: Summary of experimental conditions. Note that stress is at its peak at the beginning of the experiment and decreases due to an increase in surface area.

Experiment	PS30-1	PS30-2	PS3010-1 (1)	PS3010-1 (2)	PS10-1	PSA-1
Load [kg]	30	30	30	10	10	0
Area pre-deformation [cm^2]	4.83	4.20	4.83	n\a	5.06	4.90
Area post-deformation [cm^2]	5.10	5.88	n\a	5.00	5.06	4.90
Length pre-deformation [cm]	3.90	4.00	3.90	n\a	3.95	3.95
Stress [MPa]	0.59±0.02	0.70±0.05	0.60±0.01	0.19±0.05	0.20±0.01	0
Mean temperature [°C]	-2.5	-2.9	-2.6	-2.6	-2.5	-2.5
Loading time [min]	180	20	60	0	0	0

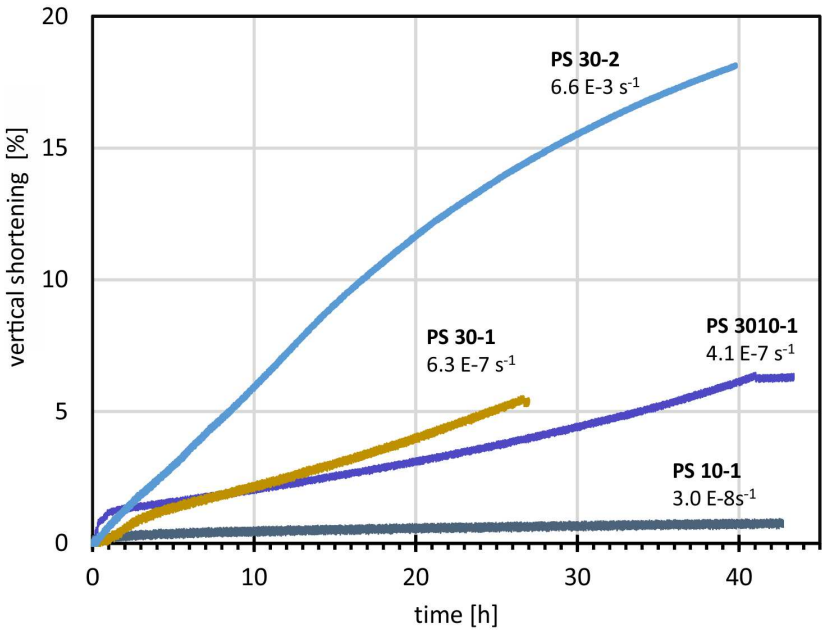

Figure 2.2: Shortening plotted against time for all deformed samples. Differences in the shortening history at the same load (PS30-1 and PS3010-1 step 1) can be attributed to minor flaws in the sample preparation technique, including not completely planar surfaces and slight aberrations in sample size (Table 2.1). Approximate shortening rates (next to curves) were calculated from averaging over the last 4 h of each experiment. For the stress-reduction sample PS3010-1 no shortening was incurred after the stress reduction, the given approximate shortening rate was hence only calculated over the last 4 h in the first stress step.

2.2.2 EBSD imaging and microstructural analysis

Mapping was performed in a Zeiss Sigma SEM, equipped with a variable pressure (VP) system employing nitrogen gas to control charging on the sample's surface. An Emitech K1250 cryo-stage kept samples at a constant temperature of -100°C during imaging. Mapping was conducted with an acceleration voltage of 30 kV, an aperture of 300 μm at a working distance of 39 mm. A montage function within the preinstalled HKL INCA Premium Synergy Integrated EDS/EBSD system (Oxford Instruments) enabled a consecutive automated collection of small maps and fitting of large areas of an entire samples cross-section.

EBSD maps, pole figures and grain size histograms were generated with the MTEX 4.0.12 plug-in for Matlab (Bachmann *et al.*, 2010). For reasons explained later on, a minimum misorientation angle of 10° was employed to demarcate between grains and sub-

grains. Because EBSD datasets are susceptible to poor indexing or misindexing that can lead to artefacts when grains are solely defined by a low number of indexed pixels (Bestmann and Prior, 2003; Prior *et al.*, 2009), all grains below a number of 10 pixels per grain were removed. Grain size distributions were calculated in terms of the area-equivalent grain diameter. Arithmetic mean, medians and standard deviation were determined for each distribution. Grain size histograms and modes were calculated for a bin width of 50 μm. To allow for a comparison between samples imaged at a different step size, grain size parameters were later converted to larger step sizes using a 'reduction-resolution' routine (Cross *et al.*, 2017) in MTEX (Table 2.2).

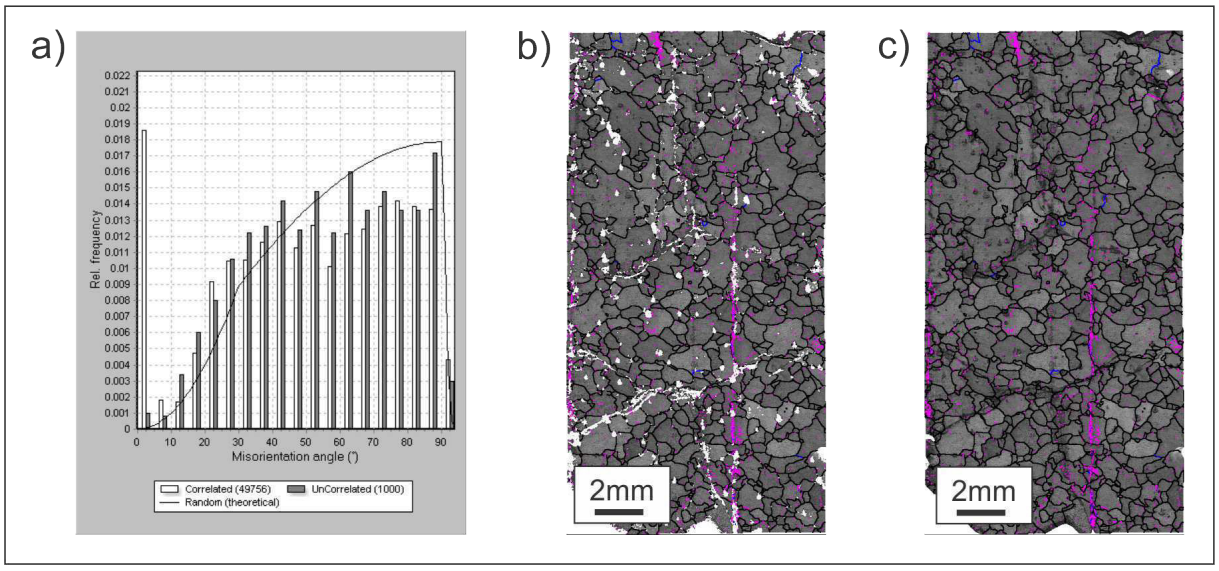

Figure 2.3: Erroneous neighbour-pair misorientations for angles below 5°, illustrated on sample PS3010-1. a) Unedited misorientation angle distribution. Neighbour-pair misorientation angles (white) show a distinctive peak for angles of 2-5° over the random-pair misorientations (grey). The theoretical curve for a random orientation dirstribution (Wheeler *et al.*, 2001) is indicated by a black line. b) Grain boundaries superimposed on an unprocessed pattern quality map. Misorientations are 2-5° (pink), 5-10° (blue) and over 10° (black). Non-indexed pixels are shown in white. Only wild spikes were removed for this map. c) Processed pattern quality map with superimposed grain boundary misorientations using the same colour-code as in (b). Non-indexed pixels were removed using a neighbour-pair extrapolation algorithm in Channel 5. Processing leaves low angle misorientations of 2-5° in former areas of low pattern quality, particularly along scratches on the sample surface.

Contoured pole figures were calculated with a 15° halfwidth. The so determined orientation distribution function (ODF) was then displayed as an equal area, lower hemisphere

stereographic projection. As pre-defined in MTEX, 493 mean orientations of grains were employed for the contouring of the pole figures, except in sample PS30-1 where only 393 'well-indexed' grains were available.

Misorientation angle distributions were calculated in Oxford Instruments' Channel 5 software from processed EBSD maps. The maps were cleaned by removing wild spikes (outliers) and performing a neighbour-pair interpolation. Then, 2000 random and neighbour-pair misorientations were employed to generate the misorientation angle distributions, respectively. Normally, minimum misorientation values of 1° or 2° are chosen for misorientation angle analyses (i.e. Trimby *et al.*, 2000; Montagnat *et al.*, 2015), as the angular error of EBSD measurements is considered to be below 1° (Dingley and Randle, 1992). In this contribution, however, the high number of neighbour-pairs below a misorientation angle of 5° was attributed to an artefact caused by the sample preparation and are hence not shown in the processed misorientation angle distributions. All samples were polished with a cryo-microtome prior to imaging and short fragments of subgrain angle boundaries with misorientations of 2-5° are aligned with lines of low quality that could be caused by scratches on the sample surfaces (Fig. 2.3). 'Real' subgrain boundaries with angles of 5-10° are longer and are also present where the map quality is good (Fig. 2.3b). Once processed, the scratches are no longer visible but the erroneous subgrain boundaries with misorientations below 5° remain to cause a peak in the neighbour-pair distribution (Fig. 2.3a,c).

2.3 Results

2.3.1 Starting material

The starting material is homogenous with equant-shaped grains and an almost random CPO (Fig. 2.4a). The quality of the EBSD orientation map is good, except for a crack in the middle. The grain size distribution is characterised by a narrow standard deviation and looks almost bell-shaped with an arithmetic mean grain size of 250 μm and a median of 244 μm at a step size of 10 μm (Fig. 2.5a). The mode of the grain size histogram is 250$\pm$25 μm. Neighbour- and random-pair distributions show only minor differences and the random-pair misorientation angle distribution (MAD) correlates strongly with the theoretical curve for ice 1h (Fig. 2.6a).

2.3.2 PS30-1 (∼0.6 MPa, 5.3 % shortening)

Prominent microstructural features in sample PS30-1 are sutured, irregular grain boundaries, interlocking grain shapes and a significant increase in grain size from the starting material (Fig. 2.4b). Grains often appear elongated in one direction. The microstructure is also spatially heterogeneous. In the lower part of the sample, larger grains and more lobate grain boundaries are observed. Along with an increase in mean grain diameter, the grain diameter distribution in sample PS30-1 is skewed with a standard deviation of over 330 μm and a maximum grain size of up to 2700 μm (Fig. 2.5b). The mode of the histogram is 150±25 μm.

The c-axes in sample PS30-1 cluster in two small circles in a 0-70° angle to the CPO's axis of symmetry (Fig. 2.4b,2.9a). Maxima with a strength greater 1.5 out of 3 (colour-coded in yellow and green) are found in an angle of approximately 10-60° to bulk shortening. There is a slight offset between the axis of symmetry of the c-axes CPO visible in the contoured pole figure of sample PS30-1, as observed in samples whose surface was not entirely planar prior to deformation (Fig. 2.9a).

2.3.3 PS30-2 (∼0.7 MPa, 18.1 % shortening)

Sample PS30-2 was deformed at a lower temperature (-0.4°C relative to the other experiments) than the other samples (Table 2.1). The microstructure of sample PS30-2 is characterised by lobate grain boundaries, entwined grain shapes and partly elongated grains (Fig. 2.4c). Small grains with a diameter of around 250 μm, similar to the starting material, are still present. There is no spatial heterogeneity in sample PS30-2, but the microstructural map of this sample covers only a fraction of the deformed cross-section. The grain diameter distribution is skewed like in sample PS30-1 but the arithmetic mean grain size and median are about 100 μm smaller at a step size of 20 μm (Table 2.2). A maximum grain diameter of 1900 μm was detected (Fig. 2.5c). The histogram displays a mode of 100±25 μm, which is even smaller than in sample PS30-1.

This sample shows a strong two cone c-axis CPO (Fig. 2.4c). In the contoured pole figures, the main clusters of c-axes orientations (strenghts>2, yellow) are located in the centre of the pole figure, at an approximate angle of 20-45° to the shortening direction (Fig. 2.4c,2.9b). A maximum CPO strength of 3 out of 3 was determined for the maximum clusters in the contoured pole figures compared to 2.5 out of 3 for sample PS30-1.

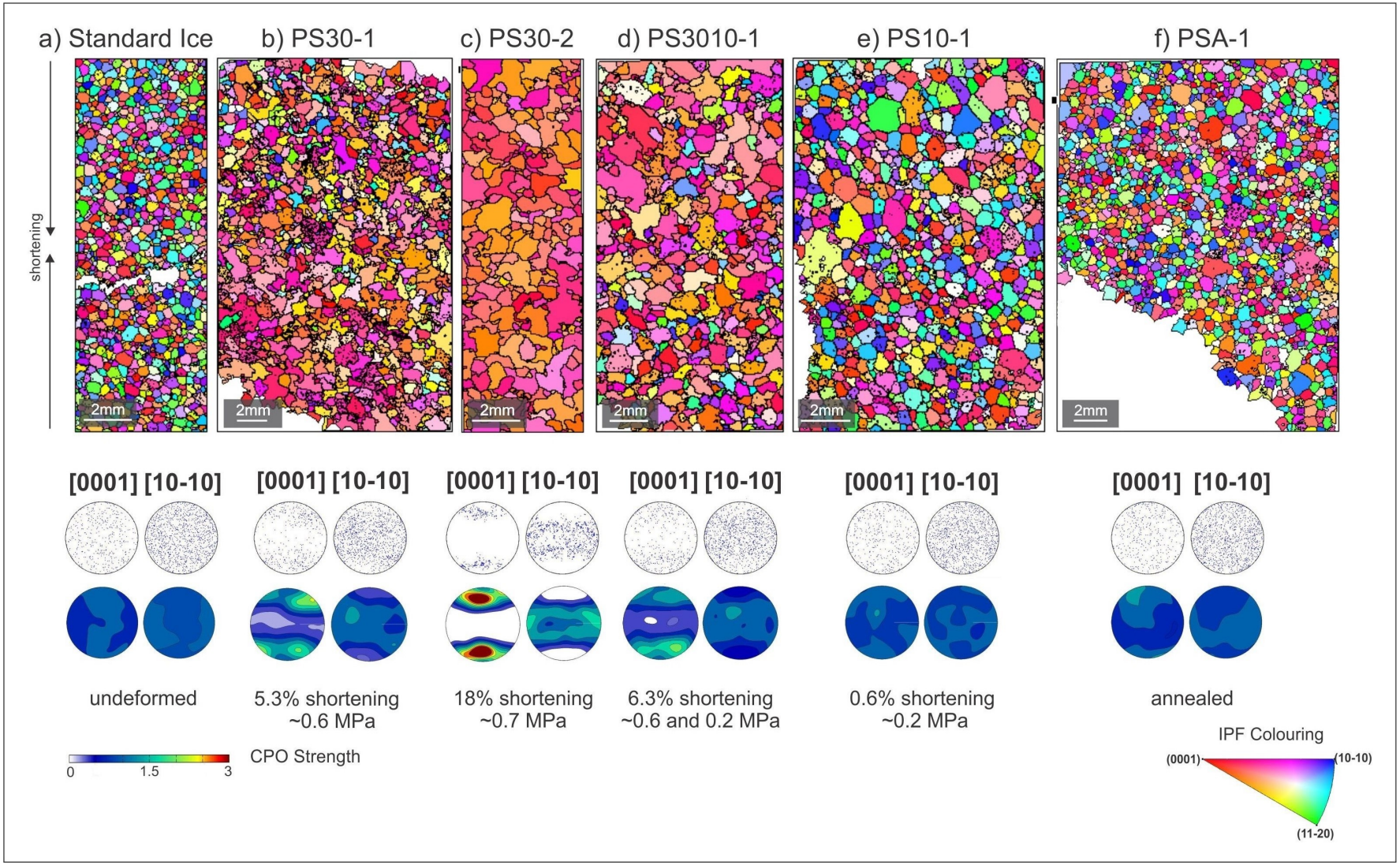

Figure 2.4: Evolution of microstructure and CPO. Pole figures are equal-area, lower hemisphere projections and contouring was performed with a halfwidth of 15°. Note that the magnification differs for each map.

2.3.4 PS3010-1 (∼0.6 MPa, 6.3 % shortening and ∼0.2 MPa, 0 % shortening)

Sample PS3010-1 was subjected to an instantaneous stress reduction in its deformation history (Table 2.1) and accommodated its final shortening value of 6.3 % entirely before the stress reduction (Fig. 2.2). In terms of microstructure and CPO development, sample PS3010-1 shows lobate grain boundaries and interlocking grain shapes that resemble sample PS30-1 (Fig. 2.4b,d). The mean grain diameter of about 500 μm, large standard deviation of 350 μm and slightly skewed grain diameter distribution are similar to the grain diameter statistics of sample PS30-1. The mode of 250±25 μm, however, is more similar to the starting material than sample PS30-1.

Sample PS3010-1 exhibits a weak two cone CPO ranging from angles of 0 to 70° to the shortening direction (Fig. 2.4d,2.9c). Maxima (contoured in yellow and green) are located at an angle of 10-54° to bulk shortening.

The MAD signature of sample PS3010-1 also deviates from the appearance of the neighbour- and random-pair distribution in sample PS30-1 (Fig. 2.6b,d). In sample PS3010, the random-pair distribution deviates within 5 % margins from the theoretical reference curve for ice, it does not exhibit the sample block-shape that was observed in sample PS30-1 (Fig. 2.6b). The offset between neighbour- and random-pair distributions is also more noticeable in sample PS3010-1 (Fig. 2.6d). There is an almost consistent 5 % surplus of neighbour-pairs for angles between 25 and 45 % that were not detected in the MAD of sample PS30-1.

2.3.5 PS10-1 (∼0.2 MPa, 0.7 % shortening)

Sample PS10-1 has randomly-oriented, equant-shaped grains similar to the starting material (Fig. 2.4e). Large grains of 150-200 μm are mainly found within the top half of the sample. Although the arithmetic mean, standard deviation, median grain size and mode of sample PS10-1 are almost twice as large as in the starting material (Table 2), sample PS10-1 shows a narrow bell-shaped grain diameter distribution similar to the starting material (Fig. 2.5e).

Random-pair misorientation angles hardly deviate from the theoretical curve (Fig. 2.6e). The neighbour-pair distribution is consistent with the random-pair distribution, except for a minor surplus (up to 8 %) of neighbour-pairs between misorientation angles of 25-45°.

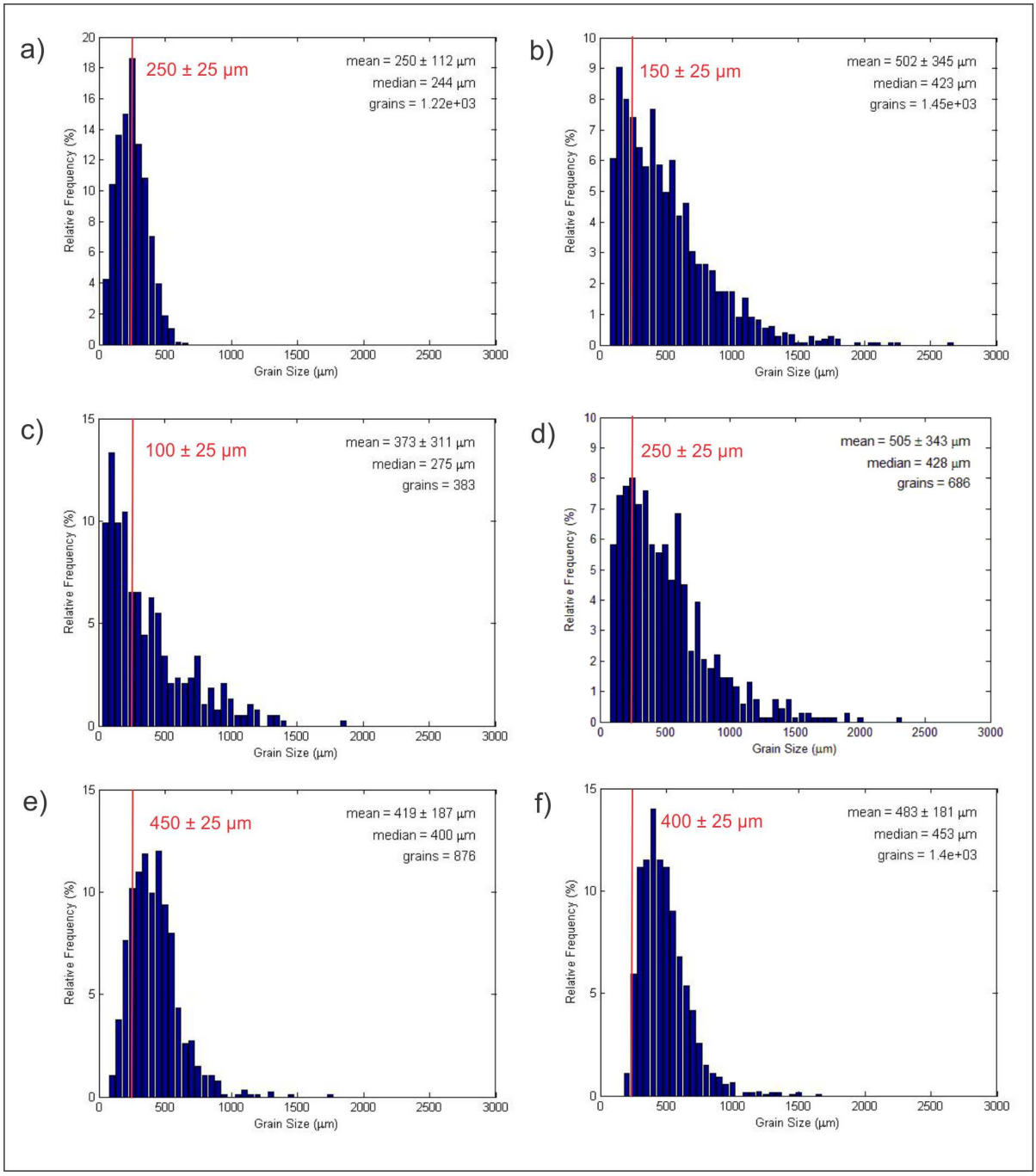

Figure 2.5: Summary of the grain size histograms and statistics from EBSD maps in Figure 2.4: a) undeformed Standard ice, b) PS30-1, c) PS30-2, d) PS3010-1, e) PS10-1 and f) PSA-1. Arithmetic mean, standard deviation, median values and numbers of grains are given at the top right of the histograms. In red, the modes of the grain size histograms (numbers) and the mode of the starting material (lines) are shown.

Table 2.2: Converted arithmetic mean, standard deviation and median grain diameters (in brackets) of the samples for different step sizes. Grain size statistics at the original step size are denoted with an asterisk.

Step size(μm)	Standard ice	PS30-1	PS30-2	PS3010-1	PS10-1	PSA-1
10	253±115* (244)		373±311* (275)			
15	265±108 (258)		410±308 (314)		419±187* (400)	
20	265±108 (258)	502±345* (423)	410±308 (314)	508±343* (428)	419±187 (400)	
40	294±095 (281)	573±338 (495)	486±302 (404)	563±333 (483)	487±175 (456)	483±181* (453)

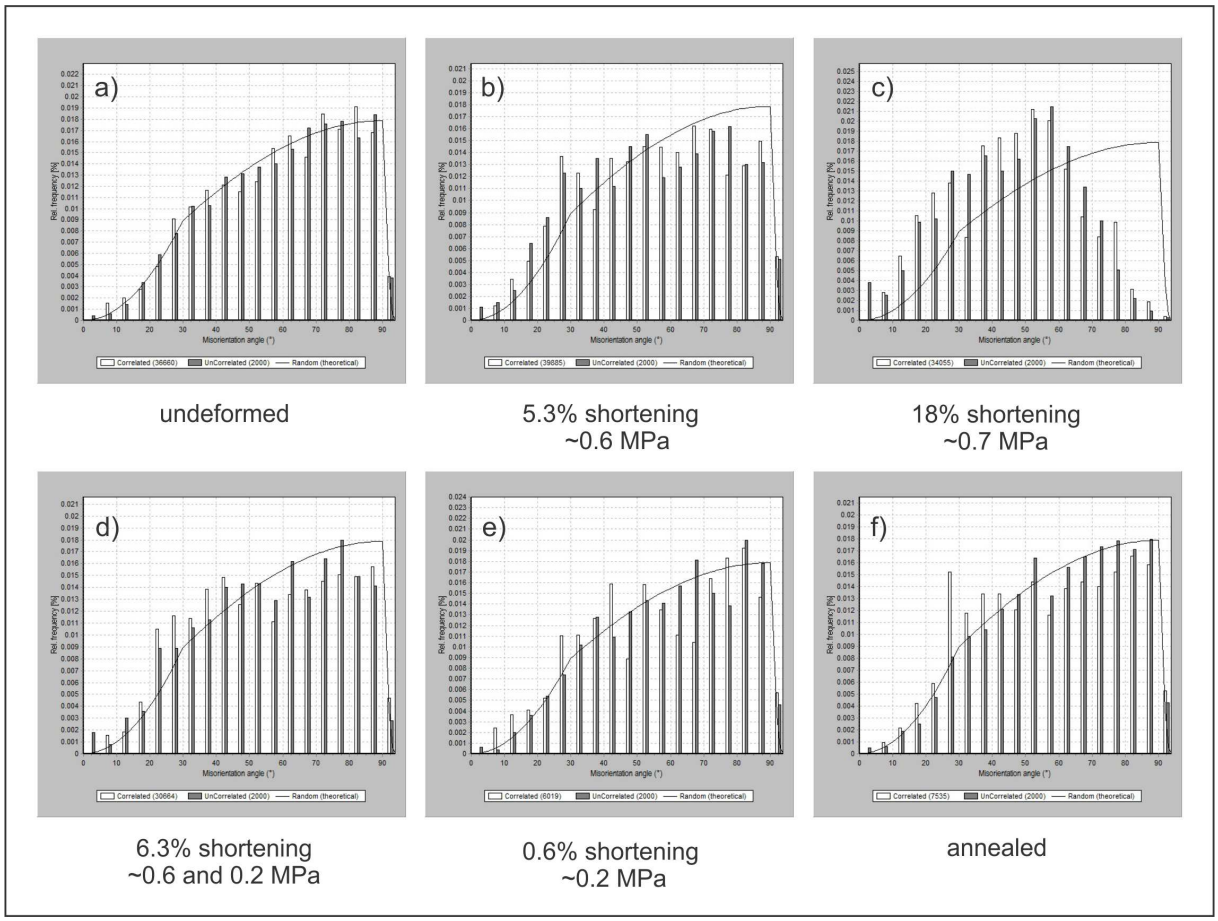

Figure 2.6: Misorientation angles distributions from EBSD maps in Figure 2.4: a) undeformed Standard ice, b) PS30-1, c) PS30-2, d) PS3010-1, e) PS10-1 and f) PSA-1.

2.3.6 PSA-1 (42.6 h annealed)

The microstructural features, random CPO and misorientation angles distribution of the annealed sample PSA-1 are almost identical to sample PS10-1 (Fig. 2.4e,f). Most grains show equant, polygonal grain shapes and an almost doubled median grain size from the starting material. The bell-shaped grain diameter distribution also has a standard deviation of about 180 μm (Fig. 2.5f). The mode of the grain size histogram is almost twice as large as in the starting material.

2.4 Discussion

2.4.1 Microstructural evolution

The sutured grain boundaries, interlocking grain shapes and increases in arithmetic mean and median grain diameters observed at high stresses of about 0.6 MPa, can be best explained by rapid grain boundary migration. Grain boundary migration has been frequently observed in the high-stress deformation of polycrystalline ice at high-homologous temperatures (Kamb, 1973; Wilson and Zhang, 1996; Wilson *et al.*, 2014) and previous studies have identified sutured, irregular grain boundaries and jigsaw-puzzle-like grain shapes to be diagnostic features of this deformation mechanism (i.e. Poirier and Nicolas, 1975; White, 1976; Urai *et al.*, 1986; Hirth and Tullis, 1992). Grain size histograms and microstructures show a selective growth of some grains up to twice as large as their initial size, while others remain the size of the starting material. Similar observations of the selective gigantic growth of grains have been made in ice (Duval, 1981). In Halite, gigantic grains have been connected to an orientation relative to the principal stress direction for every grain (Trimby *et al.*, 2000).

In other words, one consequence of selective grain growth and elimination may be the development of a CPO. C-axes display the typical two cone-structures commonly found in uniaxial compression experiments on polycrystalline ice under high-homologous temperatures (i.e. Wilson, 1982; Jacka and Maccagnan, 1984; Jacka, 1994; Piazolo *et al.*, 2013; Montagnat *et al.*, 2015; Breton *et al.*, 2016). Figure 2.7 displays a random c-axis CPO, colour-coded according to the Schmid factor value of each orientation for basal slip along (0001) <11-20> (a) and identifies the angles between high and low Schmid factor regions within the pole figure (b). A comparison between Figure 2.7 and the c-axis pole figures of the samples deformed under high-stress conditions (Fig. 2.4b,d) indicates that mainly grains with Schmid factors $S \geq 0.3$ ('easy-slip' grains) with angles between 15-70° to the compression axis survive in the initial stages of grain boundary migration. As grain boundary migration proceeds, the CPO strengthens and the upper angle bound of the two great cycles seems to move closer to the 0.5 Schmid factor line at around 45° from the axis of compression (Fig. 2.4c,2.7). Whether grains with orientations unsuitable for easy slip rotate towards the compressional axes to better accommodate shortening (Azuma and Higashi, 1985; van der Veen and Whillans, 1994a) or merely shrink until they disappear within the expanding grains cannot be determined.

In the elimination of 'hard slip' grains and strengthening of the existing fabric at high

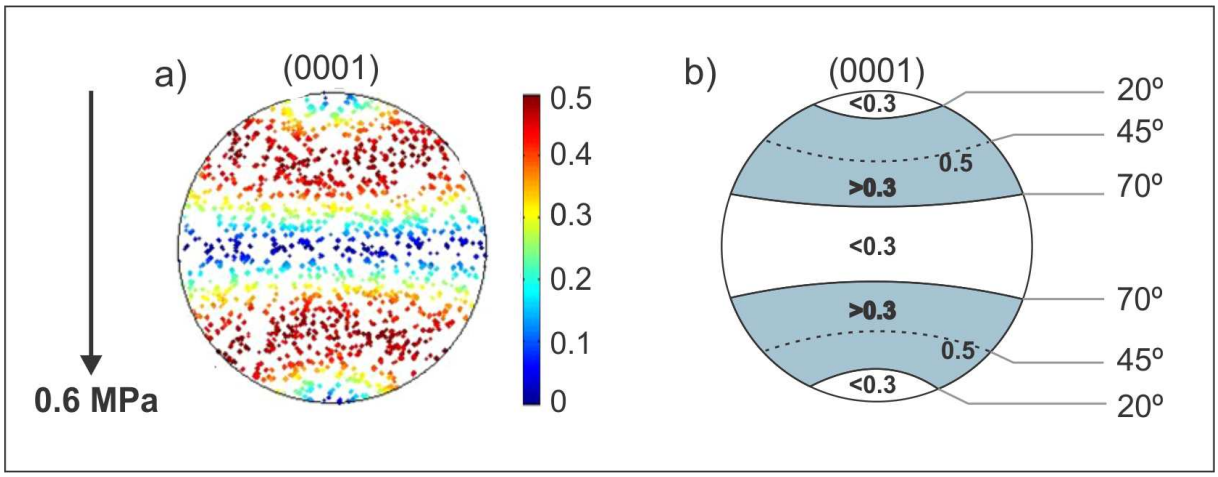

Figure 2.7: Schematic Schmid factor distribution for slip in the <11-20> direction on the basal (0001) plane and a uniaxial stress of 0.6 MPa. Only c-axes (0001) are shown. a) Equal-area, lower hemisphere pole figure of randomly oriented c-axes for basal slip, colour-coded according to the Schmid factor. b) Schematic illustration of the Schmid factor distribution for basal slip for c-axes with angles from the principal vertical stress axis. Due to the high symmetry of the Schmid factor distribution for basal slip in ice, angle measurements are assumed to be the same for all four quadrants.

stresses, new grain nucleation may play a crucial part, as well. As no further grain size coarsening was observed between 26 h and 40 h (Fig, 2.4b,c,2.5b,c), it is likely that new grain nucleation must have set in. New grain nucleation is frequently documented in the later stages of the dynamic recrystallisation of polycrystalline ice at high-homologous temperature (Wilson and Russell-Head, 1982; Wilson and Zhang, 1996; Piazolo *et al.*, 2013; Wilson *et al.*, 2014). Wilson and Russell-Head (1982) observe new grain nucleation from shortenings of 2 % in high-temperature uniaxial compression experiments but also report later onsets at higher shortenings for larger grain sizes. Figure 2.8 presents four potential nucleation sites (areas in which small new grains might have nucleated) identified in sample PS30-1 (Table 2.1). All potential nucleation sites show areas tremendously smaller than the average grain size with misorientations of 8-12° to the average of the grain. The EBSD orientation map depicts four of these areas as parts of larger grains. Due to the high Schmid factors of 0.35-0.45 in these sites, it is unlikely that any of these areas are remnants of old 'hard-slip' grains. Rotation recrystallisation can also be eliminated as a potential mechanism in case of these sites, as no significant peak of neighbour-pair MADs over the random-pair distribution was detected (Wheeler *et al.*, 2001, Fig. 2.6c). If these sites are in fact recrystallised grains, this experiment supports the findings of Duval

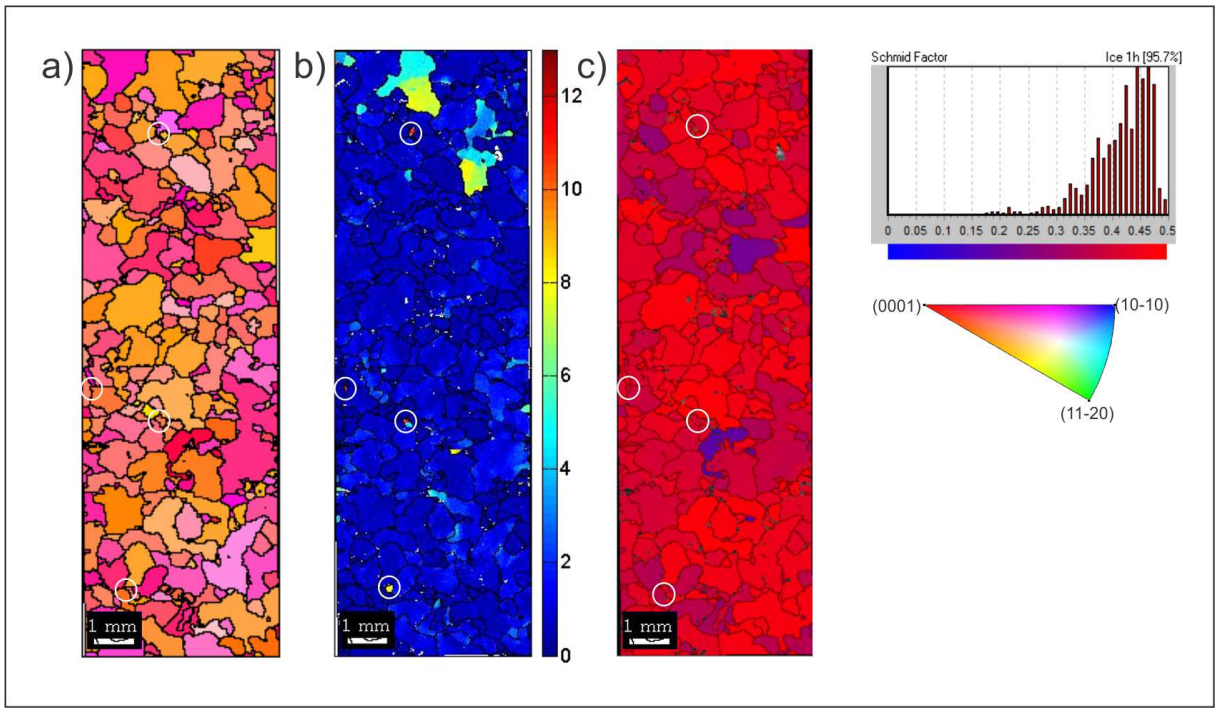

Figure 2.8: Potential nucleation sites for new grains in sample PS30-2 are indicated as white cycles in EBSD maps showing the a) orientation in an IPF reference frame colour-coded according to the shortening direction, b) misorientations within grains and c) Schmid factor for the (0001) <11-20> slip system.

(1981) and Burg *et al.* (1986), who observed new grain nucleation with similar orientations to parent grains. As the microstructure in sample PS30-2 seems to be governed by the 'easy-slip' orientation of its grains, it is unclear whether the determining factor for the orientation of recrystallised daughter grains is the orientation of the parent grain or merely the criterion of an 'easy-slip' (S≥0.3) orientation.

Our results support the findings of previous studies indicating that there is no dynamic recrystallisation and CPO development below 1 % shortening (Duval, 1981; Vaughan, 2016). The straight grain boundaries and polygonal grain shapes observed in samples PS10-1 and PSA-1 and the increase in grain size from the starting material suggest normal grain growth (annealing). The CPOs of samples PS10-1 and PSA-1 are random like in the starting material (Fig. 2.4a,e,f), which is not surprising since normal grain growth is not known to be a CPO changing mechanism (Wilson and Russell-Head, 1982). Grain size histograms show the same normal-shaped distribution but with a slightly larger standard deviation in samples PS10-1 and PSA-1 compared to the starting material (Fig. 2.5a,e,f). Moreover, the normal distribution has shifted to larger grain sizes as one would expect

for normal grain growth. The stress reduction sample PS3010-1 shows a microstructure, CPO and grain size distribution similar to the other experiments at 0.6 MPa (PS30-1, PS30-2), which indicates that no significant normal grain growth occurred during the second loading phase at 0.2 MPa and <1 % shortening. As a consequence, it is inferred that the grain growth kinetics of these samples are dissimilar to non-porous fine-grained laboratory ice (Azuma *et al.*, 2012; Becroft, 2015) but rather reflect the kinetics known from natural glacial ice samples (Cuffey and Paterson, 1994).

Contrary to expectations and even though new grain nucleation is probably present, the average and mean grain size generated during 26 and 40 h at 0.6 MPa (PS30-2 and PS3010-1) is larger than the average and mean after 43 hours under static (PSA-1) or semi-static (PS10-1 at 0.6 % shortening) conditions (Table 2.2). This observation indicates, that under the experimental conditions investigated, the driving force for strain-induced grain boundary migration may be larger than for curvature-driven normal grain growth.

2.4.2 Grain size distributions as a function of the deformation mechanism

Skewed and log-normal shaped grain size distributions seem to develop during different deformation mechanisms. During dynamic recrystallisation accommodated by grain boundary migration, grain diameter distributions become increasingly skewed between 5.3 and 18.1 % shortening (Fig. 2.5c,d). This process is characterised by a tripling of the standard deviation. Transitions from log-normal starting materials to skewed grain size distributions with axial shortening have also been reported in other high-temperature (T=-5°C) uniaxial compression studies with polycrystalline ice undergoing grain boundary migration (Montagnat *et al.*, 2015; Vaughan, 2016). Reliable grain size statistics collected with cryo-EBSD or a fabric analyser in these studies show that the transition gradually occurs between 3-7 % shortening. This is consistent with the partly skewed grain size distributions of samples PS30-1 and PS3010-1 at 5.3 and 6.3 % shortening (Fig. 2.5c,d), which show a stage between the normal distribution of the starting material and the fully skewed distribution of sample PS30-1 at 18.1 % shortening (Fig. 2.5a,c).

Log-normal shaped grain size distributions but an increase in overall grain size appear to be correlated with normal grain growth in samples PS10-1 and PSA-1 (Fig. 2.4e,f,2.5e,f). The bell-shape of the distributions is similar to the starting material, although the statistical parameters (arithmetic mean, median and standard deviation) have doubled from the starting material (Fig. 2.5a,e,f). Increased grain sizes from the starting

material were also observed in annealing experiments on previously deformed and undeformed ice samples (Wilson and Russell-Head, 1982). Whether normal grain growth produces a normal shaped grain size distribution or merely preserves the distribution from the starting material, cannot be discerned.

Generally, a decrease in the mode of the grain size histograms may be indicative of new grain nucleation. At high stresses of 0.6 MPa, where grain boundary migration is dominant and new grain nucleation presumably plays a role (Section 2.4.1), a progressive decrease in mode with strain is observed (Fig. 2.5a,b,c). In contrast to that, an increase in mode is observed in samples PS10-1 and PSA-1 undergoing normal grain growth (Fig. 2.5a,e,f).

2.4.3 Misorientation angle distributions as a function of the deformation mechanism

No link between misorientation angle distributions and the acting deformation mechanism could be constrained. For samples deformed by dynamic recrystallisation accommodated by grain boundary migration, the random pair misorientation angle distribution appears to deviate further from the random curve with progressive shortening. The random-pair MAD of the deformed samples appears block-shaped in the early stages of deformation at 5.3-6.3 % shortening (PS30-1 and PS3010-1, Fig.2.6b,d) and then normal-shaped with a pronounced difference to the theoretical curve for ice Ih at 18.1 % shortening (PS30-2, Fig. 2.6b). Similar observations on other rocks have been shown to be caused by the development of a CPO rather than by a specific deformation mechanism (Wheeler *et al.*, 2001).

Samples in which normal gain growth was attributed to be the primary mechanism of deformation (PS10-1 and PSA-1) show a small peak up to 8 % surplus in the neighbour-over the random-pair distribution for misorientation angles of 25-40° (Fig. 2.6e,f). There might be a connection between this peak and the process of normal grain growth, whose physical explanation is unclear at this point.

2.4.4 A critical look at the experimental procedure

The experiments in this contribution were primarily intended to develop and test the methods for cryo-EBSD on fine-grained ice described in Prior *et al.* (2015). Hence, the experimental technique with the deformation rig in the ECS was still under development and yielded inconsistencies between the experiments. After initial problems with instan-

taneous fracturing, the loading time between the application of the first 10 kg until the sample was subjected to the full load was initially high with 2 hours and continuously decreased with every high-stress experiment (Table 2.1).

A significantly faster loading time might have sped up the degree of vertical shortening in sample PS30-2 until a final shortening of 18.1 %, compared to PS30-1 and PS3010-1 with shortenings of 5.3-6.3 %. In addition to that, differences in the flow and chilling speeds lead to a difference of 0.4°C in experiment PS30-2 to the otherwise average temperature of about -2.6°C. Grain boundary mobility increases with temperature at high-homologous temperatures (Barnes *et al.*, 1971). The slightly lower temperature during the deformation of sample PS30-1 might have resulted in a lower rate of grain boundary migration that might present a second explanation for the comparably small average grain diameter determined in PS30-2 (Table 2.2). Moreover, the stress in experiment PS30-2 was ∼0.1 MPa higher and according to the inverse relationship between steady state grain size and strain (Jacka, 1994), a smaller grain size as in experiments PS30-1 and PS3010-1 is expected (Table 2.2).

Different extraction times of the polycrystalline ice samples from the rig until immersion into nitrogen (and the preservation of the microstructure) apply (Table 2.1). These were on the order of 12-25 minutes, in which the samples remained with no load in the silicone oil at -2.5°C. As grain growth kinetics of these samples appear similar to polar ice (Section 2.4.1), the microstructure is not expected to have been modified by normal grain growth.

Testing of the environmental control system (ECS) revealed re-occurring pump failure for running times over 45 hours. Longer running times are essential to deform samples >1 % shortening for low stresses of 0.1-0.2 MPa more similar to the stress and strain rate conditions in glaciers and ice sheets. The most likely cause for the arrest of the pump are small ice and dirt particles, which move from the Plexiglas box and copper-coil heat exchanger into the pump (Fig. 2.1b). To address this issue, a filter will have to be placed between the heat exchanger and the pump.

A potential source of uncertainty in the data processing lies in the calculation of the neighbour-pair misorientation distributions in Channel 5, which were found to be altered depending on the extent of processing by noise-reduction. Special care was taken to find a good noise-reduction routine (wild spikes extrapolation and 2x 7 neighbours) that was appropriate for all samples to ensure comparability within the samples of this study.

2.5 Conclusions

The experimental evidence presented in this chapter suggests that

- grains grow faster dynamically than statically under the same temperature conditions. Stress-induced grain boundary migration is an efficient coarsening mechanism and leads to a larger arithmetic mean and median grain diameter at high stresses of 0.6 MPa after 5.3-6.3 % shortening (after 26-41 h) as observed after 43 h of normal grain growth. Only grains with high Schmid factors of $\geq$0.3 remain with progressing grain boundary migration, which leads to the formation of the two cone CPO characteristic for uniaxial compression experiments.

- grain size coarsening as a result of grain boundary migration is finite and leads to a constant steady state grain size once new grain nucleation sets in.

- low shortenings below 1 % seem to only induce normal grain growth and microstructural features, grain size histograms and CPOs cannot be distinguished from samples annealed for the same period of time.

- the shape of grain size distributions depends on the deformation mechanism. Skewed grain diameter distributions correlate with grain boundary migration and CPO development. Normal grain growth widens the normal-shaped grain diameter distribution and causes a shift towards larger grain sizes.

- a decrease in the modes of grain size histograms from the starting material is indicative of new grain nucleation.

Acknowledgements

This work was funded by Marsden Fund grand UO1116 and a University of Otago Doctoral scholarship. Jim Woods, Leo Van Reins, Peter Fleury and Brent Pooley are thanked for technical support. Imogen Browne, Myrna Blessenohl and Jan Leunissen assisted with ice growing and deformation experiments. Jack Williams provided feedback on the manuscript.

2.6 Graphical summary

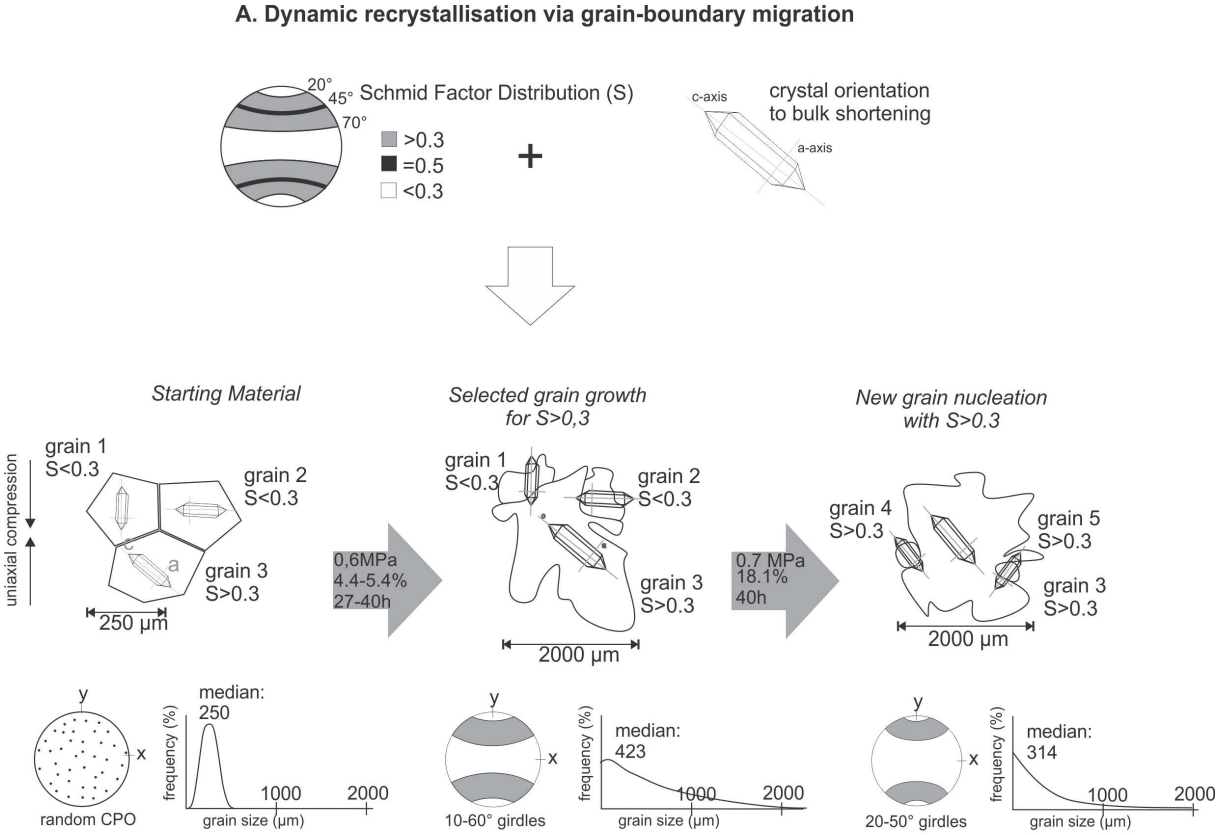

*rounded grain size statistics for a step size of 20 µm are shown

2.7 Supplementary material

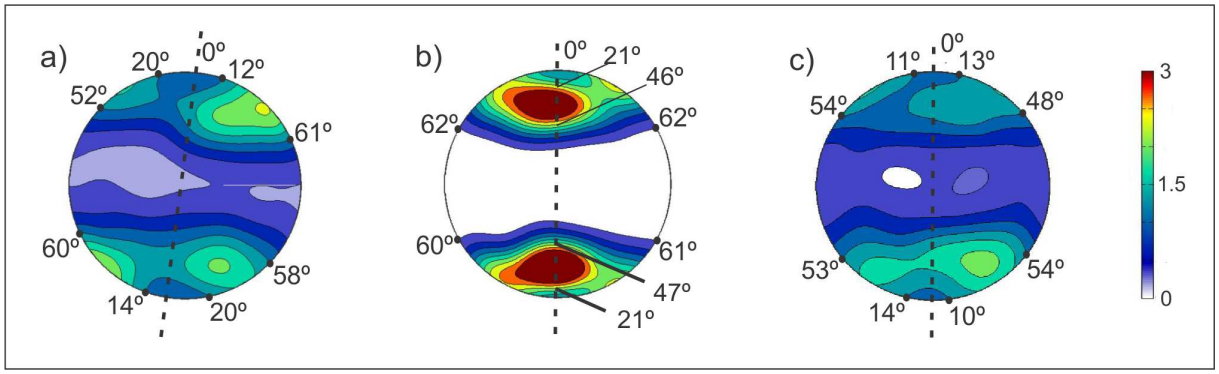

Figure 2.9: Angular constraints on development of a CPO for experiments with stresses ≥ 0.6 MPa for contoured pole figures. a) PS30-1, b) PS30-2 and c) PS3010-1. The axis of shortening is indicated as a dashed line. Angles were adjusted for experiment PS30-1 as only the right half of the top surface contacted the piston, resulting in an asymmetry in the pole figures.

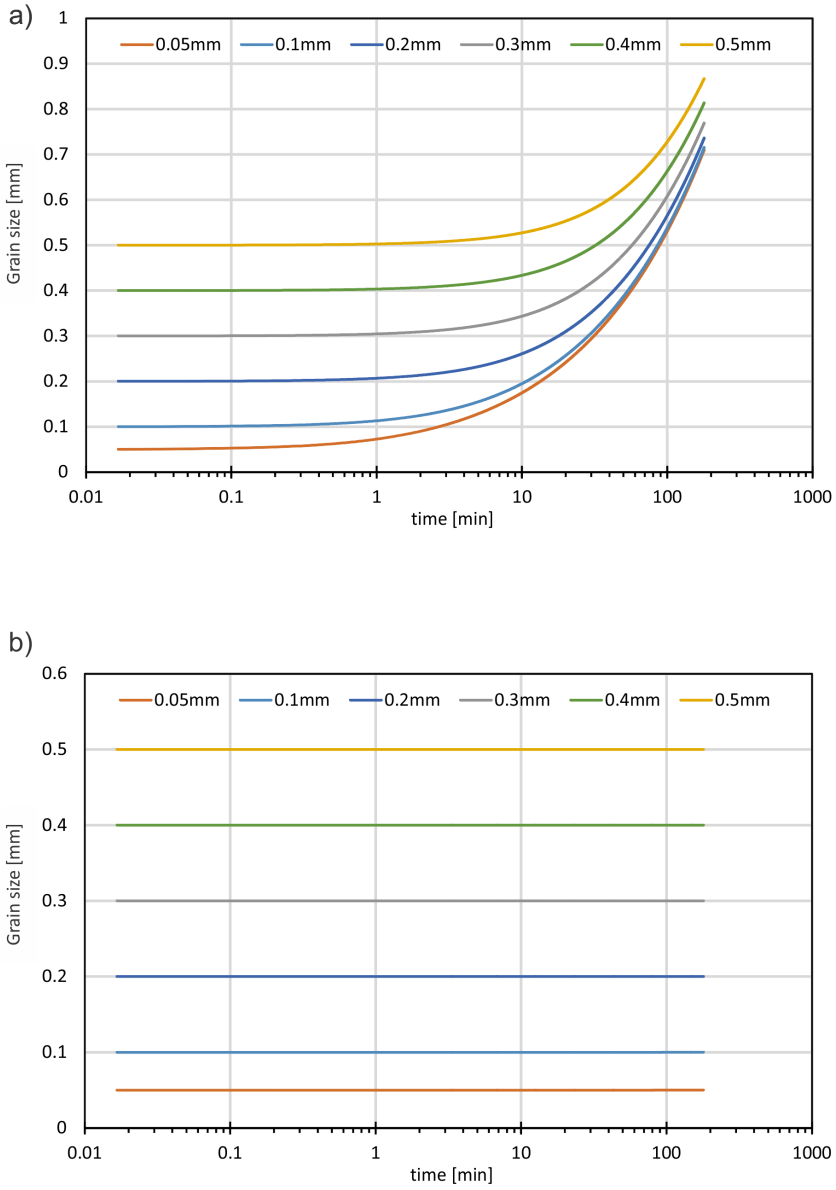

Figure 2.10: Estimated change in grain size as calculated from grain growth kinetics from a) bubble-fee polycrystalline ice in Azuma *et al.* (2012) and b) polar firn in Cuffey and Paterson (1994). Grain growth parameters were extracted from an overview in Becroft (2015).

Chapter 3

Particle image velocimetry in unconfined ice creep experiments

Meike Seidemann[1], Matthew J. Vaughan[1], Kat Lilly[1], David J. Prior[1]

[1]Department of Geology, University of Otago, Dunedin, New Zealand

Abstract

Conventional creep experiments recording mechanical data during and examining microstructures post-deformation are characterised by a lack of information on deformation heterogeneity during the experiment. To address this gap, particle image velocimetry was employed to calculate the evolution of velocity fields and strain rate distributions of two fine-grained (250 μm) polycrystalline ice samples deforming under uniaxial compression at 0.6 and 0.2 MPa with shortenings of up to 6 %. Results of the PIV analysis yielded information on spatial-temporal flow and deformation heterogeneity. Spatial heterogeneity was visible in 2-15 x higher flow magnitudes and strain rates one order of magnitude higher in the top than in the bottom half of the particle image velocimetry's region of interest and was attributed to higher stresses at the top as a consequence of the experimental boundary conditions. Temporal heterogeneity is characterised by repeated horizontal 'waves' of high velocity magnitude and transient bands of elevated strain rate at an angle of 60-80° to bulk shortening. Comparisons with post-deformation microstructures of the samples indicate that long-term (over several % shortening) spatial deformation heterogeneity may have a limited effect on the microstructure. In contrast to that, no evidence for permanent microstructural alterations due to transient bands with strain rates one

order of magnitude larger than the samples' averages were detected.

3.1 Introduction

Microstructural studies in rock deformation experiments generally acquire mechanical data during the experiment and examine microstructures post-deformation. Laboratory experiments rarely provide microstructural data from more than one point in time and multiple experiments are needed to constrain the microstructural evolution of geologic materials and its explicit connection to flow laws. Hence, microstructural studies become easily both time- and labour-intensive. Another culprit of such microstructural investigations is that only little or no information on deformation heterogeneities due to the experimental boundary conditions are available, leaving researchers with little other option than to model the experimental setup. A particle image velocimetry (PIV) approach based on time-lapse photography in unconfined deformation scenarios can provide velocity data from particle movements within the deforming sample and thus complement the existing mechanical and microstructural data with information on internal flow velocities and inconsistencies during deformation.

PIV is a non-intrusive method used to calculate and visualise flow data and has been primarily used to track and quantify the movements of fluids in the last 30 years (see Brossard *et al.*, 2009 for a summary). Its user-friendliness and high success rate have promoted applications in many other disciplines, including the geosciences i.e. with the measurement of velocities of soil deformation in geotechnical models (White *et al.*, 2003), natural convection in ice melting (Scanlon *et al.*, 2001) and large-scale, whole-field measurements of ice velocities in rivers (Ettema *et al.*, 1997). In columnar polycrystalline ice, shoe polish in combination with a similar digital image correlation (DIC) algorithm has been employed to constrain grain-scale strain localisation patters during transient creep (up to 1 % strain, Grennerat *et al.*, 2012).

The computation of both velocity and strain rate distributions is appealing for ice deformation experiments. Flow velocities are often employed to describe the movements of large ice masses as glaciers and ice sheets. Their investigation has shown that bulk flow is rarely homogeneous throughout the volume of the ice mass (i.e. Thwaites *et al.*, 1984; Cuffey and Paterson, 1994; Hulbe and Macayeal, 1999; Bons *et al.*, 2016). Contrastingly, the strain rates in laboratory experiments are calculated under the assumption that deformation proceeds homogeneously. PIV results of deformation experiments with time series of both velocity fields and strain rate distributions may provide a better understanding of

ice behaviour and address a potential gap between laboratory and field data. A related advantage to using PIV as a strain rate distribution resolution tool is the investigation of transient strains and their potential impact on the microstructure. Transient or elastic strains have been thought a phenomenon in the Earth's crust for decades (i.e. Sibson, 1980) and have been repeatedly inferred from geodetic or radar datasets for large-scale fault zones (Peltier *et al.*, 2000; Oskin and Iriondo, 2004; Ganev *et al.*, 2012). PIV may provide a way to image and constrain these transient strains in deformation experiments.

In this chapter, PIV is applied to rock deformation studies by calculating flow velocities and strain rate distributions from movement patterns of graphite particles on the surface of deforming polycrystalline ice samples under uniaxial compression. In combination with mechanical data and post-deformation microstructures, we employ the PIV results to gain a better understanding of dynamic deformation heterogeneity on a sample-scale and its potential impact on the final microstructure.

3.2 Method

3.2.1 Experimental procedure and EBSD imaging

Homogenous 21 mm x 23 mm x 39 mm block-shaped samples of polycrystalline 'Standard ice' (Stern *et al.*, 1997) with an average grain size of 250±125 μm, a polygonal microstructure and a random CPO (Fig. 3.1a-c) were cut with a diamond-bladed ring saw in a -20°C cold room environment. Prior to deformation, sample dimensions were measured in a freezer using a chilled vernier calliper. One 21 mm x 39 mm or 23 mm x 39 mm area of the samples was covered with a layer of graphite particles with lenghts of 0.1-2 mm (Fig. 3.1d). The graphite was subsequently attached in a freezer with water droplets from a diffuser. The bottom 5 mm of the samples were frozen onto a piece of wood in a metal tray, which was placed on the bottom of a glaciological Jacka rig. The rig was subsequently submerged into -2.5°C cold silicone oil within a transparent Plexiglas cage (Fig. 2.1a). A vertically moving metal plate within the Jacka rig was cautiously lowered onto the samples. The start of the experiments was marked by putting load onto the top plate. To prevent fracturing, the load was slowly increased in 10 kg increments during the first $\sim$ 2.5 h of experiment PS30-1 and $\sim$ 1h of experiment PS3010-1 (Fig. 3.2).

In the Plexiglas cage, the vertical displacement values and temperature were monitored with a linear variable differential transformer (LVDT) and two thermocouples. Sample PS30-1 was subjected to 27 h of uniaxial compression of $\sim$0.6 MPa (Table 3.1).

Experiment PS3010-1 included a load step at ∼0.6 MPa for 40 h and a subsequent load reduction to ∼0.2 MPa with a complete experimental duration of 44 h.

During deformation, a Canon EOS 1100D digital single-lens reflex camera driven by Canon Utility time-lapse software was recording images at intervals of 60 seconds. Prior to the start of the time-lapse photography, test images were taken to ensure image quality and sufficient image width to account for deformation-induced bulging of the sample diameters (Fig. 3.1d, 3.6).

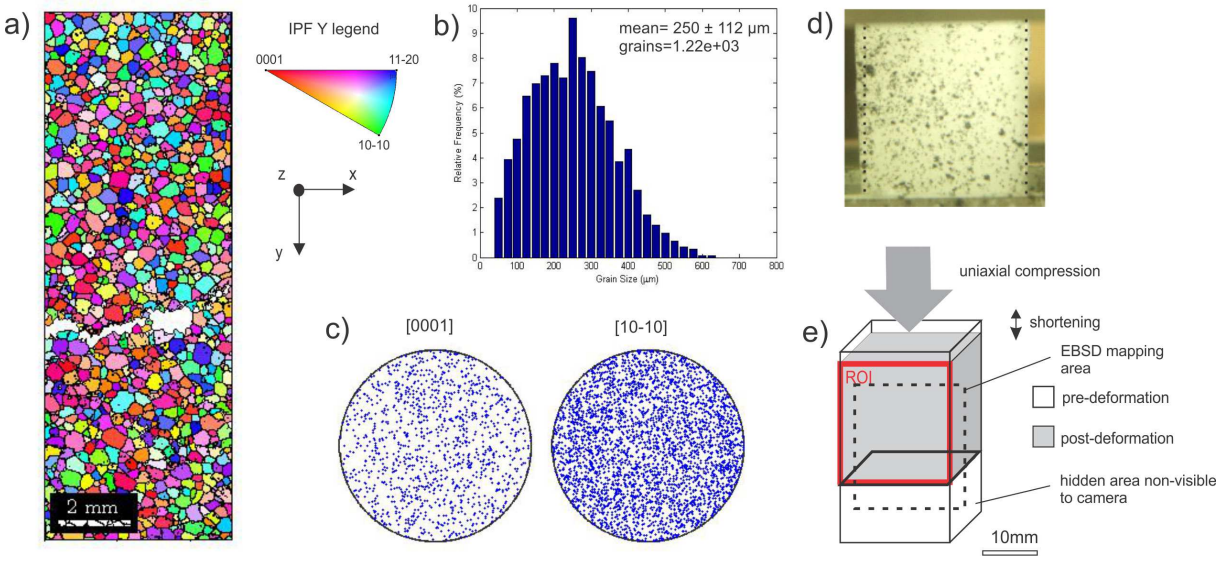

Figure 3.1: Starting material and sample preparation. a) EBSD map of Standard ice prior to deformation. b) Grain size histogram of the starting material with mean grain size and standard deviation. c) Pole figure of EBSD map in (a) containing 493 randomly selected grain orientations. d) Ice sample as viewed by the camera during deformation. The top of the samples during deformation bulges outwards, as seen with respect to the dotted lines. e) 3D view of shortening direction, definition of a region of interest (ROI) for PIV processing and surface used for EBSD mapping. Note that the bottom ∼13 mm of the samples is hidden behind the metal tray and non-visible to the camera.

After deformation, samples were extracted from the rig and submerged into cold nitrogen mist to prevent post-deformational annealing (Prior *et al.*, 2015). Once samples had cooled sufficiently to a temperature below -30°C, they were cut along their long axis (Fig. 3.1e). Up to 8.2 mm were removed at the top and bottom of each sample to allow for mounting on a 30 mm x 30 mm copper SEM ingot. The copper ingots were consecutively inserted into an Emtech cold stage within the chamber of a Zeiss Sigma scanning electron

microscope. EBSD maps were gathered below with a stage temperature of -100°C with a 30 kV beam current and ∼100 nA of beam current.

3.2.2 Data processing

Shortening rates, octahedral stresses and strain rates were determined according to the relations in section 3.7.1.

Table 3.1: Experimental conditions and mechanical parameters.

Experiment	PS30-1	PS3010-1 (1)	PS3010-1 (2)
Load [kg]	30	30	10
Duration [h]	27	40	3.6
Height pre-deformation [cm]	3.90	3.95	n\a
Mean temperature [°C]	-2.5	-2.6	-2.6
Axial stress [MPa]	0.59 ± 0.02	0.60 ± 0.01	0.19 ± 0.05
Octahedral shear stress [MPa]	0.28	0.28	0.09
Vertical strain rate [/s]	$5.5x10^{-7}$	$3.9x10^{-7}$	-
Octahedral strain rate [/s]	$4.7x10^{-7}$	$2.9x10^{-7}$	-

The photos collected with the time-lapse photography were processed in PIVlab, a digital PIV plug-in for Matlab 2013. Seven images were selected for each sample and the particle movements between the images were compared in an AB, BC, CD etc. sequence. Image pre-processing techniques in PIVlab (Thielicke and Stamhuis, 2014) were omitted because the pictures showed a strong contrast between graphite and ice and the image quality obtained with the 12.2 MP Canon EOS 1100D was excellent. To minimise computational time, a region of interest (ROI) was placed around the area of the ice sample in the last frame and applied to all other frames. Employing the last frame for ROI definition accounts for deformation induced sample bulging (Fig. 3.1d) and automatically eliminates erroneous vectors caused by the movement of the top plate into the ROI area. The sample width pre-deformation was employed to visually calibrate the ROI, as sample lengths pre-and post-deformation were often non-constant due to sample tilts induced by freezing the samples onto the sample trays. A disadvantage of this calibration method was that the sample width pre-deformation had to be approximated with 22 mm, because it was unclear which sample surface had originally been coated with the graphite

particles. The determination of the coated surface from images taken pre-deformation was impossible. Post-experimental calculation of the samples width's with the help of the samples' lengths in images taken pre-deformation (see Fig. 3.1d) was hindered by the aforementioned sample tilts and because a part of the samples' lengths in the images was hidden behind the metal trays (Fig. 3.1e).

A same-sized ROI for all frames enabled the use of the fast discrete Fourier transform (DFT) as the cross-correlation algorithm over the slower but more accurate direct cross-correlation (DCC) (Huang *et al.*, 1997). The accuracy of the DFT was increased by running 3 passes (iterations) on the same dataset to minimise the amount of background noise in the correlation matrix (Westerweel, 1997). Velocity limits were selected in a scatter plot to remove spikes, potentially as a result of spotty graphite distribution or an imprecise definition of the ROI. Erroneous velocity arrows, particularly at the rims of the ROI, were manually removed. As a method of display, the velocity magnitude (Fig. 3.3a-g,3.4a-g), velocity perpendicular (Fig. 3.3h-n,3.4h-n) and parallel to shortening (Fig. 3.3o-u,3.4o-u) were chosen for the output image series.

2D strain rates (termed 'shear rates' in PIVlab) were computed from a horizontal velocity component u in x-direction and vertical velocity component v in y-direction:

$$\dot{\epsilon}_{PIV2D}[/s] = \frac{\delta u}{\delta y} + \frac{\delta v}{\delta x} \tag{3.1}$$

and were also displayed as an output image series (Fig. 3.3v-b1,3.4v-b1). An average frame visualising the arithmetic mean values of all frames was additionally calculated for each image series (Fig. 3.3g,n,u,b1,3.4g,n,u,b1).

For a comparison with the shortening time curves (Fig. 3.2), vertical velocity (termed v-velocity in PIVlab) components were extracted to the Matlab workspace. Averaging over the number n of v-velocity components within the equally-spaced ROI grid and division by the current sample length l_c (the median strain value of each frame) yielded a 1D vertical shortening rate (Fig. 3.3c1-i1,3.4c1-i1):

$$\dot{\epsilon}_{PIV1D}[/s] = \frac{(v_1 + v_2 + ... + v_n)n^{-1}}{l_c} \tag{3.2}$$

EBSD orientation and shape factor maps (Fig 3.3j1,k1,3.4j1,k1) were processed with MTEX 4.0.12 in a Matlab 2013 environment. Non-indexed pixels were removed and grain boundaries were calculated with a minimum misorientation angle of 10°. An additional threshold of 10 pixels per grain was employed to clean the data. Orientation maps (Fig. 3.3j1,3.4j1) were generated using an IPF colour-code with respect to the shorten-

ing direction (see Nolze and Hielscher, 2016 for more details on this method of display). Shape factor maps visualise the ratio between the long and the short axis of the grain area-equivalent diameters (Fig. 3.3j1,3.4j1). Additional maps highlighting differences in area-equivalent grain diameter were exported from Oxford Instruments' channel 5 software (Fig. 3.5). The map of Standard ice in Fig. 3.5a was imaged at a small step size of 10 μm and was processed with a reduction resolution routine in MTEX (Cross *et al.*, 2017) to allow for a grain size comparison with the EBSD maps of samples PS30-1 and PS3010-1 (20 μm step size).

3.3 Results

3.3.1 Mechanical constraints

PS30-1

Sample PS30-1 was subjected to approximately 0.6 MPa for ∼26.6 h, leading to a vertical shortening of 5.4 % (Fig. 3.2a). The load was progressively increased in 10 kg increments to prevent cracking until the target load of 30 kg was reached after 3 h.

Shortening rates were approximated for the time increments employed in the PIV analysis. Due to the the long time to establish the target load, the curve below 3 % shortening is shallower than normally observed in polycrystalline ice (Budd and Jacka, 1989; Faria *et al.*, 2014; Wilson *et al.*, 2014). The fastest strain rate of 8.3x10^{-7} /s was determined for the initial increment (I) and presumably comprises a component of elastic strain and the transition from primary to secondary creep, which usually occurs at about 1% shortening. Shortening rates calculated for the remaining time increments (II-VI) progressively increase during secondary creep. The tertiary creep stage with constant shortening rates, which is generally established around 10 % shortening was not reached.

Conversion of the vertical shortening to octahedral values (section 3.7.1) yielded an octahedral shear stress of 0.28 MPa and shear strain rate of ∼4.7x10^{-7} /s, respectively (Table 3.1).

PS3010-1

Sample PS3010-1 was subjected to ∼0.6 MPa for 40 h and ∼0.2 MPa for 3.7 h (Fig. 3.2b). The final vertical shortening amounts to 6.3 %. Target stress was established after 1 hour and the stress reduction was almost instantaneous.

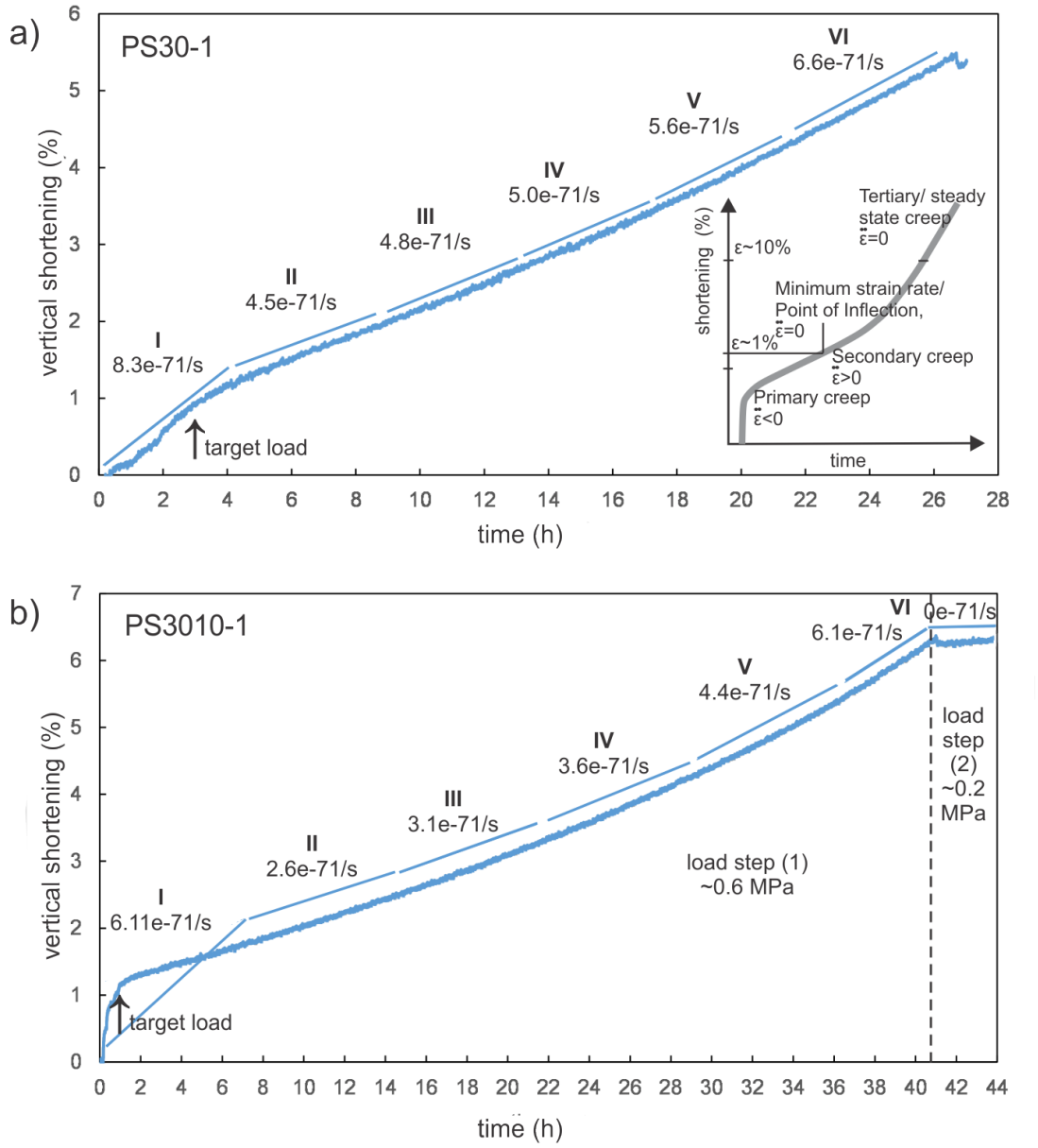

Figure 3.2: Vertical shortening versus time curves for a) PS30-1 and b) PS3010-1. Numbers above linear segments denote approximated strain rates for the time increments used in the respective PIV analyses of both samples (Fig. 3.3,3.4). A generalised shortening vs. time curve (Budd and Jacka, 1989) is shown in the bottom right corner of (a).

The time used for the loading of the sample in experiment PS3010-1 was shorter than in experiment PS30-1, leading to a better resemblance between the generalised creep curve in Fig. 3.2a and the mechanical data of PS3010-1 (Fig. 3.2b). The steep gradient in the shortening vs. time curve below 1 % shortening matches the signature of the elastic

response commonly observed during primary creep. The first time increment used for the PIV analysis (I) was commenced just after 1 % shortening (upon complete loading) to about 2.2 % shortening and presumably incorporates the transition from primary to secondary creep. In the subsequent time increments II-VI, a gradual acceleration of the shortening rates was observed as secondary creep progressed until the load reduction was performed during time increment VI. During the second load step, a gradual reduction of vertical shortening ($\sim$ 0.2 %) at a very slow rate was detected.

Octahedral shear stresses of 0.28 MPa and 0.09 MPa were calculated for the two load steps (Table 3.1). An octahedral strain rate of 2.9x10^{-7}7 /s was determined for the first load step.

PIV analysis of sample PS30-1

In general, higher velocity magnitudes were observed in the top half than in the bottom half of the ROI and the velocity direction is from top to bottom (Fig. 3.3a-g). One exception can be found during the first 1.9 % shortening, where high flow velocity magnitudes (up to 3x10^{-8} m/s) are detected in the top right corner of the ROI and correspond to velocity directions pointing to the right lower corner of the ROI (Fig. 3.3a,b). Subsequently, high velocity magnitudes of $\geq$1.5x10^{-8} m/s are found in the top half and decrease to zero towards the bottom of the ROI (Fig. 3.3c-e). The area of high velocity magnitudes within the ROI approximately covers the top quarter of the sample (Fig. 3.1e). Two bands of high velocity magnitude of about 1.5x10^{-8} m/s are detected at an 60-80° angle to the shortening direction (v+, in legend of Fig. 3.3) after 4.3 % shortening (Fig. 3.3f). One of these bands also extends into the lower half of the ROI. The calculated average velocity magnitude reflects the trends observed during deformation: high velocity magnitudes during the first 1.9 % shortening in the top right corner, velocity magnitudes >1x10^{-8} m/s in the top half of the ROI and the two bands of high velocity magnitudes detected between 4.3 and 5.4 % shortening.

U-velocities signifying the horizontal part of the velocity vector show a vertically symmetrical distribution with equally high negative u-velocities on the left side of the ROI and similarly high positive values on the right side (Fig.3.3h-n). In general, higher values in both u- and u+ directions are detected in the top half of the ROI. An exemption is noted during the first 1.9 % shortening, where positive u-velocities (flow from left to right) dominate (Fig.3.3a,b).

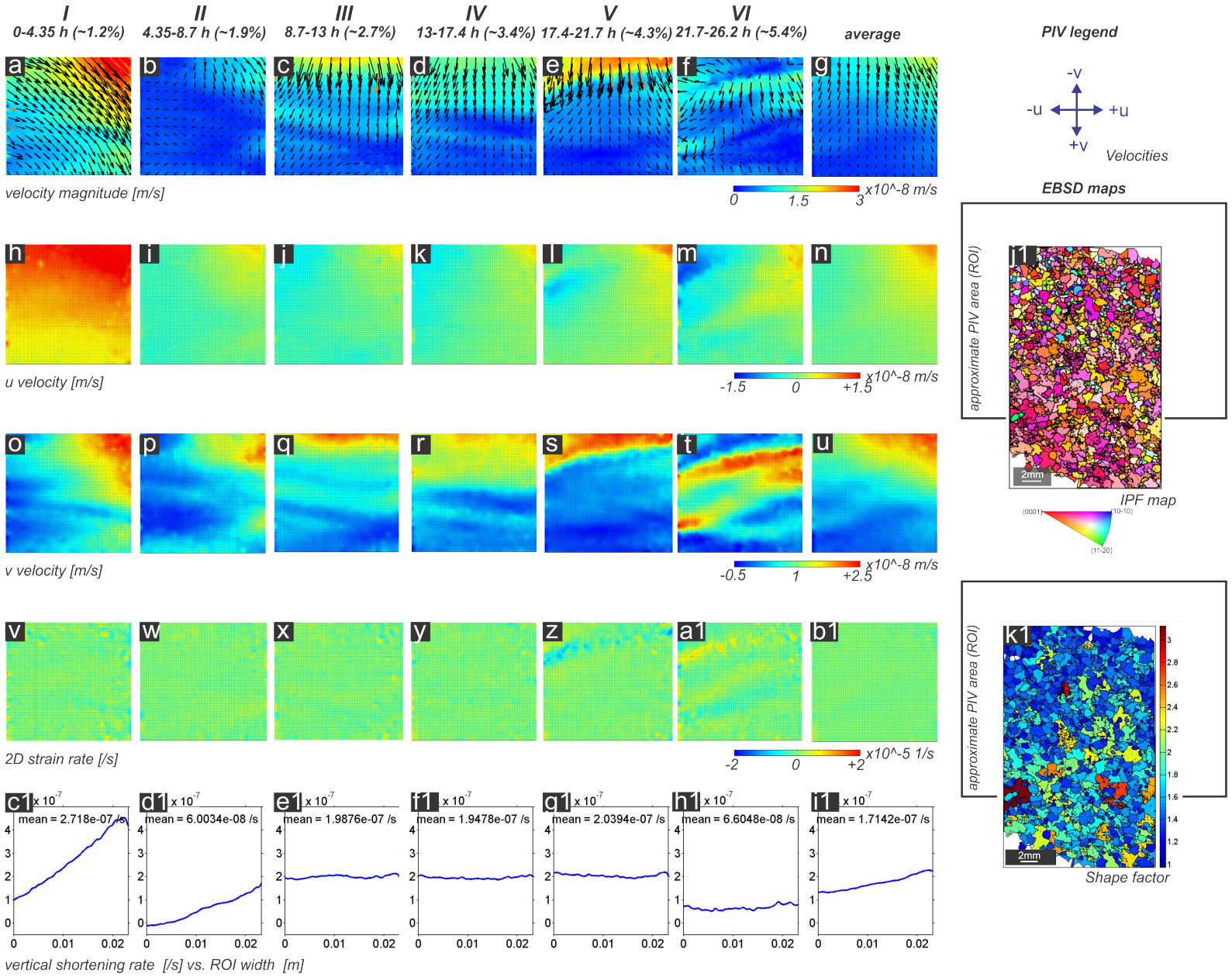

Figure 3.3: PIV analysis of experiment PS30-1. Time increments and maximum strain achieved during each time increment (in brackets) are denoted above the velocity magnitude row. Velocity arrows are shown in the velocity magnitude row. Interpolated vectors are labelled in red. Black boxes in (j1) and (l1) indicate the approximate location of the PIV area (ROI) with respect to the EBSD map.

Negative v-velocities representing flow from top to bottom were calculated for the upper two-thirds of the ROI (Fig.3.3o-t), approximately equivalent to the upper third of the sample (Fig. 3.1e). Slightly negative v-velocities (flow from bottom to top) were solely recorded in the top left corner during the initial 1.9 % shortening (Fig. 3.3a,b) and in the far bottom of the ROI (Fig. 3.3o-t). High v-velocities of 2.5x10^{-8} m/s are found at the top of the ROI and decrease towards the bottom from 2-4.75 % shortening (Fig. 3.3q-s). After 4.75 % shortening, two bands with high v-velocities (2.5x10^{-8} m/s) are detected at an oblique angle to the shortening direction in the first and second third of the ROI (Fig. 3.3t). The average is a good representation of all these trends (Fig. 3.3u).

Strain rate calculations show a relatively homogeneous distribution within a range of -2 to 2x10^{-5} m/s for the entire ROI at all times (Fig. 3.3v-a1). Exceptions include spot-like perturbations in close proximity to the borders of the ROI (i.e. Fig. 3.3x,y). These strain rate localisations around the rims of the ROI spatially correlate with areas in which the ROI overlaps the boundaries of the sample (Fig. 3.6a) and presumably result in artefacts due to missing reference points (graphite particles) in those areas. Other distinctive features are bands of elevated strain rates of $\pm$1x10^{-8} m/s at an angle of 60-80° to the compression direction. One band is located in the top quarter of the ROI between 3.7-4.3 % shortening (Fig. 3.3z). Between 4.7-6.1 % shortening, two bands with alternating positive and negative strain rates are also detected in the centre of the ROI (Fig. 3.3a1). The average strain rate distribution does not show bands or spots (Fig. 3.3b1).

Vertical shortening rates derived from v-velocities show higher values in the right than in the left part with a maximum rate of 3x10^{-7} /s calculated for the right corner of the ROI during the first 1.9 % shortening (Fig. 3.3c1,d1). The vertical shortening rate becomes more evenly distributed for from $\sim$2 % shortening. The acceleration in the shortening rates approximated from the mechanical data during secondary creep (II-VI,Fig. 3.2a) is only detected to a limited degree in the PIV derived vertical shortening rates from 1.2-4.3 % shortening (time increments II-V, Fig. 3.3e1-g1). As opposed to the mechanical observations, a decrease in the PIV derived shortening rate was observed from 1.3-5.3 % shortening (Fig. 3.3h1). The average vertical shortening rate derived from the PIV analysis ($\sim$2x10^{-7} /s) is only slightly lower than shortening rates of 4.5-8.3x10^{-7} /s approximated from the mechanical data (Fig. 3.2a,3.3i1).

Microstructure of sample PS30-1

The microstructure of sample PS30-1 is characterised by lobate grain boundaries, interlocking grain shapes and approximate grain diameters of 50-2500 μm (Fig. 3.3j1). Larger grains with diameters $\geq$ 2000 μm often have high length to width ratios $\geq$ 2 (shape factors) and are predominantly found in the bottom half of the map and bottom third of the ROI (Fig. 3.3k1,3.5b). Arithmetic mean and median grain diameters are almost twice as large as in the starting material (Fig. 3.5a,b). The relative frequency of very small grains ($\leq$200 μm) is higher than in the starting material. Generally, a higher number of small grains below 1000 μm can be found within the top of the deformed sample's map, equivalent to the top two thirds of the ROI (Fig 3.5b) and approximately top half of the sample (Fig. 3.1e).

PIV analysis of sample PS3010-1

The velocity magnitude and directions vary throughout the 43.6 h of deformation. During the initial 1.8 % shortening, the velocity magnitude distribution is homogeneous throughout the ROI with magnitudes of $\sim$8x10^{-8} m/s and velocity directions pointing towards the lower left corner of the ROI (Fig. 3.4a). Velocity magnitudes subsequently decrease to below 5x10^{-8} m/s for the majority of the ROI between shortenings of 1.8-3.3 %. A thick (one-fifth to a quarter of the ROI length) horizontal band with elevated velocity magnitudes of 7.5x10^{-8} m/s initiates at the top of the ROI (Fig. 3.4b) and progressively moves towards the upper centre (Fig. 3.4c). This process is repeated with velocity magnitudes of up to 15x10^{-8} m/s for shortenings from 3.3-5.4 % (Fig. 3.4d,e). The highest velocity magnitudes are found at the top of the ROI (Fig. 3.4d). Due to the reduction in load, reversed velocity arrows pointing to the top of the ROI and a low velocity magnitude of below 4x10^{-8} m/s were calculated between 5.4-6.3 % shortening (Fig. 3.4f). The average velocity magnitude for the entire period of investigation shows only moderate values of 7.5x10^{-8} m/s within the top half of the ROI (Fig. 3.4g). Velocity magnitudes in the bottom half are close to 0.

Generally, negative u-velocities with velocity directions from right to left are predominant (Fig. 3.4h-m). Negative u-velocities also tend to be 2-3 x higher than positive u-velocities. Higher magnitude u-velocities are in almost exclusively found within the top half of the ROI, corresponding to the top third of the sample (Fig.3.1e). The calculated average u-velocity distribution reflects all these observations (Fig. 3.4n).

The v-velocities are mostly positive (flow from top to bottom, Fig. 3.4o-t). High v-

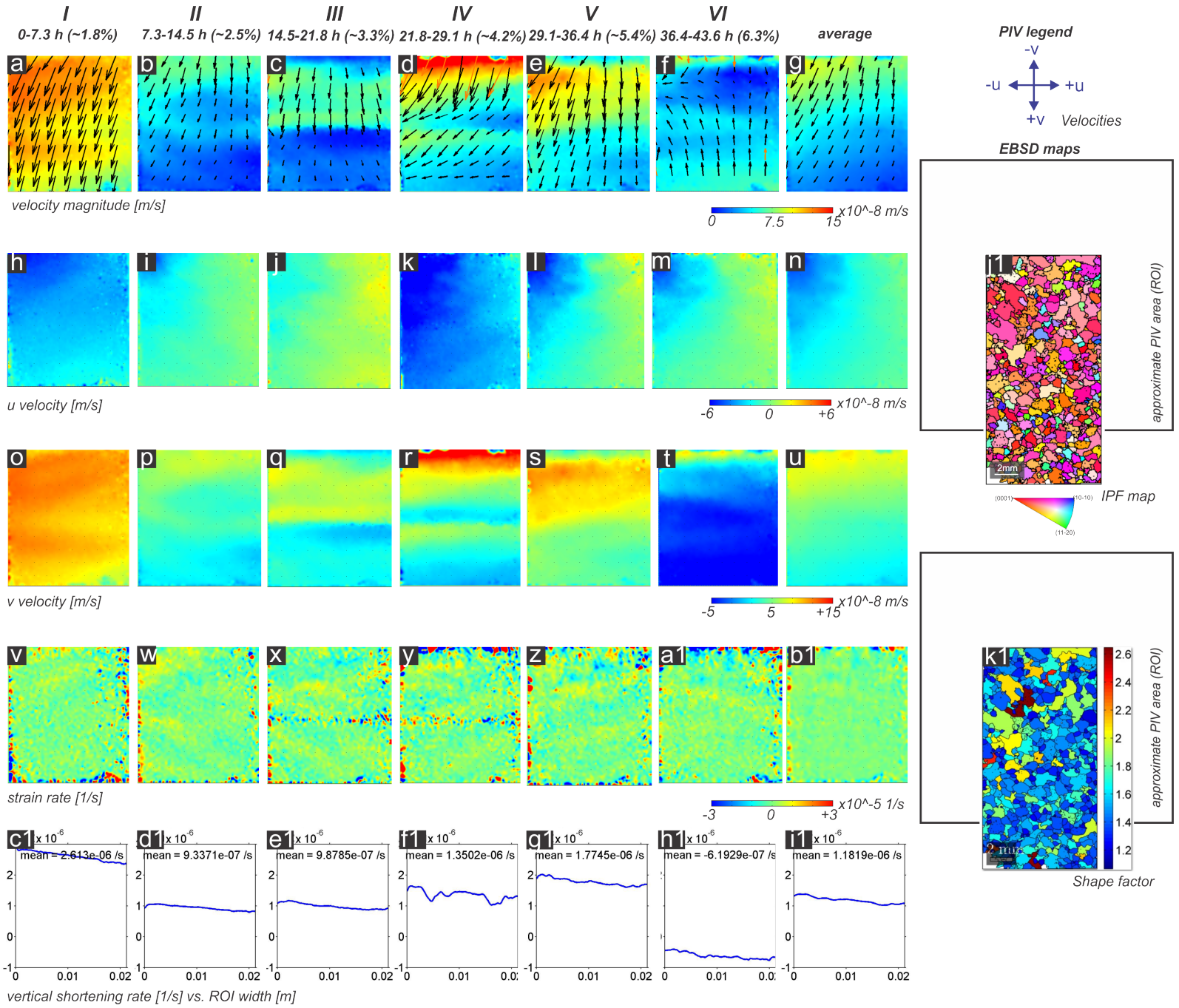

Figure 3.4: PIV analysis of experiment PS3010-1. See Fig. 3.3 for annotations.

velocities are generally concentrated in the top half of the ROI (Fig. 3.4p-s), except during the first 1.8 % shortening, where v-velocities are homogeneously distributed throughout the ROI (Fig. 3.4o). A band of high v-velocities initiates at the top of the ROI (Fig. 3.4p,r) and progresses towards the centre of the ROI ($\sim$ top third of the sample) in the next interval (Fig. 3.4q,s). The v-velocities are negative for 90 % of the ROI in the last increment (Fig. 3.4t). Positive v-velocities only occur at the far top of the ROI where many interpolated vectors are found (Fig. 3.4f,t). The average v-velocity distribution shows high v-velocities of $\sim$7x10^{-8} m/s at the top of the ROI with a progressive decrease in v-velocity magnitude towards the bottom of the ROI (Fig. 3.4u).

Strain rate distributions are relatively homogeneous throughout the ROI with values around $\pm$ 0-2x10^{-6} /s (Fig. 3.4v-a1). Higher strain rates found around the rims of the ROI are again artefacts stemming from a discrepancy between sample boundaries and the rectangular ROI (Fig. 3.4v-a1, 3.6b). The high strain rates in a band across the centre of the ROI between 2.5-4.2 % shortening are not detected in the strain rate distributions of PS30-1 and are presumably also an artefact (Fig. 3.3v-b1,3.4x,y). Bands of elevated strain rates ($\sim$1x10^{-5} /s) are detected at an oblique angle to bulk shortening (Fig. 3.4v-a1). For shortenings $\geq$4.2 %, these bands span over the entire width of the ROI with only little change in orientation to bulk shortening (Fig. 3.4z,a1). The average strain rate (on a scale of -3 to +3x10^{-5} /s) does not show any bands but depicts strain rate localisations at the outer rims of the ROI (Fig. 3.4b1).

Vertical shortening rates determined via the PIV analysis reflect the initially high shortening rate (I), low shortening rate (II) and subsequent acceleration of the shortening rate (II-V) observed in the mechanical data (Fig. 3.2b,3.4c1-g1). A negative, one order of magnitude slower shortening rate of 6.6x10^{-8} /s was derived during the second load step (Fig. 3.4h1), which matches the slow reduction in vertical shortening in the mechanical shortening-time curve (Fig. 3.2b,VI). The PIV derived shortening rates range between $\sim$9x10^{-7} to 2x10^{-6} /s during the first load step (Fig. 3.4c1-g1) and are slightly higher than the 2.6-6.1x10x^{-7} /s approximated from the mechanical data (Fig. 3.2b).

Microstructure of sample PS3010-1

Sample PS3010-1 shows lobate grain boundaries and interlocking grain shapes (Fig. 3.4j1). Large grains with length or widths $\geq$ 2000 μm have high shape factors of $\geq$ 2 and are almost exclusively detected in the top half of the map and top two thirds of the ROI (Fig. 3.4k1,3.5c). Conversely, the bottom half of the map and lower third of the ROI ($\sim$the bottom half of the sample) is governed by grains with grain diameters below 1000 μm

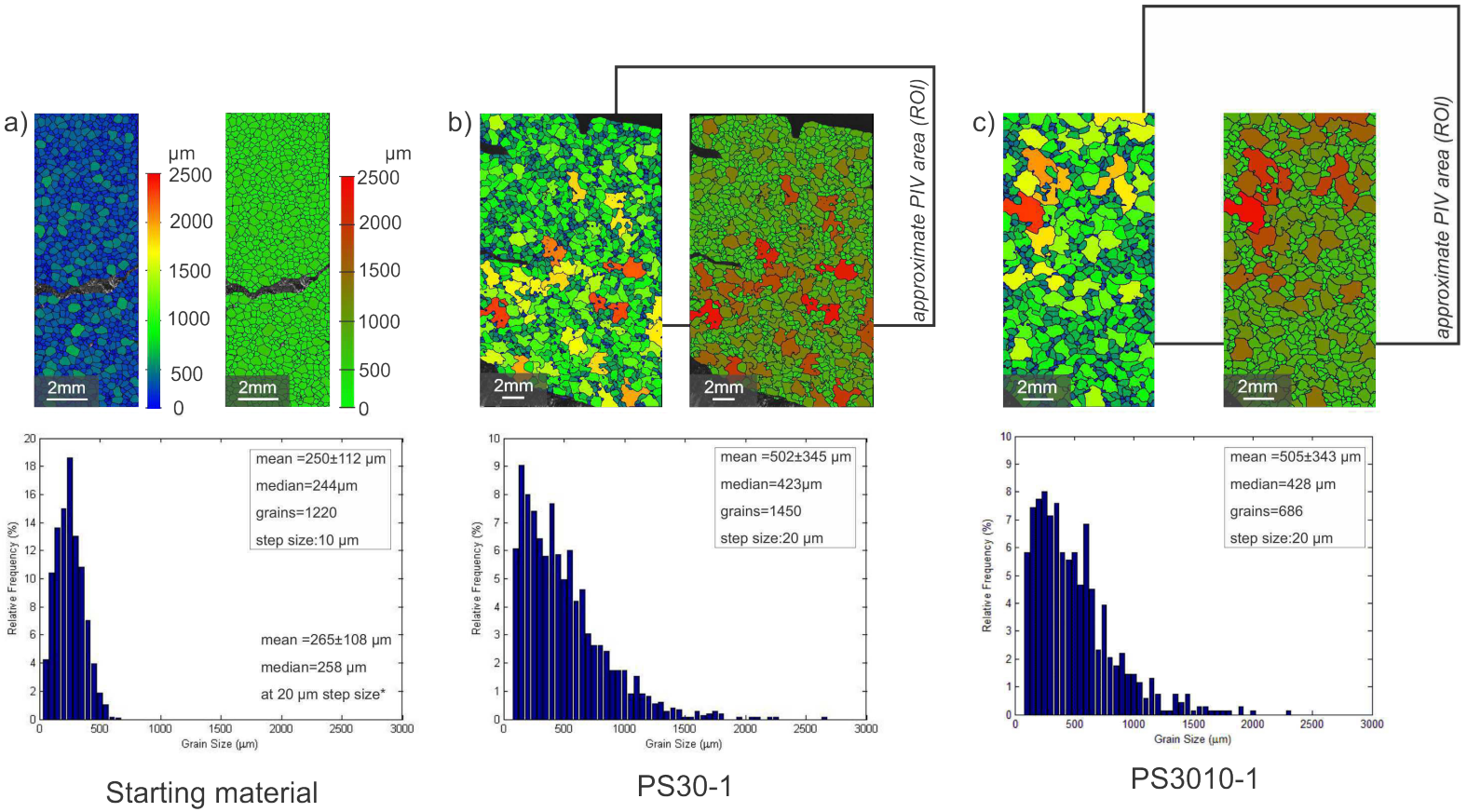

Figure 3.5: EBSD maps coloured according to the circle-equivalent grain diameter (bottom) and grain size histograms (top) of a) Standard Ice, b) PS30-1 and c) PS3010-1. Grain size statistics are given in the top right corners of the histograms: arithmetic mean and standard deviation (top row), median (middle) and the number of grains (bottom).

(Fig. 3.1e,3.5c). The overall grain size distribution is characterized by coarsening and broadening from the starting material (Fig. 3.5a,c). A higher number of very small grains below 200 μm are detected post-deformation.

3.4 Discussion

3.4.1 Spatial heterogeneity in flow, deformation and microstructure

Spatial heterogeneity is manifested in higher flow velocities within the top of the samples, whereas almost no flow occurs in the bottom half of the samples during compression at 0.6 MPa for shortenings over 1 % (Fig. 3.1e,3.3a-g,o-u,3.4a-g,o-u). However, this flow heterogeneity is only reflected in the post- deformation microstructures to a limited extent (Fig. 3.5). The microstructures of both samples are dominated by a coarsening of the grain size from the starting material, sutured grain boundaries and interlocking grain shapes indicative of dynamic recrystallisation by rapid grain boundary migration (Poirier and Nicolas, 1975; White, 1976; Nicolas, 1987; Urai *et al.*, 1986; Hirth and Tullis, 1992). Solely a couple of large grains with highly-sutured grain boundaries are detected in sample PS3010-1, pinpointing at a higher degree of stored strain energy within the top of the sample. In the microstructure of sample PS30-1 a preponderance of small, equant-shaped grains are found within the top half of the sample. The small, equant grains can be regarded as an indicator for a higher degree of new grain nucleation as a part of dynamic recrystallisation within the top of the sample (section 1.3.2). The presence of new grain nucleation during the creep of both samples is also indicated by an increase in number of recrystallised grains below 200 μm from the starting material.

The observation of horizontal high-velocity bands moving towards the centre of the samples in combination with extensive dynamic recrystallisation within the top of the samples comply with the view of Duval *et al.* (1983), that dynamic recrystallisation in ice (like in metals) is a discontinuous wavelike mechanism, which sets in once a critical strain is reached. As the dynamic recrystallisation process is highly strain-dependent, the features of the final microstructure (either large grains with sutured grain boundaries or new grain nucleation) may just be determined by the timing of the end of the experiment.

Strain rate distributions of the samples display a similar heterogeneity between top and bottom. Oblique bands on increased strain rates one order of magnitude above the average of the sample (Fig. 3.3z,a1,3.4v-a1) correlate with areas of elevated velocity magnitude

or gradient and are therefore also mainly found at the tops of the samples. In a previous laboratory study, Wilson and Zhang (1996) have observed increased strain partitioning into areas dominated by extensive dynamic recrystallisation, which may explain the minor difference in the microstructures between top and bottom of the samples.

3.4.2 Temporal heterogeneity in deformation and impact on the microstructure

Temporal heterogeneity is especially visible in the strain rate distributions of the deforming samples. Temporary bands of high strain rates 1 magnitude above the samples averages are usually only visible for a vertical shortening window of 1-1.5 %. The comparatively high magnitude of the transient strain bands is not surprising. Transient strains significantly larger than average geologic strain rates have also been deduced from tectonic geodesy and satellite radar interferometry of natural shear zones (Peltier *et al.*, 2000; Oskin and Iriondo, 2004; Ganev *et al.*, 2012). Moreover, strain localisation bands in columnar ice with strain rates one order of magnitude larger than the bulk sample's have been detected in DIC results of uniaxial compression experiments during transient creep (Grennerat *et al.*, 2012). The reported angle of the localisation bands of 30-60° to bulk shortening in Grennerat *et al.* (2012), however, is different to the 60-80° angle observed in this study. The discrepancy in angle may be an effect of the use of columnar ice samples in Grennerat *et al.* (2012), which is essentially reducing a 3D to a 2D experiment. In this study, no apparent connection between the locations of the transient strains and the specific microstructural features in the final microstructure was detected. This supports the view that transient strains may be a crucial aspect of local deformation but do not influence the final microstructure (i.e. Sibson, 1980).

3.4.3 Extrapolations to large-scale ice masses

Our results indicate, that even within small-scale laboratory studies, the rate and spatial distribution of flow within an ice sample can be heterogeneous. Similar results have been reported for the 'flow field', the large-scale flow of ice masses (Cuffey and Paterson, 1994). High velocities with higher magnitudes of up to 15 x within the top of the samples compared to the bottom in this study indicate, that spatial flow heterogeneity is most likely due to boundary conditions of the experiment. In natural systems, imposed boundaries like vertical constriction have been demonstrated to increase the ice's velocity near the constrictions up to 2-3 times (Raymond, 1971).

Rapid changes in the velocities of ice streams (a few years to few hundred years, as stresses and strain rates are significantly lower) are also very common in nature (Bindschadler, 1998; Rignot and Thomas, 2002; Joughin *et al.*, 2004; Rignot and Kanagaratnam, 2006). Not all of these accelerations and decelerations can be attributed to fluctuations in the environmental conditions but have been suspected to origin from internal ice stream processes (Tulaczyk, 2006). Our results confirm that sudden velocity changes (within ∼1% strain) are not necessarily due to changes in stress, temperature or chemical composition but may rather be a consequence of ice's inherent deformation heterogeneity. Results from high-pressure creep experiments presented in Chapter 4 support this view. In this chapter, changes in the mechanical behaviour (accelerations and decelerations in the strain rates) of the initially homogeneous ice samples without impurities can be solely explained with the development of localised zones with a reduced grain size during deformation.

One important limitation regarding the extrapolation of our results to natural conditions is, however, that deformation in this study was terminated during secondary creep, whereas deformation in glaciers and ice sheets is assumed to occur by tertiary creep. Further PIV-ice deformation experiments at large strains >10 % are required to confirm that the same micro-physical deformation heterogeneity and inconsistencies in the velocity distributions occur during tertiary creep. To our knowledge, a switch in deformation mechanism (i.e. from grain boundary migration to subgrain rotation recrystallisation) between secondary and tertiary creep has not yet been reported. It may, therefore, be likely that discontinuous wavelike recrystallisation mechanisms causing velocity and strain rate heterogeneities during secondary creep continue to produce the same features during tertiary creep, as long as the experimental boundary conditions remain constant.

3.4.4 Evaluation of the PIV approach and potential future improvements

The PIV analysis conducted in this contribution can only be validated by comparison with the mechanical data (Fig. 3.2), as microstructural information is only available after the termination of an experiment. Generally the PIV analysis provided flow directions from top to bottom, as expected from a pure shear experiment with a moving top plate. Flow velocities were generally higher in the top than in the bottom (Fig. 3.3g,u,3.4g,u), presumably as a result of the higher stress at the top, close to the moving plate. The observed bulging of the top of samples (Fig. 3.1d) is also visible in the velocity arrows

in the PIV analysis (Fig. 3.3b-e,3.4b-e). Additionally, a change in flow direction was observed during the time of the stress reduction in experiment PS3010-1 (Fig. 3.4f), corresponding to a relaxation of elastic strain of about 0.2 % in the mechanical data (Fig. 3.2b). This matches the experimental observations of Duval *et al.* (1983), which suggest that reverse strains are possible after unloading of an ice sample.

There is a discrepancy of one order of magnitude between octahedral strain rates determined for both experiments (10-7 /s) and the 2D strain rates averages calculated in the PIV analysis (10-6 /s). Vertical shortening rates derived from PIV v-velocities were subsequently calculated to better compare shortening rates from the shortening-time curves to the PIV results (Fig. 3.3c1-i1,3.4c1-i1). The 1D vertical shortening rates derived from the PIV analysis successfully trace the overall mechanical evolution of the samples, including changes in shortening rates from primary to progressive secondary creep and responses to load changes. The over- or underestimation of PIV derived vertical shortening rates by a factor of 2-3 (Fig. 3.2,3.3c1-i1,3.4c1-i1) may be related to the fact that the calibration of the ROI during the PIV analyses was relatively crude. An average of 22 mm was employed for the sample width, although the actual sample widths were either 21 or 23 mm. Another possible cause of the underestimation of PIV derived shortening rates (sample PS30-1) is that deformation in the lower third of the samples is non-visible to the camera and that potential strain rate contributions from this part were not incorporated into the PIV shortening rates.

For future experiments, modifications in the experimental setup and experimental procedure could improve the coherence between mechancal data and PIV results. The most important improvement would be to minimise the lower sample area hidden from the camera by fabricating a new sample tray. Potential inconsistencies in sample width with length prior to deformation should be more carefully documented to allow for a better calibration of the PIV analysis. Using a reference distance marker next to the deforming samples or a horizontal displacment transducer monitoring sample bulging might be another approach to improve the calibration. Sample tops and bottoms could be milled to ensure a planar surface and avoid the initial sample alignment issues reflected in the overall positive (PS30-1) or negative (PS3010-1) u-velocities throughout the sample during the first $\sim$2% strain (Fig. 3.3a,b,3.4a). Moreover, a better correlation of microstructural and PIV data could be obtained by imaging of the same surface. Graphite particles could be removed with a razor blade prior to EBSD imaging. An additional camera could provide 3D flow data to provide more information on flow patterns and flow heterogeneity. The use of pre-processing software or tools in PIVlab can potentially allow for the use of

cheaper camera equipment, as for instance 2 megapixel cameras were used to track soil deformation in geotechnical models in White *et al.* (2003). Overall, the processing of flow data in the free software PIVlab is well-documented (see Thielicke and Stamhuis, 2014) and time-effective (3-8 minutes calculation time for the examples presented in this study).

3.5 Conclusions

PIV is a time- and cost-effective method that can complement microstructural investigations in polycrystalline ice by providing additional information about flow and deformation heterogeneity in the deforming sample and by helping understand the link between velocity fields and strain rate distributions.

Preliminary results of PIV on deforming polycrystalline ice samples indicate that

- long-term (several % shortening) spatial discrepancies in velocity field and strain rate distribution may cause a spatial variation in the degree of dynamic recrystallisation in the post-deformation microstructures. This could explain why small, equant-shaped recrystallised grains are detected in the top of sample PS30-1 and large grains with sutured grain boundaries in the top of sample PS3010-1. More experiments are needed to understand this link.

- transient strains occur in bands oblique to shortening with strain rates one order of magnitude larger than the average for the sample but do not induce permanent microstructural changes.

- changing velocities with time and strain are a part of the deformation heterogeneity of the samples and are not necessarily related to changes in overall stress, boundary conditions or ice composition.

Acknowledgements

This work was funded by Marsden Fund grand UO1116 and a University of Otago Doctoral scholarship. Jim Woods, Leo Van Rens, Peter Fleury and Brent Pooley are thanked for technical support. Imogen Browne, Myrna Blessenohl and Jan Leunissen assisted with ice growing and deformation experiments.

3.6 Graphical summary

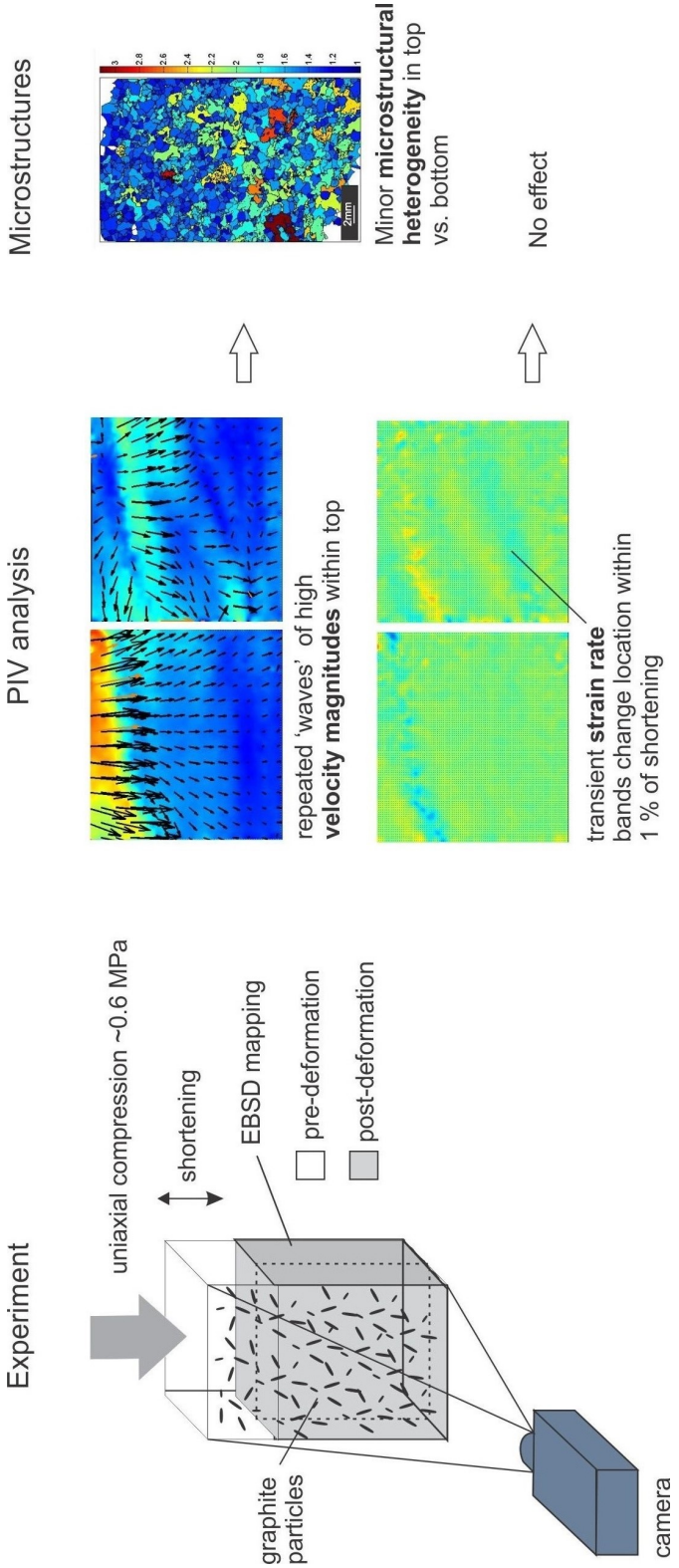

3.7 Supplementary material

3.7.1 Mathematical background

The one-dimensional shortening for uniaxial compression experiments was derived from the length of the sample l at the time t and the inital length of the sample l_0 prior to deformation:

$$\epsilon[-] = \frac{l - l_0}{l_0} \tag{3.3}$$

Dividing by the total time increment $(t - t_0)$ yields a one-dimensional shortening rate:

$$\dot{\epsilon}[/s] = \frac{\epsilon}{(t - t_0)} \tag{3.4}$$

To compare the results of the PIVlab analysis to our experiments, we need an octahedral strain rate $\dot{\epsilon_{oct}}$, which also incorporates the angular component of uniaxial compression expriments γ. The angular strain and strain rate $\dot{\gamma}$ were calculated using the initial sample width w_0 and sample width w at time t (Jun *et al.*, 1996). W was approximated with a constant volume assumption $V = V_0 = const. \rightarrow w = V/l$:

$$\gamma[-] = \frac{1}{2}\frac{(w - w_0)}{l_0} \tag{3.5}$$

$$\dot{\gamma}[/s] = \frac{\gamma}{(t - t_0)} \tag{3.6}$$

Octahedral stresses τ_{oct} and strain rates or uniaxial compression experiments are given by the following equations (Jun *et al.*, 1996):

$$\tau_{oct}[MPa] = \frac{\sqrt{2}}{3}\sigma \tag{3.7}$$

$$\dot{\epsilon_{oct}}[/s] = \sqrt{\frac{2}{3}}\sqrt{\frac{3}{4}\dot{\epsilon}^2 + \dot{\gamma}^2} \tag{3.8}$$

with σ denoting the stress on the top surface.

3.7.2 Region of interest (ROI)

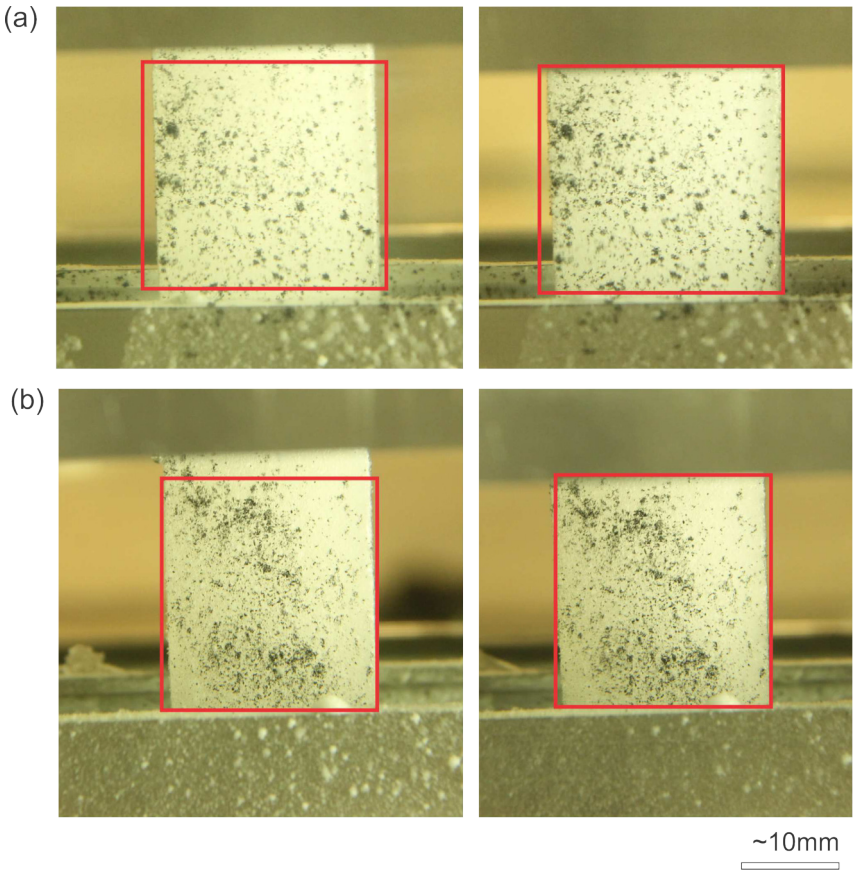

Figure 3.6: Definitions of the region of interest (ROI) for the PIV analyses of samples PS30-1 (a) and PS3010-1(b). The first (left) and last frames (right) of the analysed sequences are shown.

Chapter 4

Localisation in polycrystalline ice under high confining pressure: the link between strain distribution, microstructural heterogeneity and rheological properties

Meike Seidemann[1], Narayana Golding[2], William B. Durham[2], Susan Ellis[3], Kat Lilly[1], Matthew J. Vaughan[1], David J. Prior[1]

[1]Department of Geology, University of Otago, Dunedin, New Zealand
[2]Department of Earth, Atmospheric and Planetary Sciences, Massachusetts Institute of Technology, MA, USA
[3]GNS Science, Lower Hutt, New Zealand

Abstract

Localisation of deformation in rocks is common but not well-understood. The link between strain localisation, microstructure and rheology can be studied with conventional rock deformation experiments but this is often complicated by small sample sizes and engineering difficulties. In this contribution, comparatively large-scale localisation behaviour is studied by deforming three 25.4 mm diameter cylinders of polycrystalline ice in a triaxial apparatus, at 50 MPa confining pressure, a temperature of 240 K and constant axial loads equivalent to 3, 8, and 13 MPa. After an initial phase of strain hardening, rapid strain weakening was observed between strains of 2-7 %, leading to steady state strain rates up to a magnitude higher than during strain weakening. Strain localisa-

tions, as evidenced by several grain-diameter scale bumps and sample-scale bulging (>10 % strain), on the jackets surfaces, were detected post-deformation. Sample-scale EBSD maps reveal a bimodal grain size distribution: during secondary creep (5 % strain, sample 785) a matrix of remnant grains is intersected by groups of recystallised grains (∼70 μm). Samples 769 and 774 (>10 % strain) show remnant grains within a matrix of recrystallised grains in areas of macroscopic bulging. The rheological evolution of the samples can best be explained with a two phase model, assuming that recrystallised grains undergo grain size sensitive creep and act as a 'weak' secondary phase. The onset of strain weakening commences with new grain nucleation yielding a load-bearing framework with few highly-viscous recrystallised grains in a matrix of remnant grains. The transition to steady state strain rates occurs as the weaker recrystallised grains interconnect, signifying an interconnected weak phase model. Numerical simulations suggest that strain localisation initially occurs because the boundary conditions of the experimental setup promote higher strain rates in certain areas.

4.1 Introduction

Localisation of deformation is a common phenomenon in many rocks, including polycrystalline ice, across a wide range of deformation conditions and scales. However, our understanding of how localisation evolves and relates to the overall stress conditions, microstructural properties, rheology and deformation history is still limited (i.e. Bésuelle and Rudnicki, 2003). Conventional rock mechanics studies are fairly restricted to small sample sizes to achieve the high-stresses required for the creep of rocks. Polycrystalline ice is per definition a rock and a popular analogue for the deformation of quartz (i.e. Wilson *et al.*, 2014), the most abundant mineral in the Earth's crust. But in contrast to other rocks, polycrystalline ice deforms at comparatively low stresses and allows for the experimental investigation of localisation on larger samples.

Previous research has targeted localisation 1) on a grain-scale due to a hard inclusion larger than the grains (Mansuy *et al.*, 2000, 2002), 2) in initially anisotropic ice (Wilson and Sim, 2002), 3) in ice mixtures (Cyprych *et al.*, 2016) and 4) under fast strain rate conditions (10^{-5}-10^{-1} /s) leading to failure at low strains of ∼2 % by nucleation of a single plastic fault (Golding *et al.*, 2010, 2012).

Experimental studies originally designed to constrain the rheology of polycrystalline ice under low temperatures and high confining pressure, have also provided some evidence of localisation. For instance, macroscopic strain localisation is manifested in a local widening

of the sample diameters for strain above 10 % (Durham *et al.*, 1983, 2001), sometimes in combination with heterogeneous grain sizes and rheological weakening (Durham *et al.*, 2001).

Evidence for recrystallisation and grain size reduction are present in several studies (Durham *et al.*, 1983, 1997; Stern *et al.*, 1997; Durham *et al.*, 2001) but microstructural information is scarce and more work is needed to better constrain the link between localisation and the microstructural evolution. One of the key questions is whether recrystallisation occurs dynamically during loading and may aid the development of localisation behaviour (i.e. Xu *et al.*, 2001, 2008). In ice, evidence from high-strain rate experiments indicates that recrystallisation occurs during loading but is not spatially linked to the later development of a plastic fault (Golding *et al.*, 2012).

In rocks, localisation in space is generally associated with rheological weakening (Poirier, 1980). However, the connection between localisation and rheological weakening has not been demonstrated for polycrystalline ice. Rheological weakening processes in rocks generally include weakening by dynamic recrystallisation (i.e. White *et al.*, 1980), geometrical weakening due to the formation and intensification of a crystallographic preferred orientation (CPO) (i.e. Poirier, 1980; De Raadt *et al.*, 2014), weakening by transition to grain size sensitive (GSS) creep (de Bresser *et al.*, 1998; De Bresser *et al.*, 2001), thermal weakening by frictional heating (i.e. Brun and Cobbold, 1980; Kelemen and Hirth, 2007) and weakening due to the interconnection of a weak phase in polyphases (i.e. Holyoke and Tullis, 2006; Gerbi *et al.*, 2016). Some of these weakening processes have been extrapolated to polycrystalline ice.

Rheological weakening in polycrystalline ice has been primarily attributed to a combination of weakening by dynamic recrystallisation and development of a CPO (i.e. Kamb, 1973; Burg *et al.*, 1986; Wilson *et al.*, 1986; Budd and Jacka, 1989; Wilson and Peternell, 2012). Evidence for grain size sensitive creep or more specifically grain boundary sliding in ice has accumulated in experimental studies (Stern *et al.*, 1997; Goldsby and Kohlstedt, 1997, 2001; Durham *et al.*, 2001; Goldsby, 2006), providing another possible cause for rheological weakening. For fast strain rates and semi-brittle deformation, thermal softening has been inferred from thermal spikes in strain localised regions during plastic faulting (Golding *et al.*, 2010). Rheological weakening as a consequence of interconnection of a previously separated weak phase (Holyoke and Tullis, 2006; Gerbi *et al.*, 2016) could also become applicable to a monophase like ice, if aggregates of smaller grains deformed by grain size sensitive creep and acted as a 'weak' second phase

In this study, localisation behaviour in polycrystalline ice under high confining pres-

sure is investigated. I focus on the interplay between stress state, strain localisation, microstructure and rheology and their impact on the initiation and evolution of localisation by analysing three ∼25.4 mm x 50.0 mm deformed ice cylinders deformed under differing axial stresses. Cryogenic electron backscatter diffraction was employed to obtain both sample-scale and detailed microstructural maps. Numerical modelling with finite-element code SULEC was used to validate some of the interpretations.

4.2 Methods

4.2.1 Sample fabrication

Polycrystalline 'Standard ice' was fabricated by placing 180-250 μm sieved ice particles (made from deionized water) into 2.54 cm (1-inch) diameter moulds, packing to 40 % porosity, flooding with degassed, deionized water and freezing the mixtures uniaxially from the bottom (Stern *et al.*, 1997). Samples are transparent with no porosity, once a small bubbly section at the top is removed. The texture is homogeneous, with polygonal grains with a grain size of $\sim 250\pm100$ μm (at a step size of 20 μm) and a random CPO (Fig. 4.9). The samples' lengths were measured with a pre-chilled Vernier calliper with an accuracy of ±0.02 mm in a ∼243 K environment (Table 4.1). The samples were sealed into thin-walled indium jackets, flanked by a steel end cap at the bottom and a ZrO_2 spacer and force gauge (here referred to as internal force gauge) on top of the sample (Durham *et al.*, 1983; Stern *et al.*, 1997). Special care was taken to avoid abrupt temperature differences during the measurements and welding of the indium jackets to avoid fracturing due to thermal shock.

Table 4.1: Initial (pre-deformation) lenghts of the ice samples.

Sample	initial length [m]
ice 769	$57.912\text{x}10^{-3}$
ice 785	$59.436\text{x}10^{-3}$
ice 774	$48.895\text{x}10^{-3}$

4.2.2 Experimental procedure and EBSD mapping

Constant load creep experiments were performed in a triaxial apparatus equipped with a cooling alcohol bath (Durham *et al.*, 1983; Heard *et al.*, 1990). Nitrogen gas was

employed as the confining medium, while a screw-loading mechanism applied uniaxial compression from the bottom. The experimental procedure and uncertainties related to piston alignment and force gauge readings are given in Durham *et al.* (1983). Tests were run at a constant temperature of 240 K and 50 MPa confining pressure. The sample assembly was introduced into the pre-chilled pressure cell and left to equilibrate for 15-45 minutes before the confining pressure was slowly built-up. Once the internal force gauge had stabilised (45-90 minutes), the samples were loaded with uniaxial forces equivalent to ∼13 MPa (ice 769), 8 MPa (ice 785) and 3 MPa (ice 774), respectively. We attempted to maintain a constant stress during the experiments by dynamically adjusting the axial load to the changes in sample length and cross-sectional area (Stern *et al.*, 1997; Durham *et al.*, 2001). Because the internal force gauge is susceptible to changes in temperature and pressure (i.e. diurnal rhythm), zero force gauge readings were taken at the beginning and end of each experiment (Durham *et al.*, 1983). During the 3.5 day run 774, zero forge gauge readings were additionally taken during the experiment by temporarily removing the uniaxial compression (Fig. 4.1a). Experiments were terminated once the target strain value was reached by subsequently retracting the piston and removing the confining pressure. The sample assemblies remained in the rig for 45 minutes before they were extracted from the pressure cell and slowly immersed into nitrogen mist above liquid nitrogen. After a minimum cooling time of 10 minutes, the sample assemblies were imaged from several angles with a digital SLR camera. The samples were subsequently removed from the indium jackets with a razor blade and wrapped in pre-chilled aluminium foil for long-term storage in a liquid nitrogen dewar.

Post-deformation, samples were photographed, cut along their long axis and imaged using an approach for cryogenic electron backscatter diffraction (cryo-EBSD) for fine-grained ice (Prior *et al.*, 2015). Samples were cut along their long axis, parallel to the shortening direction using a scroll saw. Sample 769 was prone to breaking at the top and was hence cut by hand with a scroll saw blade at a slower rate. Mounting on 30 mm by 40 mm SEM ingots (Prior *et al.*, 2015) was performed with a piece of wet tissue (water temperature of 0°C). Ingot and sample temperatures before mounting were at approximately +2 and <-130°C, respectively. Grinding plates, pre-chilled to a temperature of -40 to -70°C were employed to obtain a flat surface.

EBSD data were gathered on a Zeiss FEG-SEM using 6-8 Pa of nitrogen pressure to avoid charging. EBSD patterns were collected with a Nordlys camera and Oxford Instruments AZTEC software with an acceleration voltage of 30 kV and a beam current of 50 to 90 nA. Due to the large, 30 mm by 34 mm sample size, a long working distance

between 28 and 31 mm was chosen. An Emitech K1250 cryo-stage kept the samples at a constant stage temperature of -95 to -100°C during imaging. A single sublimation by pressure cycle (Prior *et al.*, 2015) with a minimum stage temperature of -75°C was employed to remove surface frost prior to imaging.

4.2.3 Data reduction

Mechanical data

Stress was calculated during the experiments from recorded load data and the current sample area A. The change in area was approximated by assuming a constant volume, regardless of strain, and employing current displacement u, initial sample length l_0 and the initial sample area A_0 (Stern *et al.*, 1997, Formula 4.1). Post-deformation, the stress values were additionally corrected for potential errors caused by a drift of the force gauge Δf (Durham *et al.*, 1983, Formula 4.2).

Incremental strain rates (comparing the current strain to the previous strain value within a given time increment delta t) were chosen. A time increment of 32 seconds (the minimum sampling rate of experiment 769) proved appropriate for the 1.5 hour long experiment 769 but produced high noise-data ratios for the slower experiments 785 and 774 (Fig. 4.10d). To correct for the higher resolution due to higher sampling rates per strain increments during the slower experiments, the strain rates of the latter were smoothed with a moving average filter in Matlab 2013a (`https://au.mathworks.com/help/curvefit/smooth.html`). The filter compared the current value over a span of 5 values (experiment 785) and 118 (experiment 774) values, respectively (Fig. 4.1b, 4.10e). This averaging procedure mimicked the sampling rate of approximately 40 samples per unit of strain in experiment 769 and produced a sufficient decrease in noise. An example for calculating a moving average of a strain rate over a span of 5 values is given in the supplementary material (Formula 4.5).

EBSD data

A combination of Oxford Instruments Channel 5 software and the open-source MTEX toolbox for Matlab (Bachmann *et al.*, 2010) was employed to process EBSD data. Orientation maps were generated with Oxford Instruments' Channel 5 software module Tango, as they generally provided better visibility of details like grain boundary curvature. MTEX was preferred regarding the computation of grain size histograms, statistics, and pole figures. In both cases, a misorientation value of 10° was chosen to demarcate high angle

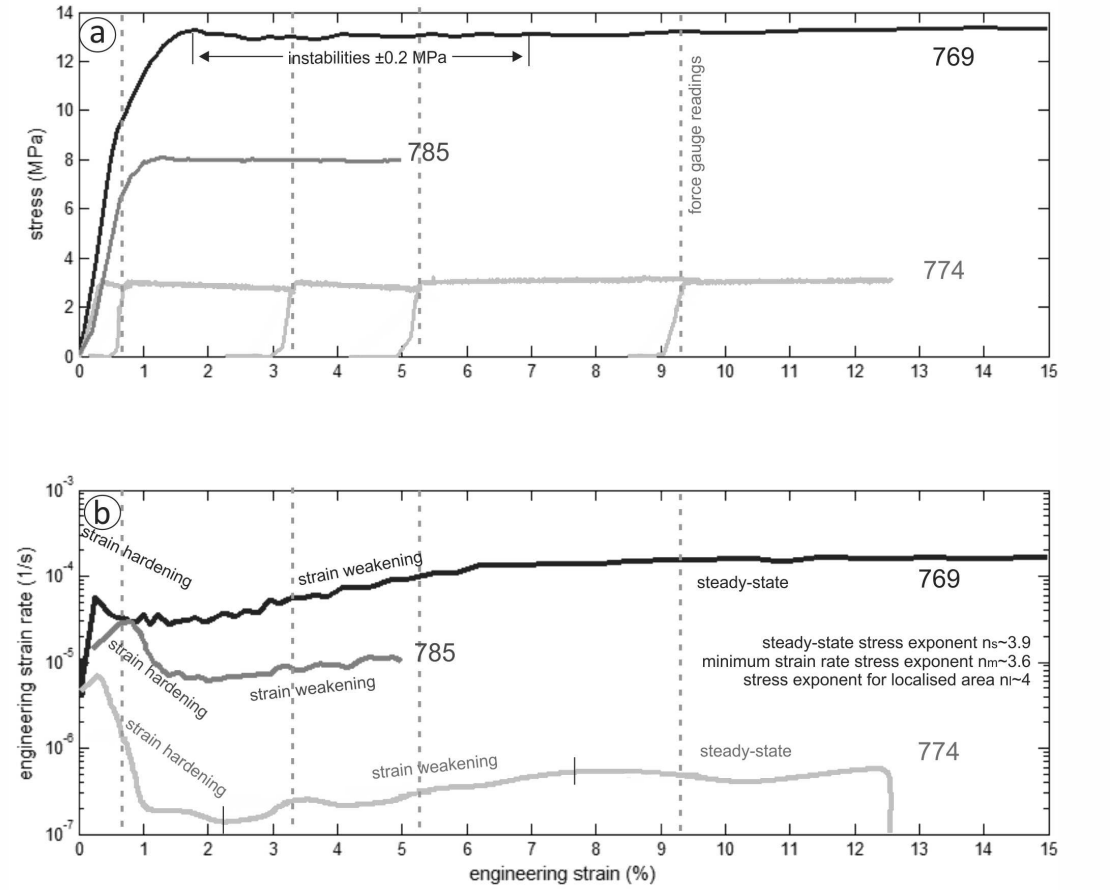

Figure 4.1: Mechanical data in stress vs. engineering strain (a) and strain vs. strain rate plots (b). Dotted light grey lines indicate force gauge readings in sample 774, which incorporated temporarily removing axial load. Stress exponents in (b) were determined from steady state strain rates (n_s), minimum strain rates (n_m) and accounting for localisation (n_l) as given in Fig. 4.11.

grain boundaries from subgrains. An area-equivalent grain diameter of 200 μm (below the median and average grain size of the starting material) was selected as a threshold value to distinguish between large remnant and small recrystallised grains (Fig. 4.3,4.5,4.12). This duplex way of processing was verified by comparing the MTEX-generated maps used to compute CPO (per pixel) and grain size histograms to the corresponding output map from Channel 5. Minor deviations in area-equivalent grain diameter were only detected on a single-grain basis within sample-scale maps (Fig. 4.3a,4.5a).

4.2.4 Numerical modelling

Numerical modelling was performed within the framework of the finite-element code SULEC (Ellis *et al.*, 2011; Buiter and Ellis, 2012; Ellis *et al.*, 2015). A general framework for a triaxial deformation apparatus was employed and supplemented with a rate-equation and values for power-law creep below 265.15 K (Frost and Ashby, 1982). The experimental parameters of ice 769 (Table 4.2) were utilised for the 2D model, which calculates displacement in compression direction, velocity and the strain rate invariant for each time step of 0.1 s. The model includes the parts of the sample assembly which share an interface with the ice: a zirconia spacer at the top and stainless steel end plug at the bottom of the sample. Because a pre-existing framework for a triaxial apparatus with axial load from the top was used, the model was rotated to match the experimental setup with a loading direction from the bottom (Fig. 4.6a). Modelling results are not affected by the rotation, as gravitational forces are disregarded. Finite thicknesses were assumed for the ice-zirconia and ice-steel interfaces. The infinitesimally thin ice-steel interface (top in the rotated model, Fig. 4.6a) generates a modelling artefact as seen in the partial wrapping of the ice around the stainless steel end plug. Boundary displacement conditions for the interfaces were derived from the friction coefficients between the two materials, respectively (Table 4.2).

4.3 Results

4.3.1 Ice 769

Mechanical response

Creep curves for the constant stress experiments are given in Fig. 4.1. The stress-strain curves shows that the target stress of ∼13 MPa was met at 1.8 % strain (Fig. 4.1a). Fluctuations in stress of about ±0.2 MPa were recorded between 1.8-7 % strain (instability phase). After 7 % strain, the target stress was maintained within the uncertainty of the internal force (∼ ±0.01, Durham *et al.*, 1983).

Ice 769 initially exhibited exponential stain hardening from 0.5 % until 1.8 % strain and a minimum strain rate of $2\text{x}10^{-5}$ /s (Fig. 4.1b). An initial peak in the strain curve correlates with a change in gears (change in slope in Fig. 4.1a) and is regarded as a stress ramping artefact present in all experiments. The instability phase in the stress-strain

Table 4.2: Modelling parameters.

static friction coefficient ice-stainless steel	0.03-0.04 [a]
static friction coefficient ice-zirconia	0.3-0.6 [a]
absolute viscosity of indium (340K)	2.156x10^{-3} Pa*s [b]
strain ϵ (769)	15.4 %
stress σ (769)	13.2 MPa
confining pressure P	50 MPa
initial length prior to deformation l_0	0.0579 m
Power-law creep equation	$\dot{\epsilon} = A * (\frac{\sigma}{\upsilon})^n * exp(-\frac{Q}{RT})$ [c]
constant A	4.32x10^{-9} s^{-1}
activation energy Q	80 kJ/mol
shear modulus υ (340K)	2660.175 MN/m^2
gas constant R	8.314458 Jmol^{-1}K^{-1}
stress exponent n	3

[a] Arithmetic mean was employed for modelling.

[b] Estimate from liquid viscosity data from Assael *et al.* (2012).

[c] Equation and constants below are given in Frost and Ashby (1982).

curve (Fig. 4.1a) corresponded to rapid strain weakening from 1.8-7 % strain (Fig 4.1b). The stress-strain rate curve stabilised once mechanical steady state was reached beyond ∼7 % strain at a strain rate of 1.6x10^{-4} /s (Fig. 4.1b).

Macroscopic strain distribution

The bulk strain distribution of sample 769 differs vastly from samples 785 and 774, due to the fact that deformation is concentrated at the top of the sample (Fig. 4.2a-c). A buckle at an inclination of ∼70° to bulk shortening (25 mm on the right to 20 mm on the left from the bottom of the sample) is visible. Above the buckle, the cylinder axis of the sample is slightly oblique to bulk shortening and presumably lead to piston misalignment during deformation. Uniform and mostly symmetric thickening to a diameter of 26 mm is observed below the buckle (Fig. 4.2c).

The substructure of the indium jacket also displays marked differences between the top and bottom of the sample (Fig. 4.2a-c). In the top part >18 mm from the bottom (Fig. 4.2b), lens- or s-shaped pronounced bumps are visible on the jacket's surface. More of these bumps with higher protrusions are generally observed within the bulge in areas of high macroscopic strain about 22-43 mm from the bottom. The bumps are between 2.5-12 mm long, approximately 1-3 mm wide and their long axes tend to be inclined 60-90° to the bulk shortening direction. Longer (>3 mm length), especially protruding bumps often change their orientation to bulk shortening, leading to snake-shapes with long axes oriented perpendicular or semi-perpendicular to bulk shortening. In contrast to that, the jackets' surface is mostly smooth below the buckle.

Deformation microstructure and correspondence to macroscopic strain distribution

Microstructural heterogeneity in ice 769 correlates with the macroscopic strain distribution (Fig. 4.3a). Where macroscopic bulging of the jacket is observed (22-43 mm from the bottom), there are more grain boundaries and small grains (<200 μm). Grains below the buckle appear more polygonal and more similar in grain size (∼300 μm) to the starting material.

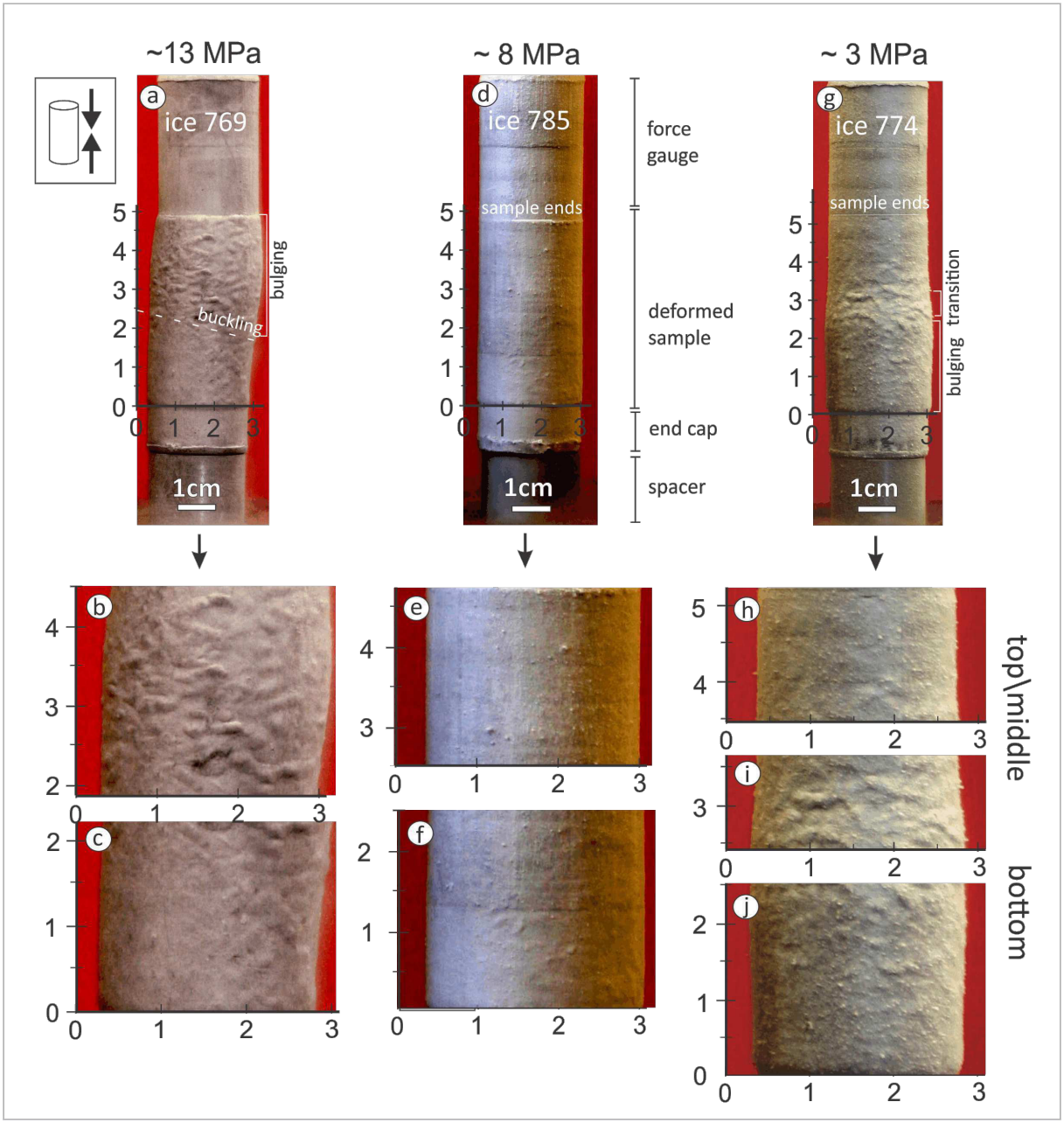

Figure 4.2: Deformed ice samples in the original sample assembly with spacer and metal end cap at the bottom and the lower part of the force gauge on top. Units are given in x10 mm. The surface structure of the indium jackets is partly characterized with horizontally or sub-horizontally elongated bumps. Images were overexposed and contrast-enhanced for better visualisation of the jackets' substructures.

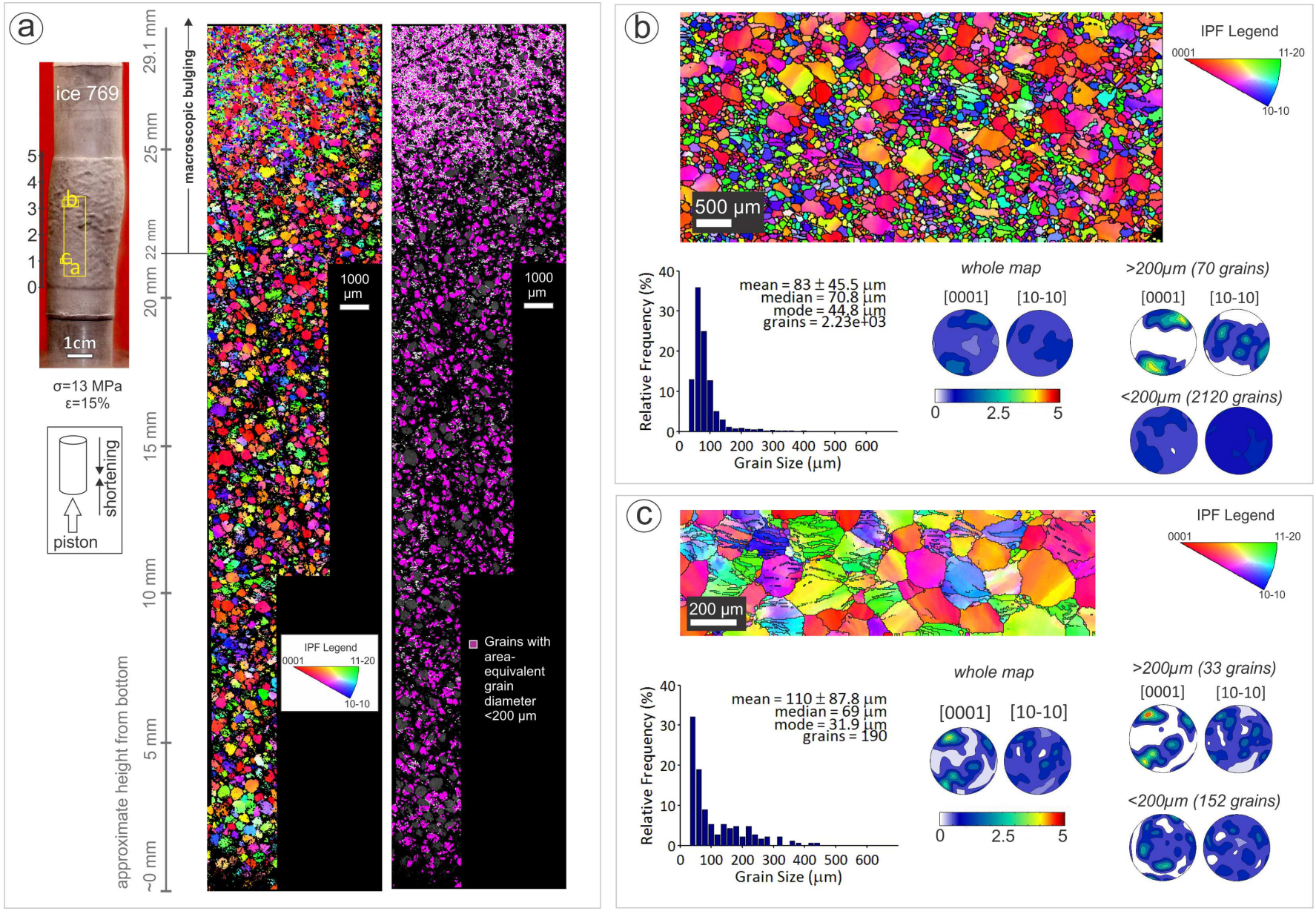
a
ice 769
1cm
σ=13 MPa
ε=15%
piston
shortening
macroscopic bulging
approximate height from bottom
29.1 mm
25 mm
22 mm
20 mm
15 mm
10 mm
5 mm
~0 mm
1000 µm
1000 µm
IPF Legend
0001
11-20
10-10
Grains with area-equivalent grain diameter <200 µm
b
500 µm
IPF Legend
0001
11-20
10-10
Relative Frequency (%)
mean = 83 ± 45.5 µm
median = 70.8 µm
mode = 44.8 µm
grains = 2.23e+03
Grain Size (µm)
whole map
[0001]
[10-10]
0
2.5
5
>200µm (70 grains)
[0001]
[10-10]
<200µm (2120 grains)
c
200 µm
IPF Legend
0001
11-20
10-10
Relative Frequency (%)
mean = 110 ± 87.8 µm
median = 69 µm
mode = 31.9 µm
grains = 190
Grain Size (µm)
whole map
[0001]
[10-10]
0
2.5
5
>200µm (33 grains)
[0001]
[10-10]
<200µm (152 grains)

Figure 4.3: Microstructural heterogeneity in sample 769: a) an EBSD orientation map shows a vertical cross-section from the middle of the sample to the bottom. On the right, area-equivalent diameters <200 μm are highlighted (violet) on a pattern quality map. White lines denote grain boundaries with misorientations >10°. More detailed IPF orientation maps (10 μm step size), grain size statistics and CPOs characterising the microstructure at top (b) and bottom (c) of the sample, respectively. CPOs are equal-area, upper hemisphere projections. Contouring was performed with a 10° halfwidth and CPO strength is plotted on a scale from 0 to 5. Note that each kink fragment in (c) is counted as separate grain as long as it is surrounded by grain boundaries >10°. Grain size histograms have bin widths of 20 μm.

The microstructure at the top of the sample (Fig. 4.3a), consists of matrix of small (<200 μm), equant-shaped grains with a median grain diameter of ∼70 μm (Fig. 4.3b). These grains are far below the minimum grain size of the starting material and are reasonably interpreted as recrystallised grains. Within the matrix of recrystallised grains, few large equant-shaped grains with area-equivalent grain diameters from 200-400 μm are found. These larger grains have mostly straight grain boundaries and are due to their similarity in size and shape, interpreted as remnant grains. Remnant grains display no signs of internal distortion, except from occasional subgrain boundaries.

The overall CPO is a weak two cone CPO with a maximum (strength of ∼2) about 20-30° to bulk shortening (Fig. 4.3b). A similar CPO with a higher CPO strength of 4 is detected for remnant grains (>200 μm). Contrastingly, small recrystallised grains (<200 μm) show a random CPO.

The microstructure up to 12 mm from the bottom is characterised by randomly-oriented polygonal remnant grains with grain diameters of 200-400 μm (Fig. 4.3a,c). A more detailed map of the microstructure about 10 mm from the bottom reveals pockets of equant shaped recrystallised grains (< 50 μm) at triple or quadrupole junctions of remnant grains (Fig. 4.3c). Kinking, as indicated by sharp grain boundaries semi-perpendicular to shortening, is present in several grains. The overall grain size distribution is skewed with a median grain diameter of 70 μm.

The CPO of the bottom map and the CPO of the large grains is random with minor clustering of the c-axes (Fig. 4.3c). The CPO of the small grains (including grains fragmented by kinking and newly nucleated grains in grain junctions, Fig. 4.12b) is random. Non-kinked remnant grains with grain diameters above 200 μm show a cluster of c-axis orientations about 30-40° to bulk shortening.

4.3.2 Ice 785

Mechanical response

Sample 785 was deformed at an axial stress of 8±0.1 MPa to a maximum engineering strain of 5 % to obtain information on the microstructure during strain weakening (Fig. 4.1a). The target stress was achieved at about 1 % strain. After 1 % strain, the strain rate vs. strain curve exhibits exponential strain hardening (Fig. 4.1b). Strain hardening continued to be observed until the minimum strain rate of ∼6x10^{-6} /s was reached at 2 % strain. Subsequently, strain weakening was recorded until the experiment was terminated at a final strain rate of ∼1.2x10^{-5} /s.

Macroscopic strain distribution

Sample 785 appears similar to undeformed samples with straight sample shapes and a smooth jacket surface (Fig. 4.2d). Close-ups of the respective top and bottom of the sample, however, show minimal homogenous thickening (+0.1 mm) through the bottom of the sample (Fig. 4.2f). Up to 15 mm from the bottom spacer, several faint elongated s-shaped bumps with lengths below 3 mm, widths below 1 mm and an overall inclination of about 60° to bulk shortening are visible. In contrast to that, the top displays a slightly lesser degree of thickening and an absence of bumps on the jackets surface (other than round frost pieces).

Deformation microstructure and correspondence to macroscopic strain distribution

Detailed microstructural maps from the top, middle and bottom of the sample show a homogeneous microstructure with only little spatial variation (Fig. 4.4a-d). The majority of the microstructure consists of polygonal, randomly-oriented grains with little internal distortion and straight or slightly curved grain boundaries. The grain shape and grain diameters of around 200-400 μm are consistent with the microstructural properties of the starting material and are reasonably interpreted as remnant grains. Equant-shaped recrystallised grains with grain diameters between few microns up to 50 μm are often accompanied by similar-sized neighbours and nucleate mostly in triple junctions of remnant grains (white circles, Fig. 4.4a-d). A local microstructural exception is found in the map in Fig. 4.4b from the middle rim of the sample: kinking, as identified by sharp, straight low angle and high angle grain boundaries and kink bands with alternating orientations

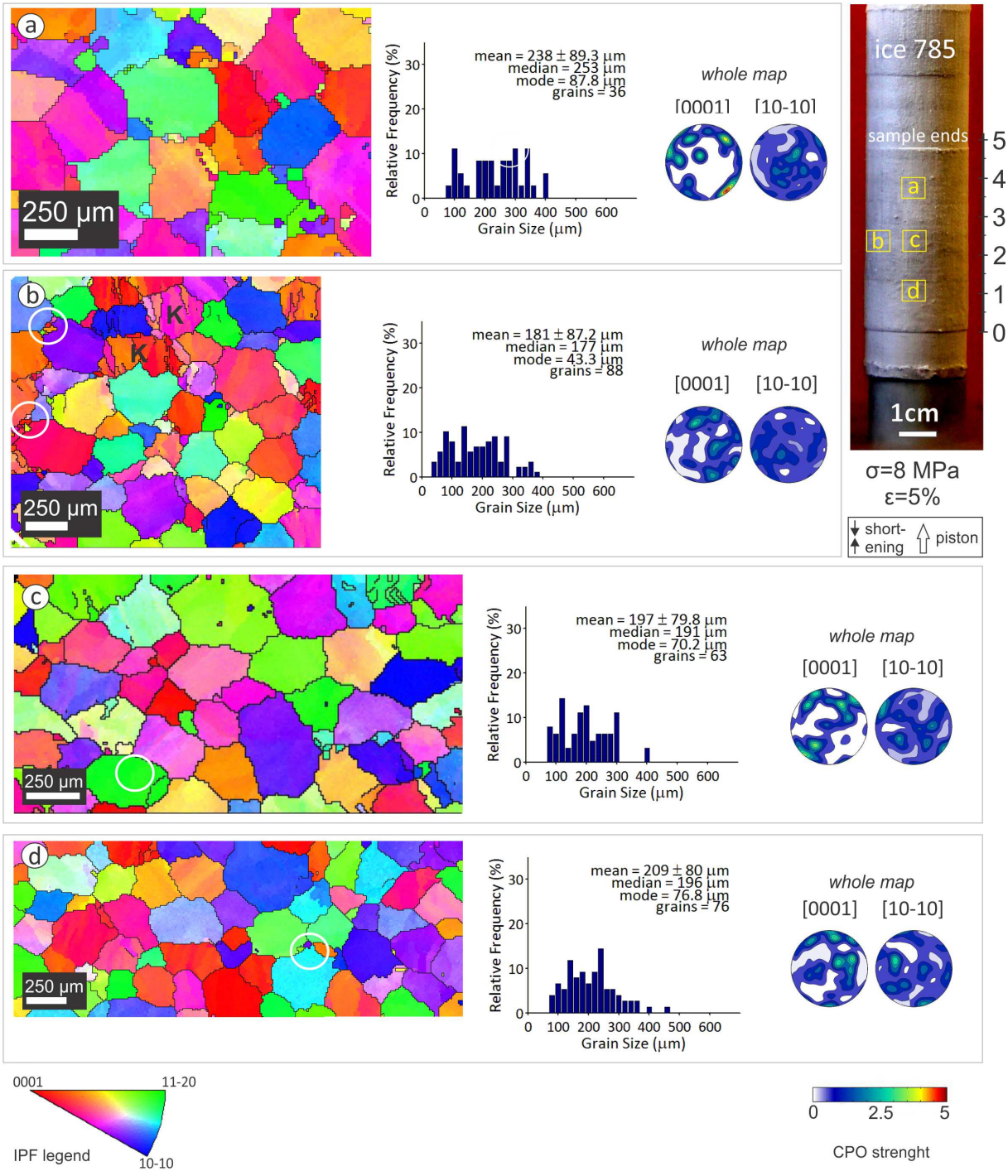

Figure 4.4: EBSD IPF orientation maps, colour-coded in bulk shortening orientation of sample 785 (8 MPa axial stress, 5 % strain). The legend in the top right corner displays the approximate location of the map within the sample. The size of the boxes were exaggerated for better visibility. Pole figures are equal-area, upper hemisphere projections showing the mean orientation for each grain. CPO strength was colour-coded according to the legends below the projections. All maps were imaged at a step size of 10 μm, to allow for an easy comparison with the detailed maps of samples 769 (Fig. 4.3b,c) and 774 (Fig. 4.5c,d).

is visible in several grains within the top of the map.

Grain size histograms of the respective maps depict distributions ranging from box- to log-normal shaped. More small grains are found within the maps taken from the bottom and centre of the sample (Fig. 4.4b-d) and result in median grain diameter of 177-191 μm compared to a median grain diameter of $\sim$250 μm calculated for the map from the top of the sample (Fig. 4.4a).

4.3.3 Ice 774

Mechanical response

The target stress of $\sim$3 MPa was reached after only 0.4 % strain, twice as fast as in high-stress experiment 769 (Fig. 4.1a). Deviations from the target stress of $\pm$0.2 MPa were mainly related to zero force calibrations of the internal force gauge; stress decreased linearly between force gauge readings and peaked imminently after the reading was performed.

The strain rate vs. strain curve of experiment 774 is similar to experiment 769: a long phase of strain hardening is encountered after target stress was met, followed by strain weakening until a mechanical steady state is established (Fig. 4.1b). Strain hardening starts at 0.5 % strain (as in experiment 769) but the exponential strain hardening is more profound as in higher-stress experiments 769 and 785. The minimum strain rate of 5x10^{-8} /s is observed at $\sim$2.2 % strain. Strain weakening is recorded from 2.2 % until about 7-8 % strain, with exacerbated rates of weakening occurring after force gauge readings. From 7-8 % until the end of the experiment at 12.5 % strain, a mechanical steady state with an approximate strain rate of $\sim$4.5-4x10^{-7} /s is established.

Macroscopic strain distribution

Bulk strain in sample 774 is localised within a macroscopic, symmetrical bulge at the bottom of the sample, 0-25 mm from the end spacer (Fig. 4.2g,j). The bulging of about 2 mm is homogeneous but decreases linearly around the centre of the sample, 25-35 mm from the bottom. Contrastingly, the top of the sample (above 35 mm) does not display any evidence of bulging (Fig. 4.2g,h).

Faint bumps with lengths of approximately 5 mm and thicknesses of around 1-2 mm are sparingly visible on the jacket. These bumps are primarily found 15-25 mm from the bottom and spatially coincide with the top half of the bulge (Fig. 4.2g,h). More pronounced bumps in both thickness and length are observed within the transition zone

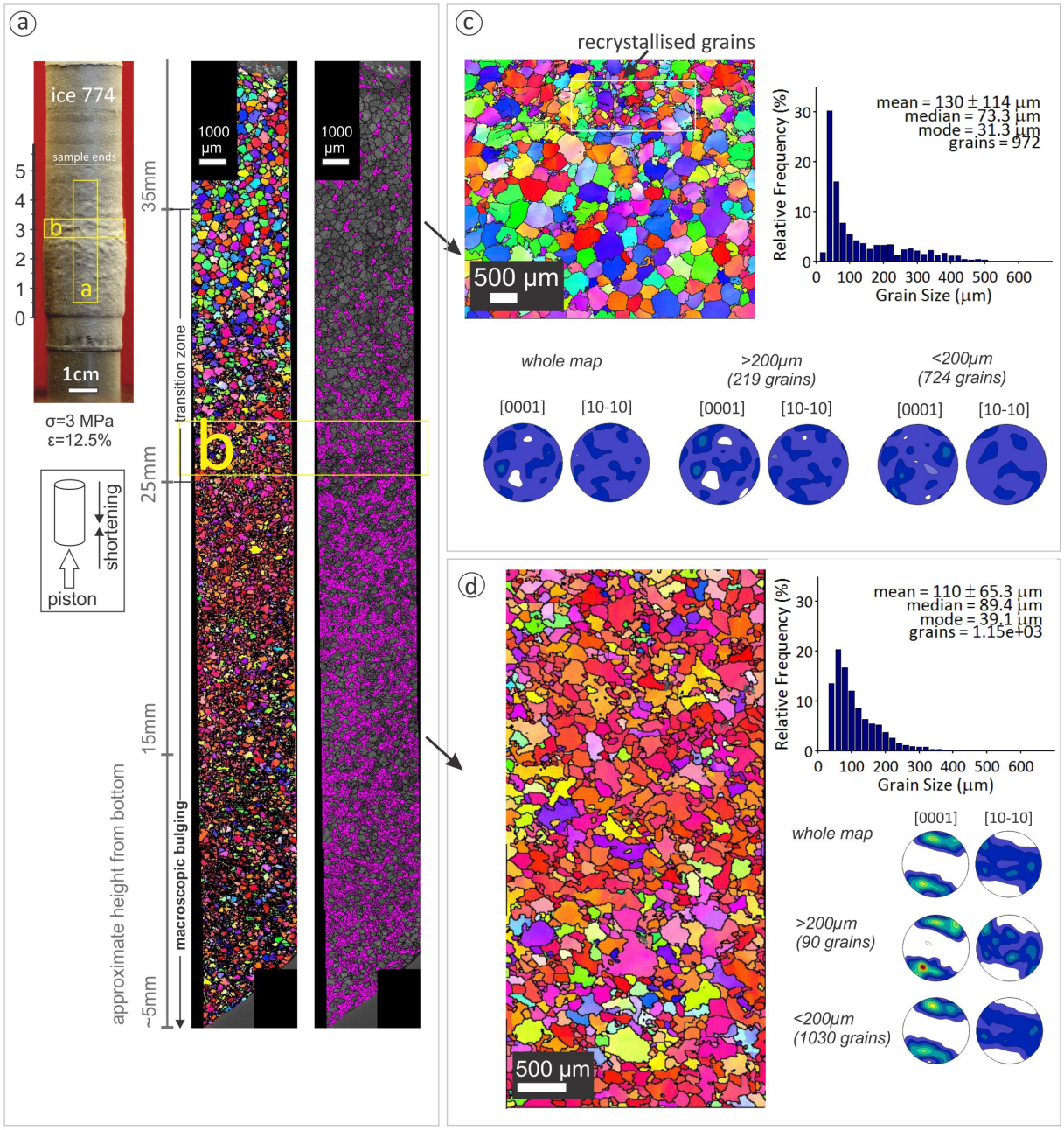
a
ice 774
sample ends
b
a
1cm
σ=3 MPa
ε=12.5%
piston
shortening
1000 µm
1000 µm
35mm
25mm
15mm
~5mm
transition zone
macroscopic bulging
approximate height from bottom
b
c
recrystallised grains
500 µm
mean = 130 ± 114 µm
median = 73.3 µm
mode = 31.3 µm
grains = 972
Relative Frequency (%)
Grain Size (µm)
whole map
>200µm
(219 grains)
<200µm
(724 grains)
[0001]
[10-10]
d
500 µm
mean = 110 ± 65.3 µm
median = 89.4 µm
mode = 39.1 µm
grains = 1.15e+03
>200µm
(90 grains)
<200µm
(1030 grains)
b
1000 µm

Figure 4.5: EBSD maps of sample 774. The location of the map within the sample is indicated in the top left corner. a) Orientation map of a vertical cross-section through the middle of ice 774 (left map) with IPF colour-coding with respect to the shortening direction. Grains with area-equivalent grain diameters below 200 μm are highlighted in pink on a pattern quality map (right map). b) Horizontal (perpendicular to bulk shortening) cross-section taken in the 'transition zone', in which horizontal bulging decreases (Fig. 4.2i). c) Close-up of the microstructure in the top, where small grain bands are only sparingly found. d) More detailed microstructural map of the bottom of the sample, where grain size is reduced and a CPO is present.

(25-35 mm), where horizontal widening decreases towards the top (Fig. 4.2i). The long axes of the protrusions on ice 774 are mostly oriented perpendicular or semi-perpendicular to bulk shortening. No bumps are found at the top of the sample above 40 mm from the bottom (Fig. 4.2g,i), where no bulging of the sample is observed.

Deformation microstructure and correspondence to macroscopic strain distribution

The microstructure of ice 774 is spatially heterogeneous and corresponds to the macroscopic strain distribution (Fig. 4.5a). The microstructure at the top of the sample (>35 mm from the bottom) mainly consists of randomly-oriented, polygonal grains with grain diameters of >200 μm (Fig. 4.5a). These grains are reasonably identified as remnant grains. Clusters of small grains with grain diameters <200 μm (below the grain diameter of the starting material) are only found sparingly within the larger polygonal grains. These grains are identified as recrystallised grains. Within the transition zone from wide to small sample diameter (25-35 mm), the number of recrystallised grains is higher. The recyrstallised grains form bands with lengths of several grain diameters, and 1-2 grain diameter widths at 40-90° orientations to bulk shortening (Fig. 4.5a,b). Spacings within the bands often comprise several grain diameters (500-1500 μm). Within the bulge, below 25 mm from the bottom, the recrystallised grains outnumber the remnant grains to form an interconnected matrix with isolated clusters of remnant grains. (Fig. 4.5a).

More detailed maps (step size of 10 μm) are employed to further describe the microstructure, CPO and grain size statistics outside and within the strain localised area at the bottom (Fig. 4.5c,d). The exact location of the detailed maps within the sample was not recorded during imaging. Hence, their approximate location (top > 35 mm or bottom <25 mm) was determined post-imaging by using the microstructural information in the overview map in Fig. 4.5a.

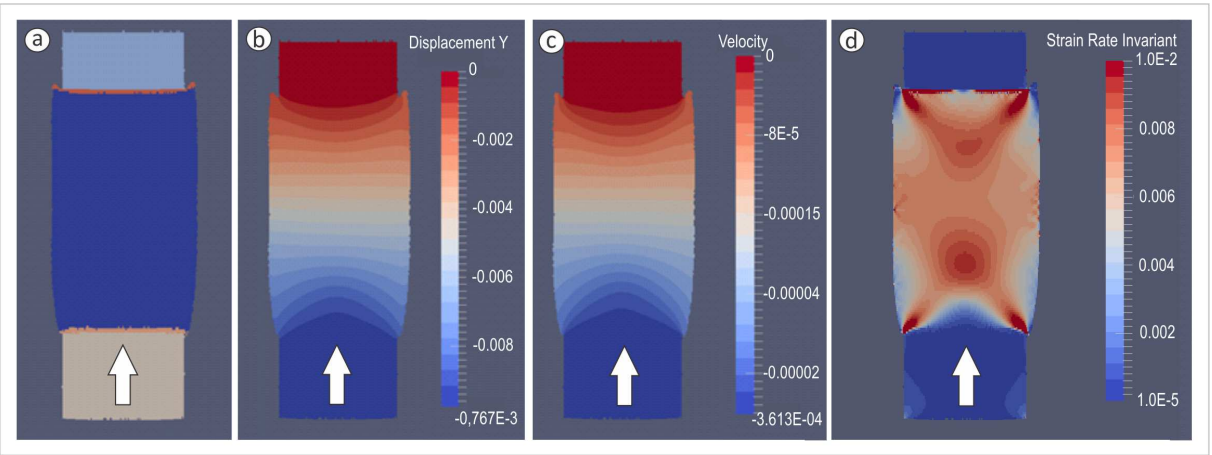

Figure 4.6: Modelling of ice 769 (∼13 MPa axial load) with finite-element code SULEC. (a) Modelling setup of the sample assembly. Interfaces are shown in red. The positions of the zirconia spacer and the end plug are reversed from their original positions in the experimental setup (see Fig. 4.2). Piston movement providing axial compression is indicated with the white arrow. Ice flowing around the end plug is a modelling artefact due to the finite thickness of the boundary. Results are displayed as (b) displacement [m] in shortening direction, (c) velocity [m/s] and (d) the second strain rate invariant [1/s] (section 4.3.4).

The microstructure at the top of the sample is dominated by remnant grains with slightly lobate grain boundaries (Fig. 4.5c). The remnant grains are occasionally intersected by pockets of recrystallised grains. The grain size distribution for this map is skewed, with a median grain diameter of 73 μm. The CPO at the top of the sample is random. Recrystallised and remnant grains also display random CPOs, respectively (Fig. 4.5c).

The microstructure within the macroscopic bulge at the bottom of the sample (<25 mm) is dominated by a network of recystallised grains (Fig. 4.5a,d). All grains are odd-shaped, with highly sutured grain boundaries (Fig. 4.5d). The grain diameter distribution is skewed, with a median grain diameter of ∼90 μm.

No differences between the CPOs of recrystallised and remnant grains can also be observed at the bottom of the sample within the area of macroscopic bulging (Fig. 4.5d). The overall c-axis CPO is a two cone distribution with maxima at angles of 20-45° to bulk shortening.

4.3.4 Numerical modelling

Numerical modelling results show homogenous bulging of the ice sample between the zirconia spacer and stainless steel end cap (Fig. 4.6a). The maximum displacement derived from the model is similar to the maximum shortening of 0.89x10^{-3} m achieved during the experiment (Table 4.2, Fig. 4.6b). Normalising the maximum velocity with the initial sample length yields a maximum strain rate of 6.2x10^{-3} /s, which is a magnitude higher than the experimentally determined strain rate (Fig. 4.1b,4.6c). The second invariant of the strain rate tensor (invariant under rotation, providing an estimate of the bulk strain rate) displays two major concentrations about 10 mm from the top and bottom of the sample (Fig. 4.6d). The height of the strain rate concentrations correlates with areas of maximum bulging in samples 769 and 774 (Fig. 4.2a,g). Between the two maxima, a wide girdle of elevated strain rate invariants is found. Small high-strain rate regions are also found at the outer corners of the ice-zirconia and ice-steel interfaces.

4.4 Discussion

4.4.1 Overall context

Strain localisation, rheological weakening and microstructures as observed in this study are no isolated feature. Localisation as manifested in bumps and localised bulging can also be extracted from earlier triaxial constant displacement and constant stress studies on polycrystalline ice under high confinement for strains >10 % (Durham *et al.*, 1983, 2001). In constant stress experiments incorperating a sequence of different loads Durham *et al.* (2001), bumps and bulging also correlate with rheological weakening. Microstructures from the inner surface of the indium jackets of sample 449 in Durham *et al.* (2001) (deformed at a temperature of 220 K and 50 MPa confining pressure) show a bimodal grain size distribution similar to samples 769 and 774.

4.4.2 Initiation of localisation

Recrystallisation in sample 785 at 5 % strain occurs homogeneously (Fig. 4.7a). No spatially preferred recrystallisation sites (Fig. 4.4) were detected at top or bottom, where bulging occurs at higher strains in samples 769 and 774 (Fig. 4.2a,g). These observations suggest that the localisation of a bulge of high strain rates at the top or bottom of the sample is not related to where recrystallisation initiates. Our results match the findings

of Golding *et al.* (2012), who also found no preponderance of recrystallised grains in areas where plastic faulting subsequently developed with progressive strain.

The onset of strain localisation may instead be related to a geometrical constraint imposed by the boundary conditions of the experimental setup. Numerical simulations of sample 769 (Fig. 4.6) predict elevated strain rates approximately 10 mm of the sample length from top and bottom. Regions subject to high strain-rates spatially correspond to the strain-localised areas (bulges) in samples 769 and 774, respectively. The influence of the boundary conditions in the development of localisation behaviour has also been deduced from theoretical considerations and numerical modelling for other rocks and experimental setups (i.e. Hobbs *et al.*, 1990; Gao and Zhao, 2015).

4.4.3 Deformation microstructure in strain-localised regions

Comparisons of sample-scale EBSD maps and the overall strain distributions demonstrate a correlation between high-strain areas and a reduced grain size (Fig. 4.7b). High-strain areas are identified by macroscopic widening (bulging) in high-strain (>10 %) samples 769 and 774 (Fig. 4.2b,j). These areas are dominated by a matrix of recrystallised grains with median grain diameters of about 70 μm (ice 769) and 90 μm (ice 774, Fig. 4.3b, 4.5d). This represents a marked grain size reduction from the starting material. In the transition zone in sample 774, where the diameter of the sample linearly decreases towards the top over a length of 10 mm, the number of recrystallised grains decreases towards the top (Fig. 4.3i,4.5a,b). Sample 785 and low-strain areas in samples 769 and 774 (Fig. 4.3c,4.4,4.5c) show a lesser degree of recrystallisation. Recrystallised grains are only detected in isolated pockets containing a few grains. These findings support the view that areas of high-strain amplitudes are favourable sites for recrystallisation (Golding *et al.*, 2012; Montagnat *et al.*, 2015).

The microstructure in the highly strain-localised bulge in samples 769 and 774 displays a homogeneous two cone CPO (Fig. 4.3b,4.5d). This CPO is consistent with high-temperature uniaxial compression experiments (i.e. Jacka, 1994; Montagnat *et al.*, 2015; Vaughan, 2016). However, the two cone CPO in high-temperature ($\geq$-10°C) uniaxial compression experiments usually intensifies with progressive strain. It is therefore surprising that the microstructure in the localisation in ice 774 (12.5 % strain) shows a significantly stronger CPO than the localisation in ice 769 ($\sim$15 % strain). Similar to the high-temperature results of Qi *et al.* (2017), this finding may indicate that CPO formation and strengthening are strain rate dependent.

On a smaller scale, further localisation is detected in the form of bumps on the jackets

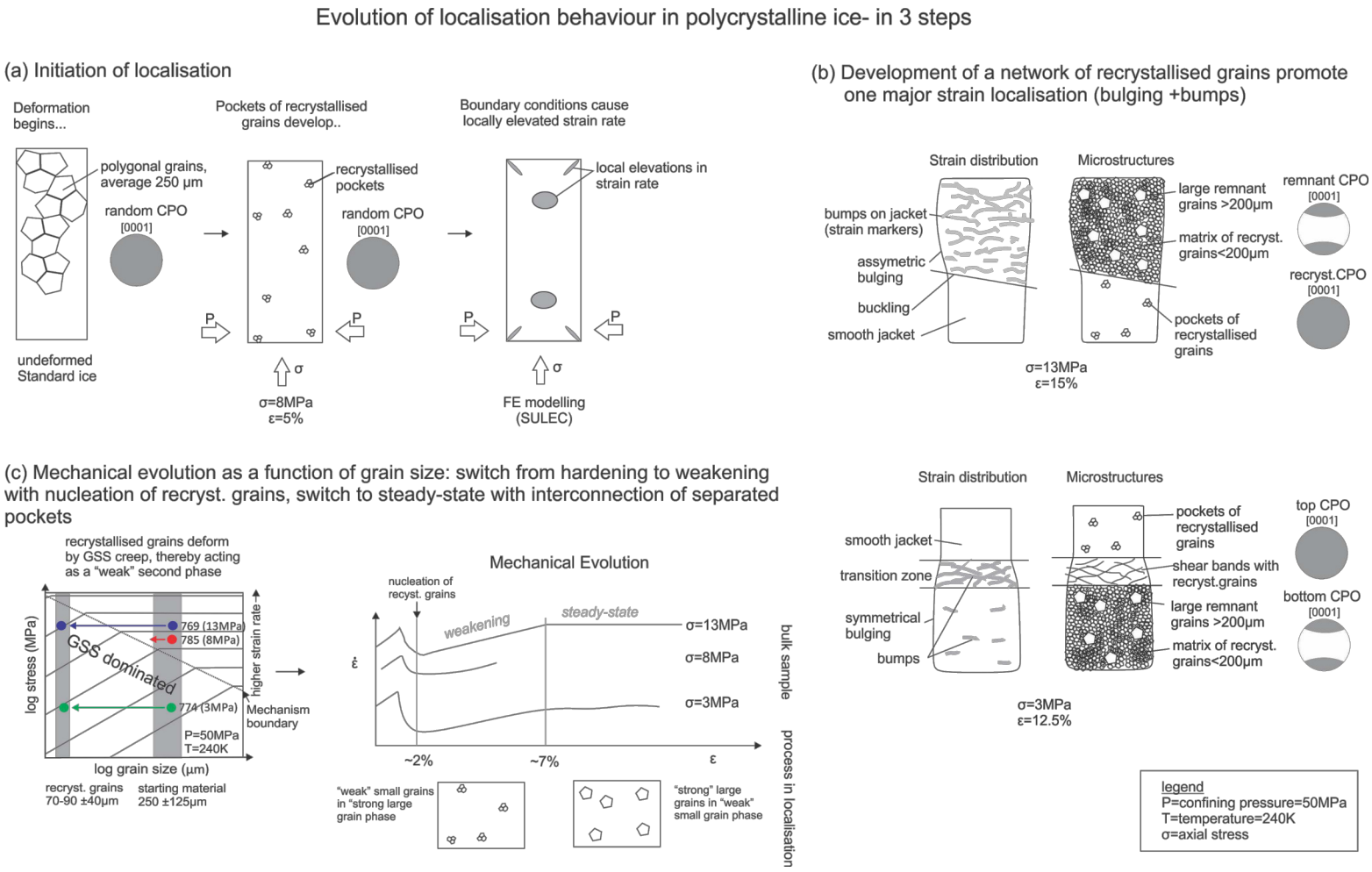

Figure 4.7: Evolution of localisation behaviour of polycrystalline ice under high confining pressure, based on mechanical records, strain localisation and microstructural evolution of ice 769, 785 and 774.

surface where macroscopic bulging in the jacket is observed and appears to be caused by a mixture of remnant and recrystallised grains in the microstructure (Fig. 4.2b,i,j). No bumps are detected where remnant grains dominate (ice 769 Fig. 4.2c,4.3c, ice 774 Fig. 4.2h,4.5c) but they appear in areas where few remnant grains are surrounded by a matrix of recrystallised grains (ice 769 Fig. 4.2b,4.3b, ice 774 Fig. 4.2j,4.5d). Most protruding bumps are found in the transition zone of sample 774 where bands of recrystallised grains form the same semi-perpendicular angles to shortening. The spacing between the recrystallised bands (500-1500 μm) approximately corresponds to the widths of the bumps (1-2 mm) detected on the sample's surface (Fig. 4.2i,4.5b) and indicates that remnant grains may behave like rigid particles in a matrix of higher plasticity and that this difference in plasticity induces strain localisations on a micro-scale. This conclusion, however, needs to be treated with caution as no recrystallised grain size piezometer is available for polycrystalline ice, yet (this work is currently in progress). Hence, the cut-off value between recrystallised and remnant grains was arbitrarily chosen and may not reflect the grain size at which mechanical properties may change due to an increasing contribution of grain size sensitive creep mechanisms to the overall strain rate (Fig. 4.8). A difference in plasticity between large and small grains due to the development of a CPO is less likely, as sample 774 shows the same two cone CPO for both recrystallised and remnant grains where bumps the surface of the jacket occur (Fig. 4.2j,4.5d).

4.4.4 Rheological evolution

Existing models for the rheological evolution of polycrystalline ice at high-homologous temperatures can only partly explain the rheological evolution of samples within this study. Transition along the various creep stages in polycrystalline ice is often attributed to CPO formation and intensification (i.e. Budd and Jacka, 1989; Wilson and Russell-Head, 1982; Vaughan, 2016). Although the strain-strain rate curves follow the traditional creep curves know from the high-temperature deformation of polycrystalline ice (see Budd and Jacka, 1989; Wilson *et al.*, 2014 for reviews), the mechanical evolution is unlikely to be a function of CPO development. Sample 769 does not have a strong overall CPO and the number of remnant grains with a mechanically anisotropic two cone CPO in the strain localised region is limited (Fig. 4.3b,c). The fact that this sample still undergoes the same mechanical evolution as sample 774 with a strong two cone CPO within the strain-localised region (Fig. 4.5d) suggests that the development of a CPO is not the rheology-driving mechanism. Another explanation from the high-temperature deformation of polycrystalline ice suggests weakening as a consequence of a thermal instability

(Golding *et al.*, 2010). However, this explanation is associated with continuous rheological weakening until the sample fails or the experiment is terminated and cannot explain the transition to a mechanical steady state at approximately 7 % strain (Fig. 4.1b).

The rheological evolution we observe is best explained as a function of the grain size evolution (Fig. 4.7c). Small grain sizes are associated with strain weakening of the aggregate due to a higher contributions of grain size sensitive (GSS) creep mechanisms to the overall strain rate (i.e. De Bresser *et al.*, 2001; Bestmann and Prior, 2003; Warren and Hirth, 2006). The principle of a transition to GSS-dominated creep due to reduction in grain size is illustrated in a plot of the stress vs. the grain size in Figure 4.8. The bend in the strain rate contours represents the mechanism boundary, where both grain size insensitive (GSI) dislocation creep and GSS creep contribute equally to the strain rate (Frost and Ashby, 1982; de Bresser *et al.*, 1998; De Bresser *et al.*, 2001). A reduction in grain size in samples 769 and 774 promotes a transition from slower dislocation creep-dominated strain rates to up to one order of magnitude faster strain rates dominated by the contributions of GSS creep to the total strain rate.

To assess how an increasing component of 'weak' recrystallised grains with strain impacts the rheological response of the aggregate, we need to estimate the strength of the aggregate based on two phases with different mechanical properties (Fig. 4.7c). A common end-member theory in structural geology describes the rheological properties of an aggregate based on the transitions from a load bearing framework (LBF, strong phase with weak inclusions) to an interconnected weak phase (IWF) with only few strong inclusions. Results of early numerical studies targeting the two end-members are not applicable as they focused on two phases undergoing dislocation creep (Tullis *et al.*, 1991; Handy, 1994). But a newer study based on a difference in viscosity between the phases demonstrates that small weak phase inclusions in a strong phase cause initial strain hardening, followed by a longer phase of weakening of the aggregate (Takeda and Griera, 2006). A corresponding scenario is present in sample 785 at 5 % strain, which exhibits rheological weakening while recrystallised grains are found in a matrix of remnant grains. Numerical results of Takeda and Griera (2006) and an experimental study by Pieri *et al.* (2001) also suggest that steady state behaviour is expected as soon as the weak phase interconnects. This scenario corresponds to samples 769 and 774 which have reached a constant or semi-constant strain rate and exhibit a network of recrystallised grains in strain-localised regions. As a consequence of this line of thought, the mechanical behaviour of the aggregate is determined by the mechanical properties of the grain size distribution within the localisation.

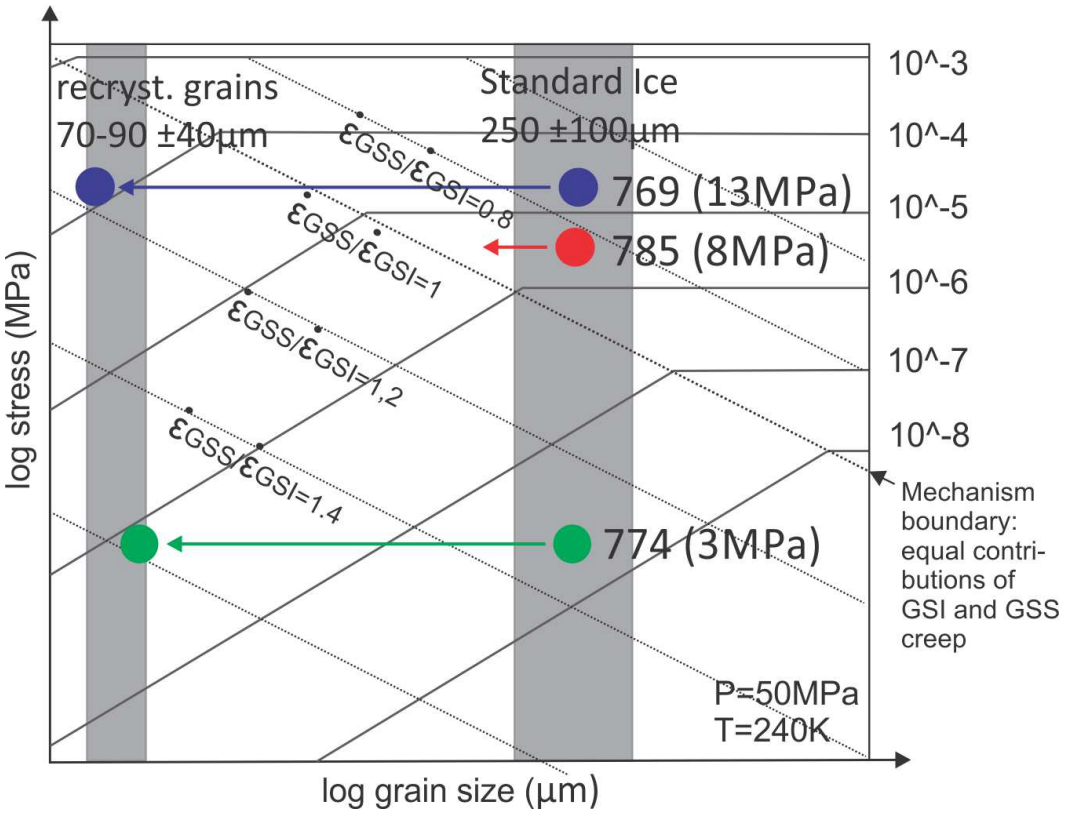

Figure 4.8: Schematic deformation mechanism map illustrating the principle of strain weakening by a shift into GSS-dominated creep regime. Slopes of constant strain rates contours were derived from plotting rheologies for GSS creep (Goldsby and Kohlstedt, 1997, 2001) and dislocation creep (Durham *et al.*, 1997). Spacings between the strain rate contours were adjusted based on the minimum and steady state strain rates (Fig. 4.1b) and median grain size values from within the bulge (Fig. 4.3b) of ice 769. Ice 785 was not deformed beyond secondary creep, therefore only the minimum strain rate corresponding to a vast majority of remnant grains was labelled in the map. Ice 774 was additionally plotted but the observed steady state strain rate does not match with what is expected when the measured grain size reduction (using the median within the bulge, Fig. 4.5d) is inserted . It is remarked here that the maximum differential stress for this experimental setup equals the axial stress (see Durham *et al.*, 1997).

4.4.5 Remaining questions

The microstructural signature caused by GSS creep is still up for debate. The microstructural properties of the recrystallised grains in sample 769 (equant-grain shapes, straight grain-boundaries and a random CPO) are consistent with GSS creep in rocks (Boullier and Gueguen, 1975; Evans and Kohlstedt, 1995; Goldsby and Kohlstedt, 1997; Bestmann and Prior, 2003; Warren and Hirth, 2006). Other studies argue that GSS creep leads to the formation of a CPO (Peltier *et al.*, 2000; Hansen *et al.*, 2011). Studies naming grain boundary sliding as a component of GSS creep have additionally identified quadropole junctions as a characteristic feature (Goldsby and Kohlstedt, 1997; Bestmann and Prior, 2003). It is, however, unclear how many different forms of GSS creep may exist and if its microstructural signature is restricted to the diagnostic criteria described before. For GBS only, several different mechanisms have been discussed (Zelin and Mukherjee, 1996; Langdon, 2006). The lobate grain boundaries in the strain-localised region in sample 774 (Fig. 4.5d) indicate that GSS creep may be microstructurally superposed with grain boundary migration. More case studies in nature and experiment exploring the link between mechanical data to microstructural processes are needed to better constrain the microstructural signature of GSS creep in rocks and its impact on overall deformation.

In the ice literature, there is disagreement on whether GSS creep can explain rheological weakening and under which deformation conditions it is to be expected (see Wilson *et al.*, 2014 for a summary). Generally, it is thought that GSS creep is hard to achieve under high-homologous temperatures and that GSS creep mechanisms do not affect rheologies with stress exponents n>3. Contrastingly, the results presented in this paper suggest that a mixture of GSS creep and dislocation creep may cause steady state strain exponents of n≈4. It is hoped that with the rise of large-scale imaging methods (cryo-EBSD and for grains $\gg 100$ μm, the fabric analyser or AITA) the existing rheologies for fine-grained polycrystalline ice will be refined.

4.5 Conclusions

We analysed localisation behaviour in three polycrystalline ice cylinders deformed in a triaxial apparatus at a temperature of 340 K, 50 MPa confining pressure and varying axial stresses and strains. Our results suggest that

- the rheological evolution of the samples is driven by progressive recrystallisation in the strain-localised region, if recrystallised grains deform by grain size sensitive

creep and act as a 'weak' phase within the 'stronger' remnant grains.

- sample 785 (8 MPa, 5 % strain) underwent strain weakening during secondary creep due to the nucleation of homogeneously distributed pockets of recrystallised grains within a framework of remnant grains.

- strain localises in a macroscopic bulge ∼10 mm from top or bottom in samples 769 (13 MPa, 14 % strain) and 774 (3 MPa, 12.5 % strain) during tertiary creep. Transition to a steady state strain rate during tertiary creep occurs as recrystallised grains with median grain diameters of 70 μm in the strain localised areas interconnect.

- strain localisation is initially promoted by the boundary conditions of the experimental setup.

- strain localisation and the rheological evolution occur irrespective of whether recrystallised grains develop a CPO or not. More work is required to constrain the microstructural properties of GSS creep in rocks and refine the rheology for fine-grained polycrystalline ice.

4.6 Graphical summary

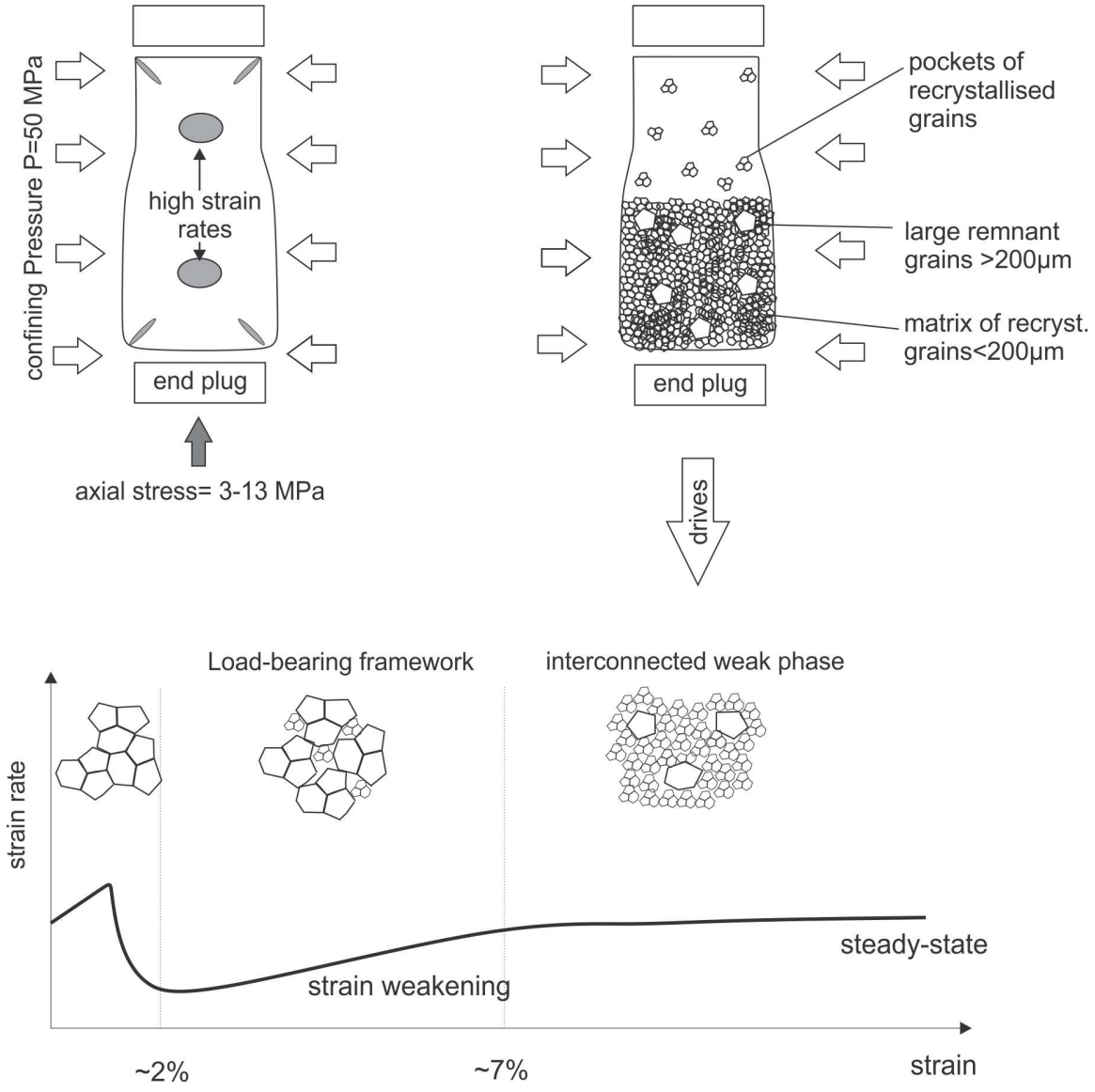

4.7 Supplementary material

4.7.1 Microstructural properties of the starting material 'Standard ice'

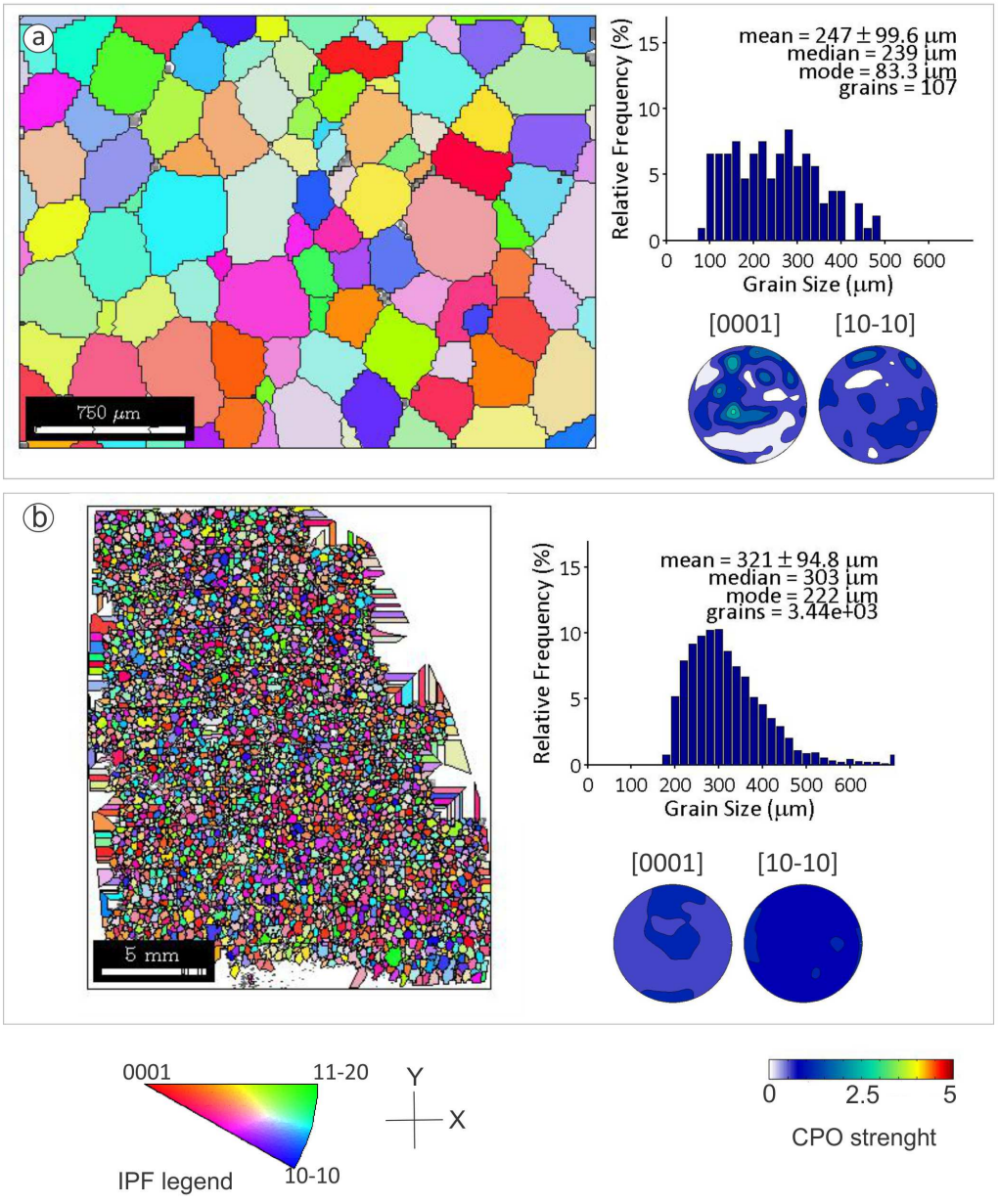

Figure 4.9: EBSD orientation maps (IPF Y colour-coding), grain size histograms, and contoured CPO for undeformed Standard Ice imaged at a step size of 20 μm (a) and 50 μm (b), respectively (Ref2). Clusters in the c-axis orientations in (a) are an artefact due to the small number of grains. Border grains in the montage map (b) are an artefact of the MTEX processing, which defines grains based on a number of 10 indexed pixels.

Table 4.3: Grain size and CPO summary of other undeformed 'Standard ice' samples. Grain size statistics for sample Ref2 are given in Fig. 4.9.

Sample	step size [μm]	grain diameter [μm]	number of grains	CPO
Ref4	5	223±115	95	random
	40	286±86	965	random
Ref5	20	286±116	320	random

4.7.2 Formulas employed for processing of the mechanical data

Stress was calculated dynamically from recorded load data and the initial sample area A_0. The current area A was approximated by assuming a constant volume, regardless of strain, and employing current displacement U, initial sample length l_0 and the initial sample area (Stern *et al.*, 1997):

$$\begin{aligned} V = const. \Rightarrow A * l = A_0 * l_0 \quad [\mathrm{m}^3] \\ \rightarrow A = A_0 * l_0/l = A = A_0 * l_0/(l_0 - U) \quad [\mathrm{m}^3] \\ \rightarrow \sigma = F/A = F * (l_0 - U)/A_0 * l_0 \quad [\mathrm{MPa}] \end{aligned} \tag{4.1}$$

Post-deformation, the stress values were additionally corrected for potential errors caused by a constant drift of the force gauge Δf between two force gauge readings $f_1(t_1)$ and $f_2(t_2)$ (Durham *et al.*, 1983):

$$\begin{aligned} \Delta f = (f_2(t_2) - f_1(t_1))/(t_2 - t_1) \quad [\mathrm{MPa/s}] \\ \rightarrow f(t) = f_1 + \Delta f * t \quad [\mathrm{MPa}] \\ \rightarrow \sigma(t) = F(t) - f(t) \quad [\mathrm{MPa}] \end{aligned} \tag{4.2}$$

with the time of the first force gauge reading t_1, the time of the second force gauge reading t_2 and any time between them t. $F(t)$ enotes the actual force gauge reading at the time t and $f(t)$ the correction at the time t.

Strain was determined in engineering values:

$$\epsilon = l/l_0 = (l_0 - U)/l_0 \quad [\text{-}] \tag{4.3}$$

Incremental strain rates (comparing the current strain to the previous strain value within a given time increment delta t) were chosen for the strain rate vs. strain plots, as

calculating strain rates with the initial strain values at the start of the experiment were found to misrepresent trends of acceleration or slowing that were clearly visible in the strain vs. time curves (Appendix).

$$\dot{\epsilon_i} = (\epsilon_i - \epsilon_{(i-1)})/(t_i - t_{(i-1)}) \quad [1/\mathrm{s}] \qquad \text{with } i\text{= index for time increment} \qquad (4.4)$$

For the shortest experiment 769 of 1.5 hours, the time increment of 32 seconds, equal to the minimum sampling rate was chosen. Using the same time interval to constrain strain rates for the slower experiments 785 and 769 (less strain within the same time increment), lead to a high noise-data ratio (Fig. 4.10d). To correct for a higher comparative sampling rate, the strain rates of experiments 785 and 774 were smoothed with a moving average filter in Matlab 2013a (https://au.mathworks.com/help/curvefit/smooth.html) comparing the current value over a span of 5 values and 118 values respectively (Fig. 4.1b,4.10e). This averaging mimicked the sampling rate of approximately 40 samples per strain experiment 769 and yielded a sufficient decrease in noise (Fig. 4.1b).

Example for the moving average filter for span of 5:

$$\dot{\epsilon_4} = (\dot{\epsilon_2} + \dot{\epsilon_3} + \dot{\epsilon_4} + \dot{\epsilon_5} + \dot{\epsilon_6})/5 \quad [1/\mathrm{s}] \qquad (4.5)$$

4.7.3 Processing of strain rate vs. strain curves

This section explains the processing of the strain rate vs. strain curves with reference to Fig. 4.10: a) Glaciological strain-time curves of experiments 769 and 785 indicate that 769 has reached mechanical steady state and an increase in the strain rate towards the end of experiment 785. b) The strain-time curve of experiment 774 shows fluctuations in the strain rate (i.e. slowing of deformation at about 80 hours, an increase in strain rate prior to the termination of the experiment). c) The trends visible in the strain-time curves are absent when strain rates are calculated with reference to the start of the experiment. d) Incremental strain rates (calculated for time steps of 32 seconds) reflect the strain rate trends from the strain-time curves. However, the short time step interval is only appropriate for the shorter experiments (769 and 785) and results in a high noise-data ratio in experiment 774. e) Smoothed strain rate-strain curves: A moving average filter (Formula 4.5) was employed to smooth the data in d). The amount of values used for averaging was based on the experimental duration. All strain values and strain rate values were calculated according to the engineering convention (Formula 4.3).

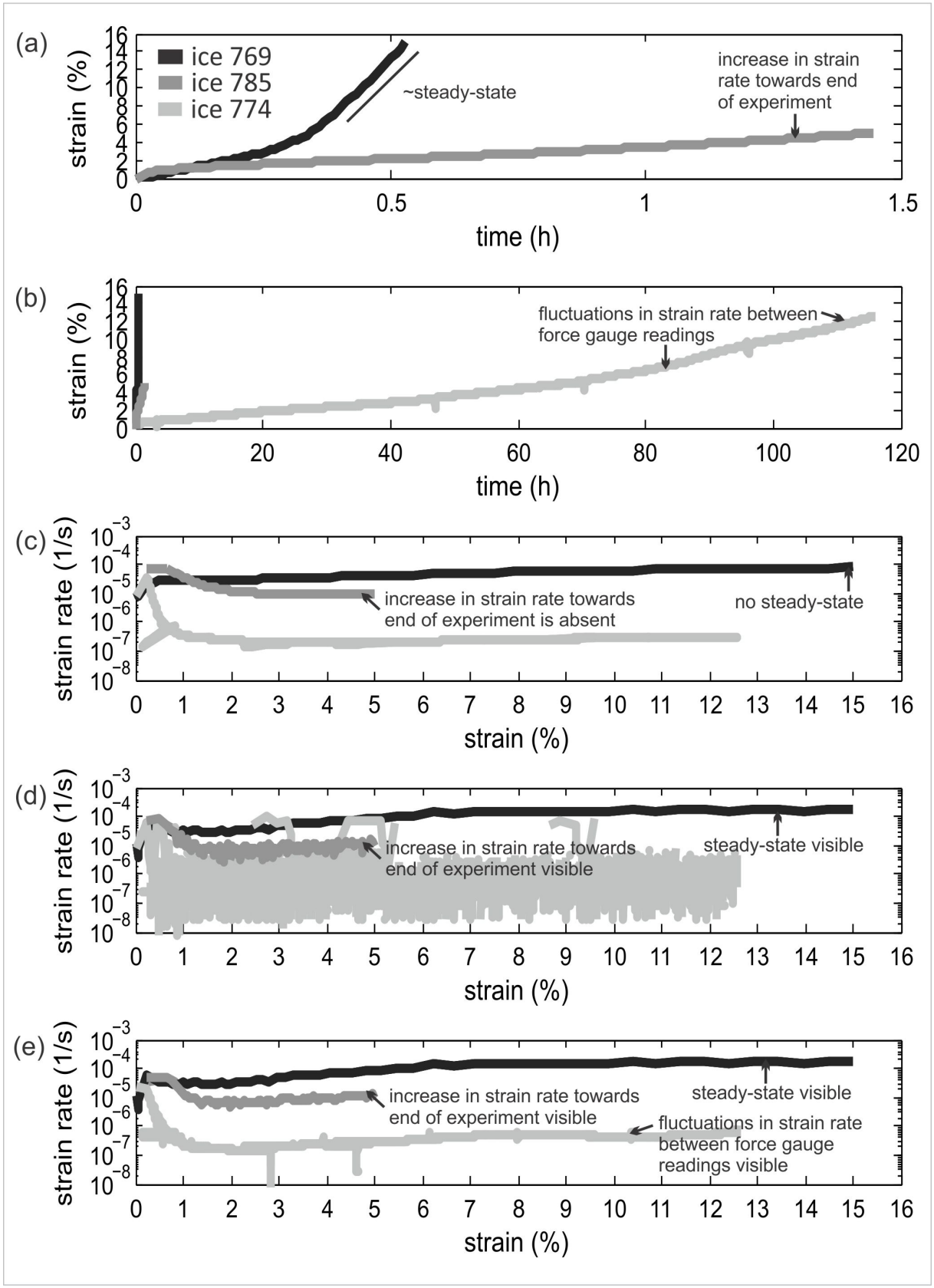
(a)
strain (%)
ice 769
ice 785
ice 774
~steady-state
increase in strain rate towards end of experiment
time (h)
(b)
strain (%)
fluctuations in strain rate between force gauge readings
time (h)
(c)
strain rate (1/s)
increase in strain rate towards end of experiment is absent
no steady-state
strain (%)
(d)
strain rate (1/s)
increase in strain rate towards end of experiment visible
steady-state visible
strain (%)
(e)
strain rate (1/s)
increase in strain rate towards end of experiment visible
steady-state visible
fluctuations in strain rate between force gauge readings visible
strain (%)

Figure 4.10: Illustration of the data reduction of the mechanical data shown in Fig. 4.1. a) strain vs. time curve for the 'shorter' experiments 769 and 785. b) strain vs. time curve for ice 774. c) strain rate vs. strain curve with strain rates calculated with reference to the value recorded at the start of the experiment. d) strain rate vs. strain curve showing incremental strain rates (Formula 4.4) and e) strain rate vs. strain curves additionally processed with a moving average filter (Formula 4.5).

4.7.4 Determination of stress exponents (n-values)

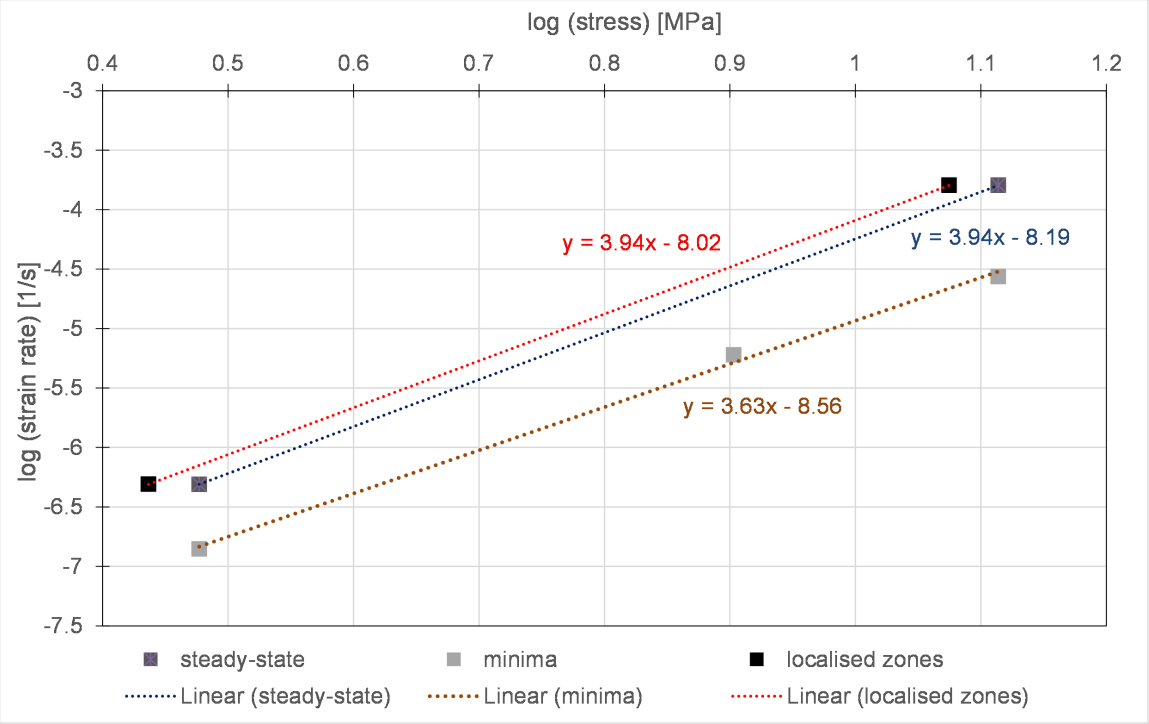

Figure 4.11: Determination of stress exponents in Fig. 4.1b assuming a power-law creep equation (see section 1.4.2, i.e. Formula 1.4). All stress exponents were determined with n=Δln(strain rate)/Δln(stress). The steady state stress exponent n_s was approximated using an average of 4 values of the steady state strain rates of samples 769 and 774 but contains uncertainties due to localisation. Data for the stress exponent for minimum strain rates n_m was available from all experiments (769, 785, 774); this n_m is regarded as more robust because minimum strain rates are measured prior to the onset of localisation. The localised stress exponent n_l accounts for the stress reduction, which is expected due to bulging in the localised zone in sample 769 and 774. The length of the localised zones was measured from pictures (Fig. 4.2) and the area of the bulge was approximated with a constant volume assumption.

4.7.5 EBSD maps and grain size statistics corresponding to the pole figures in Fig. 4.3 and 4.5.

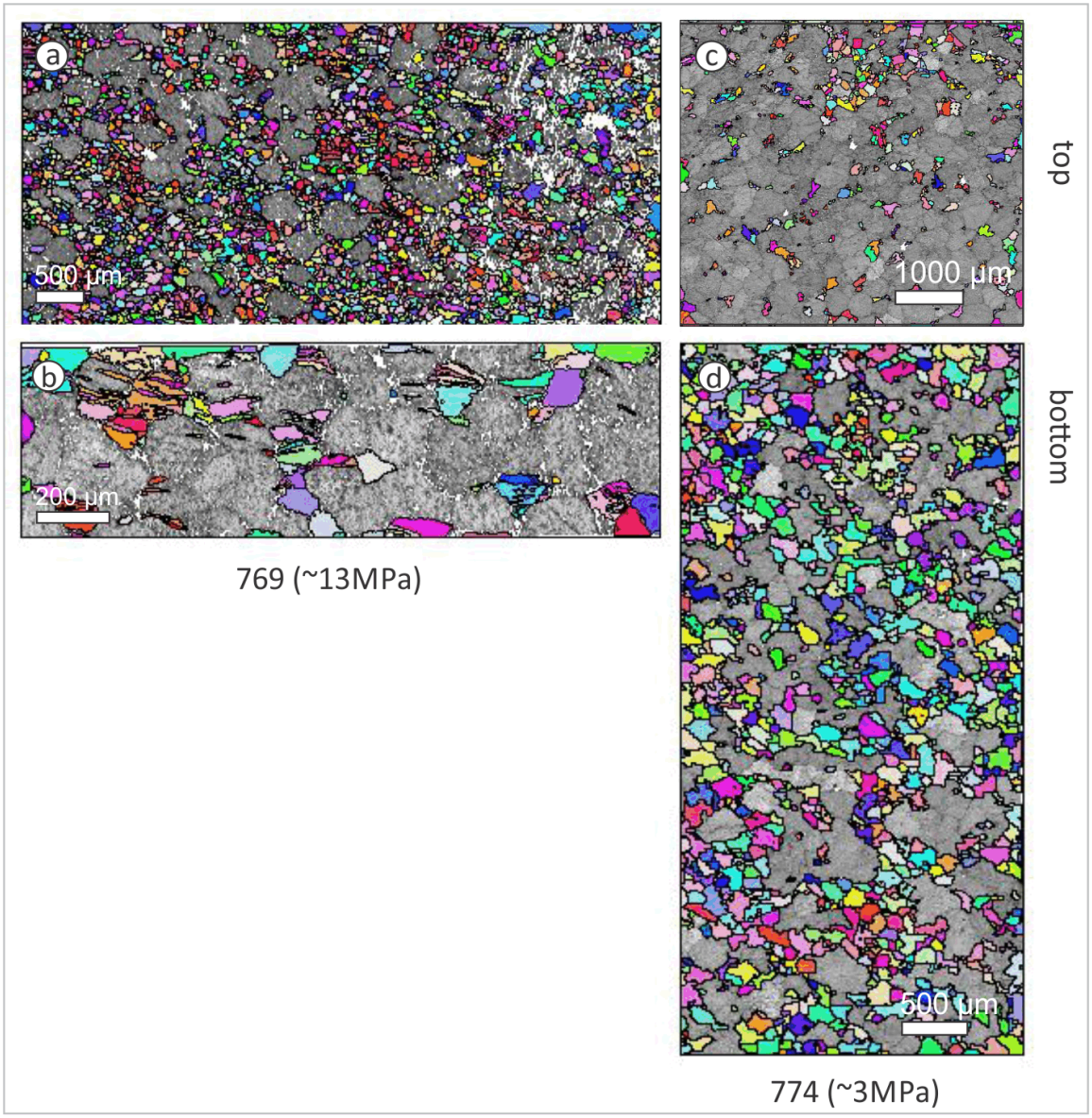

Figure 4.12: EBSD maps outlining grains below an area-equivalent grain diameter >200 μm.

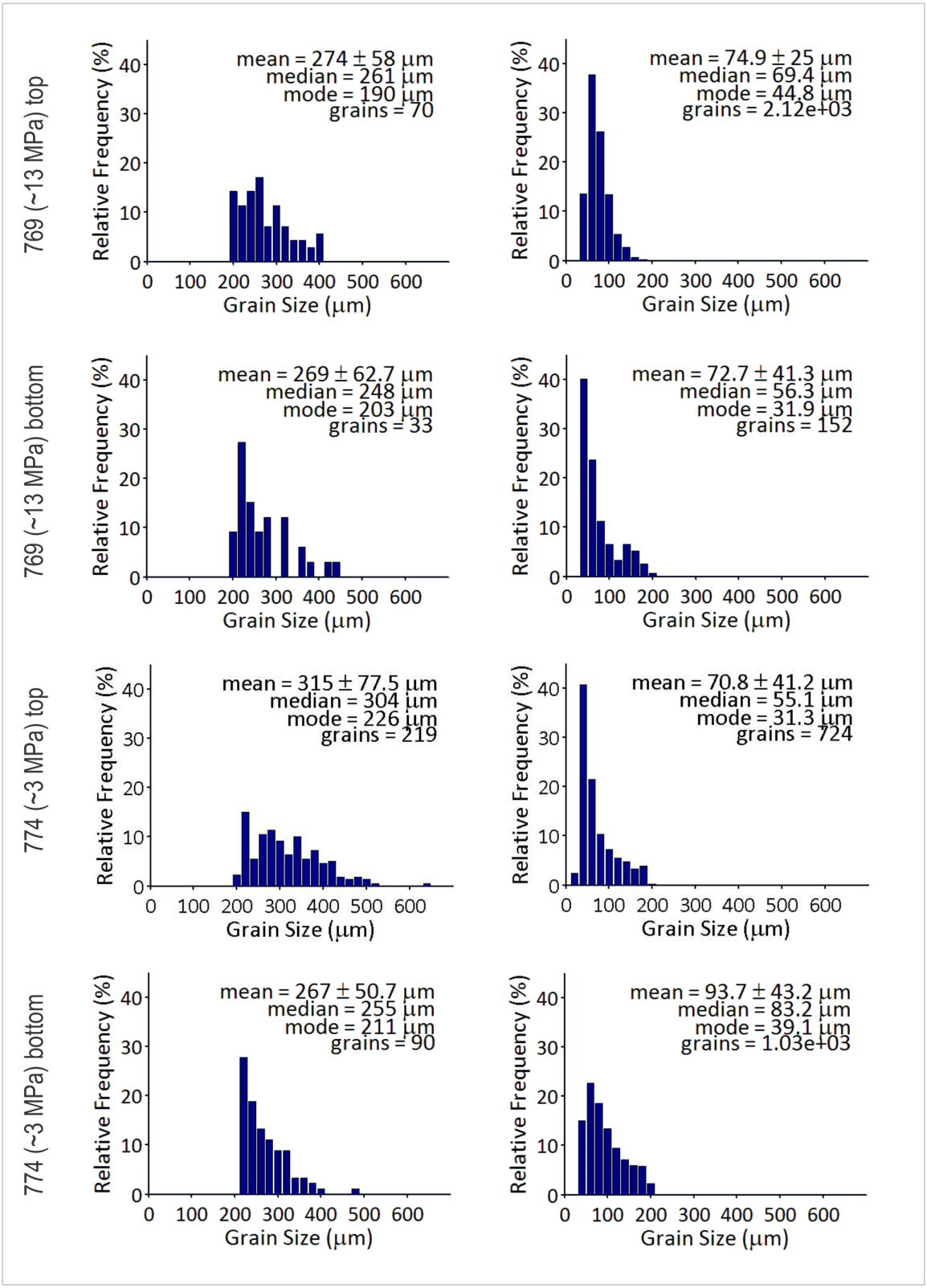

Figure 4.13: Grain size statistics for large (left histogram column) and small grains (right column) for EBSD maps in Fig 4.12. Arithmetic mean, standard deviation, median, mode and number of grains annotated in the top right corner of the histograms.

Chapter 5

The role of kink boundaries in the shear localisation of polycrystalline ice

Meike Seidemann[1], David J. Prior[1], Narayana Golding[2], William B. Durham[2], Kat Lilly [1], Matthew J. Vaughan[1]

[1]Department of Geology, University of Otago, Dunedin, New Zealand

[2]Department of Earth, Atmospheric and Planetary Sciences, Massachusetts Institute of Technology, MA, USA

Abstract

Shear localisation still poses a major obstacle to our understanding of the deformation of rocks. Here, strain localisation and shear zone development are studied via constant stress creep experiments on 25.4 mm diameter cylinders of polycrystalline ice at a temperature of 240 K, 50 MPa confining pressure and axial stresses of ∼13 and ∼3 MPa, respectively. Identical microstructural properties of recrystallised grains and kinked remnant grains surrounding shear zones suggest a grain size reduction by kinking. On a grain-scale, kinks boundaries with misorientations between 2-80° are tilt boundaries created by basal slip on two a-axes. General kink boundaries (>10° misorientations) are composed of basal dislocations and induce strong stress and strain heterogeneities, as visible in secondary kinks in neighbouring grains and non-basal dislocations adjacent to kink boundaries. On an aggregate level, strain is primarily accommodated by low angle kinking (<10°) in remnant grains at the rim of the shear zone and general kinking (>10°) between recrystallised grains. Basal slip on two a-axes, with a preferred <21-30> slip direction, dominates and

is locally supplemented by non-basal dislocations.

5.1 Introduction

Shear localisation is an important process in metals and rocks, including polycrystalline ice. However, the microstructural mechanisms responsible for shear zone formation are not fully understood. High-temperature rock deformation studies are often associated with relatively small samples as high stresses are required and high confining pressures are needed to prevent sample cracking. Deformation experiments on polycrystalline ice at comparable homologous temperatures require significantly lower stresses and confining pressures, and thus provide the opportunity to study localisation behaviour in rocks at a larger scale. High-homologous temperatures in ice experiments do not entail the significant engineering problems associated with deformation at high-homologous temperatures for most other rocks.

The deformation of polycrystalline ice is in many cases an analogue to the deformation of quartz (i.e. Wilson 2014). At high-homologous temperature, both ice and quartz show a similar recrystallisation behaviour with a tendency to accommodate strain primarily by subgrain rotation recrystallisation and grain boundary migration recrystallisation with new grain nucleation (i.e. Stipp *et al.*, 2001; Schulson, 2002; Faria *et al.*, 2014). What is more, ice and quartz share a similar crystal symmetry and slip on a single crystal level occurs mostly in the basal plane, although also combinations of basal and prismatic slip have been reported at high-homologous temperature for both materials (Hirth and Tullis, 1992; Wei and Dempsey, 1994).

With respect to shear localisation, ice and quartz both exhibit the ability to form shear zones governed by equant-shaped grains and a drastically reduced grain size (i.e. Schulson, 2002; Vernooij *et al.*, 2006). Sample-scale shear zones resulting from fully ductile failure (so termed plastic faulting or P-faulting) in the high-temperature deformation of polycrystalline ice have been associated with high confinement conditions (confining pressure $\gg$ axial stress) and shear heating as a major softening mechanism (Golding *et al.*, 2010, 2012). On the other hand, shear localisation in high-temperature plane strain studies on polycrystalline ice with inclusions has been found to coincide with deformation kinking (Mansuy *et al.*, 2000, 2002). The spatial link between ice shear zones (or localisation bands) and kinking has also been inferred from modelling results (Lebensohn *et al.*, 2009; Montagnat *et al.*, 2011; Grennerat *et al.*, 2012). Mansuy *et al.* (2000) propose that stable kink bands occurring parallel to the basal plane can lead to the development of shear

zones.

Kinking is a process that leads to the creation of new high angle grain boundaries within existing grains by sharp bending of the crystal lattice. Deformation kinking is similar to deformation twinning, except that kinking can extend over a range of crystallographic planes and rotation angles (Passchier and Trouw, 2005, Fig. 5.1a). Only a limited amount of strain can be accommodated with deformation twinning as slip happens solely across particular lattice planes in specific directions, which results in a specific geometric relationship and rotation angle for a given mineral (Fig. 5.1b).

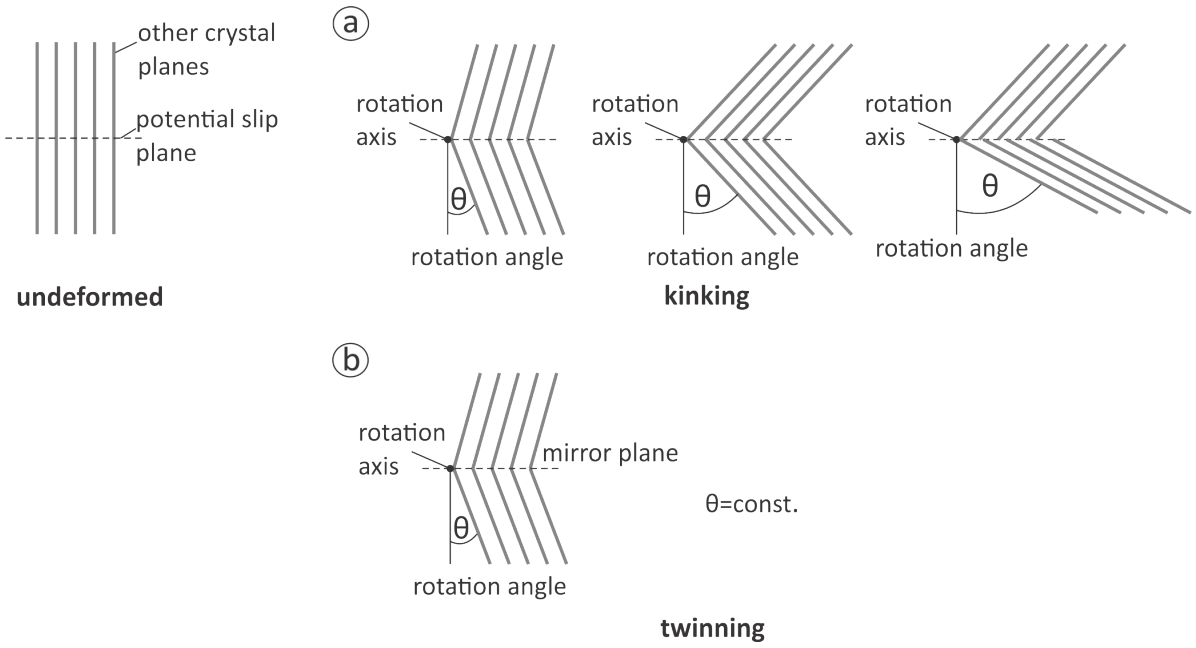

Figure 5.1: Schematic diagram illustrating the difference between kinking and twinning. a) Kinking possesses a larger degree of freedom: several slip systems with a variety of slip planes and dislocation types can participate causing a variety of rotation angles. b) Twinning is accommodated by a single slip system, which results in a constant maximum rotation angle.

The primary identifying feature of kinking (or kink band boundaries) are the kink bands, the domains between two kink boundaries, which often crosscut the parent grain with alternating orientations. Kinking predominantly occurs in materials with one dominant easy-slip system and has been repeatedly observed during the high-temperature (>-15°C) creep of polycrystalline ice (Wilson *et al.*, 1986; Manley and Schulson, 1997; Mansuy *et al.*, 2000, 2002; Montagnat *et al.*, 2011, 2015; Piazolo *et al.*, 2015). Efforts to constrain the microstructural processes behind kinking have been made (Wilson *et al.*, 1986; Piazolo *et al.*, 2008; Montagnat *et al.*, 2011, 2015; Piazolo *et al.*, 2015). How-

ever, observations of kinking are so far limited to experimentally deformed ice at high temperatures, where kinking coincides and may be partially overprinted by dynamic recrystallisation (i.e. Wilson *et al.*, 1986; Montagnat *et al.*, 2011) or, to prevent dynamic recrystallisation, limited to low strains of 1-2 %. In addition to that, trace analyses allowing for a deduction of prominent slip systems have been limited to low strains and mostly, low angle (<10°) misorientations.

In this contribution, the role of kinking in the development of shear localisation in polycrystalline ice deformed at high pressures (50 MPa confining pressure) and relatively low-homologous temperature (T=240 K) is investigated. Deformed samples at axial loads of 13 and 3 MPa showing significant macroscopic strain localisation are selected for electron backscatter diffraction (EBSD) mapping and analysis. EBSD maps are then employed to describe the microstructures associated with the macroscopic shear zones.

5.2 Method

5.2.1 Sample preparation, experimental procedure and EBSD imaging

Cylinders of fine-grained polycrystalline 'Standard ice' were fabricated in the laboratory, deformed in an triaxial apparatus adapted for ice experiments and subsequently imaged with cryo-EBSD. Details on sample fabrication, experimental procedure and EBSD mapping can be found in sections 4.2.1 and 4.2.2.

5.2.2 EBSD data processing

EBSD data were processed with Oxford Instruments Channel 5 software by Oxford Instruments. A minimum misorientation value of 10° was chosen as a threshold to distinguish subgrains from grains. Non-indexed pixels were removed and filled with neighbouring values using a 'wild spikes' extrapolation and a neighbour-pair interpolation in the noise reduction tab. Misorientation profiles and single grain subsets were defined in Channel 5's map module Tango. The thus collected orientation data was plotted in the Mambo module in a pole figure (PF) or inverse pole figure (IPF) reference frame. Geometrically necessary dislocation (GND), internal misorientation maps and contoured CPOs were calculated and plotted in the MTEX 4.0.12 texture analysis toolbox within a Matlab 2013a environment (Bachmann *et al.*, 2010), using the same minimum misorientation angle of 10° for grain definition.

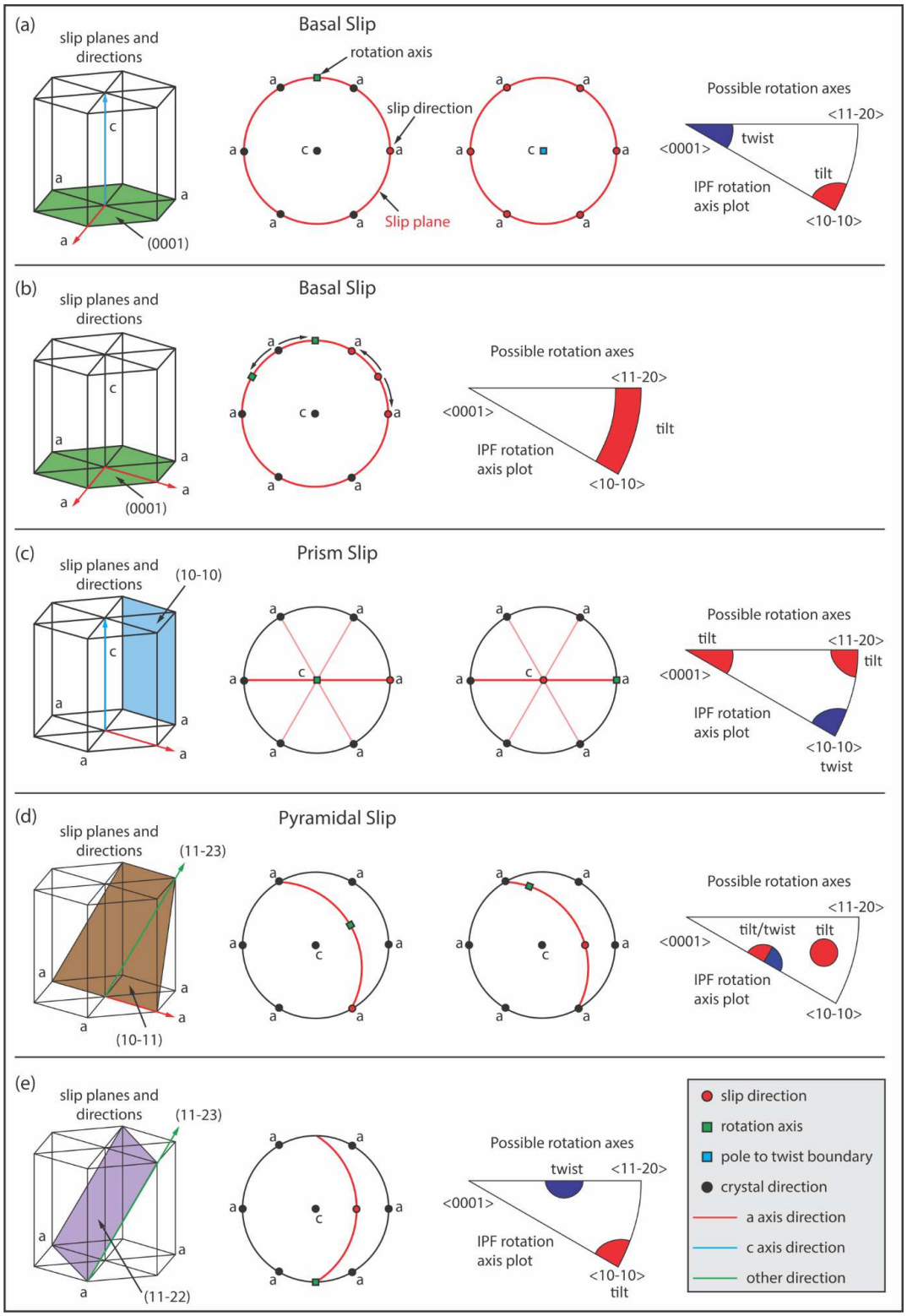

Figure 5.2: Predictions of slip systems and their respective rotation axes for polycrystalline ice (Vaughan, 2016). The slip plane and possible slip directions are shown on the left. The middle shows the slip direction, rotation axis and slip plane in a stereographic projection (upper hemisphere pole figure). IPFs on the right show possible rotation axis and whether the respective rotation axis corresponds to a tilt or a twist boundary.

5.2.3 Rotation axes analysis in IPFs and boundary maps

A combination of misorientation axes distributions in IPFs for single kinked grains, trace analyses for selected grain boundaries, and misorientation axes distributions in overall maps were employed to constrain the slip systems responsible for kinking on a grain- and sample-scale (sections 5.3.4, 5.3.5). Misorientation axes distributions alone can be ambiguous, as more than one slip system can generate the same rotation axis (Fig. 5.2). Trace analyses provide additional information on the dislocation type to better constrain slip systems. Another complication of a misorientation axes are their erroneous nature for small datasets below 5° misorientation (Prior, 1999). Hence, grain boundaries with differing misorientations were selected for the trace analyses. For the misorientation axes distributions displayed in IPFs, It was also ensured that the rotation axes for values below 5° matched the higher misorientation values (5-10°) for the low angle range (2-10°) (Table 5.1).

Table 5.1: Boundary classification scheme.

Boundary type	grain boundary	kink boundary
low angle (2-10°)	all within misorientation range (excluding kink boundaries)	straight, rotation axis in basal plane
general (10-90°)	all within misorientation range (excluding kink boundaries)	straight, rotation axis in basal plane
high angle (50-70°)	none, see general grain boundaries	straight, rotation axis in basal plane

5.3 Results

5.3.1 Mechanical data

The mechanical responses of samples 769 and 774 are given in stress vs. engineering strain curves and strain rate vs. strain curves (Fig. 5.3) and described in detail in sections 4.3.1 and 4.3.3.

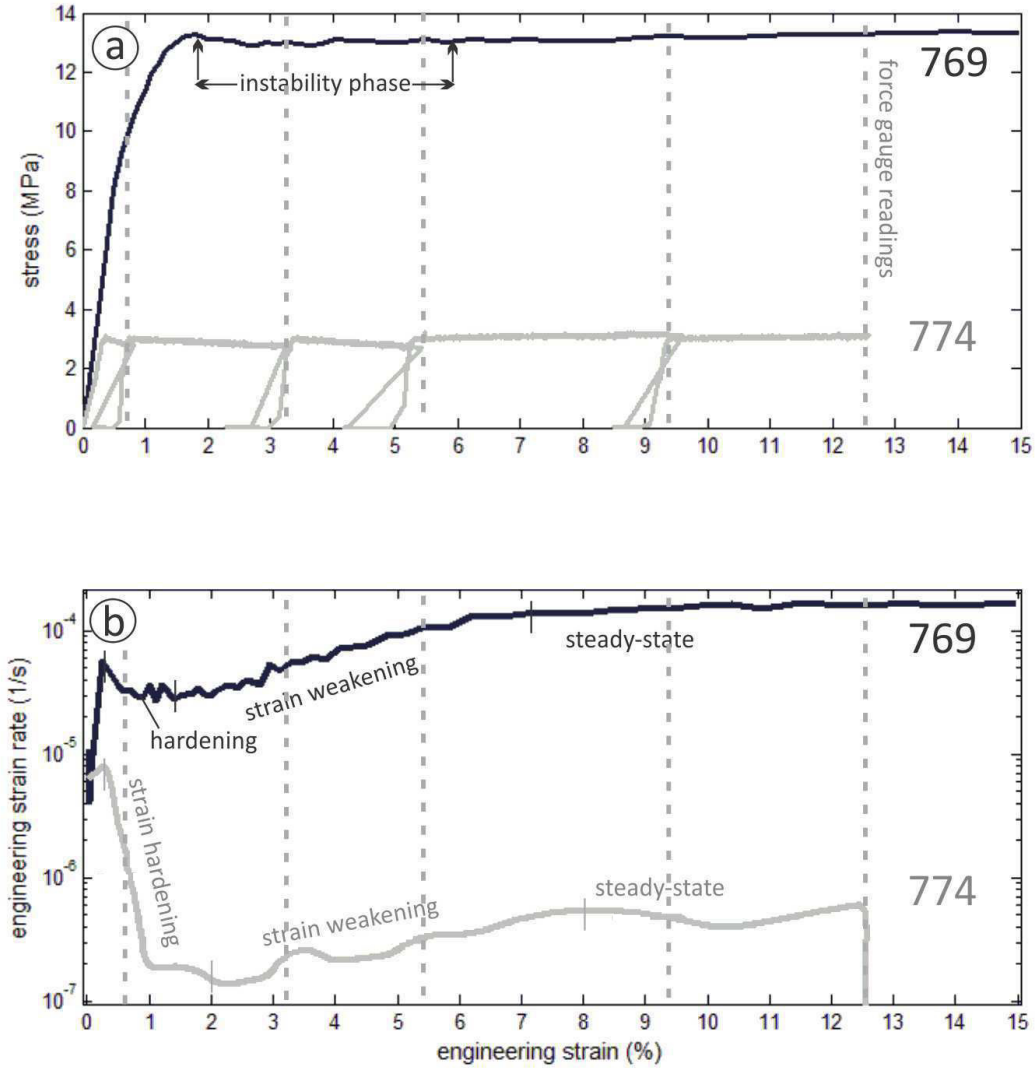

Figure 5.3: Stress-strain (top) and strain rate-strain curves (bottom) for experiments 769 and 774. Stress was calculated by dynamically correcting for an increase in area with shortening using a constant volume assumption (Stern *et al.*, 1997). Zero readings to correct for force gauge drift were performed before loading and after unloading in experiment 769. Additional force gauge readings were taken for calibration purposes every 48 hours for experiment 774 (indicated by grey dotted lines in the plots). Points of inflection in the strain rate curves are labelled with thin horizontal lines.

5.3.2 Macroscopic strain distributions

Pictures of the sample assemblies of ice 769 and 774 taken post-deformation show a high degree of strain heterogeneity. In ice 769, the bulk strain concentrates in a convexly shaped bulge with a maximum diameter of 30 mm, taking up the top 26-34 mm of the sample (Fig. 5.4a). Small, horizontally elongated bumps are visible on the surface of the jacket where bulging is observed. The bumps long axes lengths are 8 mm by ∼3 mm and are mostly oriented at an angle of ∼60-80° to the macroscopic shortening orientation. The connection of several single segments can give the bumps a worm-shaped appearance with cumulative lengths of up to 10 mm. A buckle oriented at an approximate angle of 70° separates the bumpy, bulged top from the bottom of the sample. Buckling commonly occurs in experiments with axial loads of >8 MPa under the given temperature and confining pressure conditions (unpublished sample catalogue W.B Durham, Appendix B Fig. B.2) and is associated with piston misalignment. In the absence of bumps and bulging, the bottom of the sample looks less deformed than the top.

The strain distribution in sample 774 is also heterogeneous (Fig. 5.4b). The bulk strain was accommodated by uniform thickening with a diameter of 28 mm in the bottom 24 mm of the sample. The thickened part reveals lens-shaped bumps on the surface of the jacket, with maximum lengths below 5 mm and widths below 2 mm. A transition zone in the centre of the sample connects the bottom to the straight, even top part of the sample. Prominent bumps, twice as thick, wide and long as in the bottom of the sample are found exclusively in the transition zone.

5.3.3 Microstructures

EBSD maps were collected as partial cross-sections in the centre of each sample (Fig. 5.5). The maps were taken from the transition from a narrow to a wide diameter in both samples (see Fig. 5.5 legends).

Grains in the microstructure of sample 769 are mostly small grains (<100 μm) with equant or elongated angular grain shapes (Fig. 5.5a). These have grain sizes smaller than the starting grain size and are reasonably interpreted as recrystallised grains. A few large grains (grain diameters of around 250 μm) with equant grain shapes and mostly straight grain boundaries are scattered within the recrystallised grains. The size and shape indicate that the large grains are remnant grains preserved from the original microstructure of the starting material.

Remnant grains show a strong (4.5) two cone c-axis CPO with maxima at 40° (top) and

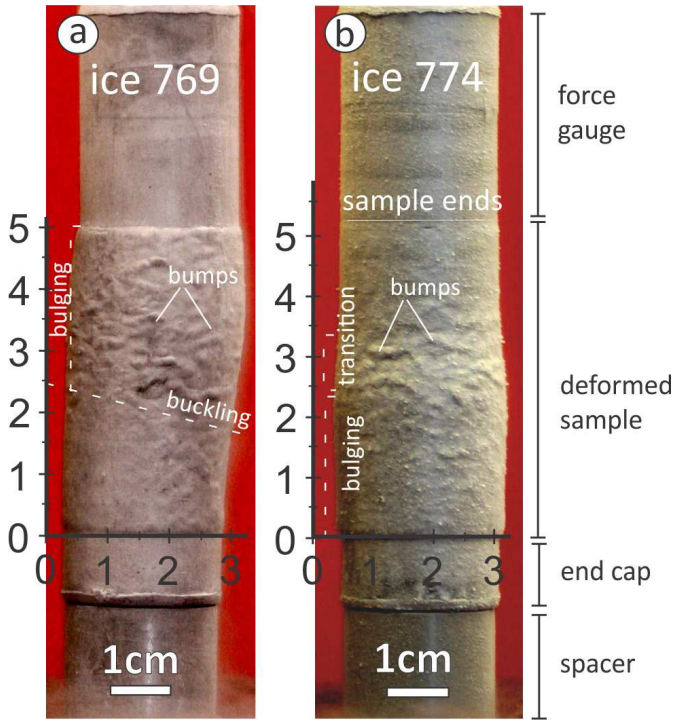

Figure 5.4: Deformed sample assemblies of ice 769 (a) and 774 (b), coated in grey indium jackets. Units are given in x10 mm. Sample 769 is characterised by a buckle across the centre of the sample, whereas the top is asymmetrically bulging outwards. Bulging continues with less displacement to the bottom of the sample. Small bumps on the surface of the jacket are found above the buckle. Sample 774 bulged in the bottom part but the top has the same straight rims as found in undeformed samples. The most prominent bumps on the indium jacket are concentrated in the middle of ice 774 (transition), where the extent of bulging decreases with distance from the bottom.

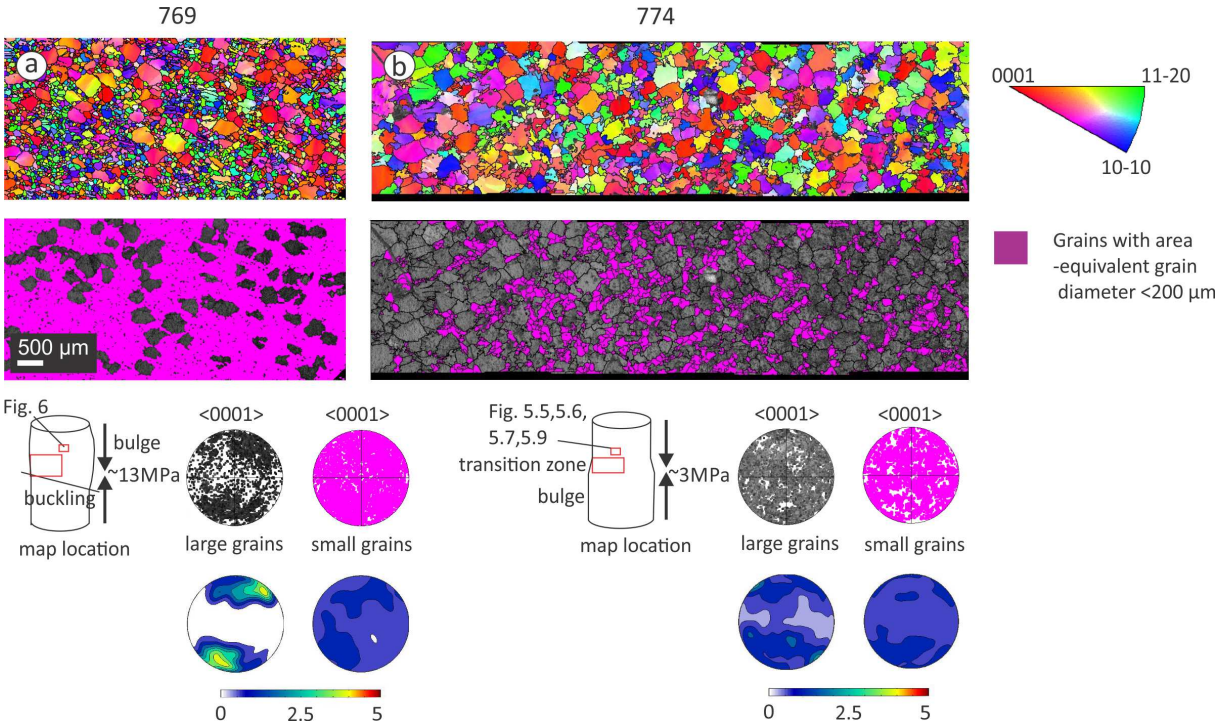

Figure 5.5: EBSD orientation maps of samples 769 (a) and 774 (b) were colour-coded according to the shortening direction (top). Mapping yielded respective indexing values of 62.4 % (a) and 69.3 % (b) at a step size of 10 μm. Area-equivalent grain diameters below 200 μm are shown on pattern quality maps to highlight the distribution of recrystallised grains (bottom). C-axes CPOs for large and small grains are shown on equal-area, upper hemisphere projections below. Contouring was performed in MTEX 4.0.12 with a 10° halfwidth. The maps of both samples were taken from the transition between narrow and wide sample diameters (big red rectangles in legends, 10 μm step size). Additionally labelled are the locations of the more detailed maps employed for Fig. 5.6, 5.7, 5.9 and 5.11.

20° to bulk shortening at the bottom. Conversely, the c-axis CPO of the recrystallised grains is almost random with only a slight preference of c-axis orientations clustering around the maxima of the remnant grain orientations.

The microstructure of sample 774 also shows a bimodal grain size distribution (Fig. 5.5b). Large (250 μm) remnant grains with straight or slightly curved grain boundaries make up the majority of the microstructure. These grains are mainly free of internal misorientation, except for one orientation (blue-violet), where irregular, curved low angle boundaries are observed. Some of the remnant grains are intersected by bands of small (25-50 μm) grains with angular grain shapes. These are reasonably interpreted as recrystallised grains. The bands are homogeneously distributed over the entire map area.

Bands are usually 1-2 grains wide and up to 10 times as long. Their long-axis is usually oriented at a 60° angle to the bulk shortening direction.

The c-axis CPO of the remnant grains is a weak (2.5) double cone with maxima at an angle of 40° to bulk shortening. Recrystallised grains show a randomised c-axis CPO (<1 on the CPO strength scale), although a slight orientation preference (+0.5 CPO strength) can be detected where maxima in the remnant grain CPO are found.

One band of recrystallised grains in ice 774 was chosen for further analysis. The band is located in an approximate angle of 60° to the bulk shortening orientation (Fig. 5.6). The definition of the rims of the band is somewhat arbitrary. The main identifier for recrystallised grains within the band was the reduced grain size from the starting material.

Recrystallised grains within the band show no obvious preferred orientation, although there are several examples of neighbouring grains with similar orientations (e.g. similar IPF colours in Fig. 5.6a). Grain boundaries between recrystallised grains mostly have misorientations of 10-80° and are remarkably straight (Fig. 5.6a,b). The misorientation patterns of the two transects are similar, with high angle grain boundaries between 10 and 50° misorientations (Fig. 5.6a). Small misorientations of below 5° are however only found in the profile parallel to the band.

Kinked grains and grains with a high number of subgrains are found in close proximity to the margin of the band of recrystallised grains. In contrast to that, the small recrystallised grains within the band (<125 μm) are distortion-free (Fig. 5.6d,e). Recrystallised grains with grain diameters of 125-200 μm within the band have straight subgrain boundaries. Internal misorientation values are not as high as in the remnant grains imminently surrounding the band, though (Fig. 5.6d). Generally, the amount of distortion decreases with recrystallised grain size over the entire map. Highest distortions are found in the large remnant grains directly adjacent to recrystallised grains.

5.3.4 The kinking mechanism in single grains

Single kinked grains are investigated in detail to investigate the mechanism that leads to the formation of straight high angle grain boundaries. Kink boundaries, per definition, were identified by straight grain boundaries and a rotation axis in the basal plane (see legend Fig. 5.7). We differentiate between low angle boundaries or low angle kink boundaries (2-10° misorientation), high angle kink boundaries in a misorientation range that appears characteristic in sample 769 (50-70°, Fig. 6b,c,7b) and general kink boundaries (10-90°) (Table 5.1).

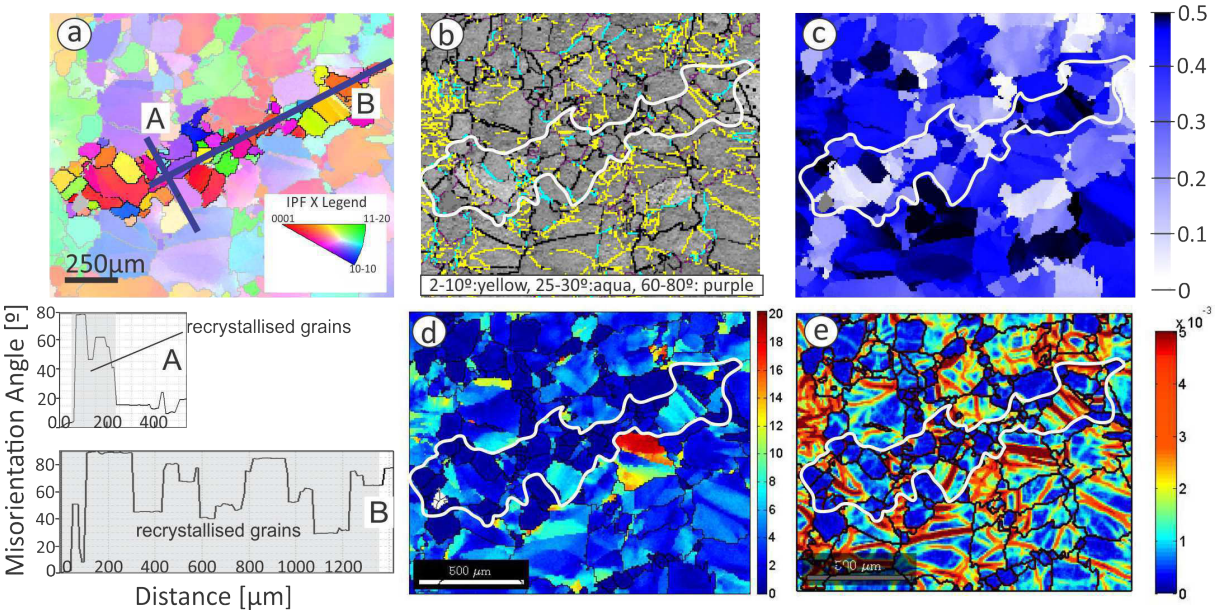

Figure 5.6: Microstructural properties of a band of recrystallised grains and surrounding remnant grains in sample 774. a) EBSD orientation map (legend and location in samples, see the small rectangle in Fig. 5.5) with misorientation profiles below. The band of recrystallised grains is highlighted in grey in the transects. b) Selected grain boundary misorientations are superimposed on a pattern quality map. c) Schmid factor map showing the amount of critical resolved shear stress (CRSS) on ice's most prominent (0001) <11-20> slip system per grain. d) Internal (within 1 grain) misorientation map showing kinked grains with misorientation gradients changing in straight lines and e) geometrically necessary dislocation (GND) map generated with MTEX 4.0.12.

Ice 769

The grain selected for the detailed analysis from sample 769 (Fig. 5.7a-f) has three distinctive (blue) kink bands and represents kinking under higher stress conditions. The kinked grain was extracted from a detailed EBSD map (2 μm step size), slightly above the overview map (Fig. 5.5a).

Most distinctive within this grain are two alternate kink orientations, separated by straight, high angle (50-65°) kink band boundaries (Fig. 5.7a,b Profile A). The orientation of the kink band boundaries is perpendicular or semi-perpendicular to the bulk shortening orientation. Along the kink bands, a gradual change in orientation can be observed (Fig. 5.7b, Profile B). The misorientation angle distribution shows peaks in the neighbour-pair over the random-pair distribution and theoretical curve (black line) for misorientation angles between 3-10° and 50-65°. The peaks in the neighbour-pair misorientation dis-

tribution correspond to subgrain boundaries along the kink bands and high angle kink boundaries, respectively (Fig. 5.7c,d). Short low angle kink boundaries, oriented parallel to bulk shortening, coincide with lattice bending across the long axis of the kink segments (Fig. 5.7c Profile B,d). Kink bands are surrounded by general kink boundaries (>10°), the majority of them in the high angle domain (50-70°) (Fig. 5.7d). The high angle kink boundaries have preferred <21-30> and <11-20> rotation axes.

The kinked grain displays a CPO (Fig. 5.7e). The two main c-axes orientations corresponding to the kink bands and non-kinked areas cluster approximately 80° degrees and 135° to the bulk shortening directions (Fig. 5.7e). The pole figures also reveal possible rotation axes that can lead to a boundary model for kink boundaries. Dispersion around the a-axes <11-20> and m-axes <10-10> can be traced to a single <21-30> rotation axis in the top of the a- and m-axes pole figure (Fig. 5.7e). A trace analysis was performed to constrain the boundary type (i.e. Prior *et al.*, 2002; Piazolo *et al.*, 2008). A tilt wall boundary can be reconstructed (black great circle) for a short straight segment of high angle kink boundaries. The potential Burgers or slip vector for a tilt solution is found in the plane perpendicular to the rotation axis (see Fig. 5.8a for an explanation), yielding a potential Burgers vector of <10-10> for the pink grain areas and <11-20> for the blue kink bands. A twist solution is unlikely as the plane perpendicular to the rotation axis (blue great circle) does not align with the boundary trace (Fig. 5.7f, Fig. 5.8b).

Slip systems and boundary misorientations were constrained for two additional grains in sample 769. A blue grain shows several general kink boundaries, inclined to bulk shortening, with misorientations between 15-30° (Fig. 5.9a). A trace analysis for a selected kink boundary gives a <10-10> rotation axis and a probable <11-20> Burgers vector (if the Burgers vector is perpendicular to the rotation axis, meaning no subsequent deformation occured) for a tilt solution. A violet grain with three kink bands and low angle (2-10°) and high angle kink boundaries (50-70°, Fig. 5.9b) contains a high angle kink boundary with a rotation axis in the basal plane (<11-20>) and a probable Burgers vector in the basal plane, 90° from the rotation axis (<10-10>).

Ice 774

Kink bands with alternating orientations were absent in grains in sample 774 but many grains have remarkably straight boundaries, which are inclined with respect to bulk shortening and may represent kinking under low axial stress conditions. A detailed analysis of a single grain from sample 774 showed several straight, inclined grain boundaries with misorientations between 2-15° and approximately 52° (Fig. 5.7g,h, Profiles A,B). In the mis-

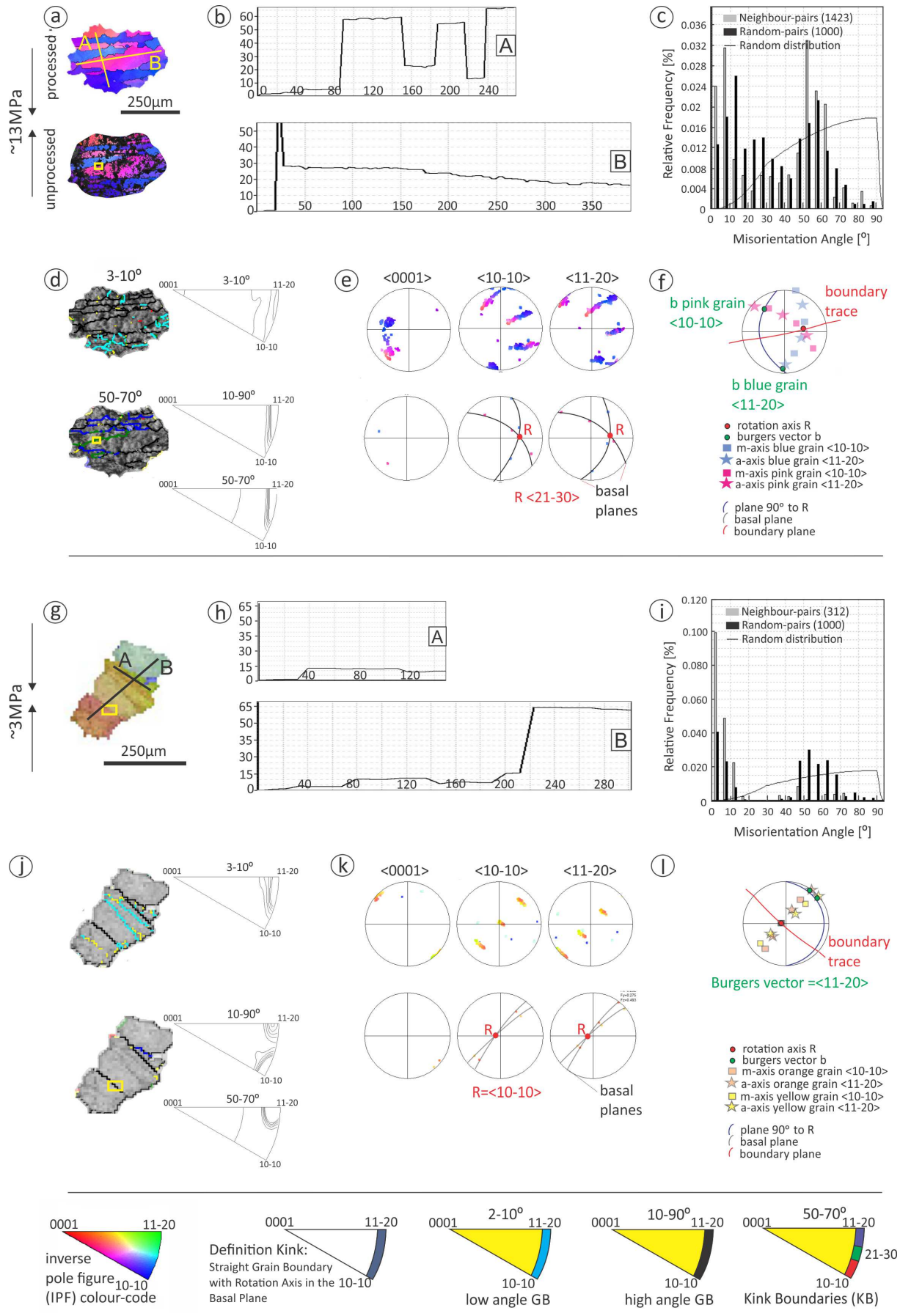
~13MPa
processed
unprocessed
250µm
A
B
Neighbour-pairs (1423)
Random-pairs (1000)
Random distribution
Relative Frequency [%]
Misorientation Angle [°]
3-10°
10-90°
50-70°
<0001>
<10-10>
<11-20>
R <21-30>
basal planes
b pink grain <10-10>
b blue grain <11-20>
boundary trace
rotation axis R
burgers vector b
m-axis blue grain <10-10>
a-axis blue grain <11-20>
m-axis pink grain <10-10>
a-axis pink grain <11-20>
plane 90° to R
basal plane
boundary plane
~3MPa
Neighbour-pairs (312)
R=<10-10>
Burgers vector =<11-20>
m-axis orange grain <10-10>
a-axis orange grain <11-20>
m-axis yellow grain <10-10>
a-axis yellow grain <11-20>
inverse pole figure (IPF) colour-code
Definition Kink:
Straight Grain Boundary with Rotation Axis in the Basal Plane
2-10°
low angle GB
high angle GB
21-30
Kink Boundaries (KB)

Figure 5.7: Detailed analysis of kinking in single grains deformed axial stresses of 13 MPa (sample 769, a-f) and 3 MPa (sample 774, g-l). a,g) EBSD orientation maps, colour-coded with respect to the shortening direction. b,h) Transects showing misorientations along (A) and perpendicular to the kink boundaries (B) (see a,g). c,i) Misorientation angle distributions. d,j) Boundary maps: grain boundaries were labelled according to their respective rotation axis (see legend). General boundaries (>10°) are displayed in black in the boundary map for misorientations of 2-10°. IPFs (right side) show the general rotation axes distribution for a given misorientation range. k,e) Pole figures (equal-area, upper hemisphere projections) display the CPO for the general grain (top) and for a selected boundary fragment (see yellow rectangles in a,d,g,j, bottom). f,l) Trace analyses.

orientation angles distributions, the neighbour-pair distribution displays matching peaks for misorientations of 2-10°, 10-15° and 45-50° (Fig. 5.7i). Rotation axes for all grain boundaries show strong clusters the basal plane (Fig. 5.7j) which identifies the grain boundaries as kink boundaries. There is no profound difference in orientation to bulk shortening between low angle and high angle kink boundaries. However, low angle kink boundaries have a preference towards <11-20> and <21-30> rotation axes, whereas general kink boundaries also have <10-10> rotation axes. For one general kink boundary with a <10-10> rotation axis (yellow rectangle), a trace analysis was performed. A probable Burgers vector for a tilt solution is <11-20>.

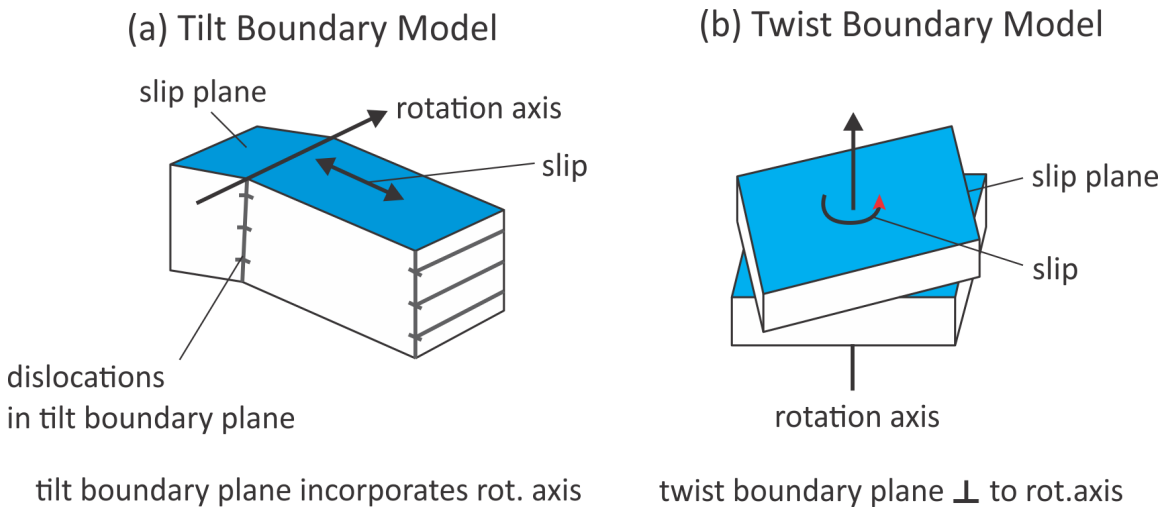

Figure 5.8: Illustration of a (a) tilt boundary model and (b) twist boundary model (modified after Prior *et al.*, 2002; Vaughan, 2016)

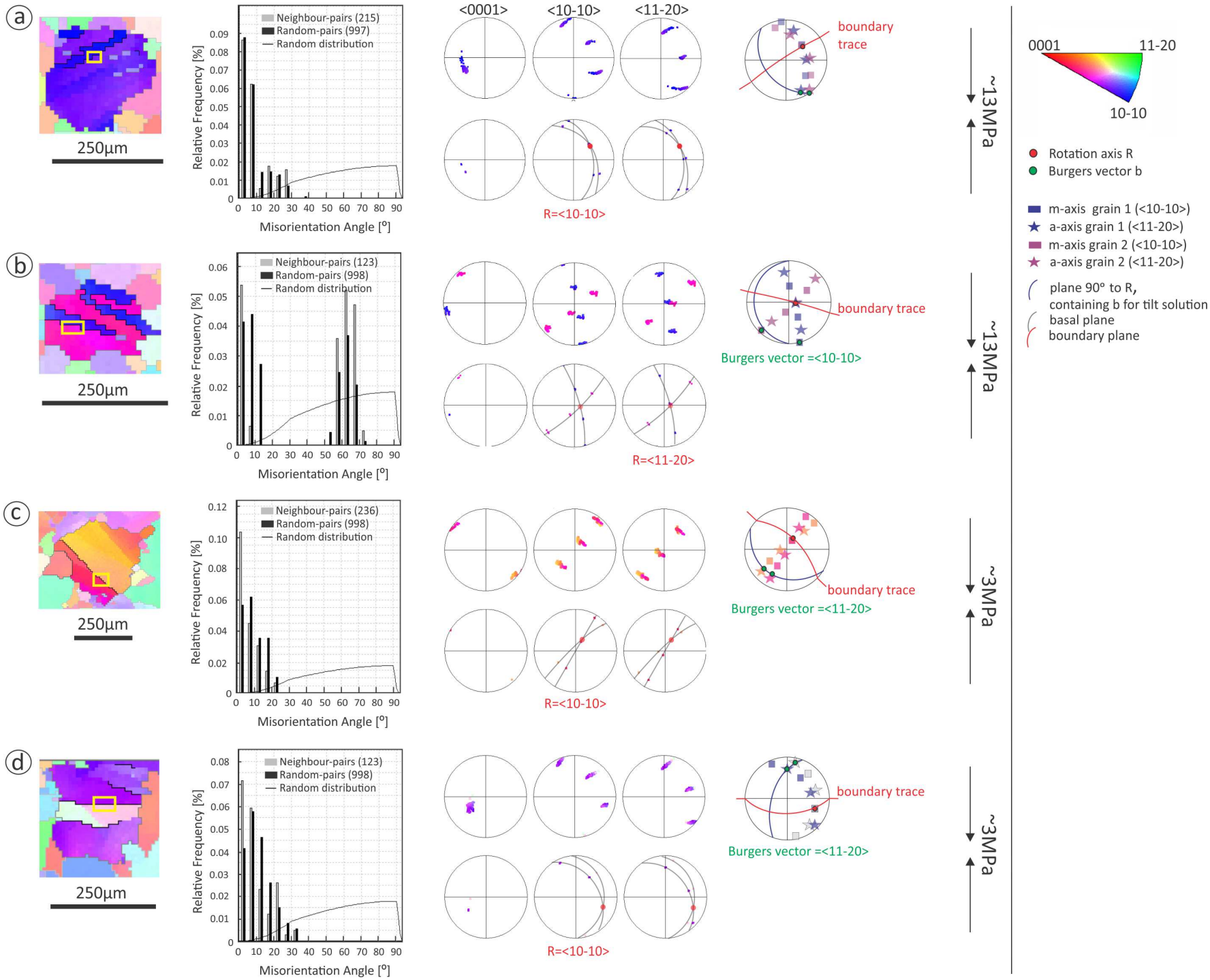
a
250µm
Neighbour-pairs (215)
Random-pairs (997)
Random distribution
Relative Frequency [%]
Misorientation Angle [°]
<0001>
<10-10>
<11-20>
R=<10-10>
boundary trace
~13MPa
b
250µm
Neighbour-pairs (123)
Random-pairs (998)
Random distribution
Relative Frequency [%]
Misorientation Angle [°]
R=<11-20>
boundary trace
Burgers vector =<10-10>
~13MPa
c
250µm
Neighbour-pairs (236)
Random-pairs (998)
Random distribution
Relative Frequency [%]
Misorientation Angle [°]
R=<10-10>
boundary trace
Burgers vector =<11-20>
~3MPa
d
250µm
Neighbour-pairs (123)
Random-pairs (998)
Random distribution
Relative Frequency [%]
Misorientation Angle [°]
R=<10-10>
boundary trace
Burgers vector =<11-20>
~3MPa
0001
11-20
10-10
Rotation axis R
Burgers vector b
m-axis grain 1 (<10-10>)
a-axis grain 1 (<11-20>)
m-axis grain 2 (<10-10>)
a-axis grain 2 (<11-20>)
plane 90° to R, containing b for tilt solution
basal plane
boundary plane

Figure 5.9: Slip systems and misorientation ranges for single kinked grains from samples 769 (a,b) and 774 (c,d). EBSD orientation maps on the far left were colour-coded with respect to the shortening direction. The yellow rectangles denote the boundary fragment selected for the trace analysis. Second from left are misorientation angles distributions for the selected grains. Rotation axes are plotted on equal-area, upper hemisphere projection and are shown for the entire grain (top row) and the selected boundary fragment, respectively (bottom row). At the far right schematic trace analyses for the boundary fragments are given.

Grain boundaries in two additional grains within sample 774 also qualify as kink boundaries (Fig. 5.9c,d). The trace analysis of a low angle (<10°) kink boundary (Fig. 5.9c) yielded a <10-10> rotation axis and <11-20> Burgers vector for a tilt solution. Because the boundary trace approximately aligns with the plane perpendicular to the rotation axis (blue great circle) a twist solution is also possible, but geometrically unlikely due to the combination of a very straight boundary and low misorientation. The second additional grain contains a general kink boundary (25-30° misorientation), oriented at an angle of 90° to bulk shortening, with a <10-10> rotation axis and a probable <11-20> Burgers vector for a tilt solution (Fig. 5.9d).

5.3.5 Kink boundary and boundary analysis for large-scale maps

Boundary maps highlighting respective rotation axes are employed to investigate how kinking may impact the deformation of the ice samples on an aggregate-level (Fig. 5.10c,d, 5.11c,d). We use the same classification system as for single kinked grains consisting of low angle (2-10°), general (10-90°) and high angle kink boundaries (50-70°, Table 5.1). For each boundary map, rotation axes were additionally plotted on IPFs to constrain the overall rotation axis distribution for a given misorientation margin (Fig. 5.10c,d,5.11c,d).

Ice 769

For analysis of sample 769, the map in Fig. 5.5a was employed (Fig. 5.10). The misorientation angle distribution shows a peak in the neighbour-pair over random-pair and theoretical distributions (black curve) for misorientations from 2-35° (Fig. 5.10b).

Low angle kinking in sample 769 is predominantly governed by a homogeneous distribution of rotation axes within the basal plane (Fig. 5.10c). Low angle kink boundaries are almost exclusively located in remnant grains and mostly show oblique orientations to bulk shortening. Shorter grain boundaries with rotation axes in the basal plane (yellow)

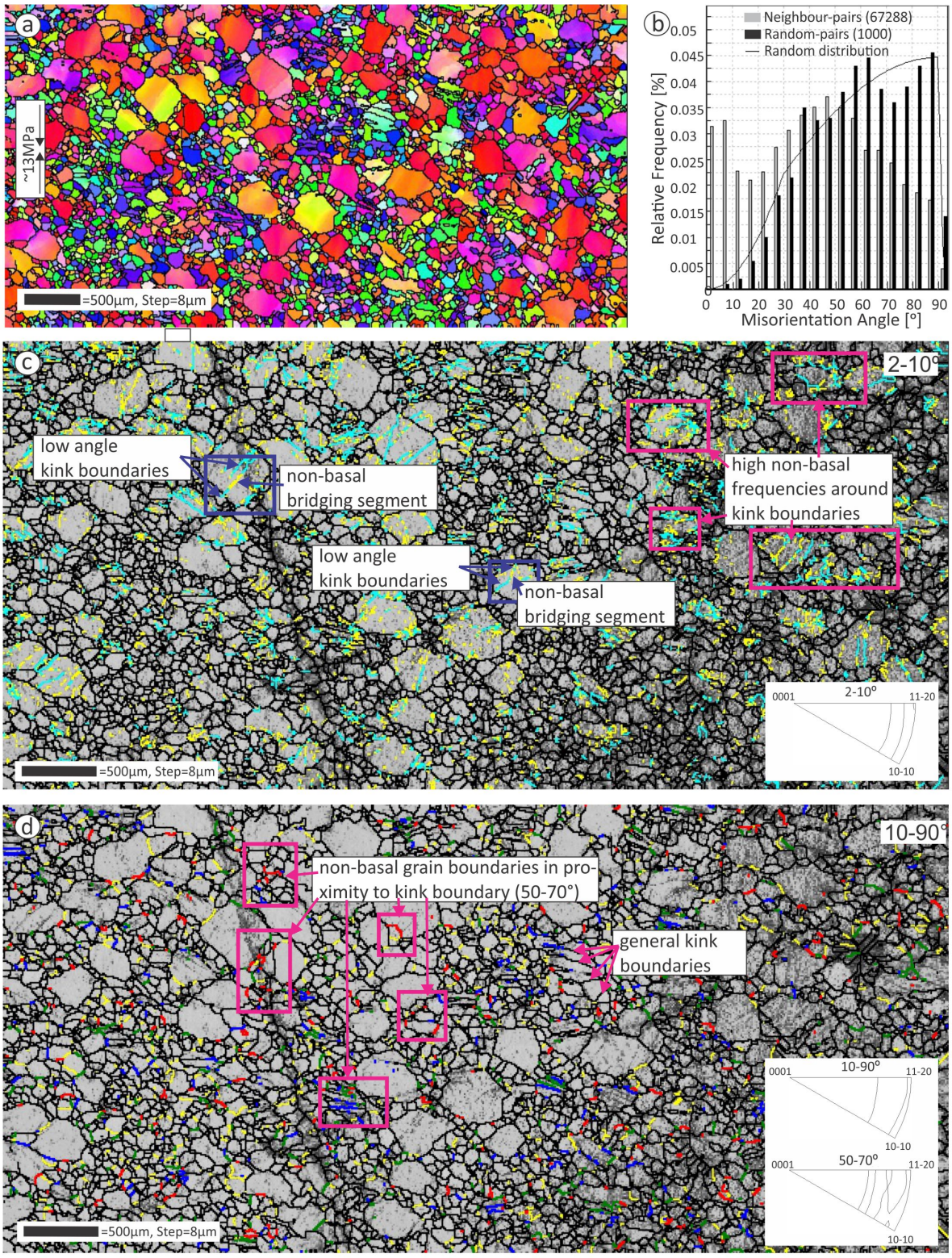
a
~13MPa
=500µm, Step=8µm
b
Neighbour-pairs (67288)
Random-pairs (1000)
Random distribution
Relative Frequency [%]
Misorientation Angle [°]
c
2-10°
low angle
kink boundaries
non-basal
bridging segment
high non-basal
frequencies around
kink boundaries
low angle
kink boundaries
non-basal
bridging segment
=500µm, Step=8µm
d
10-90°
non-basal grain boundaries in pro-
ximity to kink boundary (50-70°)
general kink
boundaries
=500µm, Step=8µm
Orientation map legend
inverse pole figure
colour-code (Y)
inverse pole figures
basal plane
Definition kink boundary:
straight grain boundary with
rotation axis in the basal (0001)
plane
Rotation axes of grain boundaries and inverse pole figures: c,d
low angle
grain boundaries
low angle
kink boundaries
general
grain boundaries
general
kink boundaries
high angle
grain boundaries
high angle
kink boundaries

Figure 5.10: Grain boundary analysis of sample 769. a) IPF orientation map colour-coded with respect to bulk shortening. b) Misorientation angle distribution for map in (a). c) Pattern quality (band contrast) map. Boundaries with basal rotation axes for misorientations from 2-10° are shown in light blue and non-basal rotation axes in yellow. Black lines denote all boundaries with misorientations >10°. d) Boundary map with non-basal rotation axes (yellow) and basal rotation axes (black) for misorientations for >10° on a pattern quality map. Superimposed are kink boundaries (fat) within a misorientation range of 50-70°, colour-coded according to their rotation axes. IPFs in the bottom left of the maps are equal-area, upper hemisphere projections.

are detected in high frequencies around low angle kink boundaries (pink rectangles) and sometimes act as bridging segments between the kink boundaries (blue rectangles). The rotation axes of the non-basal grain boundaries are just outside the basal plane (see IPF).

Nearly all general grain boundaries are kink boundaries with rotation axes in the basal plane (black) (Fig. 5.10d). Only a few, short grain boundaries with non-basal rotation axes (yellow) are located in close proximity (same grain or neighbouring grain) to high angle kink boundaries (50-70°, pink rectangles). For the high angle kink boundaries (50-70°), <11-20> (blue) and <21-30> (green) rotation axes are statistically preferred (see IPF). The cluster between the <11-20> and <10-10> axes outside of the basal plane matches the IPF signature of tilt boundaries created by pyramidal slip (Fig. 5.2d).

Ice 774

The selected map for sample 774 contains several clusters of recrystallised grains (Fig. 5.11a). The overall microstructure is the same as in Fig. 5.5b. The pattern quality for the map of sample 774 is higher as for ice 769 (Fig. 5.10), although the indexing rates are similar for both maps. The misorientation angle distribution shows a peak in the neighbour-pair over random-pair and theoretical curve for misorientation angles of 2-20° (Fig. 5.11b).

Kinking with low misorientation angles is mostly characterised by long straight boundaries with oblique to perpendicular orientations to bulk shortening (Fig. 5.11c). The kink boundaries primarily cross-cut remnant grains adjacent to recrystallised grains. Sometimes low angle kink boundaries found in remnant grains can also transect into larger (grain diameters >100 μm) recrystallised grains (blue rectangles). Within the population of remnant grains, kinks often cut through one grain and continue their path in a very similar (<5° different) orientation in an adjacent grain (pink rectangles). The rotation axes of these low angle kink boundaries lie within the basal plane (see IPF).

Low angle kink boundaries generally correlate with the presence of recrystallised grains. In the top of the map, where about 40% of the map consists of bands of recrystallised grains, low angle kink boundaries are detected in all remnant grains. At the bottom, fewer bands of recrystallised grains are found. Here, the presence of low angle kink boundaries in remnant grains decreases with distance from the recrystallised grains. In remnant grains imminently adjacent to the recrystallised bands, a grid of several low angle kink boundaries can often be found (green rectangles). Grains further away mostly show only one or two low angle kink boundaries with the same orientation. Remnant grains with more than two grain diameters distance from a band of recrystallised grains do not exhibit any low angle kink boundaries (black rectangles).

In areas of high kink densities (several low angle kink boundaries in one grain), short boundaries with rotation axes just outside of the basal plane (yellow) are detected. These non-basal rotation axes grain boundaries often prolong and connect low angle kink boundaries (cyan) to each other (red rectangle).

General kink boundaries with misorientations from 10 to 90° (black) make up over 90 % of all high angle grain boundaries within the map (Fig. 9d). Only a few long, straight grain boundaries with rotation axes outside of the basal plane (yellow) are found, often at a steep angle to bulk shortening (blue rectangles). The rotation axes of these grain boundaries mirror the outline of the basal plane but have a higher misorientation to the basal plane than the non-basal rotation axes in the low angle domain (2-10°) (Fig. 5.11c).

High angle kink boundaries (50-70°) are dominated by <10-10> rotation axes (IPF & map), although also <21-30> and <11-20> rotation axis high angle kink boundaries are detected within the map. Long high angle kinks are predominantly oriented at oblique angles to bulk shortening (pink rectangles). Comparatively short high angle grain boundaries are frequently found in proximity to general kink boundaries and can exhibit abrupt changes in orientation to bulk shortening, which can result in an overall zigzag shape (green rectangles). The non-basal rotation axes within a misorientation range of 50-70° show a cluster, as expected for tilt boundaries generated by pyramidal slip (Fig. 5.2d).

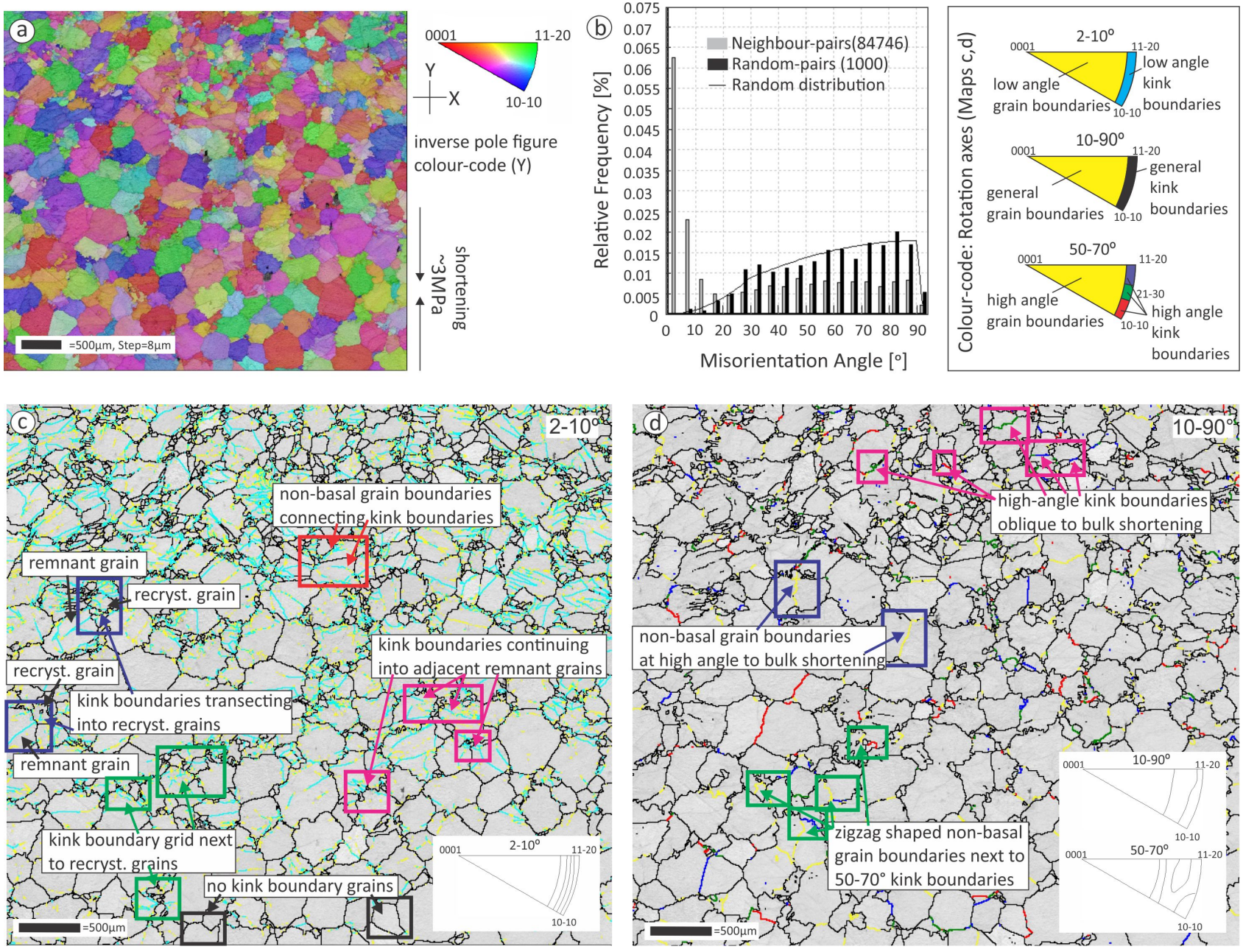

Figure 5.11: Boundary analysis of sample 774. See Fig. 5.10 for annotations.

5.4 Discussion

The rheological weakening during deformation, strain heterogeneity on the deformed samples' jackets coupled with bands of recrystallised grains in the microstructure can best be explained by shear zone formation. Similar ductile shear zones, oriented oblique to bulk shortening and high misorientation angles between recrystallised grains have been detected in an experimentally deformed single quartz crystal (Vernooij *et al.*, 2006). The process associated with the formation of the quartz shear zones is a cataclastic one, characterised by brittle fracturing along the rhomb planes. Subgrain boundary formation along these fractures and rotation lead to new, straight, high angle grain boundaries and thus, ultimately a local reduction in grain size. Grain boundary formation and a consequently occurring grain size reduction via (micro-) fracturing has also been explicitly and implicitly presented in previous contributions targeting other rocks and metals (Holden, 1961; Grosskreutz and Waldow, 1963; Aydin, 1978; Fitz Gerald and Stünitz, 1993; Bozkurt and Park, 1997). However, brittle fracture is assumed to be suppressed in this set of experiments, due to the high confining pressure (Karato, 2008). Instead, we propose that kinking could provide an analogue mechanism to (micro-) fracturing under fully ductile conditions, with the ability to create new grain boundaries with misorientations of 2-80° (observed within the shear zone in Fig. 5.6), locally reduce the grain size and ultimately result in the development of shear zones in polycrystalline ice.

5.4.1 Grain size reduction and shear zone formation by kinking

A local grain size reduction by kinking is likely in these samples. Microstructural evidence of kink boundaries is ample within single grains (Fig. 5.7,5.9), remnant grains around shear zones (Fig. 5.6a,b,d,e, 5.10c,d,5.11c,d) and between recrystallised grains (Fig. 5.10c,d,5.11c,d). The characteristic microstructural features of recrystallised grains within a shear zone in sample 774 (Fig. 5.6), including 1) angular grain shapes, 2) separation to surrounding grains by mostly general (10-90°) straight grain boundaries and 3) similar crystallographic orientations of neighbouring grains can be explained with grain boundary formation, and consequently grain fragmentation due to kinking. Large-scale maps with boundaries colour-coded according to their respective rotations axes (Fig. 5.10c,d,5.11c,d) demonstrate that over 90 % of grain boundaries in both have rotation axes in the basal plane and are most likely a result of deformation kinking. Kinking as a strong strain accommodation mechanism in the absence of dynamic recrystallisation has been inferred from modelling of columnar ice aggregates under high-temperature

compression creep (Lebensohn *et al.*, 2009; Grennerat *et al.*, 2012). In these models and our deformed samples, the favourably oriented grains for basal slip do not deform more than other grains as expected by other common dynamic recrystallisation-driven recovery mechanisms (i.e. during grain boundary migration) (Fig. 5.6c). Kinking as a primary grain size reduction mechanism could also explain why recrystallised grains <100 μm do not exhibit kink boundaries (Fig. 5.6,5.10c,d,5.11c,d). Studies on deformation twinning, a process very similar to deformation kinking (Fig. 5.1), have shown that twinning in metals and alloys first appears in large grains at a given stress and only affects smaller grain sizes if the overall stress is increased (Christian and Mahajan, 1995; Dobron *et al.*, 2011).

Small, equant-shaped grains with straight boundaries are microstructural indicators for grain size sensitive creep in the form of grain boundary sliding (GBS), as shown for low-temperature polycrystalline ice (Goldsby and Kohlstedt, 1997). Recrystallised grains presumably fragmented by kinking also show a randomised CPO (Fig. 5.5), as often associated with GBS (Bestmann and Prior, 2003; Prior and Bestmann, 2004; Warren and Hirth, 2006). However, these samples in this study do not exhibit quadruple grain junctions and grain flattening at high strains, which seem characteristic of low-temperature GBS creep in ice (Goldsby and Kohlstedt, 1997).

5.4.2 Deformation in single kinked grains

Deformation kinking

Previous analyses of kinking in polycrystalline ice have often focused on the orientation of kink boundaries to the main axis of compression (i.e. Wilson *et al.*, 1986) or crystallographic axes or planes within the kinked crystal (i.e. Piazolo *et al.*, 2015). The CPOs of the kink boundaries investigated within this study (Fig. 5.7e,k,5.9) support the general impression that kink boundaries in rocks develop semi-perpendicular to the basal plane (Starkey, 1968; Wilson *et al.*, 1986).

Our analysis based on the constraining of the potential slip systems with rotation axes reveals that all kink boundaries within single grains are, in fact, tilt boundaries generated by basal slip (Fig. 5.7,5.9). Rotation axes have successfully been employed to determine slip systems and dislocation types in other rocks (i.e. Prior *et al.*, 2002; Boyle *et al.*, 1998; Reddy *et al.*, 2007; Barrie *et al.*, 2008). Our results indicate, that kink boundaries are generated by a variety of rotation axes and Burgers vectors within the basal plane (Fig. 5.7,5.9). A variety of rotation axes within the basal plane are only possible if

crystal slip occurs on two coupled a-axes (Fig. 5.2). Within the low angle kink boundary range (2-10°, Fig. 5.9c), the determined a-rotation axis (<11-20>), tilt boundary model and interpretation of a possible coupled two a-axis slip match earlier results from trace analyses for low angle kinking (<10°) for ice deformed at higher temperatures (Piazolo *et al.*, 2008; Montagnat *et al.*, 2015). In addition to that, our results suggest a further analogy between quartz and polycrystalline ice: a study analysing and modelling kink bands in naturally deformed quartz has also concluded that kinking exclusively resulted from slip within the basal plane (Nishikawa and Takeshita, 1999).

Non-basal dislocations

Kink boundaries within single grains appear to be accompanied by short grain boundaries with rotation axes outside the basal plane (Fig. 5.7d,j). The rotation axes outside the basal plane (Fig. 5.2) and the short nature of the segments compared to kink boundaries created by basal dislocations (Shearwood and Worth, 1989; Shearwood and Whitworth, 1991; Hondoh *et al.*, 1990), suggest that these grain boundaries were created by non-basal slip systems. To accommodate locally increased stresses in strain localised regions, non-basal slip systems are often required (Montagnat *et al.*, 2011). The short boundaries with non-basal dislocations appear to prolong or connect existing kink boundaries (Fig. 5.7d,j). Our observation supports the findings of high-temperature creep studies in polycrystalline ice, indicating that even though kink formation is commenced by slip on the basal plane (Wilson *et al.*, 1986), well-defined kink boundaries may be linked to the activation of non-basal slip systems (Piazolo *et al.*, 2008; Montagnat *et al.*, 2011; Piazolo *et al.*, 2015).

5.4.3 Locking angles and spacing between kink boundaries

The misorientations of the kink boundaries investigated within this study appear to depend on the stress configuration. Previous work on kinking in multi-layered aggregates suggests that kink bands have a 'locking angle', which will not be exceeded for a given differential stress (Reches and Johnson, 1976; Johnson, 1977; Collier, 1978). A potential relationship between the maximum misorientation angle for a kink boundary and the differential stress may explain why maximum kink angles often amount up to 80° in sample 769 (Fig. 5.7a-d,5.9b) and mostly below 25° in sample 774 (Fig. 5.7h-j,5.9c,d). Another difference between kinking in the two samples investigated in this study is the width of the spacing between one kink boundary to the next: the spacing between kink boundaries in sample 769 is generally much narrower as in sample 774 (Fig. 5.9). Results from the

investigation and modelling of kink bands in naturally deformed quartz suggest that kink band width may also be related to the overall stress conditions (Nishikawa and Takeshita, 1999).

5.4.4 Kinking at a multiple grain level

Our results suggest that kinking with coupled basal slip on two a-axes predominantly accommodates deformation on a multiple grain-scale (Fig. 5.10c,d,5.11c,d). For both low and high misorientations and 3 MPa and 13 MPa axial stress, rotation axes in the basal plane are statistically preferred. This is consistent with crystal slip on two coupled a-axis in the basal plane (5.2b). To determine the preferred slip orientation, we calculated Schmid factor distributions for the large-scale kink maps in Fig. 5.10 and 5.11. The maximum Schmid factor (critical resolved shear stress accommodated by a specific slip system) is higher for (0001) <21-30> than for (0001) <11-20> and (0001) <10-10> (Fig. 5.12). The maximum amount of shear stress in both samples is thus accommodated by slip in the <21-30> direction, which is consistent with basal slip on two a-axes with odd components.

Kinking in polycrystalline ice appears to influence the local stress or strain field, as evidenced by the occurrence of non-basal dislocations adjacent (same grain or neighbouring grain) to kink boundaries (Fig. 5.10c,d,5.11c,d). A second indicator for stress or strain field modifications induced by kinking that reach beyond single grains may be the observation that kink boundaries often extend into neighbouring grains with little change in orientation. The extended stress or strain field impact of propagating kink bands has also recently been reported for a Cu-Nb nanolaminate (Nizolek *et al.*, 2017).

In sample 774, we observe that the non-basal dislocations are predominantly detected around the rims of shear zones (Fig. 5.11c,d). The occurrence of these non-basal dislocations is energetically less preferable than basal dislocations and hint at elevated stresses in and surrounding the shear zones (Chauve *et al.*, 2017). Their rotation axes are found close to the basal plane in the IPFs, indicating that pyramidal slip might have played a role (Fig. 5.2d). These results are in good agreement with fast Fourier transform modelling of columnar ice samples featuring kinking and high-strain localisation bands: the overall aggregate is dominated by basal slip (90.7 %), but pyramidal slip (7.6 %) may help resolve local strain heterogeneities (Lebensohn *et al.*, 2009). A potential contribution of pyramidal slip (1.7 % in Lebensohn *et al.*, 2009) may, however be masked in our analysis, as prism slip results in <11-20> and <10-10> rotation axis that cannot be differentiated from basal slip (Fig. 5.2b,c).

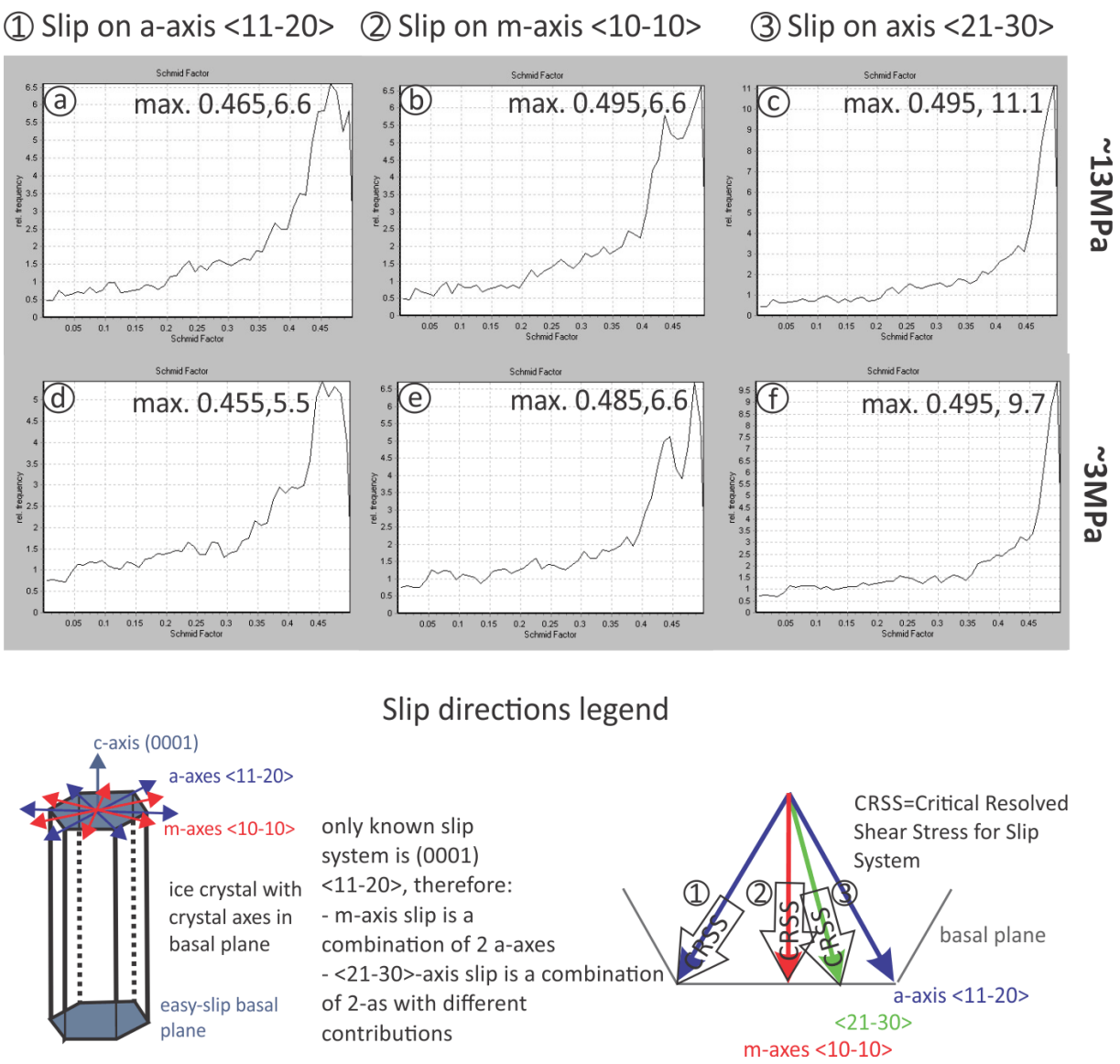

Figure 5.12: The Schmid factor distributions and maximum values for three differing slip directions in the basal plane. The top row shows results for a map of sample 769 (Fig. 5.10), the bottom row for sample 774 (Fig. 5.11). Slip systems employed were the commonly known a-axis slip on the basal plane on (0001) <11-20> (column 1, blue). If slip on two <11-20> axes happened simultaneously with equal amounts of slip being accommodated by either of the axes, the result would be an m-slip direction in (0001) <10-10> (column 2, red). However, slip could also be performed on two <11-20> axes with one a- axis dominating. This scenario was created by assuming slip in a (0001) <21-30> direction (green). Numbers in the top right corner of the plot denote the maximum Schmid factor and corresponding relative frequency of the respective distribution.

5.4.5 A model for shear zone development by kinking

Because brittle deformation is suppressed under the experimental conditions investigated, the often brittle precursors associated with shear zone initiation in rocks are unlikely to play a role (i.e. Goncalves *et al.*, 2016). We propose a model that is based on kinking as a dominant strain accommodation mechanism and locally aided by non-basal slip systems. In this model, low misorientation kinking could locally commence for two reasons. First, a local stress peak could be induced due to boundary conditions (Hobbs *et al.*, 1990 demonstrated that shear bands are expected in an oblique angle to shortening in a triaxial apparatus). Alternatively, kinking could also be triggered to resolve strain incompatibilities between neighbouring grains with differing orientations (Piazolo *et al.*, 2015). With progressive stress and strain, the misorientation of kinks presumably increases until the locking angle specific to the stress state is met. As a result, small grains with angular grain shapes develop on the boundary to unkinked remnant grains. A difference in size can lead to stress concentration on the interface between remnant and recrystallised grains, as demonstrated for monocrystalline inclusion experiments in a fine-grained ice matrix (Mansuy *et al.*, 2000, 2002). The stress concentrations on the interface promote kinking in favourably orientated remnant grains and locally raise the stress to activate non-basal slip systems (Montagnat *et al.*, 2011). High angle grain boundaries formed by kinking and non-basal dislocations subdivide the remnant grain into smaller fragments, which again induces stress concentrations with surrounding remnant grains.

5.5 Conclusions

Triaxial deformation of 25.4 mm diameter cylinders of polycrystalline ice with a starting grain size of 250 μm, at 50 MPa confining pressure and a temperature of 240 K yielded macroscopic strain localisation and shear zone development in the microstructure. A microstructural analysis of mature shear zones at an axial stress of 13 MPa (with a majority of recystallised grains) and intermediate shear zones at 3 MPa (with a mixture of remnant grains and recrystallised grains in shear zones) suggests that

- under the conditions investigated, kinking is the predominant strain accommodation mechanism. Recrystallisation is driven by the creation of new straight grain boundaries by kinking, as evidenced by 1) preponderance of grains with high frequencies of low angle kink boundaries around the rims of the shear zones 2) angular grain shapes within the shear zone and 3) similar crystallographic orientations of

neighbouring recrystallised grains within the shear zone.

- grains with angular shapes, straight boundaries and sizes below the grain size of the starting material are recrystallised grains generated by general (>10° misorientation) kinking.

- single kink boundaries with misorientations from 2-80° are created by coupled slip on two a-axes within the basal plane, which results in a variety of rotation axes and Burgers vectors within the basal plane.

- maximum kink band misorientation and spacing between two kink bands with similar orientations to bulk shortening depends on the stress configuration.

- deformation on a multiple grain-scale, in and around the shear zones, is dominated by basal slip with two coupled a-axes on (0001) <11-20>. The critical resolved shear stress is highest in the <21-30> direction, indicating that slip is unevenly distributed along the two a-axes.

- where kinking occurs at the rim of shear zone boundaries, slip on (0001) <11-20> is supplemented by non-basal dislocations. The non-basal dislocations have rotation axes with only a few degrees out of the basal plane, as theoretically inferred for pyramidal slip.

- kinking appears to induce changes in the local stress or strain field, as indicated by 1) the occurrence of non-basal dislocations in kinked or neighbouring grains and 2) kink propagation into neighbouring grains.

- local peaks in stress and strain caused by kinking could serve as a driving force for shear zone propagation, triggering further grain size reduction by kinking and non-basal dislocations.

- main rotation axes and trace analyses provide complementing information to identify slip systems. Trace analyses on selected kink boundaries allowed for the investigation of kinking and rotation on a grain-scale, whereas main rotation axes can be employed to constrain slip systems at a multiple grain level.

5.6 Graphical summary

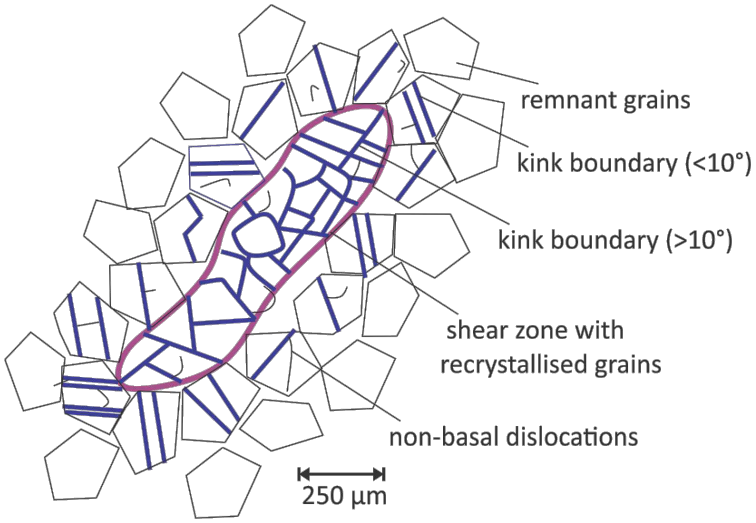

Triaxial test, P=50MPa, T=240K,
13 MPa & 3 MPa axial stress

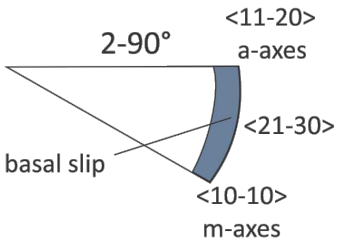

Definition Kink Boundary:
Straight Grain Boundary with Rotation Axis
and Slip vector in the Basal Plane

Crystal Plane View of
Slip Direction and
Crystal Axes:

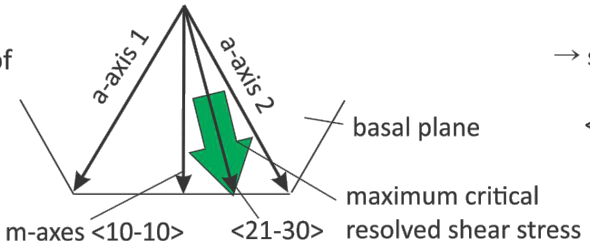

→ statistically preferred
slip direction is
<21-30>

Chapter 6

Thesis Conclusions

In this final chapter, the findings of this thesis are summarised by revisiting the research questions and objectives outlined in the introduction (Chapter 1).

6.1 Scientific questions

1. How can we quantify the microstructural evolution of polycrystalline ice with progressive strain?

Collecting of statistically significant datasets with cryo-EBSD allowed for a potential parameterisation of deformation mechanisms in terms of crystallographic preferred orientation (CPO), grain size statistics and misorientation angles distributions (Chapter 2). The main conclusions can be summarised as:

- New grain nucleation is best observed as a decrease in mode in the grain size statistics.
- Grain boundary migration (GBMR) yields broad, skewed grain size distributions with large standard deviations.
- Normal grain growth results in bell- or log normal- shaped grain size distributions with comparatively small standard deviations.
- Under deformation conditions where grain boundary migration is predominant, the angular constraints of the two cone CPO are indicative of the progression of the elimination of non-favourably (low Schmid factor) oriented grains and can be seen as an indirect gauge of the maturity (strain value) of the microstructure.

- Grain growth rates, as best reflected in an increase in arithmetic mean and median grain diameter, are deformation mechanism specific and can be faster during GBMR than normal grain growth.

2. What are the effects of the microstructural evolution on the rheology of the samples?

As repeatedly postulated in previous research, micro-physical or microstructural processes govern the rheology of polycrystalline ice aggregates. Four examples in this thesis provide further evidence for the strong coupling between microstructure and rheology:

- CPO formation is generally associated with strong mechanical anisotropy and under high-temperature conditions, driven by the elimination of non-favourably oriented ('hard-slip') grains and growth of favourably oriented 'easy-slip' grains (Chapter 2).
- Higher strain rates within the tops as opposed to the bottoms of approximately 20 mm x 20 mm x 40 mm block-shaped samples during deformation correlate with spatial differences in the degree of dynamic recrystallisation in the microstructures (Chapter 3).
- Under lower temperature conditions (240 K), the mechanical transitions from primary to secondary and secondary to tertiary creep appear to be a function of the recrystallised grain fraction (Chapter 4). Transition from primary to secondary creep corresponds to the nucleation of new grains, the transition to tertiary creep occurs as the recrystallised grain fraction interconnects.
- Kinking and non-basal dislocations are grain-scale processes influencing aggregate plasticity by promoting the formation of shear zones with a reduced grain size (Chapter 5).

3. How does deformation heterogeneity on a sample- and grain-scale affect the overall rheology?

Chapters 3, 4 and 5 reveal that deformation heterogeneity is an inherent part of the microstructural evolution of polycrystalline ice and will occur even under seemingly constant experimental boundary conditions. Deformation heterogeneity on an aggregate- and grain-scale was investigated and results suggest that:

- Spatially varying degrees of dynamic recrystallisation in the microstructure are related to spatial differences in strain rates and flow velocities on a sample-scale (Chapter 3).
- Transient shear zones are a part of the mechanical response of the ice samples to deformation but are not associated with permanent microstructural changes (Chapter 3).
- Shear zone formation can induce strain weakening of an entire ice aggregate but can also yield a transition to a mechanical steady state (constant strain rate under constant stress conditions) as soon as the shear zones with a reduced grain size interconnect (Chapter 4).
- Grain-scale deformation heterogeneity can influence the local stress and strain field, which could promote further localisation of deformation (Chapter 5).

4. How can we extrapolate the findings of this thesis to natural scenarios regarding ice sheets, glaciers and the creep of rocks below the BDT?

Chapters 2 and 3 have investigated the creep of polycrystalline ice under the high-temperature conditions commonly thought to prevail over the majority of ice sheets and glaciers. New insights regarding ice grain size statistics during grain boundary migration and normal grain growth (Chapter 2) can help with the mathematical exploration of the kinetics of both processes and serve as a quality control for modelling studies. The results of the particle image velocimetry (PIV) analysis in Chapter 3 have an important implication for large-scale deformation in ice sheets and glaciers, as they indicate that no changes in ice composition or overall boundary conditions are necessary to radically change ice flow velocities during secondary creep. If similar processes drive the tertiary creep of ice, the results of the PIV analysis suggest that rapid and unexpected (no change in environmental conditions) changes in the flow field of ice sheets and glaciers could also result from the inherent deformation heterogeneity of polycrystalline ice on a micro-scale. The observations in Chapter 3 stress the importance of gaining a better understanding of the micro-physics of ice in order to correctly estimate future ice sheet and glacier flow and associated climate modelling.

Regarding the creep of rocks below the BDT under high-pressure conditions, Chapters 4 and 5 have demonstrated that studying localisation processes is crucial to improve

our understanding of the mechanical repercussions of plastic deformation processes. A common argument in many geology-based studies on polymineralic crustal rocks (i.e. Herwegh and Berger, 2004) states that shear localisation occurs due to grain boundary pinning by second phases, which inhibits grain growth within shear zones. The results of deformation experiments on polycrystalline ice in Chapter 4 and 5 suggest that localisation processes within a monophase can be sufficiently efficient to promote a persistent grain size reduction (Chapter 4) and influence the stress and strain field beyond the rims of the shear zones (Chapter 5).

6.2 Technical objectives

1.Development of sample preparation procedures for deformed and undeformed polycrystalline ice samples prior to EBSD imaging:

The thermal response during sample preparation procedures as cutting, grinding and microtoming was investigated using thermocouples within dummy ice samples with the goal to create a reduced sample with a flat surface suitable for EBSD imaging. In combination with grain growth experiments on pure water ice (Becroft, 2015), the results of these thermal evolution experiments suggest that ice grain growth exponent have been overestimated in the past. Even very fine-grained ice samples (20 μm grain size) can be prepared at temperatures of ≈-30°C without causing grain growth, as long as sample preparation procedures are alternated with cooling periods below -100°C. Results are presented in more detail in Appendix A.

2. Development of a method, which allows for the visualisation of low and deformation heterogeneity during deformation within glaciological low-pressure ice deformation experiments:

Ice deformation experiments under unconfined conditions have the advantage that no jackets or confining media are necessary and, given a transparent cooling medium and rig cage, deformation can be directly observed. In Chapter 3, a transparent Plexiglas cage and silicone oil in combination with a glaciological Jacka rig were employed to enable the monitoring of the deformation via time-lapse photography. The images of the ice samples during deformation were processed with a particle image velocimetry (PIV) plug-in in Matlab and yielded a time series of velocity and strain rate distributions during deformation. The results of the PIV analysis were successfully validated by comparing

PIV calculated to displacement data derived vertical shortening rates.

3. Development of mechanical data processing and microstructural analysis techniques to characterise localisation of deformation and microstructural change:

Main findings regarding data processing and microstructural analysis techniques for large datasets comprise the following:

- Statistical parameters as the standard deviation or mode of the grain size distribution as indicators for the dominance of a certain deformation mechanism or new grain nucleation can facilitate the microstructural analysis of large data sets (Chapter 2).
- Grain growth exponents derived from secondary strain rates (prior to the onset of localisation, point of inflection used in glaciology, Fig. 1.5) may be more robust than tertiary (mechanical steady state) values usually employed in rock mechanics (Chapter 4, Fig. 4.11). Moreover, processing of the mechanical data for display as strain rate-stress curves has shown that solely incremental strain rates (comparing the current strain value to its precursor rather than the value at the start of the experiment, Formula 4.4) correctly represent trends of acceleration and deceleration observed in the strain-time curves (Fig. 4.10).
- Slip systems and deformation mechanisms for statistically significant data sets can be constrained from large-scale microstructural maps colour-coding the rotation axes of grain boundaries in combination with statistical rotation axes distributions in inverse pole figures (Chapter 5).

6.3 Future research

Potential avenues for future research include:

- Studying microstructural overprinting, as defined as changes in the microstructure under more complicated stress paths, in polycrystalline ice using the results in appendix B.
- Investigating the effect of grain-scale localisations on the local strain and stress field of polymineralic rocks using an ice composite (i.e. ice-graphite, ice-calcite or ice-dirt).

- Exploring deformation heterogeneity in glaciers and ice sheets, as manifested in flow field and strain distribution heterogeneity, under larger strains ($\gg 10$ %) and lower stresses (< 0.2 MPa) using PIV in unconfined ice experiments.

Bibliography

Alley, R. B. (1988). Fabrics in Polar Ice Sheets: Development and Prediction. *Science*, *240*(4851), 493–495.

Alley, R. B., Clark, P. U., Huybrechts, P., and Joughin, I. (2005). Ice-Sheet and Sea-Level Changes. *Science*, *310*(5747).

Alley, R. B., Perepezko, J. H., and Bentley, C. R. (1986a). Grain growth in polar ice: I. Theory. *J. Glaciol.*, *32*(112), 425–433.

Alley, R. B., Perepezko, J. H., and Bentley, C. R. (1986b). Grain growth in polar ice: II. Application. *J. Glaciol.*, *32*(112), 425–433.

Assael, M. J., Armyra, I. J., Brillo, J., Stankus, S. V., Wu, J., and Wakeham, W. A. (2012). Reference Data for the Density and Viscosity of Liquid Cadmium, Cobalt, Gallium, Indium, Mercury, Silicon, Thallium, and Zinc. *J. Phys. Chem. Ref. Data*, *41*(3), 033101.

Aydin, A. (1978). Small Faults Formed as Deformation Bands in Sandstone. In *Rock Frict. Earthq. Predict.*, 913–930. Basel: Birkhäuser Basel.

Azuma, N. and Higashi, A. (1985). Formation processes of ice fabric pattern in ice sheets. *Ann. Glaciol.*, *6*(120), 130–134.

Azuma, N., Miyakoshi, T., Yokoyama, S., and Takata, M. (2012). Impeding effect of air bubbles on normal grain growth of ice. *J. Struct. Geol.*, *42*, 184–193.

Bachmann, F., Hielscher, R., and Schaeben, H. (2010). Texture Analysis with MTEX - Free and Open Source Software Toolbox. *Solid State Phenom.*, *160*, 63–68.

Bailey, J. E. and Hirsch, P. B. (1962). The recrystallization process in some polycrystalline metals. *Proc. R. Soc. London*, *A267*, 11–30.

Banks, M. E. and Pelletier, J. D. (2008). Forward modeling of ice topography on Mars to infer basal shear stress conditions. *J. Geophys. Res.*, *113*(E1), E01001.

Barnes, P., Tabor, D., and Walker, J. C. F. (1971). The Friction and Creep of Polycrystalline Ice. *Proc. R. Soc. A Math. Phys. Eng. Sci.*, *324*(1557), 127–155.

Barr, A. C. and McKinnon, W. B. (2007). Convection in Enceladus' ice shell: Conditions for initiation. *Geophys. Res. Lett.*, *34*(9).

Barr, A. C. and Milkovich, S. M. (2008). Ice grain size and the rheology of the martian polar deposits. *Icarus*, *194*, 513–518.

Barreiro, J. G., Lonardelli, I., Wenk, H. R., Dresen, G., Rybacki, E., Ren, Y., and Tom, C. N. (2007). Preferred orientation of anorthite deformed experimentally in Newtonian creep. *Earth Planet. Sci. Lett.*, *264*(1-2), 188–207.

Barrie, C. D., Boyle, A. P., Cox, S. F., and Prior, D. J. (2008). Slip systems and critical resolved shear stress in pyrite: an electron backscatter diffraction (EBSD) investigation. *Mineral. Mag.*, *72*(6), 1181–1199.

Becroft, L. (2015). *New grain growth experiments in water ice*. Master thesis, University of Otago.

Bestmann, M. and Prior, D. (2003). Dynamic recrystallization in naturally deformed calcite marble: diffusion accommodated grain boundary sliding as a result of subgrain rotation recrystallization. *J. Struct. Geol.*, *25*(10), 1597–1613.

Bésuelle, P. and Rudnicki, J. W. (2003). Chapter 5 Localization: Shear bands and compaction bands. *Int. Geophys.*, *89*(C), 219–321.

Bindschadler, R. (1998). Changes in the West Antarctic Ice Sheet Since 1963 from Declassified Satellite Photography. *Science*, *279*(5351), 689–692.

Blumenfeld, P. and Wilson, C. (1991). Boundary migration and kinking in sheared naphthalene. *J. Struct. Geol.*, *13*(4), 471–483.

Bons, P. D., Jansen, D., Mundel, F., Bauer, C. C., Binder, T., Eisen, O., Jessell, M. W., Llorens, M.-G., Steinbach, F., Steinhage, D., and Weikusat, I. (2016). Converging flow and anisotropy cause large-scale folding in Greenland's ice sheet. *Nat. Commun.*, *7*, 11427.

Boullier, A. M. and Gueguen, Y. (1975). SP-Mylonites: Origin of some mylonites by superplastic flow. *Contrib. to Mineral. Petrol.*, *50*(2), 93–104.

Boyle, A. P., Prior, D. J., Banham, M. H., and Timms, N. E. (1998). Plastic deformation of metamorphic pyrite: new evidence from electron-backscatter diffraction and forescatter orientation-contrast imaging. *Miner. Depos.*, *34*(1), 71–81.

Bozkurt, E. and Park, R. G. (1997). Microstructures of deformed grains in the augen gneisses of southern Menderes Massif (western Turkey) and their tectonic significance. *Geol. Rundschau*, *86*(1), 103–119.

Breton, D. J., Baker, I., and Cole, D. M. (2016). Microstructural evolution of polycrystalline ice during confined creep testing. *Cold Reg. Sci. Technol.*, *127*, 25–36.

Brossard, C., Monnier, J., and Barricau, P. (2009). Principles and applications of particle image velocimetry. *Aerosp Lab J*, *03*(1), 1–11.

Brun, J. and Cobbold, P. (1980). Strain heating and thermal softening in continental shear zones: a review. *J. Struct. Geol.*, *2*(1-2), 149–158.

Budd, W. and Jacka, T. (1989). A review of ice rheology for ice sheet modelling. *Cold Reg. Sci. Technol.*, *16*(2), 107–144.

Buiter, S. and Ellis, S. (2012). SULEC: Benchmarking a new ALE finite-element code. *Geophys. Res. Abstr. EGU Gen. Assem. Phys. Geol. Process.*, *14*(2), 2012–7528.

Burg, J., Wilson, C., and Mitchell, J. (1986). Dynamic recrystallization and fabric development during the simple shear deformation of ice. *J. Struct. Geol.*, *8*(8), 857–870.

Burke, J. and Turnbull, D. (1952). Recrystallization and grain growth. *Prog. Met. Phys.*, *3*, 220–292.

Chauve, T., Montagnat, M., Piazolo, S., Journaux, B., Wheeler, J., Barou, F., Mainprice, D., and Tommasi, A. (2017). Non-basal dislocations should be accounted for in simulating ice mass flow. *Earth Planet. Sci. Lett.*, *473*, 247–255.

Chevy, J., Fressengeas, C., Lebyodkin, M., Taupin, V., Bastie, P., and Duval, P. (2010). Characterizing short-range vs. long-range spatial correlations in dislocation distributions. *Acta Mater.*, *58*(5), 1837–1849.

Christian, J. W. and Mahajan, S. (1995). Deformation twinning. *Prog. Mater. Sci.*, *39*(1-2), 1–157.

Clark, P. U., Alley, R. B., and Pollard, D. (1999). Northern Hemisphere Ice-Sheet Influences on Global Climate Change. *Science*, *286*(5442).

Collier, M. (1978). Ultimate locking angles for conjugate and monoclinal kink bands. *Tectonophysics*, *48*(1-2), 1–6.

Cross, A. J., Prior, D. J., Stipp, M., and Kidder, S. (2017). The recrystallized grain size piezometer for quartz: An EBSD-based calibration. *Geophys. Res. Lett.*, *44*(13), 6667–6674.

Cuffey, K. and Paterson, W. S. B. (1994). *The Physics of Glaciers*. Butterworth-Heinemann.

Cuffey, K. M., Conway, H., Gades, A., Hallet, B., Raymond, C. F., and Whitlow, S. (2000). Deformation properties of subfreezing glacier ice: Role of crystal size, chemical impurities, and rock particles inferred from in situ measurements. *J. Geophys. Res.*, *105915*(10), 895–27.

Cyprych, D., Piazolo, S., Wilson, C. J. L., Luzin, V., and Prior, D. J. (2016). Rheology, microstructure and crystallographic preferred orientation of matrix containing a dispersed second phase: Insight from experimentally deformed ice. *Earth Planet. Sci. Lett.*, *449*, 272–281.

de Bresser, J. H. P., Peach, C. J., Reijs, J. P. J., and Spiers, C. J. (1998). On dynamic recrystallization during solid state flow: Effects of stress and temperature. *Geophys. Res. Lett.*, *25*(18), 3457–3460.

De Bresser, J. H. P., Ter Heege, J. H., and Spiers, C. J. (2001). Grain size reduction by dynamic recrystallization: Can it result in major rheological weakening? *Int. J. Earth Sci.*, *90*(1), 28–45.

De La Chapelle, S., Castelnau, O., Lipenkov, V., and Duval, P. (1998). Dynamic recrystallization and texture development in ice as revealed by the study of deep ice cores in Antarctica and Greenland. *J. Geophys. Res. Solid Earth*, *103*(B3), 5091–5105.

De Raadt, W. S., Burlini, L., Kunze, K., and Spiers, C. J. (2014). Effect of pre-existing crystallographic preferred orientation on the rheology of Carrara marble. *J. Struct. Geol.*, *68*, 44–57.

Dingley, D. J. and Randle, V. (1992). Microtexture determination by electron back-scatter diffraction. *J. Mater. Sci.*, *27*(17), 4545–4566.

Dobron, P., Chmelík, F., Yi, S., Parfenenko, K., Letzig, D., and Bohlen, J. (2011). Grain size effects on deformation twinning in an extruded magnesium alloy tested in compression. *Scr. Mater.*, *65*(5), 424–427.

Drury, M. and Pennock, G. (2007). Subgrain rotation recrystallization in minerals. *Mater. Sci. forum*, *550*, 95–104.

Drury, M. R., Humphreys, F. J., and White, S. H. (1985). Large strain deformation studies using polycrystalline magnesium as a rock analogue. Part II: dynamic recrystallisation mechanisms at high temperatures. *Phys. Earth Planet. Inter.*, *40*(3), 208–222.

Drury, M. R. and Urai, J. L. (1990). Deformation-related recrystallization processes. *Tectonophysics*, *112*, 235–253.

Durham, W., Heard, H., and Kirby, S. (1983). Experimental deformation of polycrystalline H2O ice at high pressure and low temperature: Preliminary results. *J. Geophys. Res.*, *88*, 377–392.

Durham, W. B., Kirby, S. H., and Stern, L. A. (1997). Creep of water ices at planetary conditions: A compilation. *J. Geophys. Res.*, *102*(E7), 16293–16302.

Durham, W. B., Stern, L. A., and Kirby, S. H. (2001). Rheology of ice I at low stress and elevated confining pressure. *J. Geophys. Res.*, *106*(6), 11,031–11,042.

Duval, P. (1981). Creep and Fabrics of Polycrystalline Ice Under Shear and Compression. *J. Glaciol.*, *27*(95), 129–140.

Duval, P., Ashby, M. F., and Andermant, I. (1983). Rate-Controlllng Processes in the Creep of Polycrystalline Ice. *J. Phys. Chem.*, *87*(1), 4066–4074.

Duval, P. and Castelnau, O. (1995). Dynamic Recrystallization of Ice in Polar Ice Sheets. *J. Phys. IV*, *05*, C3–197–C3–205.

Duval, P. and Montagnat, M. (2006). Physical deformation modes of ice in glaciers and ice sheets. In *Glacier Sci. Environ. Chang.*, Chapter 59, 303–308. Blackwell Science Ltd.

Duval, P., Montagnat, M., Grennerat, F., Weiss, J., Meyssonnier, J., and Philip, A. (2010). Creep and plasticity of glacier ice: a material science perspective. *J. Glaciol.*, *56*(200), 1059–1068.

Ellis, S., Fagereng, A., Barker, D., Henrys, S., Saffer, D., Wallace, L., Williams, C., and Harris, R. (2015). Fluid budgets along the northern Hikurangi subduction margin, New Zealand: The effect of a subducting seamount on fluid pressure. *Geophys. J. Int.*, *202*(1), 277–297.

Ellis, S. M., Little, T. A., Wallace, L. M., Hacker, B. R., and Buiter, S. J. H. (2011). Feedback between rifting and diapirism can exhume ultrahigh-pressure rocks. *Earth Planet. Sci. Lett.*, *311*, 427–438.

Ettema, R., Fujita, I., Muste, M., and Kruger, A. (1997). Particle-image velocimetry for whole-field measurement of ice velocities. *Cold Reg. Sci. Technol.*, *26*(2), 97–112.

Evans, B. and Kohlstedt, D. (1995). Rheology of rocks. In T. Ahrens (Ed.), *Handb. Phys. constants part 3 - Rock Phys. phase relations*, 148–165. AGU, Washington DC.

Faria, S. H., Weikusat, I., and Azuma, N. (2014). The microstructure of polar ice. Part II: State of the art. *J. Struct. Geol.*, *61*, 21–49.

Fitz Gerald, J. and Stünitz, H. (1993). Deformation of granitoids at low metamorphic grade. I: Reactions and grain size reduction. *Tectonophysics*, *221*(3-4), 269–297.

Fossen, H. (2016). *Structural geology* (2 ed.). Cambridge: Cambridge University Press.

Frost, H. J. and Ashby, M. F. (1982). *Deformation-mechanism Maps*. Oxford: Pergamon.

Ganev, P. N., Dolan, J. F., McGill, S. F., and Frankel, K. L. (2012). Constancy of geologic slip rate along the central Garlock fault: implications for strain accumulation and release in southern California. *Geophys. J. Int.*, *190*(2), 745–760.

Gao, Z. and Zhao, J. (2015). Fabric Evolution and Its Effect on Strain Localization in Sand. In C. KT. and Z. J. (Eds.), *Bifurc. Degrad. Geomaterials New Millenium* (Springer S ed.)., 21–26. Springer, Cham.

Gerbi, C., Johnson, S. E., Shulman, D., and Klepeis, K. (2016). Influence of microscale weak zones on bulk strength. *Geochemistry, Geophys. Geosystems*, *17*, 4064–407.

Glen, J. W. (1952). Experiments on the deformation of ice. *J. Glaciol.*, *2*(12), 111–114.

Glen, J. W. (1955). The creep of polycrystalline ice. *Proc. R. Soc. London*, *228*(1175), 519–538.

Golding, N., Schulson, E. M., and Renshaw, C. E. (2010). Shear faulting and localized heating in ice: The influence of confinement. *Acta Mater.*, *58*(15), 5043–5056.

Golding, N., Schulson, E. M., and Renshaw, C. E. (2012). Shear localization in ice: Mechanical response and microstructural evolution of P-faulting. *Acta Mater.*, *60*(8), 3616–3631.

Goldsby, D. and Kohlstedt, D. (1997). Grain boundary sliding in fine-grained Ice I. *Scr. Mater.*, *37*(9), 1399–1406.

Goldsby, D. L. (2006). Superplastic flow of ice relevant to glacier and ice-sheet mechanics. In *Glacier Sci. Environ. Chang.*, Chapter 60, 308–314.

Goldsby, D. L. and Kohlstedt, D. L. (2001). Superplastic deformation of ice: Experimental observations. *J. Geophys. Res. Solid Earth*, *106*(B6), 2156–2202.

Goncalves, P., Poilvet, J. C., Oliot, E., Trap, P., and Marquer, D. (2016). How does shear zone nucleate? An example from the Suretta nappe (Swiss Eastern Alps). *J. Struct. Geol.*, *86*, 166–180.

Graham, F. S., Morlighem, M., Warner, R. C., and Treverrow, A. (2017). Implementing an empirical scalar constitutive relation for ice with flow-induced polycrystalline anisotropy in large-scale ice sheet models. *Cryosph.*, *12*(3), 1047–1067.

Grennerat, F., Montagnat, M., Castelnau, O., Vacher, P., Moulinec, H., Suquet, P., and Duval, P. (2012). Experimental characterization of the intragranular strain field in columnar ice during transient creep. *Acta Mater.*, *60*(8), 3655–3666.

Grosskreutz, J. and Waldow, P. (1963). Substructure and fatigue fracture in aluminum. *Acta Metall.*, *11*(7), 717–724.

Guillope, M. and Poirier, J. P. (1979). Dynamic recrystallization during creep of single-crystalline halite: An experimental study. *J. Geophys. Res.*, *84*(B10), 5557–5567.

Handy, M. R. (1994). Flow laws for rocks containing two non-linear viscous phases: A phenomenological approach. *J. Struct. Geol.*, *16*(3), 287–301.

Hansen, L. N., Zimmerman, M. E., and Kohlstedt, D. L. (2011). Grain boundary sliding in San Carlos olivine: Flow law parameters and crystallographic-preferred orientation. *J. Geophys. Res.*, *116*(B8), B08201.

Heard, H. C., Durham, W. B., Boro, C. O., and Kirby, S. H. (1990). A triaxial deformation apparatus for service at 77 $\leq$ T $\leq$ 273 K. In A. G. Duba, W. B. Durham, J. W. Handin, and H. F. Wang (Eds.), *Brittle-Ductile Transit. Rocks*, 225–228. Washington D. C.: American Geophysical Union.

Herwegh, M. and Berger, A. (2004). Deformation mechanisms in second-phase affected microstructures and their energy balance. *J. Struct. Geol.*, *26*(8), 1483–1498.

Herwegh, M. and Handy, M. R. (1996). The evolution of high-temperature mylonitic microfabrics: evidence from simple shearing of a quartz analogue (norcamphor). *J. Struct. Geol.*, *18*(5), 689–710.

Hillert, M. (1965). On the theory of normal and abnormal grain growth. *Acta Metall.*, *13*(3), 227–238.

Hirth, G. and Tullis, J. (1992). Dislocation creep regimes in quartz aggregates. *J. Struct. Geol.*, *14*(2), 145–159.

Hobbs, B. E. (1968). Recrystallization of single crystals of quartz. *Tectonophysics*, *6*(5), 353–401.

Hobbs, B. E., Muhlhaus, H.-B., and Ord, A. (1990). Instability, softening and localization of deformation. *Geol. Soc. London, Spec. Publ.*, *54*(1), 143–165.

Holden, J. (1961). The formation of sub-grain structure by alternating plastic strain. *Philos. Mag.*, *6*(64), 547–558.

Holyoke, C. W. and Tullis, J. (2006). Mechanisms of weak phase interconnection and the effects of phase strength contrast on fabric development. *J. Struct. Geol.*, *28*(4), 621–640.

Hondoh, T. (2000). Nature and behavior of dislocations in ice. In *Phys. ice core Rec.*, Sapporo, 3–32. Hokkaido University Press.

Hondoh, T., Iwamatsu, H., and Mae, S. (1990). Dislocation mobility for non-basal glide in ice measured by in situ X-ray topography. *Philos. Mag. A*, *62*(1), 89–102.

Huang, H., Dabiri, D., and Gharib, M. (1997). On errors of digital particle image velocimetry. *Meas. Sci. Technol.*, *8*(12), 1427–1440.

Hulbe, C. L. and Macayeal, D. R. (1999). A new numerical model of coupled inland ice sheet, ice stream, and ice shelf flow and its application to the West Antarctic Ice Sheet. *J. Geophys. Res.*, *104366*(10), 349–25.

Humphrey, F. J. and Hatherly, M. (1996). *Recrystallization and related annealing phenomena*. Pergamon.

Humphreys, F., Hatherly, M., Humphreys, F., and Hatherly, M. (2004). Chapter 7 Recrystallization of Single-Phase Alloys. In *Recryst. Relat. Annealing Phenom.*, 215–IV.

Jacka, T. (1994). The steady-state crystal size of deforming ice. *Ann. Glaciol.*, *20*(1), 13–18.

Jacka, T. H. and Maccagnan, M. (1984). Ice crystallographic and strain rate changes with strain in compression and extension. *Cold Reg. Sci. Technol.*, *8*(3), 269–286.

Johnson, A. M. (1977). *Styles of folding : mechanics and mechanisms of folding of natural elastic materials*. Elsevier Scientific Pub. Co.

Joughin, I., Abdalati, W., and Fahnestock, M. (2004). Large fluctuations in speed on Greenland's Jakobshavn Isbr{æ} glacier. *Nature*, *432*(7017), 608–610.

Jun, L., Jacka, T. H., and Budd, W. F. (1996). Deformation rates in combined compression and shear for ice which is initially isotropic and after the development of strong anisotropy. *Ann. Glaciol.*, *23*, 247–X28.

Kamb, B. (1973). Experimental recrystallization of ice under stress. In *Flow Fract. Rocks*, Volume 16, 211–241. Washington D. C.: American Geophysical Union 2013.

Karato, S.-i. (2008). *Deformation of Earth Materials*. Cambridge: Cambridge University Press.

Kelemen, P. B. and Hirth, G. (2007). A periodic shear-heating mechanism for intermediate-depth earthquakes in the mantle. *Nature*, *446*(7137), 787–790.

Kidder, S., Hirth, G., Avouac, J.-P., and Behr, W. (2016). The influence of stress history on the grain size and microstructure of experimentally deformed quartzite. *J. Struct. Geol.*, *83*, 194–206.

Koehle, R. O. (1964). Deformation of the Ross Ice Shelf, Antarctica. *GSA Bull.*, *75*(4), 259–286.

Kohlstedt, D. L. and Weathers, M. S. (1980). Deformation-induced microstructures, paleopiezometers, and differential stresses in deeply eroded fault zones. *J. Geophys. Res. Solid Earth*, *85*(B11), 6269–6285.

Küster, M. and Stöckhert, B. (1999). High differential stress and sublithostatic pore fluid pressure in the ductile regime microstructural evidence for short-term post-seismic creep in the Sesia Zone, Western Alps. *Tectonophysics*, *303*, 263–277.

Langdon, T. G. (2006). Grain boundary sliding revisited: Developments in sliding over four decades. *J. Mater. Sci.*, *41*(3), 597–609.

Larour, E., Khazendar, A., Borstad, C. P., Seroussi, H., Morlighem, M., and Rignot, E. (2014). Representation of sharp rifts and faults mechanics in modeling ice shelf flow dynamics: Application to Brunt/Stancomb-Wills Ice Shelf, Antarctica. *J. Geophys. Res. Earth Surf.*, *119*(9), 1918–1935.

Lebensohn, R. A., Montagnat, M., Mansuy, P., Duval, P., Meysonnier, J., and Philip, A. (2009). Modeling viscoplastic behavior and heterogeneous intracrystalline deformation of columnar ice polycrystals. *Acta Mater.*, *57*(5), 1405–1415.

Lile, R. C. (1978). The Effect of Anisotropy on the Creep of Polycrystalline Ice. *J. Glaciol.*, *21*(85), 475–483.

Little, T. A., Holcombe, R. J., and Ilg, B. R. (2002). Ductile fabrics in the zone of active oblique convergence near the Alpine Fault, New Zealand: Identifying the neotectonic overprint. *J. Struct. Geol.*, *24*(1), 193–217.

Mackenzie, J. K. (1964). The distribution of rotation axes in a random aggregate of cubic crystals. *Acta Metall.*, *12*(2), 223–225.

Mainprice, D., Lloyd, G. E., and Casey, M. (1993). Individual orientation measurements in quartz polycrystals: advantages and limitations for texture and petrophysical property determinations. *J. Struct. Geol.*, *15*(9-10), 1169–1187.

Maltman, A. J., Hubbard, B., and Hambrey, M. J. (2000). Deformation of glacial materials: introduction and overview. *Geol. Soc. London Spec. Publ.*, *176*(1), 1.

Manley, M. E. and Schulson, E. M. (1997). On the strain-rate sensitivity of columnar ice. *J. Glaciol.*, *43*(145), 408–410.

Mansuy, P., Meyssonnier, J., and Philip, A. (2002). Localization of deformation in polycrystalline ice: experiments and numerical simulations with a simple grain model. *Comput. Mater. Sci.*, *25*(1-2), 142–150.

Mansuy, P., Philip, A., and Meyssonnier, J. (2000). Identification of strain heterogeneities arising during deformation of ice. *Ann. Glaciol.*, *30*(1), 121–126.

McKinnon, W. B. (1999). Convective instability in Europa's floating ice shell. *Geophys. Res. Lett.*, *26*(7), 1944–8007.

Means, W. D. (1981). The concept of steady-state foliation. *Tectonophysics*, *78*(1-4), 179–199.

Mellor, M. and Cole, D. M. (1982). Deformation and failure of ice under constant stress or constant strain-rate. *Cold Reg. Sci. Technol.*, *5*(3), 201–219.

Montagnat, M., Blackford, J. R., Piazolo, S., Arnaud, L., and Lebensohn, R. a. (2011). Measurements and full-field predictions of deformation heterogeneities in ice. *Earth Planet. Sci. Lett.*, *305*(1-2), 153–160.

Montagnat, M., Chauve, T., Barou, F., Tommasi, A., Beausir, B., and Fressengeas, C. (2015). Analysis of Dynamic Recrystallization of Ice from EBSD Orientation Mapping. *Front. Earth Sci.*, *3*.

Montagnat, M., Weiss, J., Chevy, J., Duval, P., Brunjail, H., Bastie, P., and Gil Sevillano, J. (2006). The heterogeneous nature of slip in ice single crystals deformed under torsion. *Philos. Mag.*, *86*(27), 4259–4270.

Montési, L. G. J. and Hirth, G. (2003). Grain size evolution and the rheology of ductile shear zones: From laboratory experiments to postseismic creep. *Earth Planet. Sci. Lett.*, *211*(1-2), 97–110.

Nicolas, A. (1987). *Principles of Rock Deformation* (1st ed.). Dordrecht: Springer Netherlands.

Nishikawa, O. and Takeshita, T. (1999). Dynamic analysis and two types of kink bands in quartz veins deformed under subgreenschist conditions. *Tectonophysics*, *301*(1-2), 21–34.

Nizolek, T., Begley, M., McCabe, R., Avallone, J., Mara, N., Beyerlein, I., and Pollock, T. (2017). Strain fields induced by kink band propagation in Cu-Nb nanolaminate composites. *Acta Mater.*, *133*, 303–315.

Nolze, G. and Hielscher, R. (2016). Orientations perfectly colored. *J. Appl. Crystallogr.*, *49*(5), 1786–1802.

Nye, J. (1953). The Flow Law of Ice from Measurements in Glacier Tunnels, Laboratory Experiments and the Jungfraufirn Borehole Experiment. *Proc. R. Soc. A Math. Phys. Eng. Sci.*, *219*, 477–489.

Okudaira, T., Jerabek, P., Stunitz, H., and Fusseis, F. (2012). High-temperature fracturing and subsequent grain-size-sensitive creep in lower crustal gabbros: Evidence for coseismic loading followed by creep during decaying stress in the lower crust? *J. Geophys. Res. Solid Earth*, *120*, 1–23.

Orowan, E. (1940). Problems of plastic gliding. *Proc. Phys. Soc.*, *52*(1), 8–22.

Oskin, M. and Iriondo, A. (2004). Large-magnitude transient strain accumulation on the Blackwater fault, Eastern California shear zone. *Geology*, *32*(4), 313–316.

Pappalardo, R. T., Head, J. W., Greeley, R., Sullivan, R. J., Pilcher, C., Schubert, G., Moore, W. B., Carr, M. H., Moore, J. M., Belton, M. J. S., and Goldsby, D. L. (1998). Geological evidence for solid-state convection in Europa's ice shell. *Nature*, *391*(6665), 365–368.

Passchier, C. W. and Trouw, R. A. J. (2005). Deformation Mechanisms. In *Microtectonics* (1 ed.)., 25–66. Berlin-Heidelberg: Springer-Verlag.

Paterson, M. S. (2013). *Materials science for structural geology.* Springer.

Peltier, R., Goldsby, D. L., Kohlstedt, D. L., and Tarasov, L. (2000). Ice-age ice-sheet rheology: Constraints from the Last Glacial Maximum form of the Laurentide ice sheet. *Ann. Glaciol.*, *30*(1955), 163–176.

Petrenko, V. F. and Whitworth, R. W. (1999). *Physics of ice.* Oxford University Press.

Piazolo, S., Montagnat, M., and Blackford, J. R. (2008). Substructure characterization of experimentally and naturally deformed ice using cryoEBSD. *J. Microsc.*, *230*(May 2007), 509–519.

Piazolo, S., Montagnat, M., Grennerat, F., Moulinec, H., and Wheeler, J. (2015). Effect of local stress heterogeneities on dislocation fields: Examples from transient creep in polycrystalline ice. *Acta Mater.*, *90*, 303–309.

Piazolo, S., Wilson, C. J. L., Luzin, V., Brouzet, C., and Peternell, M. (2013). Dynamics of ice mass deformation: Linking processes to rheology, texture, and microstructure. *Geochemistry, Geophys. Geosystems*, *14*(10), 4185–4194.

Pieri, M., Burlini, L., Kunze, K., Stretton, I., and Olgaard, D. L. (2001). Rheological and microstructural evolution of Carrara marble with high shear strain: results from high temperature torsion experiments. *J. Struct. Geol.*, *23*(9), 1393–1413.

Pimienta, P. and Duval, P. (1987). Rate controlling processes in the creep of polar glacier ice. *J. d Phys. (Paris), Colloq.*, *48*(3), 243–248.

Poirier, J. and Nicolas, A. (1975). Deformation-Induced Recrystallization Due to Progressive Misorientation of Subgrains , with Special Reference to Mantle Peridotites. *J. Geol.*, *83*(6), 707–720.

Poirier, J. P. (1980). Shear localization and shear instability in materials in the ductile field. *J. Struct. Geol.*, *2*(1-2), 135–142.

Poirier, J.-P. (1985). *Creep of crystals : high-temperature deformation processes in metals, ceramics, and minerals*. Cambridge University Press.

Prior, D. J. (1999). Problems in determining the misorientation axes , for small angular misorientations , using electron backscatter diffraction in the SEM. *J. Microsc.*, *195*(3), 217–225.

Prior, D. J. and Bestmann, M. (2004). Recrystallization and grain growth in rocks and minerals. *Mater. Sci. Forum*, *470*, 545–550.

Prior, D. J., Lilly, K., Seidemann, M., Vaughan, M., Becroft, L., Easingwood, R., Diebold, S., Obbard, R., Daghlian, C., Baker, I., Caswell, T., Golding, N., Goldsby, D., Durham, W. B., Piazolo, S., and Wilson, C. J. L. (2015). Making EBSD on water ice routine. *J. Microsc.*, *259*(3), 237–256.

Prior, D. J., Mariani, E., and Wheeler, J. (2009). Electron Backscatter Diffraction in Materials Science. In A. J. Schwartz, M. Kumar, B. L. Adams, and D. P. Field (Eds.), *Electron Backscatter Diffr. Mater. Sci.*, Chapter 26, 345–360. Boston, MA: Springer US.

Prior, D. J., Wheeler, J., Peruzzo, L., Spiess, R., and Storey, C. (2002). Some garnet microstructures: an illustration of the potential of orientation maps and misorientation analysis in microstructural studies. *J. Struct. Geol.*, *24*(6-7), 999–1011.

Qi, C., Goldsby, D. L., and Prior, D. J. (2017). The down-stress transition from cluster to cone fabrics in experimentally deformed ice. *Earth Planet. Sci. Lett.*, *471*, 136–147.

Randle, V. (2006). 'Five-parameter' analysis of grain boundary networks by electron backscatter diffraction. *J. Microsc.*, *222*(2), 69–75.

Raymond, C. F. (1971). Flow in a Transverse Section of Athabasca Glacier, Alberta, Canada. *J. Glaciol.*, *10*(58), 55–84.

Reches, Z. and Johnson, A. M. (1976). A theory of concentric, kink and sinusoidal folding and of monoclinal flexuring of compressible, elastic multilayers. *Tectonophysics*, *35*(3), 295–334.

Reddy, S. M., Timms, N. E., Pantleon, W., and Trimby, P. (2007). Quantitative characterization of plastic deformation of zircon and geological implications. *Contrib. to Mineral. Petrol.*, *153*(6), 625–645.

Rignot, E. and Kanagaratnam, P. (2006). Changes in the Velocity Structure of the Greenland Ice Sheet. *Science*, *311*(5763), 986–90.

Rignot, E. and Thomas, R. H. (2002). Mass Balance of Polar Ice Sheets. *Science*, *297*(5586), 1502–6.

Rios, P. R., Siciliano Jr, F., Sandim, H. R. Z., Plaut, R. L., and Padilha, A. F. (2005). Nucleation and growth during recrystallization. *Mater. Res.*, *8*(3), 225–238.

Scanlon, T. J., Stickland, M. T., and Lacombe, M. (2001). A PIV and CFD Analysis of Natural Convection Ice Melting. In *9th Int. Conf. Laser Anemometry*, Limerick, Ireland.

Schmid, E. and Boas, W. (1935). *Kristallplastizitaet mit besonderer Beruecksichtigung der Metalle* (1 ed.). Berlin: Springer Verlag.

Schulson, E. (2002). Compressive shear faults in ice: plastic vs. Coulombic faults. *Acta Mater.*, *50*(13), 3415–3424.

Schulson, E. M. and Duval, P. (2009). *Creep and fracture of ice.* Cambridge University Press.

Shearwood, C. and Whitworth, R. W. (1991). The velocity of dislocations in ice. *Philos. Mag. A*, *64*(2), 289–302.

Shearwood, C. and Worth, R. W. W. (1989). X-ray topographic observations of edge dislocations glide on non-basal planes in ice. *J. Glaciol.*, *35*(120), 289–302.

Sibson, R. (1980). Transient discontinuities in ductile shear zones. *J. Struct. Geol.*, *2*(1-2), 165–171.

Skrotzki, W. and Welch, P. (1983). Development of texture and microstructure in extruded ionic polycrystalline aggregates. *Tectonophysics*, *99*(1), 47–61.

Starkey, J. (1968). The geometry of kink bands in crystals — a simple model. *Contrib. to Mineral. Petrol.*, *19*(2), 133–141.

Stern, L. A., Durham, W. B., and Kirby, S. H. (1997). Grain-size-induced weakening of H 2 O ices I and II and associated anisotropic recrystallization. *J. Geophys. Res.*, *102*(B3), 5313–5325.

Stipp, M., Stunitz, H., Heilbronner, R., and Schmid, S. M. (2001). Dynamic recrystallization of quartz: correlation between natural and experimental conditions. *Geol. Soc. London, Spec. Publ.*, *200*(1), 171–190.

Takeda, Y. T. and Griera, A. (2006). Rheological and kinematical responses to flow of two-phase rocks. *Tectonophysics*, *427*(1-4), 95–113.

Thielicke, W. and Stamhuis, E. J. (2014). PIVlab Towards User-friendly, Affordable and Accurate Digital Particle Image Velocimetry in MATLAB. *J. Open Res. Softw.*, *2*(1).

Thorsteinsson, T. (2007). Anisotropy and Flow of Ice. In *Glacier Sci. Environ. Chang.*, 315–317. Malden, MA, USA: Blackwell Publishing.

Thwaites, R. J., Wilson, C. J. L., and McCray, A. P. (1984). Relationship Between Bore-Hole Closure and Crystal Fabrics in Antarctic Ice Core from Cape Folger. *J. Glaciol.*, *30*(105), 171–179.

Trepmann, C. and Stöckhert, B. (2001). Mechanical twinning of jadeite – an indication of synseismic loading beneath the brittle–plastic transition. *Int. J. Earth Sci.*, *90*(1), 4–13.

Trepmann, C. A. and Stöckhert, B. (2002). Cataclastic deformation of garnet: a record of synseismic loading and postseismic creep. *J. Struct. Geol.*, *24*, 1845–1856.

Trepmann, C. A. and Stöckhert, B. (2003). Quartz microstructures developed during non-steady state plastic flow at rapidly decaying stress and strain rate. *J. Struct. Geol.*, *25*, 2035–2051.

Treverrow, A., Budd, W. F., Jacka, T. H., and Warner, R. C. (2012). The tertiary creep of polycrystalline ice: experimental evidence for stress-dependent levels of strain-rate enhancement. *J. Glaciol.*, *58*(208), 301–314.

Treverrow, A., Warner, R. C., Budd, W. F., Jacka, T., and Roberts, J. L. (2015). Modelled stress distributions at the Dome Summit South borehole, Law Dome, East Antarctica: a comparison of anisotropic ice flow relations. *J. Glaciol.*, *61*(229), 987–1004.

Trickett, Y., Baker, I., and Pradhan, P. (2000). The orientation dependence of the strenght of ice single crystals. *J. Glaciol.*, *46*, 41–44.

Trimby, P. W., Drury, M. R., and Spiers, C. J. (2000). Recognising the crystallographic signature of recrystallisation processes in deformed rocks: a study of experimentally deformed rocksalt. *J. Struct. Geol.*, *22*(11-12), 1609–1620.

Tulaczyk, S. (2006). Fast Glacier Flow and Ice Streaming. In *Glacier Sci. Environ. Chang.*, 353–359. Malden, MA, USA: Blackwell Publishing.

Tullis, T. E., Horowitz, F. G., and Tullis, J. (1991). Flow laws of polyphase aggregates from end-member flow laws. *J. Geophys. Res.*, *96*(B5), 8081–8096.

Twiss, R. J. (1977). Theory and applicability of a recrystallized grain size paleopiezometer. *Pure Appl. Geophys. PAGEOPH*, *115*(1-2), 227–244.

Urai, J. L., Means, W. D., and Lister, G. S. (1986). Dynamic recrystallization of minerals. 161–199.

van der Veen, C. and Whillans, I. (1994a). Development of fabric in ice. *Cold Reg. Sci. Technol.*, *22*(2), 171–195.

van der Veen, C. J. and Whillans, I. M. (1994b). Development of fabric in ice. *Cold Reg. Sci. Technol.*, *22*(2), 171–195.

Vaughan, D. G. (2006). The Antarctic Ice Sheet. In *Glacier Sci. Environ. Chang.*, 209–220. Malden, MA, USA: Blackwell Publishing.

Vaughan, M. J. (2016). *Creep behaviour, elastic, and anelastic properties of polycrystalline ice.* Ph. D. thesis, University of Otago.

Vernon, R. H. (2004). *A Practical Guide to Rock Microstructure*. Cambridge: Cambridge University Press.

Vernooij, M. G., Kunze, K., and den Brok, B. (2006). 'Brittle' shear zones in experimentally deformed quartz single crystals. *J. Struct. Geol.*, *28*(7), 1292–1306.

Wadee, M. A., Völlmecke, C., Haley, J. F., and Yiatros, S. (2012). Geometric modelling of kink banding in laminated structures. *Philos. Trans. R. Soc. London A Math. Phys. Eng. Sci.*, *370*(1965), 1827–1849.

Warren, J. M. and Hirth, G. (2006). Grain size sensitive deformation mechanisms in naturally deformed peridotites. *Earth Planet. Sci. Lett.*, *248*(1), 438–450.

Wei, Y. and Dempsey, J. P. (1994). The motion of non-basal dislocations in ice crystals. *Philos. Mag. A*, *69*(1), 1–10.

Weikusat, I., DE Winter, D. a. M., Pennock, G. M., Hayles, M., Schneijdenberg, C. T. W. M., and Drury, M. R. (2010). Cryogenic EBSD on ice: preserving a stable surface in a low pressure SEM. *J. Microsc.*, *242*(3), 295–310.

Weikusat, I., Miyamoto, A., Faria, S. H., Kipfstuhl, S., Azuma, N., and Hondoh, T. (2011). Subgrain boundaries in Antarctic ice quantified by X-ray Laue diffraction. *J. Glaciol.*, *57*(201), 111–120.

Westerweel, J. (1997). Fundamentals of digital particle image velocimetry. *Meas. Sci. Technol.*, *8*(12), 1379–1392.

Wheeler, J., Jiang, Z., Prior, D., Tullis, J., Drury, M., and Trimby, P. (2003). From geometry to dynamics of microstructure: using boundary lengths to quantify boundary misorientations and anisotropy. *Tectonophysics*, *376*(1-2), 19–35.

Wheeler, J., Prior, D., Jiang, Z., Spiess, R., and Trimby, P. (2001). The petrological significance of misorientations between grains. *Contrib. to Miner. Pet.*, *141*(1), 109–124.

White, D. J., Take, W. A., and Bolton, M. D. (2003). Soil deformation measurement using particle image velocimetry (PIV) and photogrammetry. *Géotechnique*, *53*(7), 619–631.

White, S. (1976). The Effects of Strain on the Microstructures, Fabrics, and Deformation Mechanisms in Quartzites. *Philos. Trans. R. Soc. A Math. Phys. Eng. Sci.*, *283*(1312), 69–86.

White, S., Burrows, S., Carreras, J., Shaw, N., and Humphreys, F. (1980). On mylonites in ductile shear zones. *J. Struct. Geol.*, *2*(1), 175–187.

Wilson, C., Burg, J., and Mitchell, J. (1986). The origin of kinks in polycrystalline ice. *Tectonophysics*, *127*(1), 27–48.

Wilson, C. J. and Russell-Head, D. S. (1982). Steady-state preferred orientation of ice deformed in plane strain at -1C. *J. Glaciol.*, *28*(98), 145–160.

Wilson, C. J. L. (1982). Fabrics in polycrystalline ice deformed experimentally at 10C. *Cold Reg. Sci. Technol.*, *6*(2), 149–161.

Wilson, C. J. L. and Peternell, M. (2012). Ice deformed in compression and simple shear: control of temperature and initial fabric. *J. Glaciol.*, *58*(207), 11–22.

Wilson, C. J. L., Peternell, M., Piazolo, S., and Luzin, V. (2014). Microstructure and fabric development in ice: Lessons learned from in situ experiments and implications for understanding rock evolution. *J. Struct. Geol.*, *61*, 50–77.

Wilson, C. J. L. and Sim, H. M. (2002). The localization of strain and c-axis evolution in anisotropic ice. *J. Glaciol.*, *48*(163), 601–610.

Wilson, C. J. L. and Zhang, Y. (1996). Development of microstructure in the high-temperature deformation of ice. *Ann. Glaciol.*, *23*(1), 293–301.

Xu, Y., Zhang, J., Bai, Y., and Meyers, M. A. (2008). Shear localization in dynamic deformation: Microstructural evolution. *Metall. Mater. Trans. A Phys. Metall. Mater. Sci.*, *39 A*(4), 811–843.

Xu, Y., Zhong, W., Chen, Y., Shen, L., Liu, Q., Bai, Y., and Meyers, M. (2001). Shear localization and recrystallization in dynamic deformation of 8090 AlLi alloy. *Mater. Sci. Eng. A*, *299*(1-2), 287–295.

Zelin, M. and Mukherjee, A. (1996). Geometrical aspects of superplastic flow. *Mater. Sci. Eng. A*, *208*(2), 210–225.

Appendix A

Making cryo-EBSD routine

Note: Appendix A has been removed for copyright issues. Please see

Prior, D.J., Lilly, K., Seidemann, M., Vaughan, M., Becroft, L., Easingwood, R., Diebold, S., Obbard, R., Daghlian, C., Baker, I., Caswell, T., Golding, N., Goldsby, D., Durham, W.B., Piazolo, S., Wilson, C.J.L., 2015. Making EBSD on water ice routine. J. Microsc. 259, 237–256. doi:10.1111/jmi.12258

Appendix B

Summary of the high confining pressure experiments

This appendix contains a full summary of mechanical, strain distribution and microstructural results of the high confining pressure experiments conducted at the Massachusetts Institute of Technology. It contains otherwise unmentioned experiments with more complicated stress paths, which were conducted in addition to the constant stress experiments shown in Chapters 4 and 5. These complicated stress path experiments could not be analysed any further as the role of localisation phenomena under the experimental conditions investigated was still unclear (section 1.6). The figures are structured as in Chapter 4 and were generated using the same processing techniques.

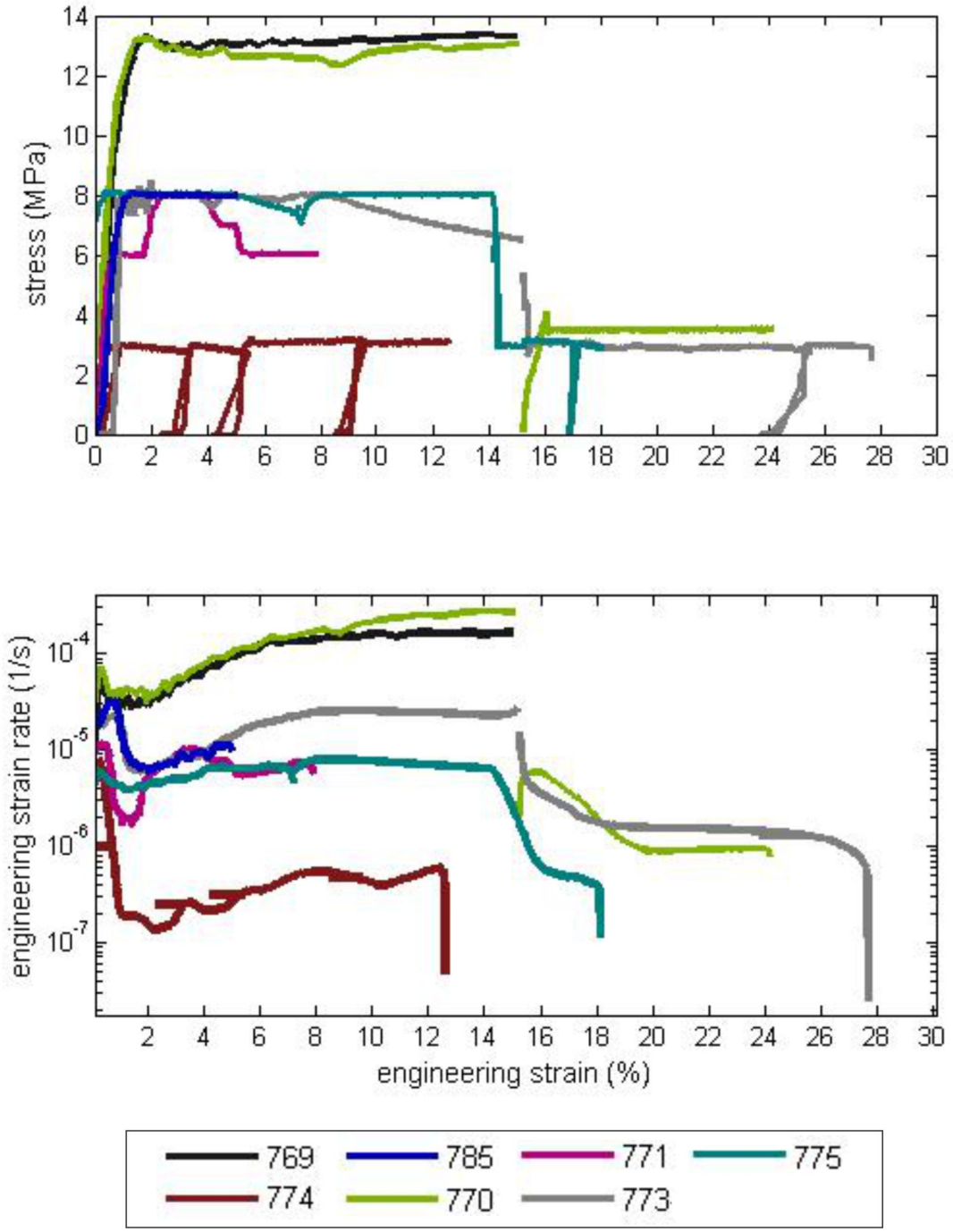

Figure B.1: Mechanical data for deformed Standard ice (250±100 μm starting grain size) and 50 MPa confining pressure at 240 K. Engineering strain vs stress curves are given at the top and strain vs. strain rate curves at the bottom. The processing procedure is described in section 4.2.3. Note that strain rates during steps at ∼3 MPa increase by a magnitude if samples were previously deformed at a higher stress.

Figure B.2: Photos of deformed ice sample in the original sample assemblies with spacer and metal end cap below and the lower part of the force gauge on top of the samples. Numbers in brackets below the photos denote load steps, followed by the target stress and the final engineering strain. All images were contrast-enhanced and partly darkened to better visualise strain markers, such as bumps and dents, on the jackets surfaces. White rectangles display approximate locations of the EBSD maps in Fig. B.3.

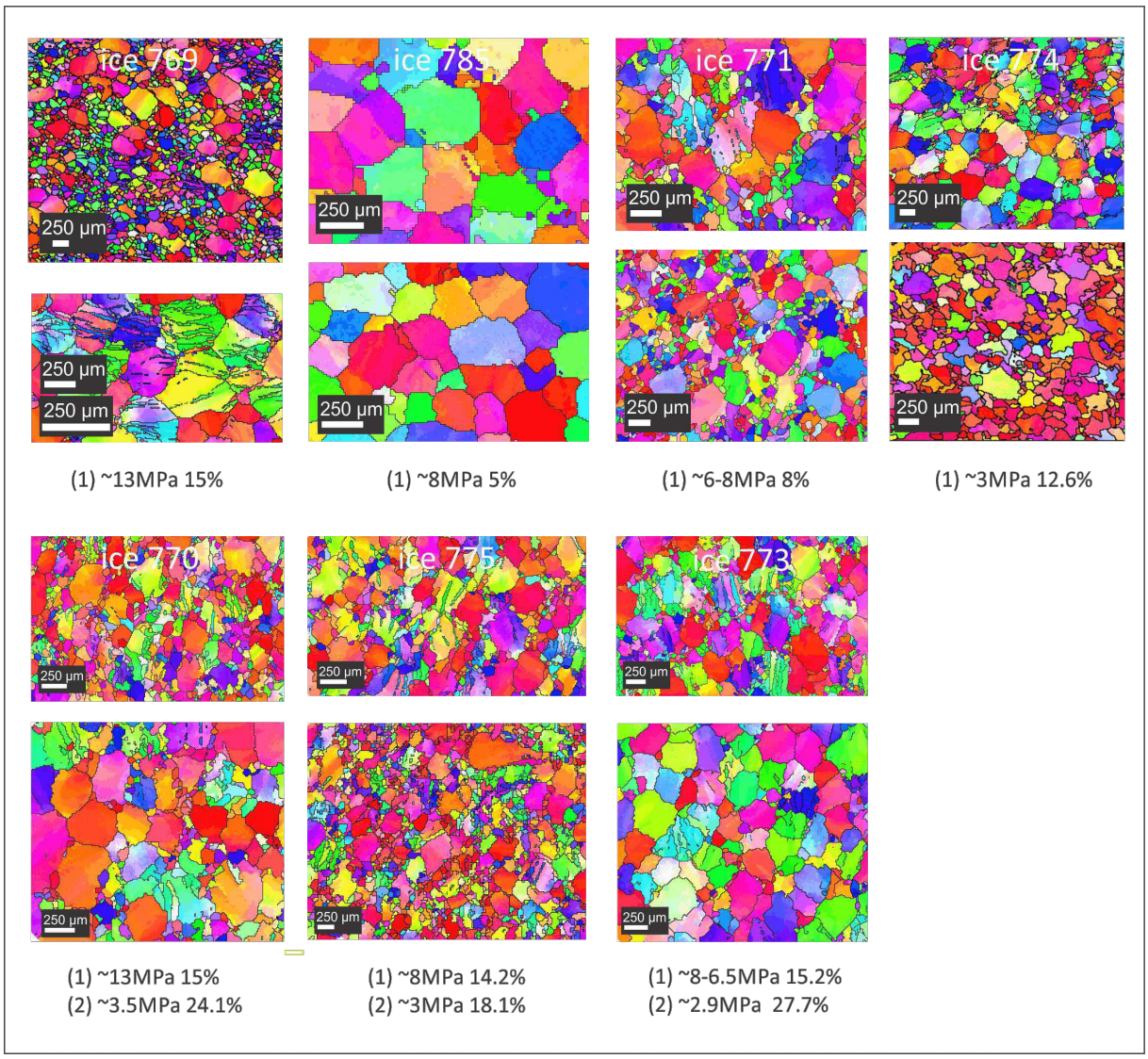

Figure B.3: EBSD orientation maps of the deformed samples. Sample numbers are given in white at the top of the maps. The approximate locations of the maps are indicated in Fig. B.2 with white rectangles. The top map always corresponds to the top rectangle. Single stress and stress drop experiments are shown in top and bottom rows, respectively.